THE UNIVERSITY *of* EDINBURGH

Molecule-based Magnetic Materials of the Re^{IV} ion

Anders Hjordt Pedersen

A thesis submitted for the degree of Doctor of Philosophy

School of Chemistry

University of Edinburgh

May 2017

Til Kasper, Gitte og Ole

Det var ikke lykkedes uden jer

Abstract

The $[ReCl_6]^{2-}$, $[ReBr_6]^{2-}$ and $[ReCl_4(ox)]^{2-}$ anions are crystallised with the organic 4,4'-bipyridinium dication (4,4-H_2bipy). Magnetometry reveals exotic behaviour of the [4,4'-H_2bipy][$ReCl_6$] and [4,4'-H_2bipy][$ReBr_6$] salts which demonstrate spin-canting, antiferromagnetic exchange interactions and metamagnetism. Single crystal X-ray structures at T = 3, 14 and 20 K of the [4,4'-H_2bipy][$ReBr_6$] salt reveal the behaviour to be purely of magnetic origin as no structural changes are observed. For the [4,4'-H_2bipy][$ReCl_4$(ox)] compound an antiferromagnetic exchange interaction of 10.2 cm^{-1} between the anions is observed (Chapter 2).

The complexes $(NBu_4)_2[(ReCl_5)_2(\mu\text{-pyrazine})]$, $(NBu_4)_2[(ReBr_5)_2(\mu\text{-pyrazine})]$, $(NBu_4)_2[(ReBr_5)_2(\mu\text{-pyrimidine})]$ and $(NBu_4)_2[(ReBr_5)_2(\mu\text{-triazine})]$ are structurally and magnetically characterised in Chapter 3. Magnetic measurements reveal the Re^{IV} ions bridged by a 1,4-heterocyclic amine to exhibit strong antiferromagnetic coupling induced by the linearity of the bridging ligand. The two dimers bridged by a 1,3-heterocyclic amine exhibit intramolecular ferromagnetic exchange and at low temperature an intermolecular antiferromagnetic coupling is observed for the $(NBu_4)_2[(ReBr_5)_2(\mu\text{-triazine})]$ complex due to the presence of short intermolecular Br···Br distances.

Six molecular $Re^{IV}Cu^{II}$ chains of formula $\{[Cu(L)_4][ReCl_6]\}_n$ (L = imidazole, 1-methylimidazole, 1-vinylimidazole, 1-butylimidazole, 1-vinyl-1,2,4-triazole or dimethylformamide) are characterised structurally and magnetically in Chapter 4. SQUID magnetometry and theoretical calculations reveal the chains to exhibit ferromagnetic exchange interactions, which increase as the Re–Cl–Cu bond angle decreases. The $\{[Cu(vinylimidazole)_4][ReCl_6]\}_n$ chain exhibit magnetic order at T_C = 2.4 K, and the $\{[Cu(imidazole)_4][ReCl_6]\}_n$ network exhibits ferrimagnetic behaviour.

Eight complexes of the $[ReCl_6]^{2-}$ and $[ReBr_6]^{2-}$ anions crystallised with the $[M^{II}(L^{\bullet})_2]^{2+}$ (M = Fe, Co or Cu) or $[Ni(L^{\bullet})(CH_3CN)_3]^{2+}$ cations ($L^{\bullet}$ = 4-dimethyl-2,2-di(2-pyridyl)oxazolidine *N*-oxide) are characterised structurally and magnetically in Chapter 5. The $[Co(L^{\bullet})_2]^{2+}$ cation shows evidence of a gradual, thermally induced spin-crossover transition in variable-temperature magnetic and structural experiments. The $[Ni(L^{\bullet})(CH_3CN)_3]^{2+}$ cation show exchange of the coordinated acetonitrile molecules for atmospheric water upon drying. The nickel-radical magnetic coupling is ferromagnetic in all cases, demonstrating spin-canting behaviour with an ordering temperature of T = 2.7 K for the $[ReCl_6]^{2-}$ based compound, and intermolecular antiferromagnetic exchange interactions for the $[ReBr_6]^{2-}$ based complex.

Acknowledgements

I'd like to first and foremost thank Prof. Euan K. Brechin for giving me the opportunity to come to Edinburgh and great supervision throughout the project. Thanks to Jose Martinez-Lillo for introducing me to Re^{IV} chemistry. A great thanks to Helen O'Connor and Ross Inglis for all the pints we have drunk and the matches we have seen. Thanks to Sergio Sanz for being a tour guide in Zaragoza, Robbie McNab and Hector Fraser for the Japan trip. Thanks to all my friends that came to visit. Thanks to Julia Vallejo for all the chemistry chat. Thanks to all the people coming through the lab as visiting students. Thanks to previous group members Priyanka Comar and Jamie Frost. Thanks to Gary S. Nichol for help with PXRD and single crystal X-ray crystallography. Thanks to Michael R. Probert for low temperature X-ray crystallography. A big thanks to Ian A. Gass for collaborating on the radical project. Thanks to Joan Cano for the calculations.

Cheers,

Anders

Declaration

I hereby declare that except where specific reference is made to other sources, the work contained in this thesis is the original work of the author. It has been composed by the candidate and has not been submitted, in whole or in part, for any other degree, diploma or other qualification.

Anders Hjordt Pedersen

Format of Thesis

Chapters 2 to 5 of the thesis are my contributions to peer-reviewed papers. The thesis has been formatted accordingly:

Chapter 1: Introduction.

- Insight into the fascinating coordination and magnetochemistry of the Re^{IV} ion.

Chapter 2: Molecular salts of the 4,4'-bipyridinium dication and the $[ReCl_6]^{2-}$, $[ReBr_6]^{2-}$ and $[ReCl_4(ox)]^{2-}$ anions.

- Low temperature structural and magnetic investigations of three novel molecular salts.

Chapter 3: Homometallic Re^{IV} dimers bridged by heterocyclic amines.

- Four paramagnetic Re^{IV} dimers characterised structurally and magnetically.

Chapter 4: A family of $Re^{IV}Cu^{II}$ chains.

- Six molecular chains of general formula $\{[Cu^{II}(L)_4][ReCl_6]\}_n$, whose magnetic coupling depends on the geometry of the Re–Cl–Cu bridge.

Chapter 5: Hexahalorhenate(IV) salts of metal oxazolidine nitroxides.

- Eight complexes comprising an organic radical, 3d transition metal and the Re^{IV} ion. One complex exhibits antiferromagnetic spin-canting.

External contributions:

José Martínez-Lillo –Fitting of magnetic data for the $[4,4'\text{-}H_2bipy][ReCl_4(ox)]$ compound

Joan Cano – Theoretical calculations of the molecular chains

Michael R. Probert – Low temperature single crystal X-ray diffraction on the $[4,4'\text{-}H_2bipy][ReBr_6]$ compound.

Publications

"Effect of Protonated Organic Cations and Anion−π Interactions on the Magnetic Behavior of Hexabromorhenate(IV) Salts" Martinez-Lillo, J.; Pedersen, A. H.; Faus, J.; Julve, M.; Brechin, E. K. *Cryst. Growth Des.*, 2015, ***15***, 2598.

"Self-assembly of the tetrachloro(oxalato)rhenate(IV) anion with protonated organic cations: X-ray structures and magnetic properties." Pedersen, A. H.; Julve, M.; Brechin, E. K.; Martinez-Lillo, J. *CrystEngComm*, 2017, **19**, 503.

"Hexahalorhenate(IV) salts of metal oxazolidine nitroxides" Pedersen, A.H; Martínez-Lillo, J; Lupton, D.W.; Murray, K.S.; Geoghegan, B. L.; Gass, I.A.; Brechin, E.K., Accepted Manuscript, *Dalton Transactions,* 2017, **46**, 5250.

"*A family of Re-Cu chains based on the* $[ReCl_6]^{2-}$ *building block.*" Pedersen, A.H.; Cano, J.; Faus, J.; Julve, M.; Martínez-Lillo, J.; Brechin, E. K. *To be submitted*.

"[4,4'-H_2*bipy][*$ReBr_6$*]: a simple salt with elaborate magnetic behaviour*" Pedersen, A. H.; Cano, J.; Julve, M.; Faus, J.; Parsons, S.; Probert, M. R.; Martínez-Lillo, J.; Brechin, E. K. *To be submitted*.

"*Paramagnetic* Re^{IV} *dimers: controlling the magnetic exchange.*" Pedersen, A.H.; Cano, J.; Faus, J.; Julve, M.; Martínez-Lillo, J.; Brechin, E. K. *To be submitted*.

Contents

Chapter 1: Introduction

1.1 Introduction

This Ph.D. project is focused on rhenium in oxidation state +4, which has 3 unpaired electrons in the 5d t_{2g} shell. Whilst the coordination chemistry and magnetic properties of the Re^{IV} ion have been studied sporadically since the 1950's, caused the discovery of the single molecule magnet (SMM) and thereof bloom of research in the field of molecular magnetism an increased focus on the Re^{IV} ion.[1, 2]

In the quest to create interesting magnetic materials, the ligand sphere of the Re^{IV} ion has been manipulated to obtain compounds containing various donor atoms or increase magnetic anisotropy. However, the robust d^3 ground state combined with the oxidation state +4 being only moderately stable, result in the coordination chemistry of the Re^{IV} ion being rather limited. Indeed, the Re^{IV} ion is prone to oxidation to Re^{V} in the presence of water thereby making solvents with a considerable water content unsuitable for synthesis.

The $[ReX_6]^{2-}$ anions, X = F, Cl, Br or I, are typical precursors for magnetic systems of the Re^{IV} ion. These anions can be synthesised by reduction of perrhenic acid in concentrated HX acid, X = Cl, Br or I, or with the fluorination of the $(NH_4)_2[ReCl_6]$ compound leading to the $[ReF_6]^{2-}$ anion (Figure 1.1).[3-5]

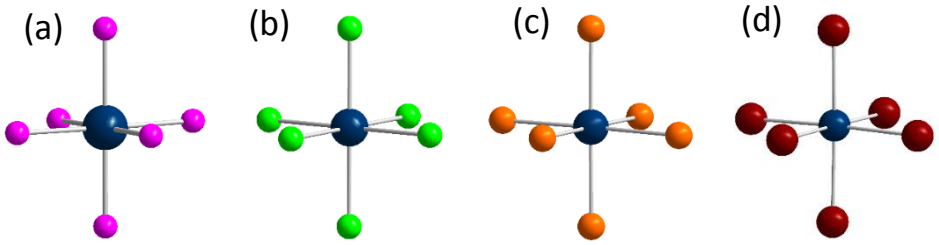

Figure 1.1. a) The $[ReF_6]^{2-}$ anion. b) The $[ReCl_6]^{2-}$ anion. c) The $[ReBr_6]^{2-}$ anion. d) The $[ReI_6]^{2-}$ anion. Colour code; Re, dark blue; I, dark red; Br, orange; Cl, green; F, magenta.

To expand on the functionality of the $[ReX_6]^{2-}$ anion, X = Cl or Br, one halide atom has been exchanged for different heterocyclic amines. This has led to the synthesis of a whole family of Re^{IV} anions with the structure $[ReX_5L]^-$, where X = Cl or Br and L = pyridine,[6] pyrazine,[7] pyrimidine,[8] pyridazine,[8] 2-pyrazinecarboxilic acid,[9] or 3,5-pyridinedicarboxylic acid (Figure 1.2).[10] Various synthetic methods have been employed for the preparation of these anionic building blocks. The $[ReCl_5(pyrazine)]^-$, $[ReCl_5(pyrimidine)]^-$ and $[ReCl_5(pyridazine)]^-$ anions have all been synthesised starting from $(NH_4)_2[ReCl_6]$ or $K_2[ReCl_6]$ together with the respective ligand dissolved in DMF and heated at 100-125°C for 3 to 5 hours.[7, 8] The Re^{IV} monomers containing the 2-pyrazinecarboxylic acid or 3,5-pyridinedicarboxylic acid ligand

were prepared as the $(NBu_4)[ReBr_5(L)]$ compound, NBu_4 = tetrabutylammonium, from $(NBu_4)_2[ReBr_6]$ and the respective ligand in a 2.2:1 isopropanol:acetone mixture heated for 3 hours at 60-70°C.[9, 10] The synthesis of the $[ReCl_5(pyridine)]^-$ anion is slightly more exotic being a solvothermal synthesis with 2-methylpyridine, 4,4'-bipyridine and $(NH_4)[ReCl_6]$ in dry pyridine heated at 150°C for 3 days to produce the (2-methylpyridinium)$_2[ReCl_5(pyridine)]$·4,4'-bipyridine compound.[6]

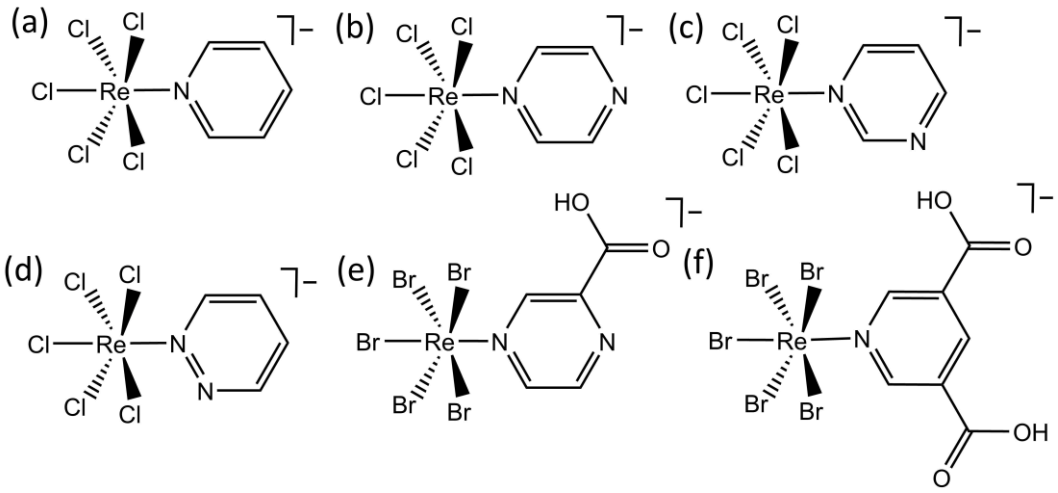

Figure 1.2. The $[ReCl_5L]^-$ anions, L = pyridine (a), pyrazine (b), pyrimidine (c) and pyridazine (d). e) The $[ReBr_5$(2-pyrazinecarboxilic acid)$]^-$ anion. f) the $[ReBr_5$(3,5-pyridinedicarboxylic acid)$]^-$ anion.

The exchange of two halide ions from the $[ReX_6]^{2-}$ moiety requires a different approach. The $[ReCl_4(ox)]^{2-}$ anion, ox = oxalate, being synthesised by the addition of triethylamine to a N_2-degassed DMF solution of $(NH_4)_2[ReCl_6]$ and oxalic acid (Figure 1.3a)[11] and the [*trans*-$ReCl_4(CN)_2]^{2-}$ anion is synthesised in a glove box from $ReCl_4(THF)_2$ by the addition of $(NBu_4)CN$ in DMF (Figure 1.3b).[12]

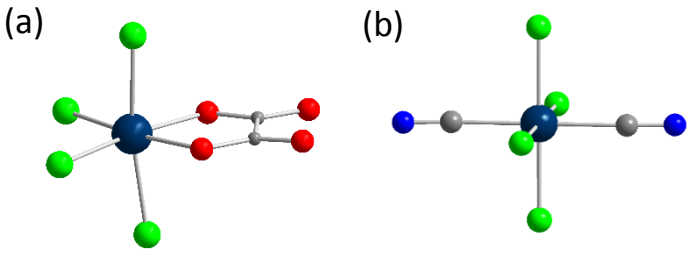

Figure 1.3. a) The $[ReCl_4(ox)]^{2-}$ anion. b) The [*trans*-$ReCl_4(CN)_2]^{2-}$ anion. Colour code; Re, dark blue; Cl, green; O, red; N, blue; C, grey.

The Re^{IV} ion exhibits interesting magnetic behaviour due to its intrinsic magnetic anisotropy, *D*, and spin delocalisation. The significant magnetic anisotropy arises from second order spin-orbit coupling and the large spin-orbit coupling constant, λ, for the free ion of around 1000

cm^{-1}. The spin-orbit coupling causes the ground and higher spin states to mix which uplifts the degeneracy of the $M_s = \pm 1/2$ and $\pm 3/2$ states of the $S = 3/2$ state, as described in equation 1.1 and depicted in Figure 1.4.

$$D = 4\lambda^2 \left(\frac{1}{\Delta_{\parallel}} - \frac{1}{\Delta_{\perp}}\right) \qquad \text{(Eq. 1.1)}$$

Where D is the anisotropy, λ the spin orbit coupling constant and $\Delta_{\parallel}$ and $\Delta_{\perp}$ are the energies separating the first excited states from the ground state (Figure 1.4).

From equation 1.1 it can be seen that when $\Delta_{\perp} > \Delta_{\parallel}$ then D is negative and *vice versa*. Calculations carried out on the $[ReCl_6]^{2-}$ ion showed that an axially compressed octahedron gives rise to a negative D value, -24.3 cm^{-1}, while a positive D value, +19.3 cm^{-1}, was observed for the elongated octahedron.[13]

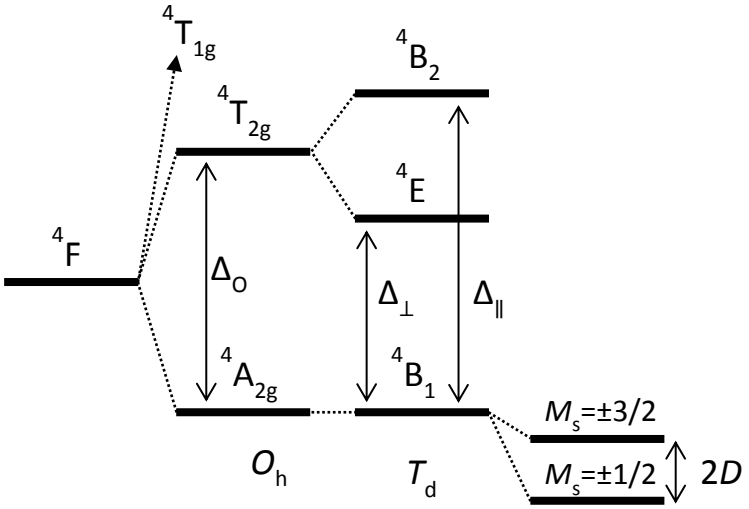

Figure 1.4. The splitting of the energy levels for the free ion and octahedral (O_h) and tetrahedral (T_d) coordination environment of the Re^{IV} ion.

Displacement of spin density from a paramagnetic metal centre onto its ligands is termed spin delocalisation (Figure 1.5a). The spin delocalisation effect increases when going from 3d to 5d transition metals due to greater size and diffuseness of the d-orbitals which leads to an increased covalence of the metal-ligand bond. This effect has been investigated by polarised neutron diffraction (PND) and density functional theory (DFT) calculations which showed it to be particular significant in the Re^{IV} ion.[14-18]

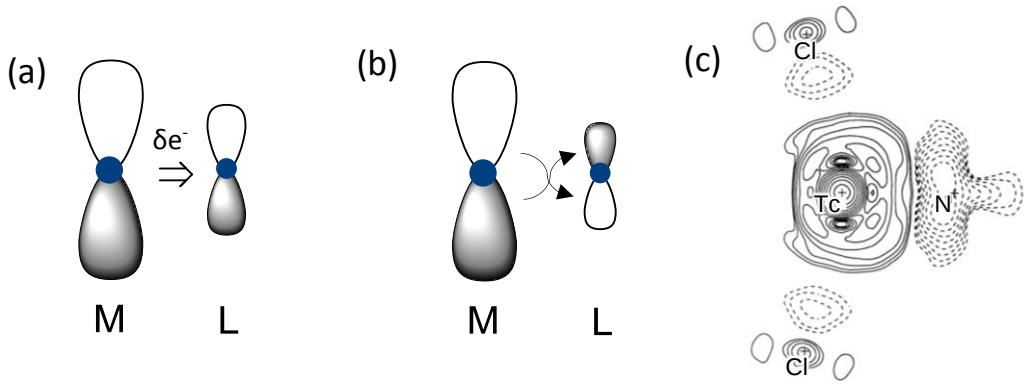

Figure 1.5. The spin delocalisation effect (a) and spin polarisation effect (b) on the metal (M) and ligand (L) atoms. c) PND spin density map of the $[TcNCl_4]^-$ anion the solid lines indicate positive spin density and dashed negative spin density. c) Manipulated from ref. [16].

A PND study on the $[ReCl_4(NH{=}CMeNHPh_2]$ complex discovered that only 53(11)% of the molecule's total magnetisation was to be found on the Re^{IV} ion (Figure 1.6).[14, 15] Comparing this value to similar 3d and 4d transition metals complexes illustrates the increased spin delocalisation in the Re^{IV} compound. PND studies of the $[FeCl_4]^-$ and $[TcNCl_4]^-$ anions revealed just 17 and 29(2)%, respectively, of the spin density to be delocalised onto the chloride ions (Figure 1.5c).[16, 17]

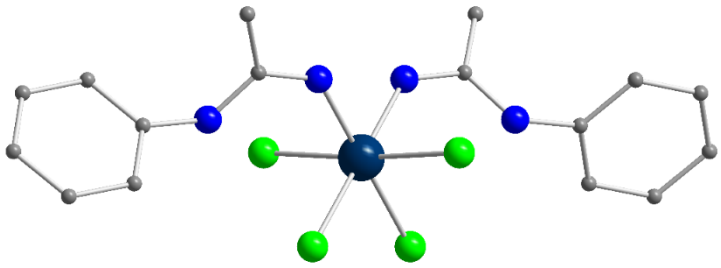

Figure 1.6. The $[ReCl_4(NH{=}CMeNHPh_2]$ complex. Hydrogen atoms are omitted for clarity. Colour code as Figure 1.3.

DFT calculations carried out on the $[ReCl_4(ox)]^{2-}$ anion also illustrate the non-negligible amount of spin density from the Re^{IV} metal centre delocalised onto the chloride ions.[18] For the $[ReCl_4(ox)]^{2-}$ complex the spin density on the Re^{IV} ion was calculated to be +2.4006 e^- $bohr^{-3}$, with the chloride ions containing a combined spin density of +0.3872 e^- $bohr^{-3}$.[18] J. Faus *et al.* also calculated the spin density for the isoelectronic $[CrCl_4(ox)]^{3-}$ complex in which they found a lesser degree of spin delocalisation; the spin density on the chromium metal centre was calculated to be +3.0703 e^- $bohr^{-3}$. These results were in accordance with the predicted trend upon going from 3d to 5d transition metals, although presenting the quantity of delocalised spin density to be smaller than that found in the PND experiment.

Spin delocalisation occurs alongside the spin polarisation mechanism in paramagnetic complexes. Spin polarisation causes the spin density of a metal ion and its coordinated atoms to be of opposite polarity (Figure 1.5b). The PND study on the $[ReCl_4(NH{=}CMeNHPh_2]$ molecule revealed significant spin polarisation on the two nitrogen atoms coordinated to the Re^{IV} ion.[14] The same kind of spin polarisation of the nitrogen ligand was detected for the $[TcNCl_4]^-$ anion (Figure 1.5c).[19] The DFT calculations on the $[CrCl_4(ox)]^{3-}$ and $[ReCl_4(ox)]^{2-}$ anions showed that spin polarisation was only present for the Cr^{III} complex and not for the Re^{IV} anion.[18] In the publication was it suggested for the Re^{IV} ion that spin delocalisation was the dominant feature.

The significant spin delocalisation in 5d transition metal ions has further consequences, in particular, it propagates magnetic coupling between Re^{IV} containing molecules through dipolar exchange interactions. This has been investigated in a plethora of molecular salts containing the $[ReX_6]^{2-}$ anion, X = Cl, Br, or I. The hexahalorhenate anions have been crystallised together with a breadth of different cations. These studies established the magnetic properties in the solid state to be greatly dependent on the packing in the crystal lattice. The cations range from organic molecules with different substituents,[18] organic radicals,[20] alkali metals,[4] ferrocenium,[21] to the SMM 'Mn_6'.[22] These systems exhibit great variation in their magnetic properties such as antiferromagnetic and ferromagnetic exchange interactions and antiferromagnetic spin-canting.[4, 23] Research on the $[ReI_6]^{2-}$ ion crystallised with the alkali metal ions from Li^+ to Cs^+ illustrated the effect of the cations size on the strength of the intermolecular Re–I···I–Re interaction (Figure 1.7). J. Faus and co-workers found the magnetic ordering temperature to increase with decreasing size of the cation.[4]

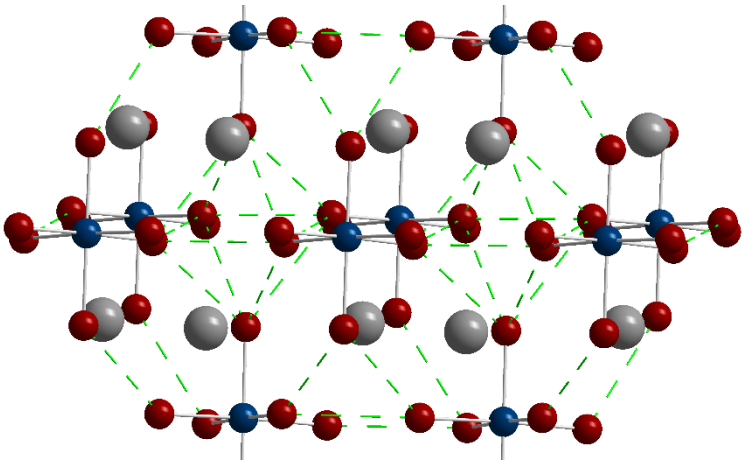

Figure 1.7. The $K_2[ReI_6]$ salt with short Re–I···I–Re interactions indicated by dashed green lines. Colour code; Re, dark blue; I, dark red; K, grey.

Another study revealed that crystallising the anisotropic $[ReCl_6]^{2-}$ ion with the well characterised SMM 'Mn_6' increased the energy barrier for spin relaxation by close to 30%.[22]

Anionic building blocks containing the Re^{IV} ion have been used to create molecular magnetic systems behaving as single ion magnets (SIM), single molecule magnets or single chain magnets (SCM); interesting examples include the [*trans*-$ReCl_4(CN)_2]^{2-}$ and $[ReCl_4(ox)]^{2-}$ anions (Figure 1.3).

The $(NBu_4)_2[ReCl_4(ox)]$ complex have undergone a thorough study of its magnetic properties. The magnetic anisotropy and rhombicity was estimated by high-field EPR spectroscopy to be D = -53 cm^{-1} with $|E/D|$ = 0.26 (Figure 1.8a).[24] The anion also exhibited frequency dependent out-of-phase ac signals in a static field behaviour characteristic of a SIM (Figure 1.8b).

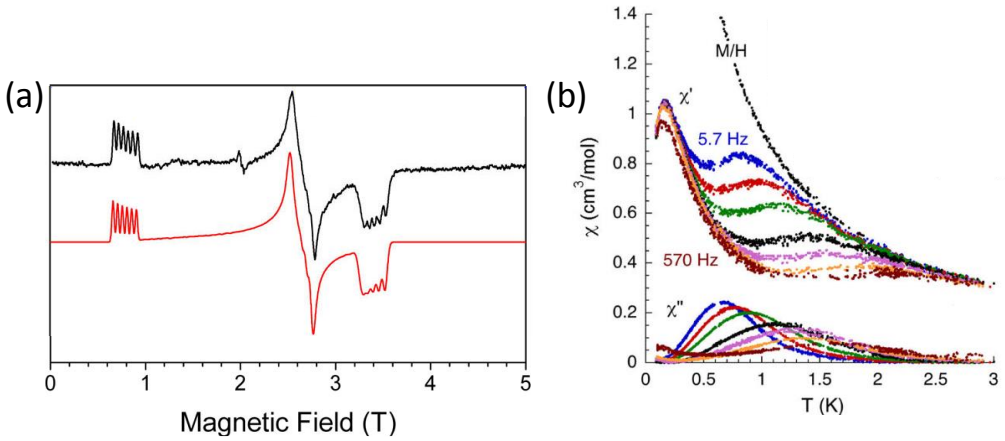

Figure 1.8. a) EPR measurement at T = 10 K and 56 GHz on the $[ReCl_4(ox)]^{2-}$ anion, black line. The red line is simulated with the main parameters being S = 3/2, D = -53 cm^{-1}, $|E/D|$ = 0.26. b) The ac susceptibility measurement in a static field of H = 2000 Oe and frequencies of 5.7-570 Hz. (a) and (b) altered from ref. [24].

The use of the $[ReCl_4(ox)]^{2-}$ anion as a building block towards 3d metals led to the synthesis of one, two and three Re^{IV} moieties coordinated to a single transition metal ion.[25-28] The $[ReCl_4(ox)]^{2-}$ anion coordinated to a single 3d metal ion was, the first time, synthesised as the complex $[ReCl_4(\mu\text{-ox})M^{II}(dmphen)_2]$ with M = Mn, Fe, Co or Ni; dmphen being 2,9-dimethyl-1,10-phenanthroline (Figure 1.9a).[25] The complexes were prepared by adding stoichiometric amounts of Re^{IV} anion, M^{II} salt and dmphen in acetonitrile and crystallised by standing at room temperature, a small quantity of DMF added to the CH_3CN that was used in the synthesis of the Co^{II} and Ni^{II} complexes. Another paper by M. Julve *et al.* also investigated a family of bimetallic $[ReCl_4(\mu\text{-ox})M^{II}(bdmpzm)_2]$, with bdmpzm = bis(3,5-dimethylpyrazol-1-yl)methane and M = Mn, Co, Ni, Cu or Zn.[28] The synthesis and magnetic behaviour of these molecules proved to be similar to that of the previous published compounds (Table 1.1).

The Re_2M compounds of formula $[\{ReCl_4(\mu\text{-ox})\}_2M^{II}(imidazole)_2]^{2-}$, with M = Mn, Co, Ni or Cu, were synthesised by slow evaporation of a 11:1 isopropanol:acetonitrile solution containing stoichiometric ratios of the metal salt, imidazole ligand and $[ReCl_4(ox)]^{2-}$ anion (Figure 1.9b).[26] The $[\{ReCl_4(\mu\text{-ox})\}_3M^{II}]^{4-}$ ions, where M = Mn, Fe, Co, Ni or Cu, completed the bidentate coordination of the Re^{IV} unit to a 3d transition metal ion. The complexes were synthesised in a 22:1 isopropanol:acetonitrile mixture with the Re^{IV} anion and M^{II} salt in a 3:1 ratio and crystallised by standing at room temperature or slow evaporation (Figure 1.9c).[27]

The study of the magnetic properties of these bi-, tri- and tetrametallic compounds illustrated the effect of 'orthogonal' magnetic orbitals leading to ferromagnetic exchange interactions. The $^3t_{2g}$ orbitals of the Re^{IV} ion interacting with the ^2e_g and ^3e_g magnetic orbitals from the Ni^{II} and Cu^{II} metal centres, respectively, gave rise to ferromagnetic coupling.[25-27] It was observed for the Mn^{II}, Fe^{II} and Co^{II} ions that competing antiferromagnetic exchange interactions appeared as the $^6t_{2g}$ orbitals became less filled (Table 1.1).[25-27]

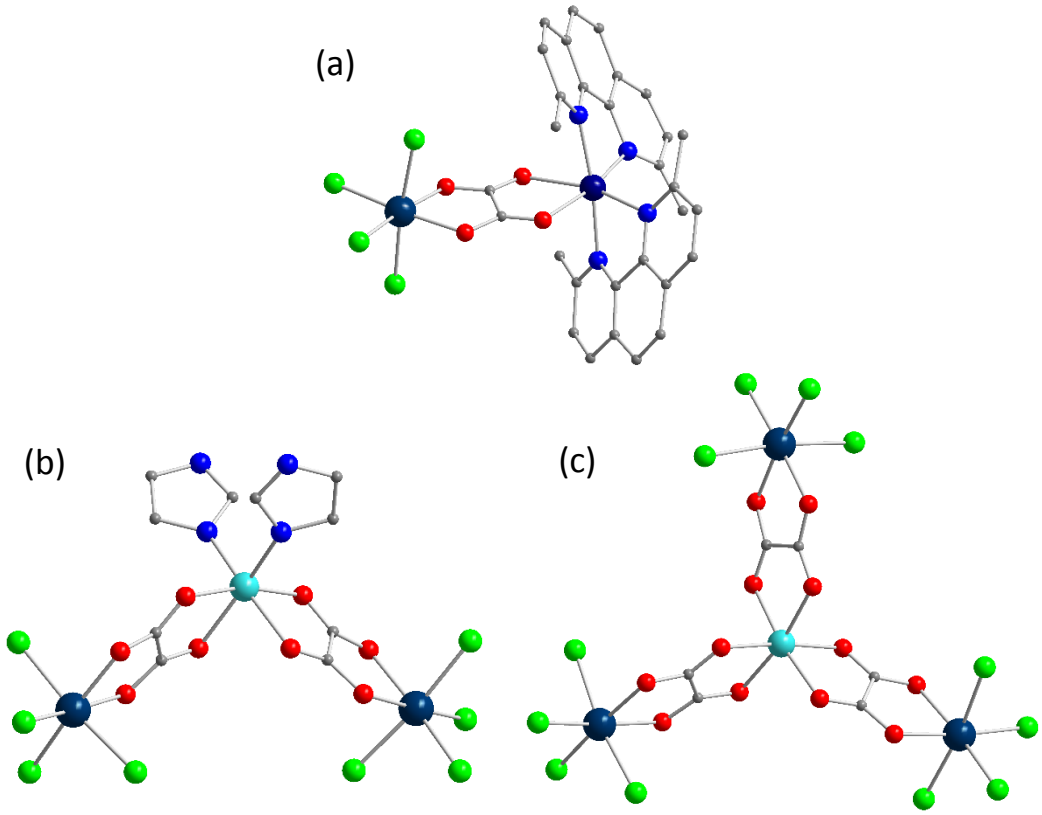

Figure 1.9. a) The $[ReCl_4(\mu\text{-ox})Co(dmphen)_2]$ complex. b) The $[\{ReCl_4(\mu\text{-ox})\}_2Ni(imidazole)_2]^{2-}$ anion. c) The $[\{ReCl_4(\mu\text{-ox})\}_3Ni]^{4-}$ anion. Hydrogen atoms are omitted for clarity. Colour code; Re, dark blue; Ni, cyan; Co, navy blue; Cl, green; O, red; N, blue; C, grey.

Table 1.1. Magnet coupling, J ($\hat{H}$ = -J convention), for the {$ReCl_4(\mu\text{-ox})\}_nM$ complexes, n = 1, 2 or 3.

J / cm^{-1}	ReM	Re_2M[c]	Re_3M[d]
Mn^{II}	-0.2[a], -1.0[b]	-0.35	-1.30
Fe^{II}	+5.6[a]	-	+1.62
Co^{II}	+10.4[a], +3.8[b]	-	+3.0
Ni^{II}	+11.8[a], +13.7[b]	+14.4	+16.3 (+5.53 Ni_3Cr)[e]
Cu^{II}	+6.6[b]	+7.7	+4.64

[a]from ref. [25]. [b]from ref. [28]. [c]from ref. [26]. [d]from ref [27]. [e]the compound [Cr{Ni(Me_6-[14]ane-N_4)(μ-ox)}$_3$](ClO_4)$_3$, taken from ref. [32].

The $(NBu_4)_4[\{ReCl_4(\mu\text{-ox})\}_3Ni^{II}]$ complex proved to be highly interesting as it was shown to possess a spin ground state of S = 11/2 with magnetic anisotropy D = -0.8(1) cm^{-1} and exhibit SMM behaviour with frequency dependent ac signals (in zero static field) and an open hysteresis loop at T = 1 K (Figure 1.10).[29]

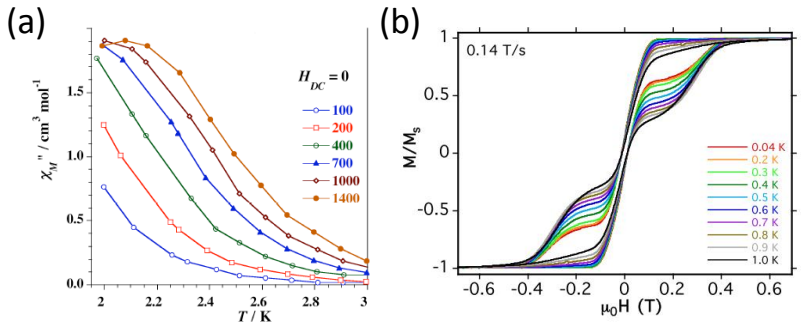

Figure 1.10. a) Ac susceptibility measurement on the $(NBu_4)_4[\{ReCl_4(\mu\text{-ox})\}_3Ni]$ complex in zero dc field. b) Magnetic hysteresis measurements at temperatures from T = 0.04 to 1 K. (a) and (b) taken from ref. [29].

The [*trans*-$ReCl_4(CN)_2]^{2-}$ anion has proved to be an excellent building block for the construction of SCMs. The anion itself was investigated by high field EPR exposing easy plane anisotropy and a large E/D value, D = +11 cm^{-1}, $|E|$ = 3.2 cm^{-1} and $|D/E|$ = 0.29.[30] The anionic building block was used to synthesise molecular chains of formula $\{[M^{II}(DMF)_4][trans\text{-}ReCl_4(CN)_2]\}_n$, with M = Mn, Fe, Co or Ni.[12] The $\{[Fe(DMF)_4][trans\text{-}ReCl_4(CN)_2]\}_n$ chain proved to be the most interesting case, exhibiting frequency dependent ac signals (in zero dc field) and an open hysteresis loop with a coercive field of H_{co} = 1 T at T = 1.8 K (Figure 1.11, and Figure 1.13a).[12] The coordination of [*trans*-$ReCl_4(CN)_2]^{2-}$ anions *cis* to a square pyramidal Cu^{II} ion led to the largest ferromagnetic exchange interaction through a cyanide bridge of +29 cm^{-1} ($\hat{H}$ = -2J convention) (Figure 1.12 and Figure 1.13b).[31]

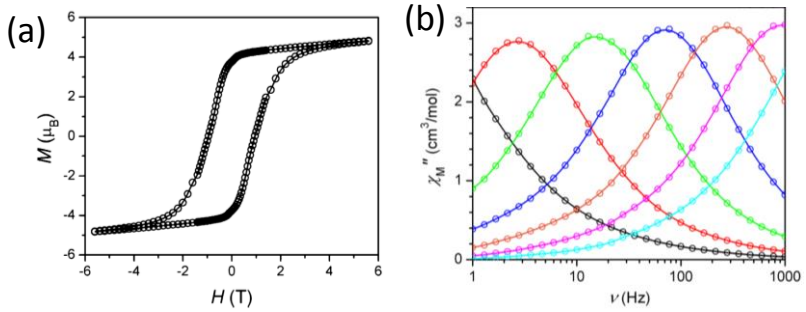

Figure 1.11. a) Magnetic hysteresis measurement at T = 1.8 K for the {[Fe(DMF)$_4$][*trans*-ReCl$_4$(CN)$_2$]}$_n$ chain. b) Frequency dependent ac signals for the {[Fe(DMF)$_4$][*trans*-ReCl$_4$(CN)$_2$]}$_n$ chain at temperatures; 3.6 K, black; 4.0 K, red; 4.4 K, green; 4.8 K, blue; 5.2 K, orange; 5.6 K, magenta; 6.0 K, cyan. (a) and (b) taken from ref. [12].

A comparison of the magnetic exchange interactions for these Re^{IV} compounds with 3d analogues reveal an increased coupling in the 5d complexes. Comparing the {Re(μ-ox)}$_3$Ni system with the Ni{(μ-ox)}$_3$Cr moiety reveal a greater coupling for the Re^{IV}Ni^{II} pair of +16.3 cm^{-1} *vs*. +5.53 cm^{-1}, respectively (Table 1.1).[27, 32] The same effect has been observed, but less pronounced, for the Re–CN–Cu coupling. The {[Cu(hydrotris(pyrazol-1-yl)borate)][*trans*-ReCl$_4$(CN)$_2$]}$_n$ 1D network contain an exchange interaction with a value of +29 cm^{-1} which is greater than the largest related Cr–CN–Cu coupling of +22.75 cm^{-1} (Figure 1.12 and Figure 1.13b).[31, 33] These examples of enhanced magnetic exchange interaction in the Re^{IV} complexes has been attributed to the greater spin delocalisation of the 5d ion with respect to the 3d metal.[27, 31-33]

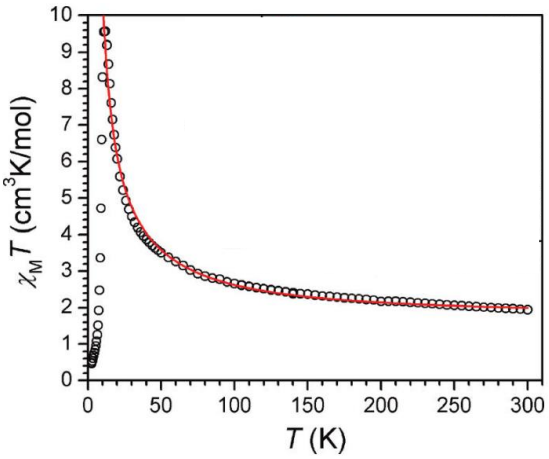

Figure 1.12. The $\chi_M T$ plot for the 1D system {[Cu(hydrotris(pyrazol-1-yl)borate)][*trans*-ReCl$_4$(CN)$_2$]}$_n$, red line illustrating the fit and black circles the experimental data. Graph taken from ref. [31].

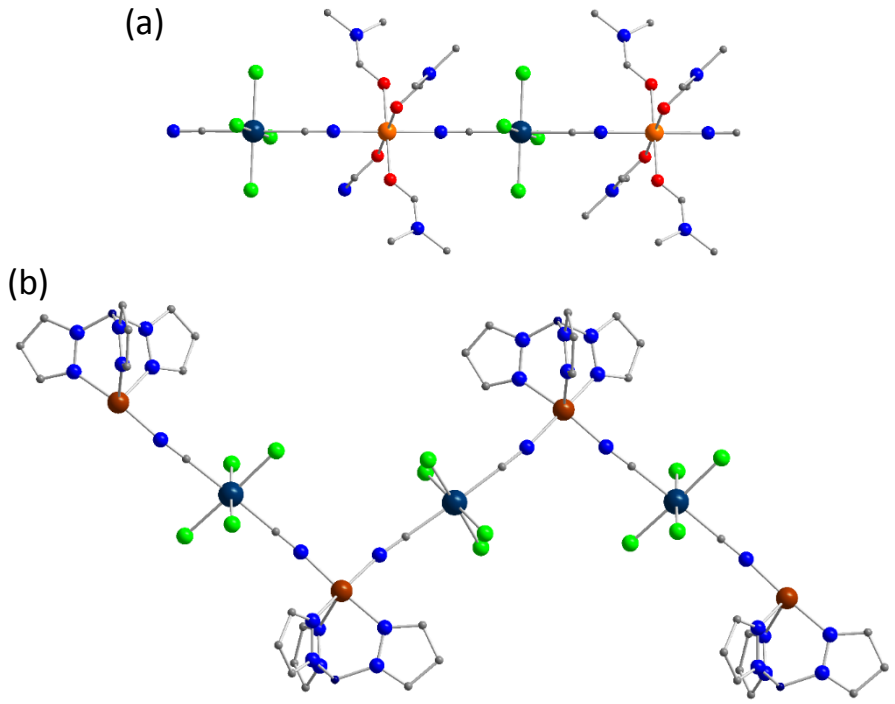

Figure 1.13. a) The {[Fe(DMF)$_4$][*trans*-ReCl$_4$(CN)$_2$]}$_n$ chain. b) The 1D network {[Cu(hydrotris(pyrazol-1-yl)borate)][*trans*-ReCl$_4$(CN)$_2$]}$_n$. Hydrogen atoms are omitted for clarity. Colour code; Re, dark blue; Fe, orange; Cu, bronze; Cl, green; O, red; N, blue; C, grey.

1.2 References

1. C. M. Nelson, G. E. Boyd and W. T. Smith, Jr., *J. Am. Chem. Soc.*, 1954, **76**, 348.
2. R. Sessoli, D. Gatteschi, A. Caneschi and M. A. Novak, *Nature*, 1993, **365**, 141.
3. J. Kleinberg, *Inorg. Synth.*, McGraw-Hill, 1963.
4. R. Gonzalez, R. Chiozzone, C. Kremer, G. De Munno, F. Nicolo, F. Lloret, M. Julve and J. Faus, *Inorg. Chem.*, 2003, **42**, 2512.
5. K. S. Pedersen, M. Sigrist, M. A. Sørensen, A.-L. Barra, T. Weyhermüller, S. Piligkos, C. A. Thuesen, M. G. Vinum, H. Mutka, H. Weihe, R. Clérac and J. Bendix, *Angew. Chem. Int. Ed.*, 2014, **53**, 1351.
6. A. Kochel, *Transition Met. Chem.*, 2010, **35**, 1.
7. J. Martinez-Lillo, D. Armentano, N. Marino, L. Arizaga, R. Chiozzone, R. Gonzalez, C. Kremer, J. Cano and J. Faus, *Dalton Trans.*, 2008, 4585.
8. L. Arizaga, R. González, R. Chiozzone, C. Kremer, M. F. Cerdá, D. Armentano, G. D. Munno, F. Lloret and J. Faus, *Polyhedron*, 2008, **27**, 552.
9. A. Cuevas, C. Kremer, M. Hummert, H. Schumann, F. Lloret, M. Julve and J. Faus, *Dalton Trans.*, 2007, 342.
10. C. Pejo, G. P. Guedes, M. A. Novak, N. L. Speziali, R. Chiozzone, M. Julve, F. Lloret, M. G. F. Vaz and R. Gonzalez, *Chem. - Eur. J.*, 2015, **21**, 8696.
11. R. Chiozzone, A. Cuevas, R. González, C. Kremer, D. Armentano, G. De Munno and J. Faus, *Inorg. Chim. Acta*, 2006, **359**, 2194.
12. T. D. Harris, M. V. Bennett, R. Clérac and J. R. Long, *J. Am. Chem. Soc.*, 2010, **132**, 3980.
13. S. K. Singh and G. Rajaraman, *Nat Commun*, 2016, **7**, 10669.
14. P. A. Reynolds, B. N. Figgis and D. Martin y Marero, *Dalton Trans.*, 1999, 945.

15. P. A. Reynolds, B. Moubaraki, K. S. Murray, J. W. Cable, L. M. Engelhardt and B. N. Figgis, *Dalton Trans.*, 1997, **2**, 263.
16. P. A. Reynolds, B. N. Figgis, J. B. Forsyth and F. Tasset, *Dalton Trans.*, 1997, 1447.
17. B. N. Figgis, P. A. Reynolds and J. B. Forsyth, *Dalton Trans.*, 1988, 117.
18. R. Chiozzone, R. González, C. Kremer, G. De Munno, J. Cano, F. Lloret, M. Julve and J. Faus, *Inorg. Chem.*, 1999, **38**, 4745.
19. B. N. Figgis, P. A. Reynolds and J. W. Cable, *J. Chem. Phys.*, 1993, **98**, 7743.
20. R. Gonzalez, F. Romero, D. Luneau, D. Armentano, G. De Munno, C. Kremer, F. Lloret, M. Julve and J. Faus, *Inorg. Chim. Acta*, 2005, **358**, 3995.
21. R. Gonzalez, R. Chiozzone, C. Kremer, F. Guerra, G. De Munno, F. Lloret, M. Julve and J. Faus, *Inorg. Chem.*, 2004, **43**, 3013.
22. J. Martinez-Lillo, J. Cano, W. Wernsdorfer and E. K. Brechin, *Chem. - Eur. J.*, 2015, **21**, 8790.
23. J. Martínez-Lillo, A. H. Pedersen, J. Faus, M. Julve and E. K. Brechin, *Cryst. Growth Des.*, 2015, **15**, 2598.
24. J. Martínez-Lillo, T. F. Mastropietro, E. Lhotel, C. Paulsen, J. Cano, G. De Munno, J. Faus, F. Lloret, M. Julve, S. Nellutla and J. Krzystek, *J. Am. Chem. Soc.*, 2013, **135**, 13737.
25. R. Chiozzone, R. González, C. Kremer, G. De Munno, D. Armentano, F. Lloret, M. Julve and J. Faus, *Inorg. Chem.*, 2003, **42**, 1064.
26. J. Martínez-Lillo, F. S. Delgado, C. Ruiz-Pérez, F. Lloret, M. Julve and J. Faus, *Inorg. Chem.*, 2007, **46**, 3523.
27. J. Martínez-Lillo, D. Armentano, G. De Munno, W. Wernsdorfer, J. M. Clemente-Juan, J. Krzystek, F. Lloret, M. Julve and J. Faus, *Inorg. Chem.*, 2009, **48**, 3027.
28. I. Gryca, J. Palion-Gazda, B. Machura, M. Penkala, F. Lloret and M. Julve, *Eur. J. Inorg. Chem.*, 2016, **2016**, 5418.
29. J. Martínez-Lillo, D. Armentano, G. De Munno, W. Wernsdorfer, M. Julve, F. Lloret and J. Faus, *J. Am. Chem. Soc.*, 2006, **128**, 14218.
30. X. Feng, J. Liu, T. D. Harris, S. Hill and J. R. Long, *J. Am. Chem. Soc.*, 2012, **134**, 7521.
31. T. D. Harris, C. Coulon, R. Clerac and J. R. Long, *J. Am. Chem. Soc.*, 2011, **133**, 123.
32. Y. Pei, Y. Journaux and O. Kahn, *Inorg. Chem.*, 1989, **28**, 100.
33. V. Marvaud, C. Decroix, A. Scuiller, C. Guyard-Duhayon, J. Vaissermann, F. Gonnet and M. Verdaguer, *Chem. Eur. J.*, 2003, **9**, 1677.

Chapter 2: Molecular salts of the 4,4'-bipyridinium dication and the $[ReCl_6]^{2-}$, $[ReBr_6]^{2-}$ and $[ReCl_4(ox)]^{2-}$ anions

2.1 Introduction

Since the discovery that certain molecules could behave like nanoscale magnets, research focussed on understanding and exploiting the structure-property relationship in molecules and molecule-based materials containing paramagnetic metal ions has flourished.[1-3] Of particular focus has been the role of anisotropy, with the coordination chemistry of the heavier *d*-block metals, lanthanides and actinides seeing a renaissance.[4-9] Among the 5d metal ions, the paramagnetic Re^{IV} ion is very appealing to magnetochemists: it is a $5d^3$ metal ion whose ground electronic state is a $^4A_{2g}$ term with three unpaired electrons and a high value of the spin-orbit coupling constant ($\lambda \approx 1000$ cm^{-1} in the free ion). The six-coordinate Re^{IV} ion possesses large magnetic anisotropy which arises from second order spin-orbit coupling; absolute values of the zero-field splitting parameter, *D*, (2*D* is the energy gap between the two Kramers doublets $M_S = \pm 3/2$ and $\pm 1/2$) are generally in the range 9-26 cm^{-1} for the compounds $A_2[ReX_6]$ (A = univalent cation and X = F, Cl, Br and I).[10-18] A zero-field splitting parameter as large as $D = 73$ cm^{-1} for the compound $(NBu_4)_2[ReBr_4(ox)]$, was recently reported and the anion proved to be the first example of a 5d-based mononuclear Single-Ion Magnet.[19]

The relatively large degree of spin delocalisation from the Re^{IV} ion onto its coordinated ligands causes for significant magnetic exchange interactions to be mediated by intermolecular contacts, even at relatively large metal-metal distances.[20-24] Exchange pathways are of the type Re–X···X–Re,[10, 14, 17, 25, 26] Re–X···(H_2O)···X–Re,[14, 18] and Re–X···π···X–Re,[14, 18] where X = halide anion. Extensive research on the hexahalorhenate anions $[ReX_6]^{2-}$ (X = Cl, Br or I) with a variety of cations ranging from organic molecules with different substituents,[22] organic radicals[27] and alkali metals,[25] to the ferrocenium ion[10] and more complex polymetallic species such as SMMs,[21] has revealed a breadth of fascinating magnetic properties, including antiferromagnetic and ferromagnetic exchange interactions and spin-canting.[14, 25, 28]

So far in the literature, no intermolecular magnetic exchange interactions between $[ReCl_4(ox)]^{2-}$ anions has been reported with the research focusing on the anion's monomeric properties and interactions with paramagnetic cations.[19, 29-32]

We have investigated the use of the 4,4'-bipyridinium dication, 4,4'-H_2bipy, a compact organic dication possible of both Re–X···π and Re–X···H interactions in the crystal lattice

(Figure 2.1). Here we present the synthesis, structure and magnetic behaviour of three molecular salts based on the 4,4'-H_2bipy dication and the Re^{IV} ion. The [4,4'-H_2bipy][$ReCl_6$] (**2.1**) and [4,4'-H_2bipy][$ReBr_6$] (**2.2**) salts demonstrate an intriguing combination of low temperature magnetic behaviours. Indeed they are the first 5d transition metal compounds to exhibit antiferromagnetic order, spin-canted antiferromagnetism and field-induced ferromagnetism (metamagnetism), a trio of phenoma only previously observed in networks of anisotropic 3d transition metal ions.[33-35] The [4,4'-H_2bipy][$ReCl_4$(ox)] salt (**2.3**) is the first investigation of intermolecular magnetic exchange interactions purely between [$ReCl_4$(ox)]$^{2-}$ anions.

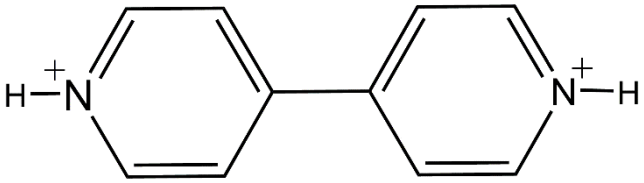

Figure 2.1. The 4,4'-bipyridinium dication.

2.2 Experimental

2.2.1 Materials and methods

All chemicals were used as received. Syntheses were carried out under aerobic conditions. $(NBu_4)_2[ReCl_6]$, $(NBu_4)_2[ReBr_6]$ and $(NBu_4)_2[ReCl_4(ox)]$ were prepared as described previously.[22, 29, 36, 37] Crystals of the three compounds were collected and left open to air for use in further analysis. Elemental analyses (C, H, N) were performed by MEDAC Ltd. Alternate and direct current (ac and dc) magnetic susceptibility measurements were collected on Quantum Design MPMS-XL SQUID and Quantum Design PPMS magnetometers equipped with 7 T dc magnets in the temperature range 1.8-300 K. Diamagnetic corrections were applied using Pascal's constants.[38]

2.2.2 Crystallography

Data were measured on Rigaku Oxford Diffraction SuperNova (**2.1**, **2.3**) and Bruker APEX2 CCD area detector (**2.2**) X-ray diffractometers using Mo-K_α (**2.1, 2.2**) or Cu-K_α (**2.3**) radiation. Structures were solved with olex2.solve (**2.3**),[39] ShelXS (**2.1**)[40] or SIR2004 (**2.2**)[41] and refined by full-matrix least-squares on F-squared using ShelXL, interfaced through Olex2.[42] All non-hydrogen atoms were refined anisotropically. H1a in **2.1** and H2 in **2.3** were seen in the difference maps before they were geometrically created in the model. The remaining hydrogen atom parameters were constrained.

2.2.3 Synthesis of $[4,4'\text{-}H_2bipy][ReCl_6]$ (2.1)

$(NBu_4)_2[ReCl_6]$ (0.1 mmol, 88 mg) and 4,4'-bipyridine (0.2 mmol, 31.2 mg) in 4 ml glacial acetic acid was stirred at 110°C overnight. A yellow solid was collected by filtration and crystallised from hot 4 M HCl acid at room temperature. Yellow crystals suitable for X-ray diffraction were grown overnight at 4 °C (31% yield). Elemental analysis (%) calculated (found) for $C_{10}H_{10}N_2Cl_6Re$: C, 21.6 (21.8); H, 1.8 (1.9); N, 5.0 (5.0).

2.2.4 Synthesis of $[4,4'\text{-}H_2bipy][ReBr_6]$ (2.2)

$(NBu_4)_2[ReBr_6]$ (0.1 mmol, 115 mg) and 4,4'-bipyridine (0.2 mmol, 31.2 mg) in 4 ml glacial acetic acid were stirred at room temperature for 2 hours after which an orange solid was collected by filtration. The solid was crystallised from 6 M HBr acid. Red crystals suitable for X-ray diffraction were grown overnight at 4 °C (35% yield). Elemental analysis (%) calculated (found) for $C_{10}H_{10}N_2Br_6Re$: C, 14.6 (14.9); H, 1.2 (2.5); N, 3.4 (3.3).

2.2.5 Synthesis of [4,4'-H_2bipy][$ReCl_4$(ox)] (2.3)

$(NBu_4)_2$[$ReCl_4$(ox)] (0.1 mmol, 90.0 mg) and 4,4'-bipyridine (0.20 mmol, 31.2 mg) were mixed in 3 ml glacial acetic acid and stirred for 2 hours. A yellow solid was obtained, collected by filtration, and recrystallized in hot 4 M HCl. Pale green crystals suitable for X-ray diffraction were grown by standing overnight at 4 °C (31% yield). Elemental analysis (%) calculated (found) for $C_{12}H_{10}O_4N_2Cl_4Re$: C, 25.1 (25.2); H, 1.8 (1.9); N, 4.9 (4.8).

2.3 Structures

2.3.1 Structure of [4,4'-H_2bipy][$ReCl_6$] (2.1)

The compound crystallises in the orthorhombic space group *Ibam*, with a quarter of the cation and half the anion at 50% occupancy in the asymmetric unit (Table 2.3.1). The doubly protonated [4,4'-H_2bipy]$^{2+}$ cation exhibits a twisted aryl-aryl bond with a [C–C–C–C] torsion angle of 38.3(3)° and contains C–C and C–N bonds with values similar to other published compounds containing the same cation (Table 2.3.3).[43, 44] The Re^{IV} ion sits in a slightly distorted octahedral geometry coordinated to six chloride atoms with bond lengths of 2.3401(9), 2.3493(8) and 2.3661(9) Å for Re(1)–Cl(1), Re(1)–Cl(2) and Re(1)–Cl(3), respectively (Figure 2.3.1). In the $[ReCl_6]^{2-}$ unit, the *cis* angles are between 89.23(3) to 90.77(3)°, with all *trans* angles being 180° due to the presence of an inversion centre situated on the Re^{IV} ion. The geometrical parameters of the $[ReCl_6]^{2-}$ moiety are in accordance with previously published molecular salts containing this anion and various organic cations.[18, 27]

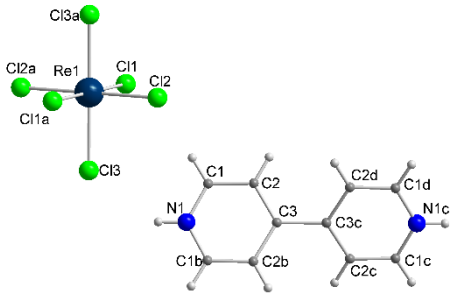

Figure 2.3.1. Molecular structure of **2.1**. Atoms labelled in accordance with Table 2.3.2. Colour code; Re, dark blue; Cl, green; N, blue; C, grey; H, white.

In the crystal lattice, **2.1** packs through a network of short Cl···Cl interactions and N–H···Cl hydrogen bonds. The shortest Cl···Cl distance between neighbouring $[ReCl_6]^{2-}$ units (Cl(3)···Cl(3)') is 3.0980(16) Å creating rows of anions travelling parallel to the crystallographic *c*-axis (Figure 2.3.2, dashed blue lines). In the crystallographic *ab*-plane, each $[ReCl_6]^{2-}$ ion interacts with four anions through short Cl···Cl separations of 3.3074(12) Å, Cl(1)···Cl(2)' (Figure 2.3.2, dashed red lines).

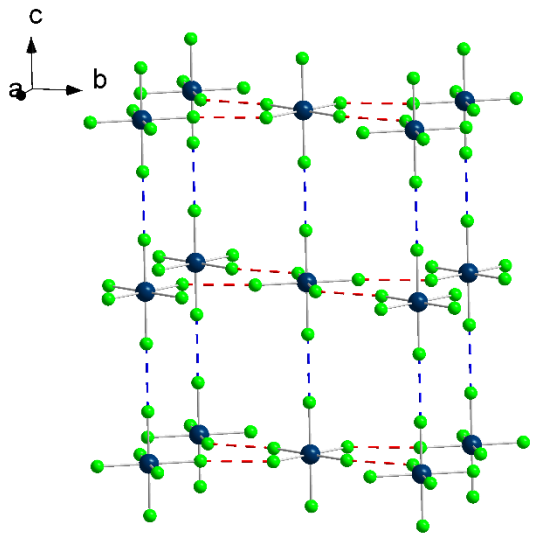

Figure 2.3.2. The packing of the $[ReCl_6]^{2-}$ anions with short Cl···Cl distance indicated by blue and red dashed lines. Colour code; Re, dark blue; Cl, green.

The $[4,4'\text{-}H_2bipy]^{2+}$ units interact through bifurcated N–H···$(Cl)_2$ hydrogen bonds to two anions positioned 'above' and 'below' the cation, with respect to the crystallographic *c*-axis (Figure 2.3.3). These hydrogen bonds travel in the direction of the crystallographic *b*-axis (Table 2.3.7 and Figure 2.3.3). The intermolecular interactions create a layered structure of cations and anions, when viewed down the crystallographic *a*- or *b*-axes (Figure 2.3.4 and 2.3.5).

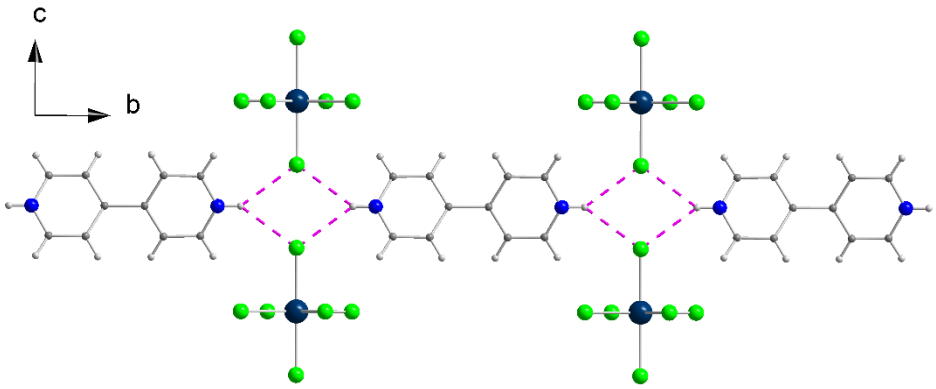

Figure 2.3.3. The hydrogen bonds, magenta lines, travelling in the crystallographic *b*-axis. Colour code as Figure 2.3.1.

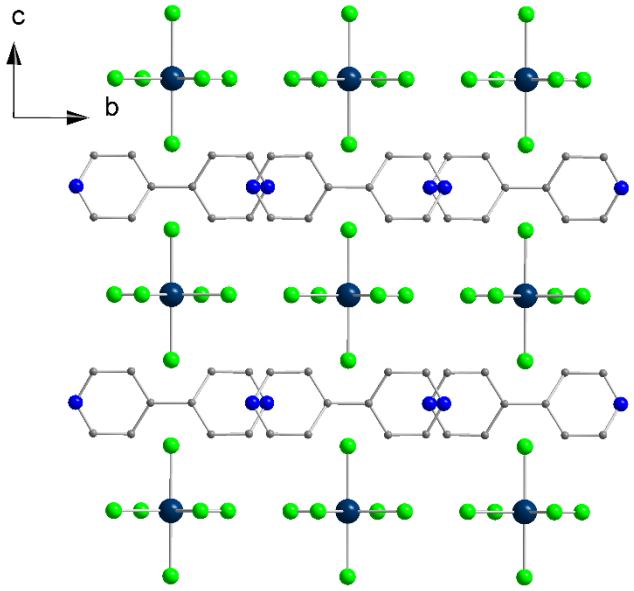

Figure 2.3.4. The crystal packing viewed down the crystallographic *a*-axis. Hydrogen atoms are omitted for clarity. Colour code as Figure 2.3.1.

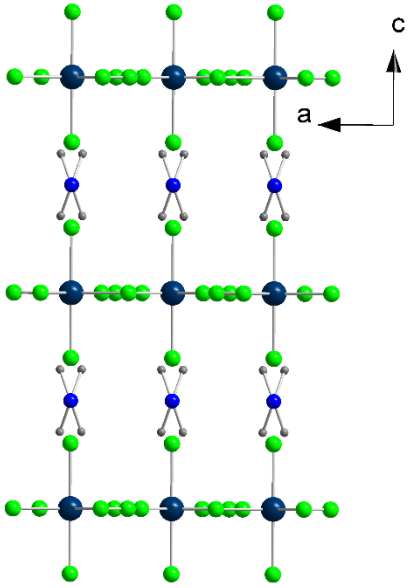

Figure 2.3.5. The crystal packing viewed down the crystallographic *b*-axis. Hydrogen atoms are omitted for clarity. Colour code as Figure 2.3.1.

2.3.2 Structure of [4,4'-H_2bipy][$ReBr_6$] (2.2)

In order to obtain structural information at low temperatures, where the various important magnetic behaviours are observed (*vide infra*) have we performed variable temperature, single crystal X-ray diffraction at T = 3.3, 14 and 20 K (Tables 2.3.1 and 2.3.2). The crystal structure described below was measured at T = 3.3 K and is very similar to those obtained at

all other temperatures, with only very small differences in bond lengths and bond angles (Figure 2.3.6 and Table 2.3.4).

The complex crystallises in the monoclinic space group *C*2/*c* and consists of the doubly protonated 4,4'-H_2bipy dication and one hexabromorhenate dianion. The asymmetric unit contains four unique, half $[ReBr_6]^{2-}$ anions and two non-equivalent $[4,4'\text{-}H_2bipy]^{2+}$ cations, giving rise to a large unit cell volume of 6667.52(3) $Å^3$ (Figure 2.3.6, Table 2.3.2).

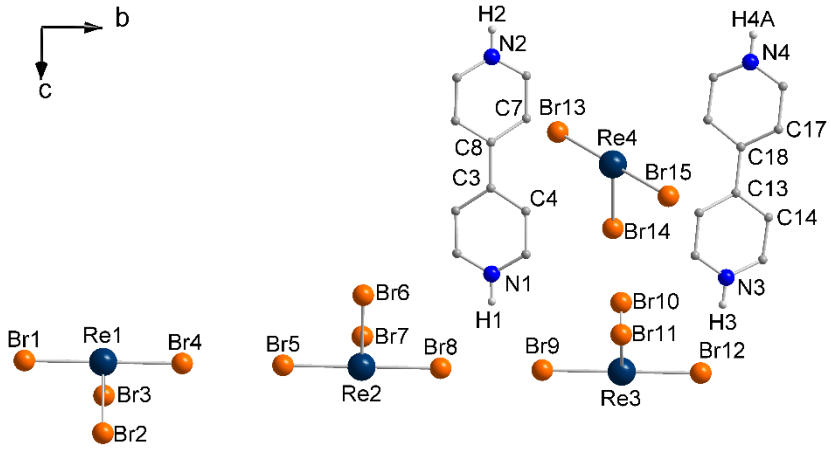

Figure 2.3.6. The asymmetric unit of **2.2**. Atoms labelled in accordance with Table 2.3.4 and 2.3.7. Only selected hydrogen atoms are shown. Colour code: Re, dark blue; Br, orange; N, blue; C, grey; H, white.

The $[4,4'\text{-}H_2bipy]^{2+}$ ions exhibit twisted aryl-aryl bonds with [C–C–C–C] torsion angles of 40.7(11)-43.6(11)°, and contain C–C and C–N bonds with values similar to other published compounds containing the same cation.[43, 44] The Re^{IV} ions sit in slightly distorted octahedral geometries coordinated to six bromide ions with bond lengths of 2.4872(7)-2.5316(10) Å. The *cis* angles range from 88.40(2) to 91.38(2)° with the most bent *trans* angle being 177.37(3)°. The geometrical parameters of the $[ReBr_6]^{2-}$ moiety are in accordance with previously published molecular salts containing this anion and various organic cations.[13, 14] In the crystal lattice, the $[ReBr_6]^{2-}$ anions pack through a network of short Br···Br and Br···π interactions, as well as Br···H–N hydrogen bonds. The shortest Br···Br distances are 3.2125(12) and 3.2422(12) Å for Br(4)···Br(5) and Br(8)···Br(9), respectively, creating a trimer of $[ReBr_6]^{2-}$ units travelling in the direction of the crystallographic *b*-axis (Figure 2.3.7).

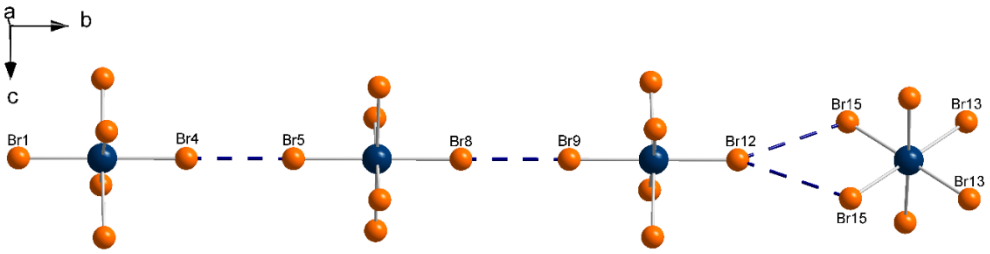

Figure 2.3.7. The repeating pattern of three parallel and one tilted $[ReBr_6]^{2-}$ anion along the crystallographic *b*-axis. Short Br···Br interactions indicated by dashed blue lines. Colour code: Re, dark blue; Br, orange.

Viewed down the crystallographic *b*-axis, the three $[ReBr_6]^{2-}$ anions are slightly rotated relative to each other. A fourth $[ReBr_6]^{2-}$ unit lies tilted by *ca*. 45°, with respect to the crystallographic *b*-axis, at the end of each trimeric moiety with slightly longer Br···Br distances of 3.6798(11) and 3.7694(11) Å for Br(1)···Br(13) and Br(12)···Br(15), respectively (Figure 2.3.7). The pattern of one tilted $[ReBr_6]^{2-}$ unit followed by the trimeric moiety, repeats itself in the direction of the crystallographic *b*-axis.

In the crystallographic *ac*-plane the anions are connected through an extended network of short Br···Br interactions to six neighbouring anions (Figure 2.3.8). The Br···Br interactions vary from 3.4546(9) to 4.1963(9) Å, as seen in Table 2.3.6 and Figure 2.3.8.

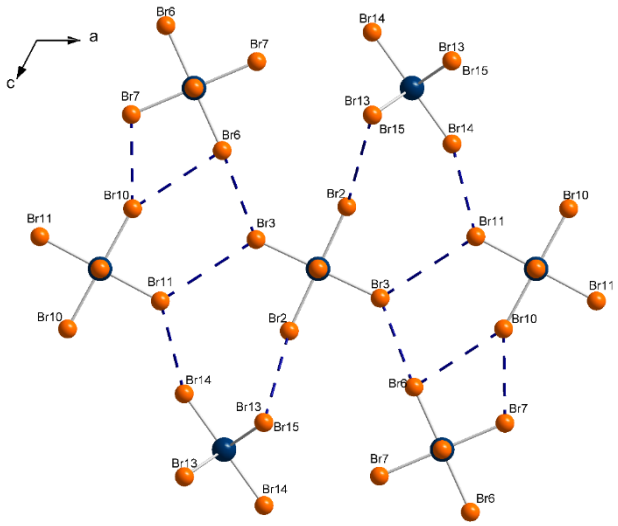

Figure 2.3.8. The anionic interactions in the crystallographic *ac*-plane. Short Br···Br interactions indicated by dashed blue lines. Atoms labelled in accordance with Table 2.3.6. Colour code as Figure 2.3.7.

The $[4,4'\text{-}H_2bipy]^{2+}$ cations pack in the crystallographic *ac*-plane through N–H···Br hydrogen bonds and π···Br interactions (Figure 2.3.9). The N–H···Br interactions are three centred N–H···$(Br)_2$ hydrogen bonds with the cation bonding to anions 'above and below' the $[4,4'\text{-}H_2bipy]^{2+}$ unit with respect to the crystallographic *b*-axis (Figure 2.3.9 and Table 2.3.7). These

bifurcated hydrogen bonds travel in the directiction of the crystallographic *c**-axis (reciprocal c-axis).

The cations pack further through short $\pi\cdots$Br distances between the 'tilted' $[ReBr_6]^{2-}$ anion and two cations (Figure 2.3.9b). The $\pi\cdots$Br interactions are 3.564(3) and 3.454(3) Å for Br(13)···N(2)ring and Br(15)···N(3)ring centroids, respectively. All of these interactions create a layered structure of cationic and anionic planes when viewed along the crystallographic *a* or *c*-axes (Figure 2.3.10 and 2.3.11).

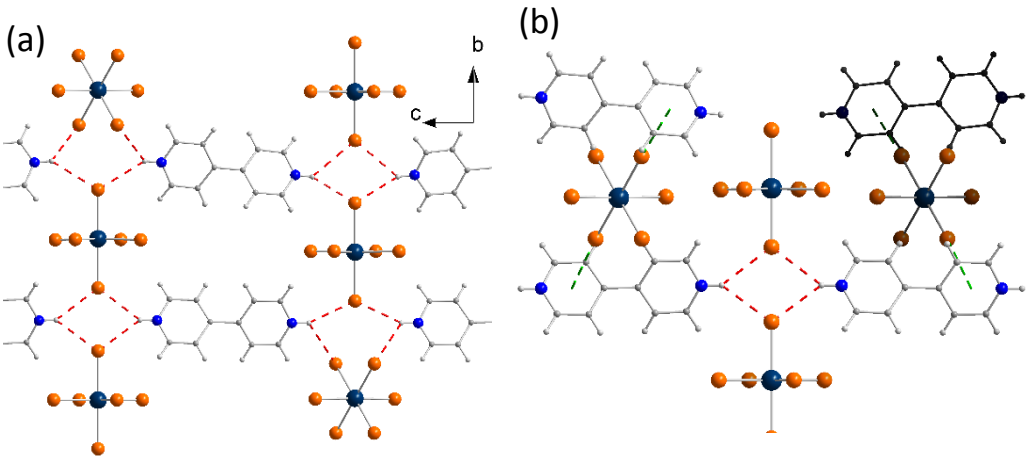

Figure 2.3.9. a) N–H···Br hydrogen bonds between cation and anions. b) N–H···Br hydrogen bonds and $\pi\cdots$Br interactions between cation and anions. Hydrogen bonds and $\pi\cdots$Br interactions are indicated by dashed red and green lines, respectively. Colour code as Figure 2.3.6.

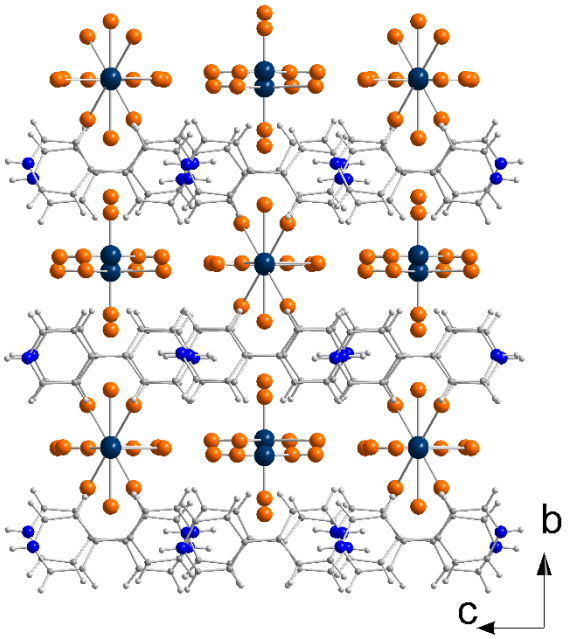

Figure 2.3.10. The packing of the molecule viewed down the crystallographic *a*-axis. Colour code as Figure 2.3.6.

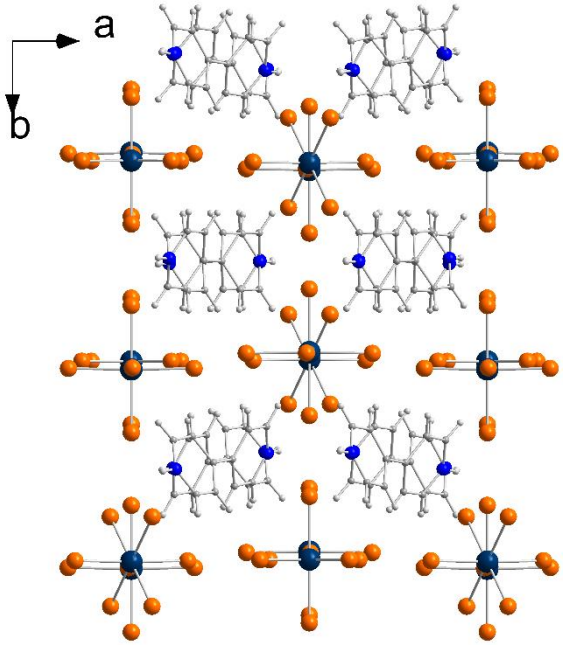

Figure 2.3.11. The packing of the molecule viewed down the crystallographic *c*-axis. Colour code as Figure 2.3.6.

2.3.3 Structure of [4,4'-H_2bipy][$ReCl_4$(ox)] (2.3)

[4,4'-H_2bipy][$ReCl_4$(ox)] crystallises in a monoclinic system with the space group *C*2/*c* (Table 2.3.1). The structure consists of one $[ReCl_4(ox)]^{2-}$ anion and the $[4,4'\text{-}H_2bipy]^{2+}$ dication with the asymmetric unit containing two chloride ions, half an oxalate molecule, half a 4,4'-bipyridinium cation, together with a rhenium(IV) ion that lies on a special position (Figure 2.3.12, labelled atoms).

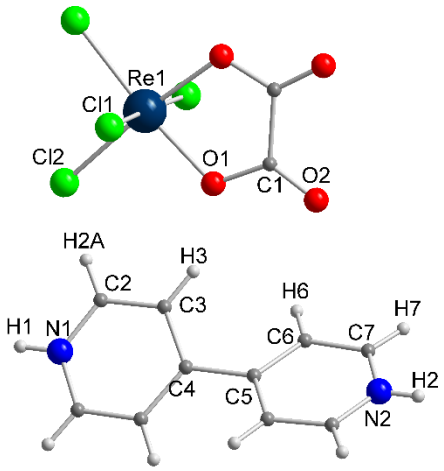

Figure 2.3.12. The [4,4'-H_2bipy][$ReCl_4$(ox)] compound. Atoms labelled in accordance with Table 2.3.5. Colour code; Re, dark blue; Cl, green; O, red; N, blue; C, grey; H, white.

The Re^{IV} ion is in a distorted octahedral geometry bonded to four chloride ions and two oxygen atoms, with the O–Re–O angle of 79.96(17)° being the main source of the distortion. The Re–Cl bond lengths of 2.3442(11) and 2.3369(10) Å and Re–O bond of 2.051(3) Å are in agreement with the previously reported $(NBu_4)_2[ReCl_4(ox)]$ compound.[29]

The 4,4'-bipyridinium cation exhibits protonation on both nitrogen atoms with the torsion angle through the aryl-aryl bond [C–C–C–C] being 31.5(3)° (Figure 2.3.12). The torsion angle and values of the C–C and C–N bond lengths are in agreement with those found in salts based on this doubly protonated organic cation.[43, 44] In the crystal lattice, the $[ReCl_4(ox)]^{2-}$ anions sit between two $[4,4'\text{-}H_2bipy]^{2+}$ cations, interacting through bifurcated N–H···$(O)_2$ and N–H···$(Cl)_2$ hydrogen bonds (Figure 2.3.13 and Table 2.3.7).

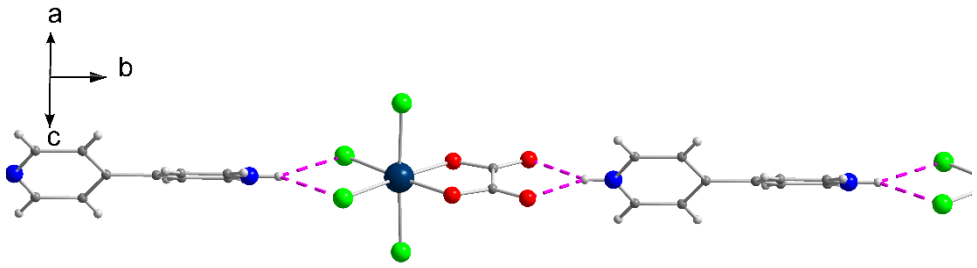

Figure 2.3.13. The hydrogen bonds, dashed magenta lines, travelling in the direction of the crystallographic *b*-axis. Colour code as Figure 2.3.12.

This leads to a 1D motif propagating along the crystallographic *b*-axis. These 1D networks interact with adjacent ones through short Cl···π distances of *ca*. 3.3 Å, in the direction of the crystallographic *a*-axis (Figure 2.3.14).

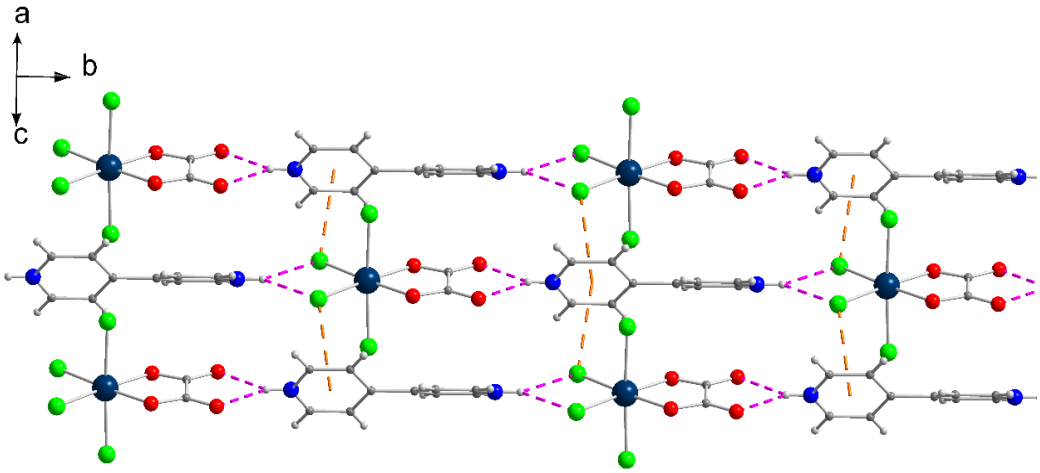

Figure 2.3.14. Intermolecular N–H···O, N–H···Cl and Cl···π interactions in the crystallographic *ab*-plane. Cl···π interactions indicated by dashed orange lines and hydrogen bonds by dashed magenta lines. Colour code as Figure 2.3.12.

The $[ReCl_4(ox)]^{2-}$ anions pack through short Cl···Cl and Cl···π interactions with distances of *circa* 3.96 and 3.30 Å, respectively, in rows propagating in the crystallographic *c*-axis with a Re···Re separation of approximately 6.72 Å (Figure 2.3.15). Adjacent anionic 1D networks interacts through short Cl···Cl distances of *ca*. 3.70 Å but greater Re···Re seperation of 7.34 Å, creating an anionic 3D network (Figure 2.3.15).

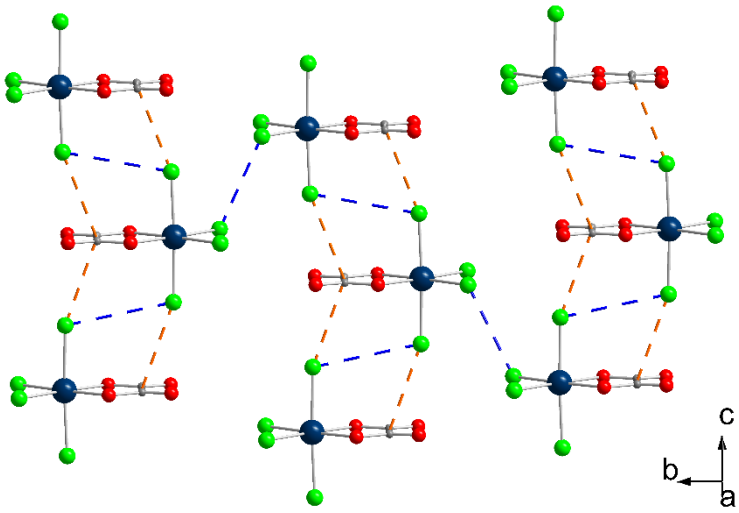

Figure 2.3.15. The packing of the anions in the crystallographic *bc*-plane. Short Cl···Cl and Cl···π interactions indicated by dashed blue and orange lines, respectively. Colour code as in Figure 2.3.12.

2.3.4 Tables of crystallographic and structural parameters

Table 2.3.1. Crystallographic parameters for **2.1**, **2.2** and **2.3**.

	2.1	**2.2**·3.3 K	**2.3**
Crystal data			
Chemical formula	$Cl_6Re{\cdot}C_{10}H_{10}N_2$	$Br_6Re{\cdot}C_{10}H_{10}N_2$	$C_2Cl_4O_4Re{\cdot}C_{10}H_{10}N_2$
M_r	557.10	823.86	574.22
Crystal system, space group	Orthorhombic, *Ibam*	Monoclinic, *C*2/*c*	Monoclinic, *C*2/*c*
Temperature (K)	120	3	120
a,	7.3559 (4),	15.9238 (4),	9.3070 (3),
b,	12.8369 (5),	31.6930 (8),	17.6267 (4),
c (Å)	15.6603 (9)	14.8880 (4)	10.8072 (3)
β (°)	90	117.452 (1)	113.592 (4)
V (Å^3)	1478.75 (14)	6667.5 (3)	1624.75 (9)
Z	4	16	4
Radiation type	Mo *K*α	Mo *K*α	Cu *K*α
μ (mm^{-1})	9.29	21.66	20.88
Crystal size (mm)	0.14 × 0.13 × 0.09	× ×	0.48 × 0.06 × 0.02
Data collection			
T_{min}, T_{max}	0.778, 0.838	× ×	0.311, 1.000
No. of measured, independent and observed [$I > 2\sigma(I)$] reflections	9397, 1369, 1179	39179, 6248, 5015	12929, 1700, 1661
R_{int}	0.040	0.031	0.066
$(\sin\theta/\lambda)_{max}$ (Å^{-1})	0.761	0.626	0.630
Refinement			
$R[F^2 > 2\sigma(F^2)]$, $wR(F^2)$, *S*	0.022, 0.041, 1.10	0.029, 0.070, 1.15	0.032, 0.086, 1.03
No. of reflections	1369	6248	1700
No. of parameters	52	348	109
No. of restraints	0	282	0
$\Delta\rho_{max}$, $\Delta\rho_{min}$ (e Å^{-3})	1.54, −0.80	2.04, −1.21	2.79, −1.23

Table 2.3.2. Crystallographic parameters for **2.2** at T = 3.3, 14.0 and 20.0 K.

	3.3 K	14.0 K	20.0 K
Crystal data			
Chemical formula	$Br_6Re{\cdot}C_{10}H_{10}N_2$	$Br_6Re{\cdot}C_{10}H_{10}N_2$	$Br_6Re{\cdot}C_{10}H_{10}N_2$
M_r	823.86	823.86	823.86
Crystal system, space group	Monoclinic, *C*2/*c*	Monoclinic, *C*2/*c*	Monoclinic, *C*2/*c*
Temperature (K)	3	14	20
a,	15.9238 (4),	15.9269 (4),	15.9297 (4),
b,	31.6930 (8),	31.6968 (7),	31.7015 (7),
c (Å)	14.8880 (4)	14.8882 (4)	14.8931 (3)
β (°)	117.452 (1)	117.449 (1)	117.464 (1)
V (Å^3)	6667.5 (3)	6669.9 (3)	6673.3 (3)
Z	16	16	16
Radiation type	Mo *K*α	Mo *K*α	Mo *K*α
μ (mm^{-1})	21.66	21.65	21.64
Data collection			
No. of measured, independent and observed [$I > 2\sigma(I)$] reflections	39179, 6248, 5015	40410, 6244, 4895	40611, 6285, 4939
R_{int}	0.031	0.030	0.030
$(\sin\theta/\lambda)_{max}$ (Å^{-1})	0.626	0.625	0.627
Refinement			
$R[F^2 > 2\sigma(F^2)]$, $wR(F^2)$, S	0.029, 0.070, 1.15	0.028, 0.065, 1.14	0.028, 0.065, 1.16
No. of reflections	6248	6244	6285
No. of parameters	348	348	348
No. of restraints	282	282	282
$\Delta\rho_{max}$, $\Delta\rho_{min}$ (e Å^{-3})	2.04, −1.21	1.61, −1.12	1.80, −1.19

Table 2.3.3. Structural parameters for [4,4'-H_2bipy][$ReCl_6$].

Bond lengths / Å		Bond angles / °	
Re(1)–Cl(1)	2.3401(9)	Cl(1)–Re(1)–Cl(2)	90.77(3)
Re(1)–Cl(2)	2.3493(8)	Cl(1)–Re(1)–Cl(3)	90.0
Re(1)–Cl(3)	2.3661(9)	Cl(2)–Re(1)–Cl(3)	90.0
N(1)–C(1)	1.345(3)		
C(1)–C(2)	1.378(4)	Torsion angle / °	
C(2)–C(3)	1.396(3)	C(2)–C(3)–C(3c)–C(2c)	38.3(3)

Table 2.3.4. Structural parameters for [4,4'-H_2bipy][$ReBr_6$] at T = 3.3, 14 and 20 K.

Bond lengths / Å	T = 3.3 K	T = 14 K	T = 20 K
Re(1)–Br(1)	2.5106(8)	2.5105(8)	2.5102(8)
Re(1)–Br(2)	2.5024(6)	2.5023(6)	2.5026(6)
Re(1)–Br(3)	2.5066(7)	2.5062(7)	2.5062(7)
Re(1)–Br(4)	2.5220(8)	2.5224(8)	2.5228(8)
Re(2)–Br(5)	2.5045(8)	2.5044(8)	2.5040(8)
Re(2)–Br(6)	2.5035(6)	2.5043(6)	2.5046(6)
Re(2)–Br(7)	2.4873(7)	2.4868(6)	2.4866(6)

Re(2)–Br(8)	2.5195(8)	2.5197(8)	2.5202(8)
Re(3)–Br(9)	2.5319(9)	2.5319(8)	2.5328(8)
Re(3)–Br(10)	2.4962(6)	2.4955(6)	2.4960(6)
Re(3)–Br(11)	2.4957(7)	2.4957(7)	2.4959(7)
Re(3)–Br(12)	2.5194(9)	2.5200(8)	2.5207(8)
Re(4)–Br(13)	2.4970(7)	2.4973(6)	2.4975(6)
Re(4)–Br(14)	2.5087(7)	2.5091(6)	2.5090(6)
Re(4)–Br(15)	2.5059(7)	2.5053(6)	2.5058(6)
Bond angles / °			
Br(1)–Re(1)–Br(2)	90.842(16)	90.842(16)	90.842(16)
Br(1)–Re(1)–Br(3)	91.123(16)	91.145(16)	91.131(16)
Br(1)–Re(1)–Br(4)	180	180	180
Br(2)–Re(1)–Br(3)	89.53(2)	89.49(2)	89.48(2)
Br(2)–Re(1)–Br(4)	89.158(16)	89.158(16)	89.158(16)
Br(3)–Re(1)–Br(4)	88.877(16)	88.855(16)	88.869(16)
Br(5)–Re(2)–Br(6)	90.254(16)	90.247(16)	90.268(16)
Br(5)–Re(2)–Br(7)	90.197(16)	90.197(16)	90.205(16)
Br(5)–Re(2)–Br(8)	180	180	180
Br(6)–Re(2)–Br(7)	91.38(2)	91.39(2)	91.37(2)
Br(6)–Re(2)–Br(8)	89.746(16)	89.753(16)	89.732(16)
Br(7)–Re(2)–Br(8)	89.803(16)	89.803(16)	89.795(16)
Br(9)–Re(3)–Br(10)	88.683(16)	88.704(16)	88.683(16)
Br(9)–Re(3)–Br(11)	89.120(16)	89.149(16)	89.134(16)
Br(9)–Re(3)–Br(12)	180	180	180
Br(10)–Re(3)–Br(11)	90.33(2)	90.31(2)	90.32(2)
Br(10)–Re(3)–Br(12)	91.317(16)	91.296(16)	91.317(16)
Br(11)–Re(3)–Br(12)	90.880(16)	90.851(16)	90.866(16)
Br(13)–Re(4)–Br(14)	89.97(2)	89.99(2)	90.04(2)
Br(13)–Re(4)–Br(15)	179.59(2)	179.60(2)	179.52(2)
Br(14)–Re(4)–Br(15)	90.37(2)	90.33(2)	90.31(2)
Torsion angle / °			
C(4)–C(3)–C(8)–C(7)	40.7(11)	39.9(10)	41(1)
C(14)–C(13)–C(18)–C(17)	-43.6(11)	-43.6(11)	-43.4(11)

Table 2.3.5. Structural parameters for [4,4'-H_2bipy][$ReCl_4$(ox)].

Bond lengths / Å		Bond angles / °	
Re(1)–Cl(1)	2.3442(11)	Cl(1)–Re(1)–Cl(2)	91.12(4)
Re(1)–Cl(2)	2.3669(10)	Cl(1)–Re(1)–O(1)	89.03(8)
Re(1)–O(1)	2.051(3)	Cl(2)–Re(1)–O(1)	94.22(9)
		O(1)–Re(1)–O(1)'	79.96(17)
		Torsion angle / °	
		C(3)–C(4)–C(5)–C(6)	31.5(3)

Table 2.3.6. Br···Br interactions in the crystal lattice of [4,4'-H_2bipy][$ReBr_6$].

Br···Br interactions	Distance / Å
Br(2)···Br(13)	3.7876(9)
Br(2)···Br(15)	4.0260(9)
Br(3)···Br(6)	3.493(1)
Br(3)···Br(11)	4.1963(9)
Br(6)···Br(10)	3.913(1)
Br(7)···Br(10)	3.4546(9)
Br(11)···Br(14)	3.5158(10)

Table 2.3.7. Hydrogen bonds in **2.1**, **2.2** and **2.3**.

Hydrogen bonds, D–H···A	D–H / Å	H···A / Å	D···A / Å	DHA / °
[4,4'-H_2bipy][$ReCl_6$]				
N(1)–H(1A)···Cl(3)	0.85(5)	2.61(4)	3.330(3)	143.6(7)
[4,4'-H_2bipy][$ReBr_6$]				
N(1)–H(1)···Br(8)	0.880(6)	2.6839(4)	3.421(6)	142.0(3)
N(1)–H(1)···Br(9)	0.880(6)	2.7163(6)	3.468(6)	144.1(1)
N(2)–H(2)···Br(1)	0.880(6)	2.6663(4)	3.481(6)	154.5(3)
N(2)–H(2)···Br(13)	0.880(6)	3.1232(7)	3.655(6)	121.0(4)
N(3)–H(3)···Br(4)	0.880(6)	2.5911(5)	3.408(6)	154.7(3)
N(3)–H(3)···Br(5)	0.880(6)	2.8943(4)	3.561(6)	133.8(3)
N(4)–H(4A)···Br(12)	0.880(6)	2.8114(5)	3.557(6)	143.4(3)
N(4)–H(4A)···Br(15)	0.880(6)	2.8149(7)	3.408(6)	126.1(4)
[4,4'-H_2bipy][$ReCl_4$(ox)]				
N(1)–H(1)···Cl(2)	0.880	2.54(1)	3.242(1)	138.8(1)
N(2)–H(2)···O(2)	0.880	2.17(1)	2.869(1)	139.9(1)

2.4 Magnetic properties

2.4.1 Magnetic properties of [4,4'-H_2bipy][$ReCl_6$] (2.1)

The susceptibility was measured from T = 300 to 2 K in a field of H = 1000 Oe and presented as the $\chi_M T$ product [χ_M being the molar magnetic susceptibility *per* Re^{IV} ion]. The $\chi_M T$ value is 1.75 cm^3 mol^{-1} K at T = 300 K, which is slightly higher than expected for a paramagnetic Re^{IV} ion with S = 3/2 and g = 1.9 (1.69 cm^3 mol^{-1} K). As the temperature is lowered the $\chi_M T$ value exhibits a minor decrease of 0.11 cm^3 mol^{-1} K going from T = 300 to T = 60 K. Upon further cooling a sharp drop is observed for the $\chi_M T$ value which ends with a final value of 0.08 cm^3 mol^{-1} K at T = 2 K (Figure 2.4.1a).

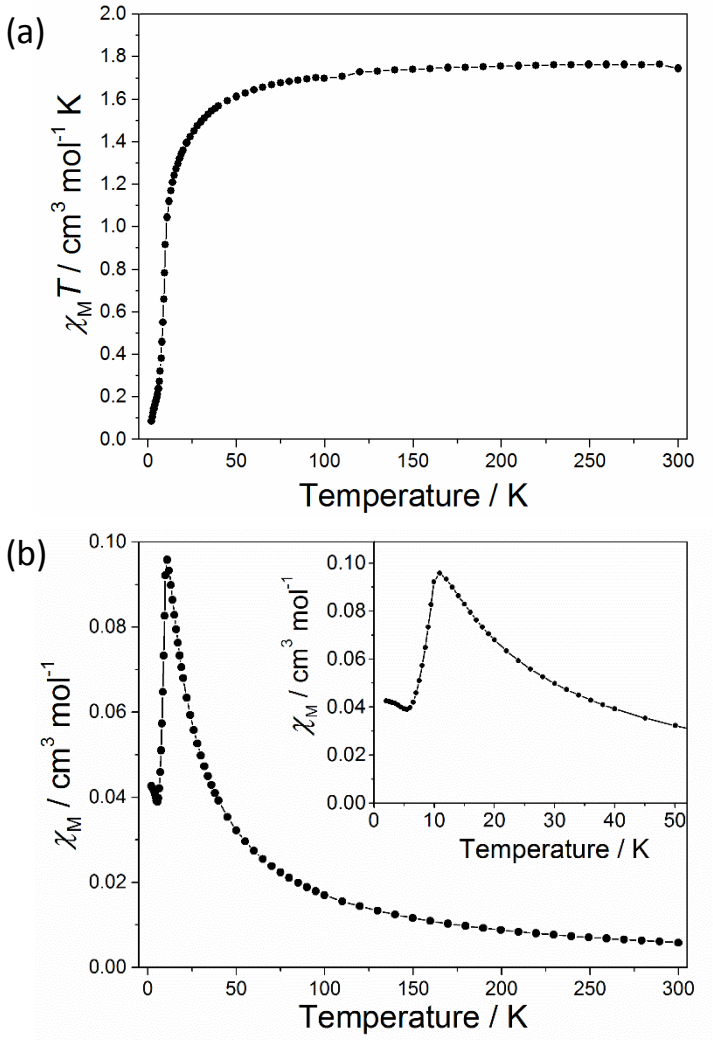

Figure 2.4.1. a) The $\chi_M T$ *versus* T for **2.1**. b) The χ_M *vs.* T plot, insert illustrating the low temperature behaviour. The solid lines are guides to the eye.

The plot of χ_M *vs.* T contains a maximum at T = 11 K indicative of significant antiferromagnetic interactions in the system (Figure 2.4.1b). The maximum is also observed by a frequency

independent peak in the in- and out-of-phase ac susceptibility measurement, indicative of magnetic ordering (Figure 2.4.1b and 2.4.2a and b).

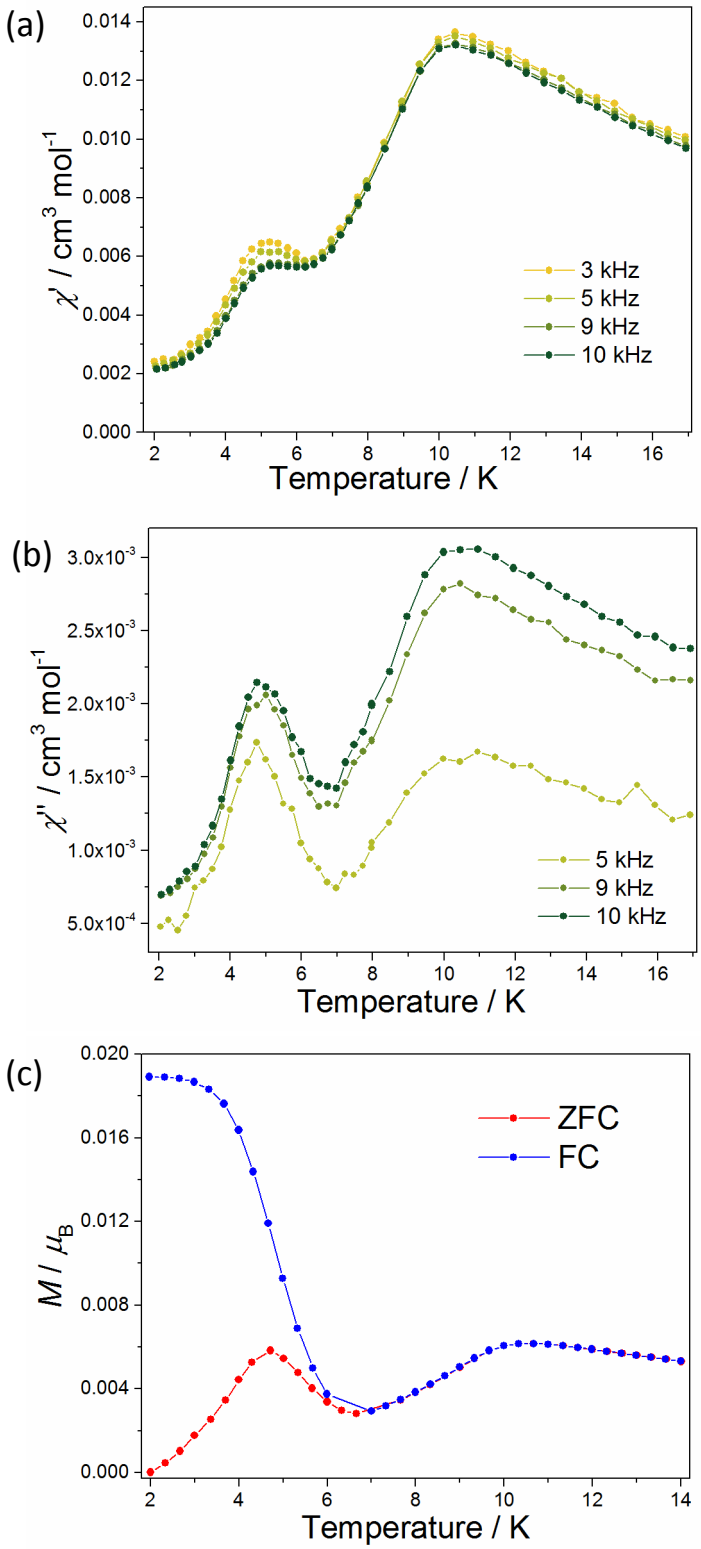

Figure2.4.2. The in-phase ‚χ'', (a) and out-of-phase ‚χ''', (b) ac susceptibility measurement at various frequencies. c) The zero-field-cooled field-cooled measurement.

The χ_M *versus* T plot also reveals a small upturn initiating at T = 5.5 K (Figure 2.4.1b, insert). Further magnetic measurements proved the slight upturn to be inversely proportional to the strength of the external field; behaviour indicative of antiferromagnetic spin-canting (Figure 2.4.3a). A peak in the in-phase and out-of-phase ac susceptibility at T = 5 K (Figure 2.4.2a and b) combined with the presence of a small but non-negligible hysteresis loop at T = 1.8 K confirmed the spin-canting phenomenon (Figure 2.4.3b). Zero-field-cooled field-cooled, ZFC-FC, measurements further corroborated the spin canted with a peak at T_c = 5 K (Figure 2.4.2c). The hysteresis loop at T = 1.8 K contain a remanent magnetisation, M_r, of 0.003 μ_b with a coercive field, H_{co}, of 370 Oe. The canting angle can be determined from the formula $\sin(\alpha) = M_c/M_s$, where α is the canting angle, M_c is the canting magnetisation induced by a weak field and M_s is the magnetic saturation value. Using the remanent magnetic moment of 0.003 μ_b for M_c and the theoretical saturation value of 2.78 μ_b for M_s leads to a canting angle of α = 0.06°, a value significantly smaller relative to other systems containing the Re^{IV} ion and exhibiting spin canted antiferromagnetism.[25, 45]

The isothermal magnetisation measurement revealed the presence of metamagnetism, where a critical field, H_c = 2.8 T, overcomes the antiferromagnetic interaction and induces a paramagnetic state (Figure 2.4.4). The metamagnetic property is also observed in the susceptibility measurements as the peak at T = 11 K is overcome when measuring in a field of $H > H_c$ (Figure 2.4.3a). At H = 7 T the sample reaches a magnetisation of 1.39 μ_b, a value similar to that of other mononuclear Re^{IV} samples.[46]

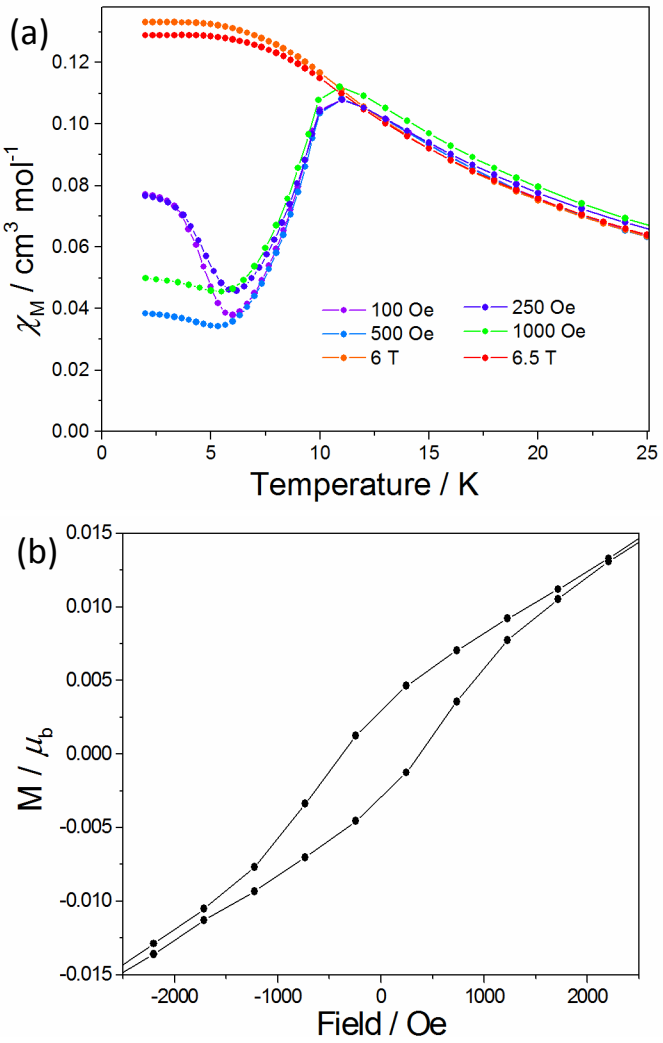

Figure 2.4.3. a) Variable-tempereture variable-field measurement illustrating the field depence below T = 5.5 K and the metamagnetism of the peak at T = 11 K. b) Hysteresis loop measured at T =1.8 K.

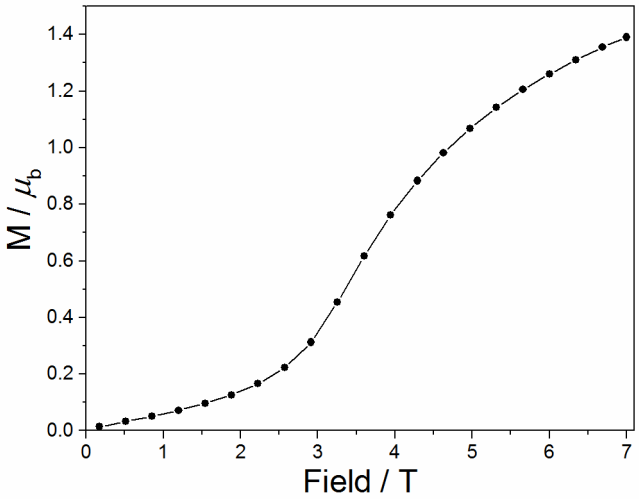

Figure 2.4.4. The magnetisation at T = 1.8 K illustrating the metamagnetism with a critical field of 2.8 T.

2.4.2 Magnetic properties of [4,4'-H_2bipy][$ReBr_6$] (2.2)

The susceptibility was measured from T = 300 to 2 K in a field of H = 1000 Oe and is shown in Figure 2.4.5 as the $\chi_M T$ product [χ_M being the molar magnetic susceptibility *per* Re^{IV} ion]. The $\chi_M T$ value is 1.66 cm^3 mol^{-1} K at T = 300 K, a value expected for a paramagnetic Re^{IV} ion with S = 3/2 and g = 1.9 (1.69 cm^3 mol^{-1} K). As the temperature is lowered the $\chi_M T$ value rises slightly to 1.84 cm^3 mol^{-1} K at T = 100 K before steadily increasing to reach a maximum of 2.21 cm^3 mol^{-1} K at T = 19 K. Upon further cooling, the $\chi_M T$ value drops abruptly to 1.34 cm^3 mol^{-1} K at T = 12 K, after which there is a sharp increase to a value of 2.02 cm^3 mol^{-1} K at T = 8.3 K, before rapidly descending once more to 0.53 cm^3 mol^{-1} K at T = 2 K (Figure 2.4.5a, insert).

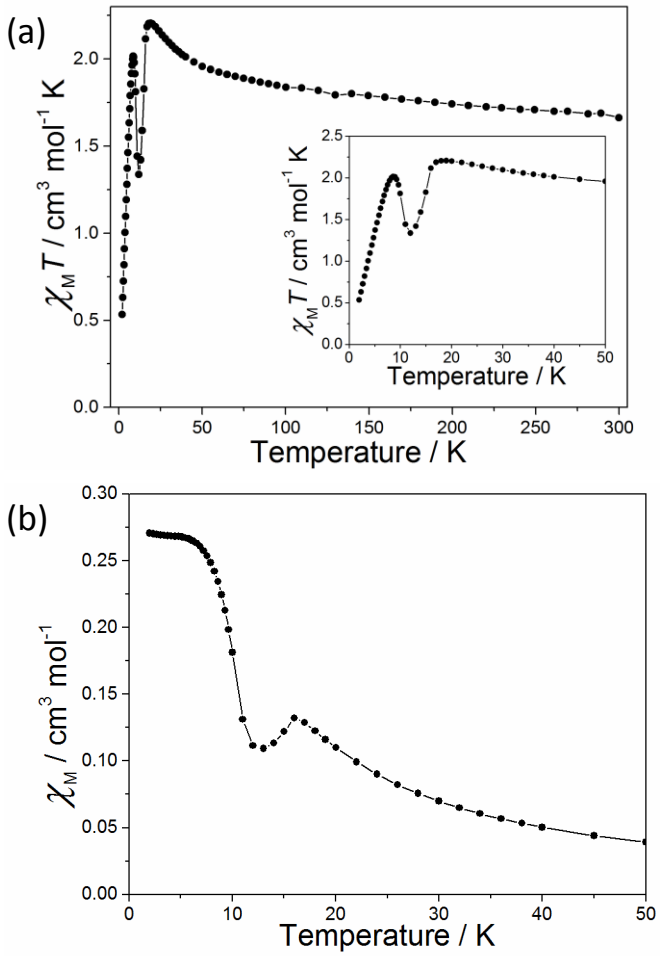

Figure 2.4.5. a) The $\chi_M T$ *versus* T plot for **2.2**. Insert shows the low temperature region.
b) The plot of χ_M *vs.* T plot. The solid lines are guides to the eye.

The maximum observed in the χ_M *vs.* T plot at T = 16 K is indicative of strong antiferromagnetic coupling (Figure 2.4.5b), this is also detected by the presence of a frequency independent peak in the in-phase ac susceptibility at the same temperature (Figure 2.4.6a).

The abrupt increase in the $\chi_M T$ value at T = 12 K exhibits a strong field dependence with the susceptibility inversely proportional to the static field (Figure 2.4.7a). ZFC-FC measurements reveal magnetic ordering at T = 9.5 K (Figure 2.4.7b), which was further corroborated by frequency independent peaks at T = 10 K in ac susceptibility measurements (Figure 2.4.6b).

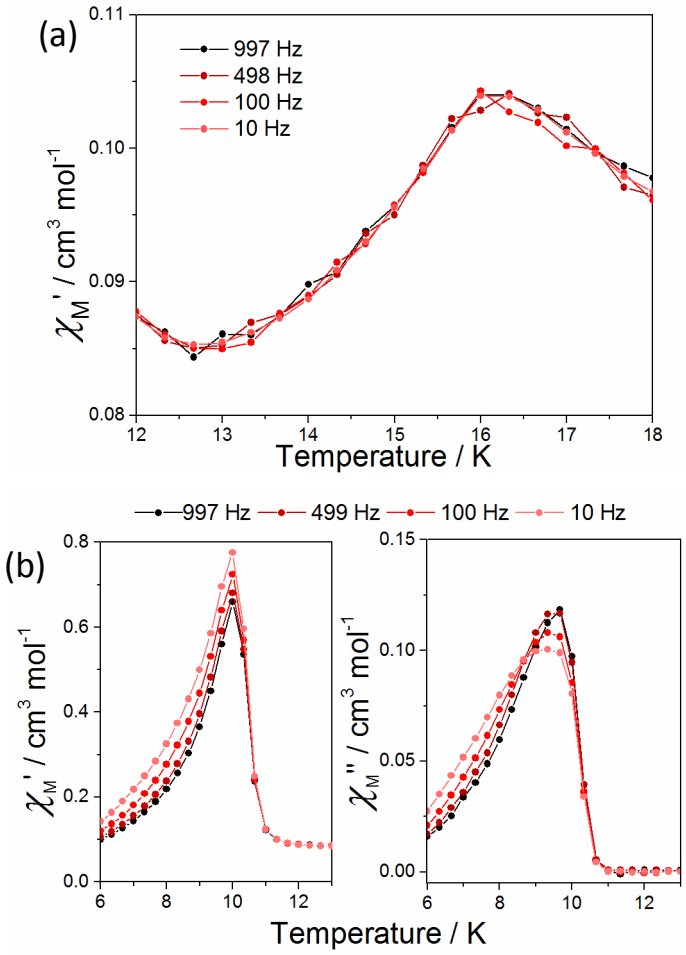

Figure 2.4.6. a) In-phase ac susceptibility for **2.2**. b) The in- and out-of-phase ac measurement from T = 9 to 12 K.

The magnetic behaviour in this temperature region is suggestive of antiferromagnetic spin-canting, which is accompanied by hysteresis loops in the isothermal magnetisation measurements at temperatures as high as T = 7 K (Figure 2.4.7c).

At T = 1.8 K the hysteresis loop has a coercive field H_{co} = 1300 Oe, with 0.080 μ_b remanent magnetisation, M_r. The canting angle can be determined from the formula $\sin(\alpha) = M_c/M_s$. Using the remanent magnetic moment of 0.080 μ_b for M_c and the theoretical saturation value of 2.78 μ_b for M_s leads to a canting angle of α = 1.6°, a value similar to other systems containing the Re^{IV} ion and exhibiting spin canted antiferromagnetism.[45] At T = 1.8 K and a

field of H = 7 T the magnetic moment reaches 1.74 μ_b, similar to the value observed for other Re^{IV} compounds.[46]

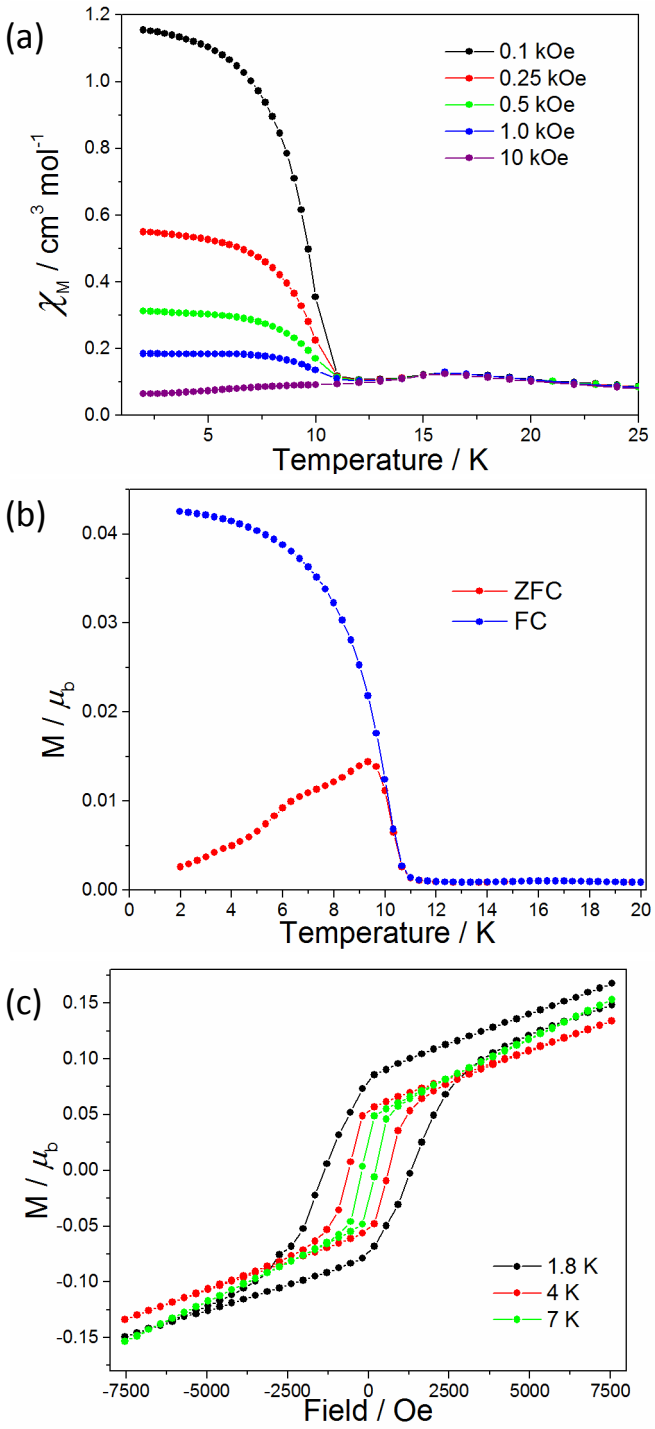

Figure 2.4.7. a) Variable-field variable-temperature measurement. b) The ZFC-FC experiment. c) Hysteresis loops measured at T = 1.8, 4 and 7 K.

The magnetisation measurements also reveal the onset of a field induced paramagnetic phase above a critical field H_c = 2.3 T symptomatic of metamagnetic behaviour (Figure

2.4.8a). A scan of the temperature in a static field $H > H_c$ overcomes the antiferromagnetic exchange interaction at T = 16 K in accordance with the metamagnetic nature of the system (Figure 2.4.8b). With no significant structural changes in the full temperature regime we can assume all of the observed magnetic phenomena arise from the structure described in section 2.3.2.

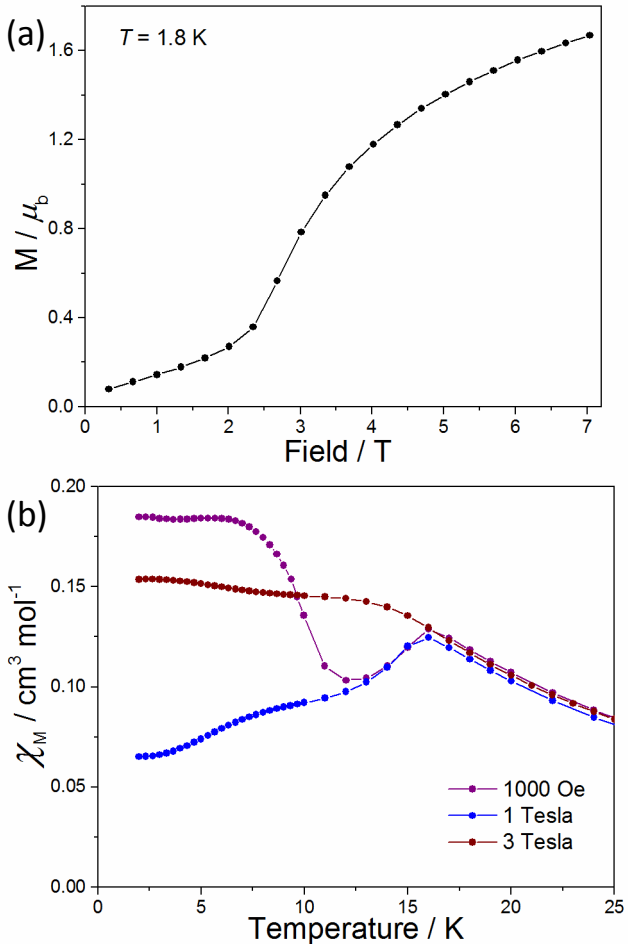

Figure 2.4.8. a) Magnetisation at T = 1.8, illustrating the metamagnetic behaviour. b) High-field low temperature susceptibility measurements.

2.4.3 Magnetic properties of [4,4'-H_2bipy][$ReCl_4$(ox)] (2.3)

The $\chi_M T$ value at T = 280 K is 1.71 cm^3 mol^{-1} K, close to the expected value of 1.52-1.69 cm^3 mol^{-1} K (g = 1.8-1.9 and S = 3/2). Throughout the temperature range of T = 280 to 2 K the $\chi_M T$ value declines with decreasing temperature ending with a $\chi_M T$ value of 0.03 cm^3 mol^{-1} K (Figure 2.4.9). This behaviour is indicative of antiferromagnetic exchange interactions

combined with the large intrinsic anisotropy of the anions. The antiferromagnetic coupling is further corroborated by a peak in the χ_M *versus T* plot at *T* = 12 K (Figure 2.4.9, insert).

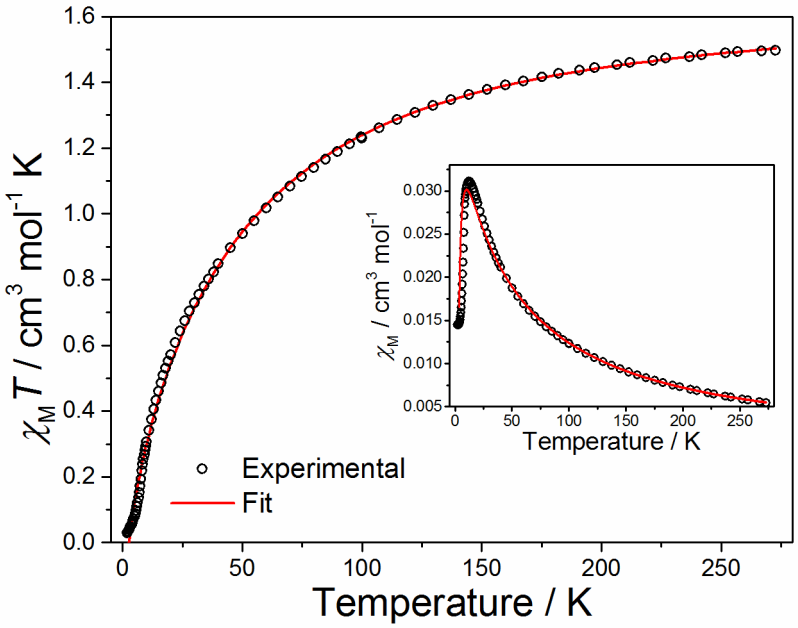

Figure 2.4.9. The $\chi_M T$ *versus T* plot for **2.3**. Insert shows the χ_M *vs*. *T* graph. Black dots are the experimental data, red line is the fit.

In order to analyse the magnetic behaviour **2.3**, the spin Hamiltonian of equation 2.4.1 was employed and its derived theoretical expression for the magnetic susceptibility, equations 2.4.2 and 2.4.3, by including a θ term (as *T*-θ) to account for the observed intermolecular interactions.[47]

$$\hat{H} = D[(\hat{S}_Z)^2 - S(S+1)/3] + g\beta H\hat{S} \qquad (2.4.1)$$

$$\chi_M = \frac{\chi_\parallel + 2\chi_\perp}{3} \qquad (2.4.2)$$

$$\chi_\parallel = \frac{N\beta^2 g_\parallel^2}{4k(T-\theta)} \frac{1 + 9\exp\left(-\frac{2D}{kT}\right)}{1 + \exp\left(-\frac{2D}{kT}\right)} \qquad (2.4.3)$$

$$\chi_\perp = \frac{N\beta^2 g_\perp^2}{k(T-\theta)} \frac{1 + (3kT/4D)[1 - \exp(-2D/kT)]}{1 + \exp(-2D/kT)}$$

The first term in equation 2.4.1 corresponds to the anisotropy and the second term the Zeeman effects.

A value of *D* = -53 cm^{-1} for the $[ReCl_4(ox)]^{2-}$ anion was used, as previously reported from HF-EPR data, and kept constant during the fitting process.[19] The resulting best least-squares fit

parameters, red line in Figure 2.4.9, are g = 1.88 and θ = - 10.2 cm^{-1} with $R = 6.8 \times 10^{-5}$ (R being the agreement factor defined as $\Sigma_i[(\chi_M T)_i^{obs} - (\chi_M T)_i^{calc}]^2 / [(\chi_M T)_i^{obs}]^2$). The g value found is in agreement with those previously reported for mononuclear Re^{IV} complexes.[17, 18, 27] The negative value of θ confirm the presence of relatively strong antiferromagnetic exchange through intermolecular Re–Cl···Cl–Re pathways (Figure 2.3.14).

2.4.4 The magnetic behaviour of [4,4'-H_2bipy][$ReCl_6$] and [4,4'-H_2bipy][$ReBr_6$]

The magnetic properties of the [4,4'-H_2bipy][$ReCl_6$] and [4,4'-H_2bipy][$ReBr_6$] compounds, **2.1** and **2.2**, are surprisingly alike, taken into account the unusual magnetic behaviour observed. The maximum in the χ_M *vs*. T plot appear at higher temperatures for **2.2** with respect to **2.1**, indicating the presence of a stronger magnetic exchange interaction (Figure 2.4.1b and 2.4.5b). This difference is presumed to be a consequence of the larger amount of spin delocalised onto the bromide *versus* chloride ions inducing a stronger coupling. The fact that magnetic anisotropy is essential for spin-canting can, by similar ways, explain the significant difference in magnitude of the canting, with it being greater for the $[ReBr_6]^{2-}$ compound. The difference in magnetic anisotropies of $[ReCl_6]^{2-}$ and $[ReBr_6]^{2-}$ is exemplified by the difference in the anisotropy for the $[ReCl_4(ox)]^{2-}$ and $[ReBr_4(ox)]^{2-}$ anions of 53 and 73 cm^{-1}, respectively.[19]

2.5 Summary

Three molecular salts based on the 4,4'-bipyridinium dication and the $[ReCl_6]^{2-}$, $[ReBr_6]^{2-}$ and $[ReCl_4(ox)]^{2-}$ anions have been characterised structurally and magnetically. They are synthesised from the (NBu_4)[$ReCl_6$] (**2.1**), (NBu_4)[$ReBr_6$] (**2.2**) or (NBu_4)[$ReCl_4$(ox)] (**2.3**) compounds and the 4,4'bipyridine precursor *via* cation exchange in glacial acetic acid and crystallised from HCl (**2.1** and **2.3**) or HBr (**2.2**) acid solutions at 4°C. The molecular salts crystallise in the orthorhombic *Ibam* (**2.1**) and monoclinic *C*2/*c* (**2.2** and **2.3**) space groups. The structures consist of the 4,4'-H_2bipy cation with protonated nitrogen atoms and twisted intramolecular aryl–aryl bond and their respective anion. In the crystal lattice, the salts pack through a broad range of halide···halide, halide···π and hydrogen bond interactions. The structure of **2.2** was measured T = 3.3, 14 and 20 K revealing no significant changes to the structure. The magnetic properties of **2.1** and **2.2** proved to contain spin-canting, antiferromagnetic exchange interactions and metamagnetism, a combination of magnetic features previously unseen in 5d molecular materials. In **2.1** the spin-canting behaviour is of

a smaller but non-negligible magnitude containing a canting angle of 0.06° and open hysteresis loop at T = 1.8 K. **2.2** contain a spin-canting angle of 1.6° with an open hysteresis loop at temperatures up to T = 7 K. The antiferromagnetic interactions is seen as the peak in the χ_M *vs*. T plot at T = 11 and 16 K for **2.1** and **2.2**, respectively. A critical field of 2.8 T (**2.1**) and 2.3 T (**2.2**) was observed in the magnetisation measurements to overcome the antiferromagnetic coupling; behaviour termed metamagnetism. The origin of the difference in magnetic behaviour of **2.1** and **2.2**, is thought to stem from the difference in magnetic anisotropy and spin delocalisation of the two anions. For **2.3**, an antiferromagnetic coupling is observed with a maximum at T = 12 K in the χ_M *vs*. T graph and a fit of the data revealed the strength of the interaction to be 10.2 cm^{-1}. The magnetic exchange interaction is assumed to be transmitted through intermolecular Cl···Cl interactions.

2.6 References

1. R. Sessoli, D. Gatteschi, A. Caneschi and M. A. Novak, *Nature*, 1993, **365**, 141.
2. G. A. Craig and M. Murrie, *Chem. Soc. Rev.*, 2015, **44**, 2135.
3. S. Demir, I.-R. Jeon, J. R. Long and T. D. Harris, *Coord. Chem. Rev.*, 2015, **289–290**, 149.
4. R. J. Blagg, L. Ungur, F. Tuna, J. Speak, P. Comar, D. Collison, W. Wernsdorfer, E. J. L. McInnes, L. F. Chibotaru and R. E. P. Winpenny, *Nat Chem*, 2013, **5**, 673.
5. M. A. Antunes, L. C. J. Pereira, I. C. Santos, M. Mazzanti, J. Marçalo and M. Almeida, *Inorg. Chem.*, 2011, **50**, 9915.
6. K. R. Dunbar, E. J. Schelter, A. V. Palii, S. M. Ostrovsky, V. Y. Mirovitskii, J. M. Hudson, M. A. Omary, S. I. Klokishner and B. S. Tsukerblat, *J. Phys. Chem. A*, 2003, **107**, 11102.
7. X.-Y. Wang, C. Avendano and K. R. Dunbar, *Chem. Soc. Rev.*, 2011, **40**, 3213.
8. J. Martínez-Lillo, D. Armentano, G. De Munno, W. Wernsdorfer, M. Julve, F. Lloret and J. Faus, *J. Am. Chem. Soc.*, 2006, **128**, 14218.
9. D. Pinkowicz, H. I. Southerland, C. Avendaño, A. Prosvirin, C. Sanders, W. Wernsdorfer, K. S. Pedersen, J. Dreiser, R. Clérac, J. Nehrkorn, G. G. Simeoni, A. Schnegg, K. Holldack and K. R. Dunbar, *J. Am. Chem. Soc.*, 2015, **137**, 14406.
10. R. Gonzalez, R. Chiozzone, C. Kremer, F. Guerra, G. De Munno, F. Lloret, M. Julve and J. Faus, *Inorg. Chem.*, 2004, **43**, 3013.
11. K. S. Pedersen, M. Sigrist, M. A. Sørensen, A.-L. Barra, T. Weyhermüller, S. Piligkos, C. A. Thuesen, M. G. Vinum, H. Mutka, H. Weihe, R. Clérac and J. Bendix, *Angew. Chem. Int. Ed.*, 2014, **53**, 1351.
12. J. Martinez-Lillo, J. Kong, W. P. Barros, J. Faus, M. Julve and E. K. Brechin, *Chem. Commun.*, 2014, **50**, 5840.
13. J. Martínez-Lillo, J. Kong, M. Julve and E. K. Brechin, *Cryst. Growth Des.*, 2014, **14**, 5985.
14. J. Martínez-Lillo, A. H. Pedersen, J. Faus, M. Julve and E. K. Brechin, *Cryst. Growth Des.*, 2015, **15**, 2598.
15. J. Martinez-Lillo, D. Armentano, N. Marino, L. Arizaga, R. Chiozzone, R. Gonzalez, C. Kremer, J. Cano and J. Faus, *Dalton Trans.*, 2008, 4585.

16. K.-i. Suzuki, T. Kodama, K. Kikuchi and W. Fujita, *Chem. Lett.*, 2010, **39**, 1096.
17. F. Pop, M. Allain, P. Auban-Senzier, J. Martinez-Lillo, F. Lloret, M. Julve, E. Canadell and N. Avarvari, *Eur. J. Inorg. Chem.*, 2014, **2014**, 3855.
18. J. Martinez-Lillo, D. Armentano, G. De Munno, N. Marino, F. Lloret, M. Julve and J. Faus, *CrystEngComm*, 2008, **10**, 1284.
19. J. Martínez-Lillo, T. F. Mastropietro, E. Lhotel, C. Paulsen, J. Cano, G. De Munno, J. Faus, F. Lloret, M. Julve, S. Nellutla and J. Krzystek, *J. Am. Chem. Soc.*, 2013, **135**, 13737.
20. J. Martinez-Lillo, D. Armentano, T. F. Mastropietro, M. Julve, J. Faus and G. De Munno, *Cryst. Growth Des.*, 2011, **11**, 1733.
21. J. Martinez-Lillo, J. Cano, W. Wernsdorfer and E. K. Brechin, *Chem. - Eur. J.*, 2015, **21**, 8790.
22. R. Chiozzone, R. González, C. Kremer, G. De Munno, J. Cano, F. Lloret, M. Julve and J. Faus, *Inorg. Chem.*, 1999, **38**, 4745.
23. P. A. Reynolds, B. Moubaraki, K. S. Murray, J. W. Cable, L. M. Engelhardt and B. N. Figgis, *Dalton Trans.*, 1997, **2**, 263.
24. P. A. Reynolds, B. N. Figgis and D. Martin y Marero, *Dalton Trans.*, 1999, 945.
25. R. Gonzalez, R. Chiozzone, C. Kremer, G. De Munno, F. Nicolo, F. Lloret, M. Julve and J. Faus, *Inorg. Chem.*, 2003, **42**, 2512.
26. J. Martinez-Lillo, D. Armentano, G. De Munno, F. Lloret, M. Julve and J. Faus, *Cryst. Growth Des.*, 2006, **6**, 2204.
27. R. Gonzalez, F. Romero, D. Luneau, D. Armentano, G. De Munno, C. Kremer, F. Lloret, M. Julve and J. Faus, *Inorg. Chim. Acta*, 2005, **358**, 3995.
28. A. H. Pedersen, M. Julve, E. K. Brechin and J. Martinez-Lillo, *CrystEngComm*, 2017, **19**, 503.
29. A. Tomkiewicz, T. J. Bartczak, R. Kruszyński and J. Mroziński, *J. Mol. Struct.*, 2001, **595**, 225.
30. S. Benmansour, E. Coronado, C. Giménez-Saiz, C. J. Gómez-García and C. Rößer, *Eur. J. Inorg. Chem.*, 2014, **2014**, 3949.
31. J. Martínez-Lillo, D. Armentano, G. De Munno, W. Wernsdorfer, J. M. Clemente-Juan, J. Krzystek, F. Lloret, M. Julve and J. Faus, *Inorg. Chem.*, 2009, **48**, 3027.
32. A. Tomkiewicz, J. Mroziński, I. Brüdgam and H. Hartl, *Eur. J. Inorg. Chem.*, 2005, **2005**, 1787.
33. O. Fabelo, L. Canadillas-Delgado, J. Pasan, P. Diaz-Gallifa, C. Ruiz-Perez, F. Lloret, M. Julve, I. Puente Orench, J. Campo and J. Rodriguez-Carvajal, *Inorg. Chem.*, 2013, **52**, 12818.
34. S. Naiya, S. Biswas, M. G. B. Drew, C. J. Gomez-Garcia and A. Ghosh, *Inorg. Chem.*, 2012, **51**, 5332.
35. D. Shao, S.-L. Zhang, X.-H. Zhao and X.-Y. Wang, *Chem. Commun.*, 2015, **51**, 4360.
36. J. Kleinberg, *Inorg. Synth.*, McGraw-Hill, 1963.
37. R. Chiozzone, A. Cuevas, R. González, C. Kremer, D. Armentano, G. De Munno and J. Faus, *Inorg. Chim. Acta*, 2006, **359**, 2194.
38. G. A. Bain and J. F. Berry, *J. Chem. Educ.*, 2008, **85**, 532.
39. L. J. Bourhis, O. V. Dolomanov, R. J. Gildea, J. A. K. Howard and H. Puschmann, *Acta Crystallogr. Sect. A*, 2015, **71**, 59.
40. G. Sheldrick, *Acta Crystallogr. Sect. A*, 2008, **64**, 112.
41. M. C. Burla, R. Caliandro, M. Camalli, B. Carrozzini, G. L. Cascarano, L. De Caro, C. Giacovazzo, G. Polidori, D. Siliqi and R. Spagna, *J. Appl. Crystallogr.*, 2007, **40**, 609.
42. O. V. Dolomanov, L. J. Bourhis, R. J. Gildea, J. A. K. Howard and H. Puschmann, *J. Appl. Crystallogr.*, 2009, **42**, 339.

43. L. Chen, F.-L. Jiang, N. Li, W.-T. Xu and M.-C. Hong, *J. Cluster Sci.*, 2008, **19**, 591.
44. H. Yang, X. Lin, B. Xu, Y. You, M. Cao, S. Gao and R. Cao, *J. Mol. Struct.*, 2010, **966**, 33.
45. J. Martínez-Lillo, F. Lloret, M. Julve and J. Faus, *J. Coord. Chem.*, 2009, **62**, 92.
46. J. Martinez-Lillo, J. Faus, F. Lloret and M. Julve, *Coord. Chem. Rev.*, 2015, **289-290**, 215.
47. O. Kahn, *Molecular Magnetism*, VCH Publisher, Inc., 1993.

Chapter 3: Homometallic Re^{IV} dimers bridged by heterocyclic amines

3.1 Introduction

The ability of the synthetic chemist to exert control over molecular structure, and hence physical properties, has always been key to the understanding and exploitation of magneto-structural relationships.[1-4] For polymetallic complexes of paramagnetic 3-5d/4f transition/lanthanide metal ions, one prominent methodology is the use of 'metalloligands' which can be combined together in a predictable fashion on account of their rigorously rigid frameworks.[5-7] Indeed using small, usually monometallic, complexes as 'ligands' from which to construct 0-3D architectures has been achieved using an enormous variety of different metal ions and organic ligand types.[8-14]

The interest in the coordination and magneto-chemistry of the Re^{IV} ion stems primarily from its significant magnetic anisotropy, with several Re^{IV} mononuclear compounds exhibiting slow relaxation of the magnetisation.[8-10] Combining these small units into larger arrays has therefore been the subject of much research focus, with the resultant 0-2D molecule-based materials exhibiting a breadth of fascinating magnetic behaviours.[11-17] For example, the SIM $[ReCl_4(ox)]^{2-}$ (ox^{2-} = oxalate anion) metalloligand has been employed to make the SMM $(NBu_4)_4[\{ReCl_4(\mu\text{-}ox)\}_3Ni^{II}]$, as well as, coordinated to the divalent 3d transition metal ions from Mn^{II} to Cu^{II}, illustrating the effect of 'orthogonal' magnetic orbital giving rise to ferromagnetic exchange interactions.[3, 8, 11, 18-21] The $[trans\text{-}ReCl_4(CN)_2]^{2-}$ anion, exhibits intriguing relaxation mechanisms and has been utilised for the creation of several 0D and 1D compounds.[9, 14-16, 22-24] an example of this is the heterobimetallic compound $[(TPA^{2C(O)NHtBu})Fe^{II}][trans\text{-}ReCl_4(CN)_2]$ ($TPA^{2C(O)NHtBu}$ = 6,6'-(pyridin-2-ylmethylazanediyl)bis(methylene)-bis(*N*-tert-butylpicolinamide) which consists of two anisotropic ions bridged by the cyanide ligand, giving rise to a ferromagnetic exchange interaction of J = +3.0 cm^{-1}, $\hat{H} = -2J$ convention, along with axial anisotropy of D = -2.3 cm^{-1} and frequency dependent signals in the out-of-phase ac measurements behaviour characteristic of a SMM.[16] The cyanide ligands being *trans* on the Re^{IV} ion led to the creation of a family of SCM, with the most prominent member, $\{[Fe^{II}(DMF)_4][trans\text{-}ReCl_4(CN)_2]\}_n$, exhibiting an open hysteresis loop with a coercive field of H_{co} = 1 T, and remanent magnetisation of 3.77 μ_B at T = 1.8 K.[14, 15, 22]

The $[Re^{IV}Cl_5(L)]^-$ building blocks, where L is a heterocyclic ligand such as pyrazine, pyrimidine or pyridazine, have been known for some time and have been characterised structurally and magnetically (Figure 3.1.1).[25, 26] It is therefore surprising that only the pyrazine version of this

metalloligand has been employed to construct larger polymetallic species, and even here this is limited to the heterometallic compounds $[\{ReCl_5(pyz)\}_2Cu^{II}(DMF)_4]$ and $\{(Cu^{I}[ReCl_5(pyz)][Re^{IV}Cl_4(\mu\text{-bpym})]\}_n$ (pyz = pyrazine) as well as the homometallic dimer $(NEt_4)[(Re^{IV}Cl_5)_2(\mu\text{-pyz})]$ which was characterised by IR spectroscopy and elemental analysis.[25, 27, 28] This is especially true given the propensity for such ligands to bridge the heavier transition metal atoms in other metal complexes.[29-31] In order to address this apparent oversight, and to un-tap a well containing an enormous number of potentially new species, we have initially targeted the synthesis of homometallic Re^{IV} dimers, and herein report the first structural and magnetic characterisation of the paramagnetic dimeric $[Re^{IV}_2]$ members of this family of formulae $[(Re^{IV}X_5)_2(\mu\text{-pyz})]^{2-}$ (X = Cl (**3.1**) or Br (**3.2**)), $[(Re^{IV}Br_5)_2(\mu\text{-pym})]^{2-}$ (**3.3**), (pym = pyrimidine) and $[(Re^{IV}Br_5)_2(\mu\text{-triz})]^{2-}$ (**3.4**), (triz = triazine).

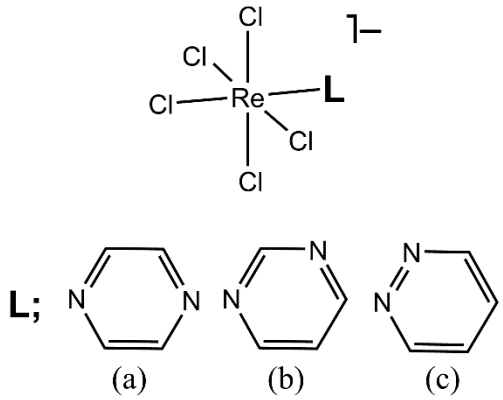

Figure 3.1.1. The $[Re^{IV}Cl_5(L)]^-$ anion with L = pyrazine (a), pyrimidine (b) and pyridazine (c).

3.2 Experimental

3.2.1 Materials and methods

All chemicals were used as received. Syntheses were carried out under aerobic conditions. $(NBu_4)_2[ReCl_6]$ and $(NBu_4)_2[ReBr_6]$ were prepared as described previously.[32, 33] Crystals of the four compounds were collected and left open to air for use in further analysis. Elemental analyses (C, H, N) were performed by MEDAC Ltd. Direct current (dc) magnetic susceptibility measurements were collected on a Quantum Design MPMS-XL SQUID magnetometer equipped with a 7 T dc magnet in the temperature range 300-2 K. Diamagnetic corrections were applied using Pascal's constants.[34]

3.2.2 Crystallography

Data were measured on Rigaku Oxford Diffraction SuperNova (**3.1**, **3.2**, **3.4**) and Rigaku Oxford Diffraction XCalibur (**3.3**) X-ray diffractometers using Mo-K_α radiation. Structures were solved with olex2.solve (**3.2**, **3.3**)[35] or ShelXS (**3.1**, **3.4**)[36] and refined by full-matrix least-squares on F-squared using ShelXL, interfaced through Olex2.[37] All non-hydrogen atoms were refined anisotropically. The hydrogen atom parameters were constrained.

3.2.3 Synthesis of $(NBu_4)_2[(ReCl_5)_2(\mu\text{-pyz})]$ (3.1)

$(NBu_4)_2[ReCl_6]$ (0.10 mmol, 88.0 mg) and pyrazine (0.20 mmol, 16.0 mg) in 4.5 ml glacial acetic acid were stirred at 90-100°C for 6-8 hours after which a dark red solid was collected by filtration. The solid was dissolved in dichloromethane (DCM) and layered with glacial acetic acid. Red crystals suitable for X-ray diffraction were collected after 3 days (17% yield). Elemental analysis (%) calculated (found) for $C_{36}H_{76}Cl_{10}N_4Re_2$: C, 33.5 (33.5); H, 5.9 (5.9); N, 4.3 (4.2).

3.2.4 Synthesis of $(NBu_4)_2[(ReBr_5)_2(\mu\text{-pyz})]$ (3.2)

$(NBu_4)_2[ReBr_6]$ (0.10 mmol, 115.0 mg) and pyrazine (0.20 mmol, 16.0 mg) in 4.5 ml glacial acetic acid was heated at 70-80°C for 4 hours with stirring. A red solid was collected from the heterogeneous mixture by filtration. From a DCM solution of the solid exposed to diethyl ether vapour did brown single crystals grow after 2 days (31% yield). Elemental analysis (%) calculated (found) for $C_{36}H_{76}Br_{10}N_4Re_2$: C, 24.9 (25.0); H, 4.4 (4.3); N, 3.2 (3.0).

3.2.5 Synthesis of $(NBu_4)_2[(ReBr_5)_2(\mu\text{-pym})]$ (3.3)

$(NBu_4)_2[ReBr_6]$ (0.10 mmol, 115.0 mg) and pyrimidine (0.20 mmol, 16 µl) was mixed in 4.5 ml glacial acetic acid. The heterogeneous solution was stirred at 70-80°C for 2 hours and a solid was collected by filtration. The solid was dissolved in DCM and layered with isopropanol. Single crystals suitable for X-ray diffraction were collected after 2-3 days (13% yield). Elemental analysis (%) calculated (found) for $C_{36}H_{76}Br_{10}N_4Re_2$: C, 24.9 (25.0); H, 4.4 (4.3); N, 3.2 (3.1).

3.2.6 Synthesis of $(NBu_4)_2[(ReBr_5)_2(\mu\text{-triz})]$ (3.4)

$(NBu_4)_2[ReBr_6]$ (0.10 mmol, 115.0 mg) and triazine (0.20 mmol, 16.2 mg) in 4.5 ml glacial acetic acid were stirred at 65-75°C for 2-4 hours. The orange solid obtained from the heterogeneous solution was dissolved in DCM and layered with glacial acetic acid. After 1-2 days orange single crystals suitable for X-ray diffraction had grown (19 % yield). Elemental analysis (%) calculated (found) for $C_{35}H_{75}Br_{10}N_5Re_2$: C, 24.2 (24.3); H, 4.4 (4.3); N, 4 (3.8).

3.3 Structures

3.3.1 Structure of $(NBu_4)_2[(ReCl_5)_2(\mu\text{-pyz})]$ (3.1)

Complex **3.1** crystallises in the monoclinic space group $P2_1/c$ and consists of two tetrabutylammonium cations and the anionic Re^{IV} dimer $[(ReCl_5)_2(\mu\text{-pyz})]^{2-}$ (Table 3.3.1). The two Re^{IV} ions occupy slightly distorted octahedral coordination spheres, each coordinated to five chloride ions and a nitrogen atom from the pyrazine ligand. The Re–Cl bond lengths vary between 2.3006(8)-2.3552(8) Å, with bond lengths of 2.180(2) and 2.175(2) Å for the Re(1)–N(1) and Re(2)–N(2) bonds, respectively (Figure 3.3.1 and Table 3.3.2). The intramolecular Re···Re separation is 7.1354(3) Å, with the pyrazine ligand twisted out of the Re_2Cl_6 plane by approximately 45°. The Re^{IV} ions are positioned out of the equatorial Cl_4 plane away from the pyrazine ligand by 0.1186(4) Å for Re(1) and 0.1207(4) Å for Re(2). The *cis* angles between the equatorial chloride ions and Re^{IV} ions are in the range 88.71(3)-91.08(3)° with the *trans* Cl–Re–N angle being 178.55(7) and 179.18(7)° for Cl(5)–Re(1)–N(1) and Cl(10)–Re(2)–N(2), respectively. The structural parameters of the Re^{IV} ions are similar to those published for the analogous $[ReCl_5(pyz)]^-$ monomer.[25] The pyrazine ligand contains C–C and C–N bond lengths in accordance to previously published results.[30, 38]

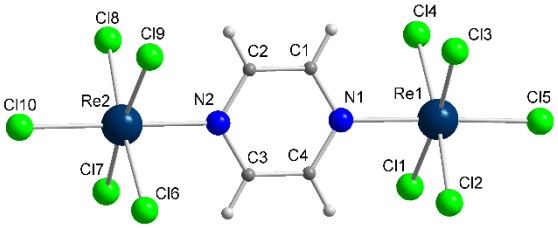

Figure 3.3.1. Structure of the $[(ReCl_5)_2(\mu\text{-pyz})]^{2-}$ dimer. Atoms labelled in accordance with Table 3.3.2. Colour code: Re, dark blue; Cl, green; C, grey; H; white.

In the extended structure each $[(ReCl_5)_2\mu\text{-pyz}]^{2-}$ unit is well isolated from adjacent anions by the NBu_4^+ cations (Figure 3.3.2). The latter pack around the anions through numerous C–H···Cl interactions with the shortest intermolecular Cl···Cl and Re···Re distances being 4.6976(11) and 8.3503(3) Å, respectively (Table 3.3.3).

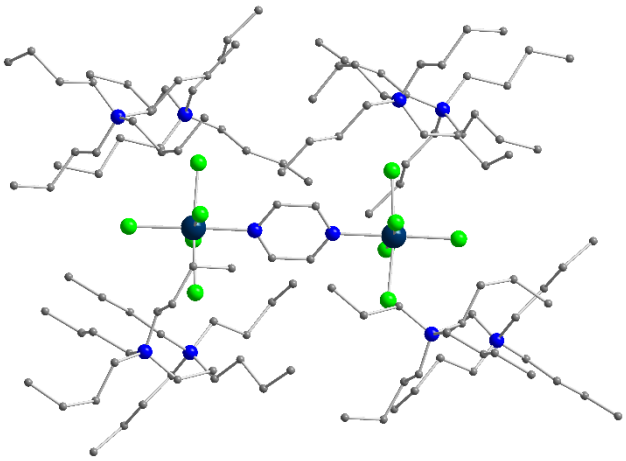

Figure 3.3.2. The packing of cations and anion. Hydrogen atoms are omitted for clarity. Colour code as in Figure 3.3.1.

3.3.2 Structure of $(NBu_4)_2[(ReBr_5)_2(\mu\text{-pyz})]$ (3.2)

3.2 crystallises in the monoclinic space group $P2_1/n$ (Table 3.3.1). The asymmetric unit contains half the $[(ReBr_5)_2\mu\text{-pyz}]^{2-}$ dimer and one NBu_4^+ cation, due to the presence of an inversion centre positioned at the centroid of the pyrazine ligand. The Re^{IV} ion is coordinated to five bromide ions and a nitrogen atom from the pyrazine ligand. The Re–Br bond lengths range from 2.4489(6) to 2.4953(6) Å with the Re–N bond being 2.196(4) Å (Table 3.3.2). The *cis* angles between the Re^{IV} ion and the bromide ions positioned perpendicular to the Br–Re–N axis are close to 90°, the Br(1)–Re(1)–N(1) angle is 178.57(11)° (Table 3.3.2 and Figure 3.3.3). In the crystal lattice, the pyrazine moeity is disordered over two positions with the plane of the ligand twisted with respect to the Re_2Br_6 plane at inter-plane angles of 40 and 44°.

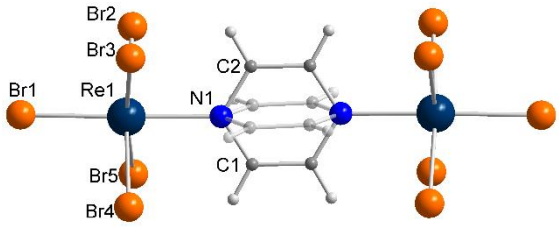

Figure 3.3.3. The $[(ReBr_5)_2(\mu\text{-pyz})]^{2-}$ anion with the two orientations of the pyrazine ligand shown. Atoms labelled in accordance with Table 3.3.2. Colour code: Re, dark blue; Br, orange; N, blue; C, grey; H, white.

The Re^{IV} ion is displaced out of the equatorial Br_4 plane away from the pyrazine ligand by 0.1148(4) Å. The geometrical parameters for the Re^{IV} ion are in accordance with the previously published $(NBu_4)[ReBr_5(N\text{-2-pyrazinecarboxylic acid})]$ structure, and the bridging pyrazine ligand contains C–C and C–N bond lengths with values similar to those found in **3.1**.[39] The intradimer Re···Re separation is 7.1723(4) Å. In the crystal lattice NBu_4^+ cations pack

around the anions *via* numerous C–H···Br interactions. The anions pack through short Br···Br interactions, the shortest distance being 3.5202(9) Å between Br(2)···Br(2)', creating a 1D network of anions interacting end-to-end along the crystallographic *a*-axis (Figure 3.3.4). This causes the shortest intermolecular Re···Re distance to be 8.4862(5) Å. These 1D anionic networks are isolated from adjacent chains by the NBu_4^+ cations, with the shortest interchain Br···Br separation being 4.1250(11) Å (Figure 3.3.5).

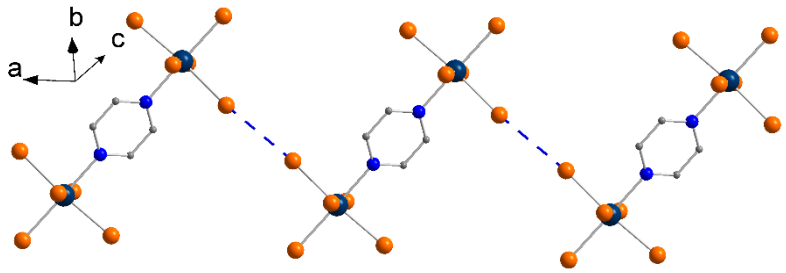

Figure 3.3.4. The 1D anionic motif. Short Br···Br distance indicated by dashed blue lines. Hydrogen atoms are omitted for clarity. Colour code as in Figure 3.3.3.

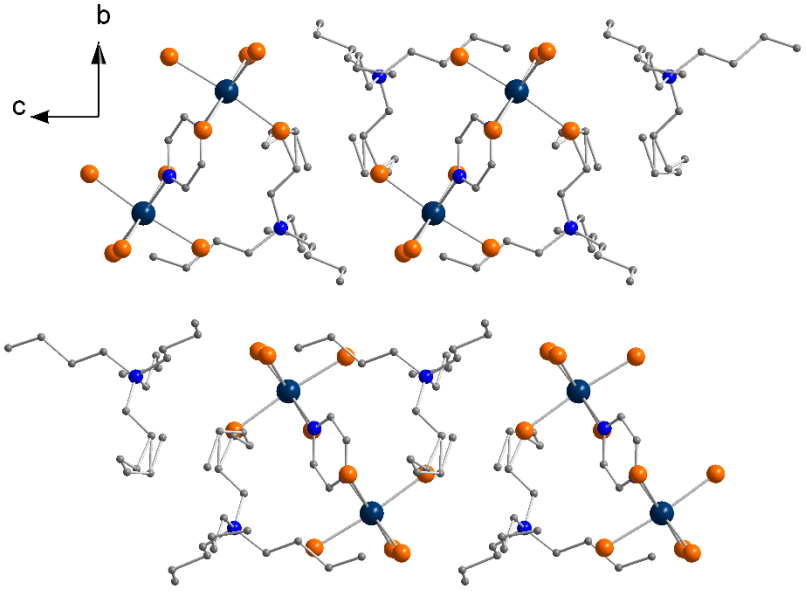

Figure 3.3.5. The packing of $(NBu_4)_2[(ReBr_5)_2(\mu\text{-pyz})]$ viewed down the crystallographic *a*-axis. Hydrogen atoms are omitted for clarity. Colour code as in Figure 3.3.3.

3.3.3 Structure of $(NBu_4)_2[(ReBr_5)_2(\mu\text{-pym})]$ (3.3)

Complex **3.3** crystallises in the monoclinic space group $P2_1$ with the asymmetric unit containing two $(NBu_4)_2[(ReBr_5)_2(\mu\text{-pym})]$ complexes (Table 3.3.1). The two $[(ReBr_5)_2(\mu\text{-pym})]^{2-}$ anions display near identical coordination geometries, with the first coordination sphere of the Re^{IV} ions similar to that one described for **3.2** (Table 3.3.2). The bridging pyrimidine ligand contains C–C and C–N bond lengths with values in accordance to previously published structures.[31] The two Re^{IV} ions are disposed at an angle of approximately 118° with respect

to the centre of the pyrimidine moiety (Figure 3.3.6), with the organic ligand positioned equidistant between the two perpendicular [$ReCl_4$] planes. The intradimer Re···Re distance is *circa* 6.1 Å with the shortest Br···Br separation being 4.006(2) Å (Br(12)···Br(18)) (Table 3.3.3).

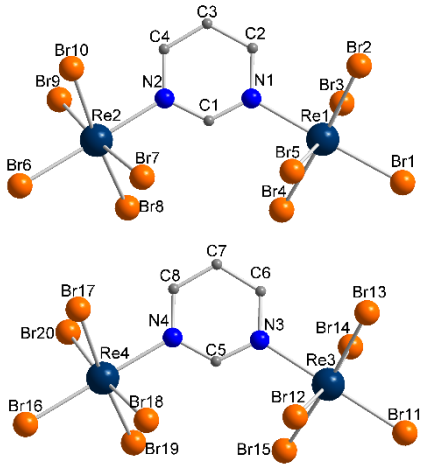

Figure 3.3.6. The two anions of **3.3** present in the asymmetric unit. Atoms labelled in accordance with Table 3.3.2. Hydrogen atoms are omitted for clarity. Colour code as in Figure 3.3.3.

In the crystal lattice, numerous C–H···Br interactions are present between anions and cations causing each [$(ReBr_5)_2(\mu$-pym)]$^{2-}$ moiety to be well isolated from neighbouring anions, with the shortest intermolecular Br···Br distance being 4.707(2) Å (Figure 3.3.7).

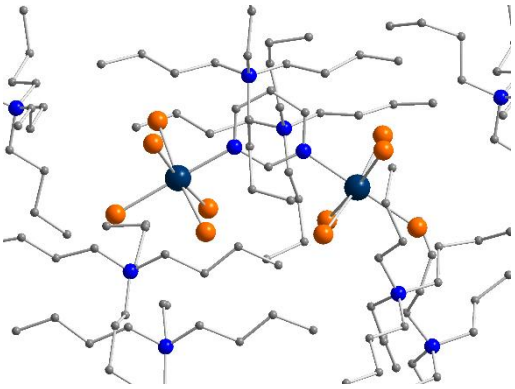

Figure 3.3.7. The anion of **3.3** encapsulated by the NBu_4^+ cations. Hydrogen atoms are omitted for clarity. Colour code as in Figure 3.3.3.

3.3.4 Structure of $(NBu_4)_2[(ReBr_5)_2(\mu$-triz)] (3.4)

The complex $(NBu_4)_2[(ReBr_5)_2(\mu$-triz)] crystallises in the monoclinic space group $I2/a$ (Table 3.3.1). The asymmetric unit contains one NBu_4^+ cation and half a [$(ReBr_5)_2(\mu$-triz)]$^{2-}$ anion due to a two-fold rotation axis intersecting the C(2) and N(2) atoms on the triazine ligand (Figure 3.3.8). The Re^{IV} ion sits in a coordination sphere similar to the one described for complex **3.2** (Table 3.3.2). The triazine ligand contains C–C and C–N bond lengths which correlate to previously published results describing the triazine molecule bridging two metal ions.[40] In the [$(ReBr_5)_2(\mu$-triz)]$^{2-}$ unit the two Re^{IV} ions are placed at angle of 121.91(4)° with respect to the

triazine centroid, with a 'through space' separation of 6.2390(4) Å. The shortest intramolecular Br···Br separation is 4.5249(4) Å for Br(2)···Br(3)' (Table 3.3.3). The organic ligand is again positioned equidistant between the two approximately perpendicular [$ReBr_4$] planes.

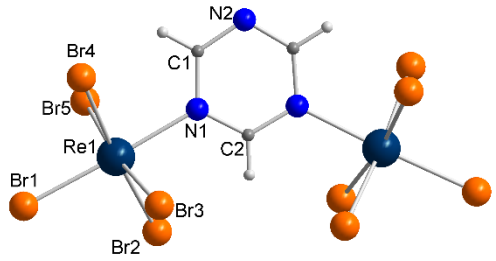

Figure 3.3.8. The $[(ReBr_5)_2(\mu\text{-triz})]^{2-}$ anion. Atoms labelled in accordance with Table 3.3.2. Colour code as in Figure 3.3.3.

In the extended structure the anions interact through short Br···Br interactions with neighbouring $[(ReBr_5)_2(\mu\text{-triz})]^{2-}$ units. The shortest intermolecular Br···Br distance is 3.4304(4) Å (Br(5)···Br(5)') which creates a 1D chain motif in the direction of the crystallographic *c*-axis (Figure 3.3.9). The shortest intermolecular Re···Re distance is 8.4090(3) Å. The NBu_4^+ cations pack around each 1D anionic network through C–H···Br interactions causing the shortest interchain Br···Br distance to be 4.8549(3) Å.

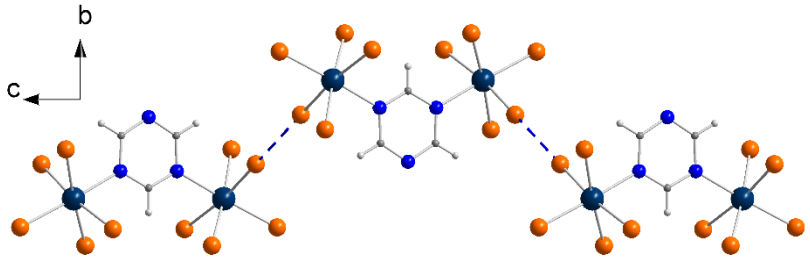

Figure 3.3.9. The Br···Br interaction in the crystal lattice of **3.4**. Short Br···Br distances indicated by dashed blue lines. Colour code as in Figure 3.3.3.

3.3.5 Tables of crystallographic and structural parameters

Table 3.3.1. Crystallographic parameters for **3.1**, **3.2**, **3.3** and **3.4**.

	3.1	**3.2**	**3.3**	**3.4**
Crystal data				
Chemical formula	$C_4H_4Cl_{10}N_2Re_2$ ·2($C_{16}H_{36}N$)	$C_4H_4Br_{10}N_2Re_2$ ·2($C_{16}H_{36}N$)	$C_4H_4Br_{10}N_2Re_2$ ·2($C_{16}H_{36}N$)	$C_3H_3Br_{10}N_3Re_2$ ·2($C_{16}H_{36}N$)
M_r	1291.96	1736.50	1736.50	1737.50
Crystal system, space group	Monoclinic, $P2_1/c$	Monoclinic, $P2_1/n$	Monoclinic, $P2_1$	Monoclinic, $I2/a$
Temperature (K)	295	120	293	120
a, b, c (Å)	15.6173(3), 19.3882(4), 16.8316(4)	11.0630 (3), 22.3446 (5), 11.9834 (4)	16.5547 (3), 15.1382 (2), 21.5926 (3)	23.7287 (5), 11.12035 (19), 20.8616 (5)
β (°)	91.5337(19)	115.626 (4)	90.122 (2)	108.371 (2)
V (Å^3)	5094.63(18)	2670.90 (14)	5411.27 (14)	5224.26 (19)
Z	4	2	4	4
Radiation type	Mo $K\alpha$	Mo $K\alpha$	Mo $K\alpha$	Mo $K\alpha$
μ (mm^{-1})	5.301	12.04	11.88	12.31
Crystal size (mm)	0.17 × 0.09 × 0.05	0.35 × 0.19 × 0.07	0.70 × 0.11 × 0.04	0.21 × 0.11 × 0.08
Data collection				
T_{min}, T_{max}	0.977, 0.992	0.755, 0.923	0.318, 0.938	0.832, 0.926
No. of measured, independent and observed [$I > 2\sigma(I)$] reflections	130073, 18129, 14396	56629, 8154, 6199	94121, 25646, 18840	66891, 7965, 7101
R_{int}	0.079	0.069	0.067	0.051
$(\sin\theta/\lambda)_{max}$ (Å^{-1})	×	0.728	0.686	0.726
Refinement				
$R[F^2 > 2\sigma(F^2)]$, $wR(F^2)$, S	0.040,0.058,1.06	0.042, 0.080, 1.05	0.045, 0.077, 0.96	0.028, 0.045, 1.12
No. of reflections	18129	8154	25646	7965
No. of parameters	477	287	973	240
No. of restraints	0	0	0	0
$\Delta\rho_{max}$, $\Delta\rho_{min}$ (e Å^{-3})	1.83, -1.14	2.09, −2.91	1.41, −1.22	1.10, −1.56

Table 3.3.2. Structural parameters of the Re^{IV} ion in **3.1**, **3.2**, **3.3** and **3.4**.

Structure	**3.1** (X; Cl)	**3.2** (X; Br)
Bond lengths / Å		
Re–X	2.3006(8)–2.3552(8)	2.4489(6)–2.4953(6)
Re–N / Å	2.180(2), 2.175(2)	2.196(4)
Bond angles / °		
X_{eq}–Re–X_{eq}	88.71(3)–91.08(3)	89.042(19)– 90.63(2)
X_{trans}–Re–N	178.55(7), 179.18(7)	178.57(11)
Out-of-plane / Å		
Re–X_{eq} plane	0.1186(4), 0.1207(4)	0.1148(4)

	3.3	**3.4**
Bond lengths / Å		
Re–Br	2.4476(14)–2.5185(14)	2.4495(3)–2.5009(3)
Re–N / Å	2.197(10)–2.221(10)	2.211(2)
Bond angles / °		
Br_{eq}–Re–Br_{eq}	87.64(5)–91.83(5)	89.732(11)–89.919(10)
Br_{trans}–Re–N	177.5(2)	177.52(6)
Out-of-plane / Å		
Re–Br_{eq} plane	0.1194(9)–0.1300(9)	0.1306(2)

Table 3.3.3. Shortest intra- and intermolecular halide···halide interactions in **3.1**, **3.2**, **3.3** and **3.4**.

	Intramolecular X···X / Å	Intermolecular X···X / Å
3.1, (X; Cl)	6.8602(11)	4.6976(11)
3.2, (X; Br)	6.9116(8)	3.5202(9)
3.3, (X; Br)	4.006(2)	4.707(2)
3.4, (X; Br)	4.5249(4)	3.4304(4)

3.4 Magnetic properties

The magnetic susceptibility was measured from T = 300 to 2 K in a static field of 1000 Oe, and is plotted as χ_M and $\chi_M T$ *versus* T [χ_M being the molar magnetic susceptibility *per* dimeric Re^{IV} unit] in Figure 3.4.1.

For **3.1**, the $\chi_M T$ value of 2.96 $cm^3\ mol^{-1}\ K$ at T = 300 K is slightly lower than expected for two uncoupled paramagnetic Re^{IV} ions (~1.52–1.69 $cm^3\ mol^{-1}\ K$ *per* Re^{IV} ion, assuming g = 1.8–1.9 and S = 3/2). As the temperature is lowered the $\chi_M T$ value decreases, at first gradually until T = 100 K where from the descent intensifies reaching 0.02 $cm^3\ mol^{-1}\ K$ at T = 2 K (Figure 3.4.1a). In the plot of χ_M *vs.* T a maximum is observed at T = 45 K indicative of significant antiferromagnetic exchange interactions in the system (Figure 3.4.1b).

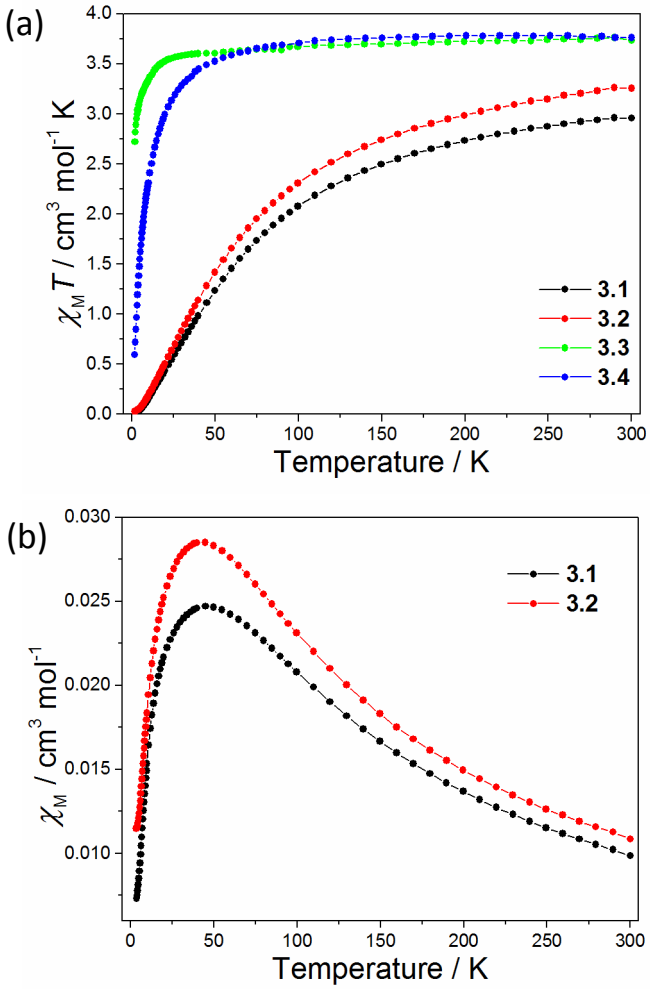

Figure 3.4.1. a) The $\chi_M T$ *versus* T graphs for the four dimers. b) The χ_M *vs.* T plot for **3.1** and **3.2**. The solid lines are guides to the eye.

The $\chi_M T$ value for **3.2** at T = 300 K is 3.26 $cm^3\ mol^{-1}\ K$, a value expected for two paramagnetic Re^{IV} ions (Figure 3.4.1a). Upon lowering the temperature the magnetic susceptibility behaves

similar to that of **3.1** with the $\chi_M T$ value being 0.02 cm^3 mol^{-1} K at T = 2 K and a maximum at T = 45 K in the χ_M *vs. T* plot (Figure 3.4.1b).

The similar magnetic behaviour of compounds **3.1** and **3.2** indicates the dominant magnetic exchange interaction to be mediated by the pyrazine ligand, indicating the difference in halide ligand has a negligible effect on the magnetic susceptibility.

3.3 exhibits a $\chi_M T$ value of 3.73 cm^3 mol^{-1} K at T = 300 K, which is higher than the value of ~3.04–3.38 cm^3 mol^{-1} K expected for two non-interacting Re^{IV} ions (Figure 3.4.1a). Upon cooling a small decrease of $\chi_M T$ value to a value of 3.54 cm^3 mol^{-1} K at T = 22 K was observed. Lowering the temperature further results in a drop of $\chi_M T$ to a value of 2.72 cm^3 mol^{-1} K at T = 2 K. No maxima is observed in the χ_M *versus T* graph.

At T = 300 K a $\chi_M T$ value of 3.76 cm^3 mol^{-1} K is measured for **3.4**, a value slightly higher than expected but similar to the one of **3.3**. The $\chi_M T$ value exhibits a slight increase (of 0.02 cm^3 mol^{-1} K) upon lowering the temperature to T = 220 K, whereafter the value decreases to 3.45 cm^3 mol^{-1} at T = 40 K (Figure 3.4.1a). Cooling the sample further causes a rapid decrease in the $\chi_M T$ value, which reaches 0.59 cm^3 mol^{-1} K at T = 2 K. In the χ_M *versus T* plot a maximum is observed at T = 3.3 K, indicative of significant antiferromagnetic interactions in the system (Figure 3.4.2).

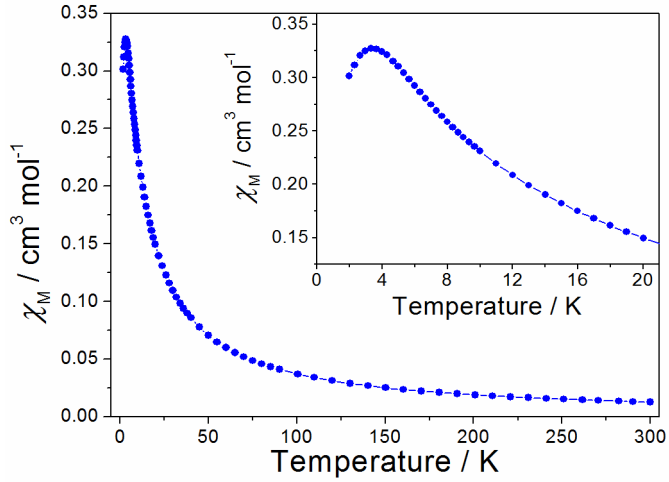

Figure 3.4.2. The χ_M *vs. T* plot for **3.4**, insert showing the peak at T = 3.3 K. The solid lines are guides to the eye.

From the susceptibility measurements it is clear that complexes **3.3** and **3.4** exhibit intramolecular ferromagnetic exchange interactions with the drop at low temperatures also being due to a combination of magnetic anisotropy, Zeeman effects and intermolecular interactions.

Antiferromagnetic exchange interactions in **3.4** is corroborated by the maximum in the χ_M *vs.* *T* plot. The absence of a maximum in the data for **3.3** could be attributed to the shorter intermolecular Br···Br distances present in the crystal lattice of **3.4** which are not found in **3.3** (Figure 3.3.9 and Table 3.3.3).

Isothermal magnetisation data at *T* = 2 K confirms the above conclusions. Compounds **3.1** and **3.2** clearly possess diamagnetic ground states at all applied fields, whereas **3.3** and **3.4** contain magnetisation curves expected for ferromagnetically coupled Re^{IV} dimers, with magnetic moments of 4.4 and 4 μ_B, at *H* = 7 T, respectively, (Figure 3.4.3). The "S shape" of the curve at low fields for **3.4** is indicative of the applied field overcoming the weak intermolecular antiferromagnetic coupling.

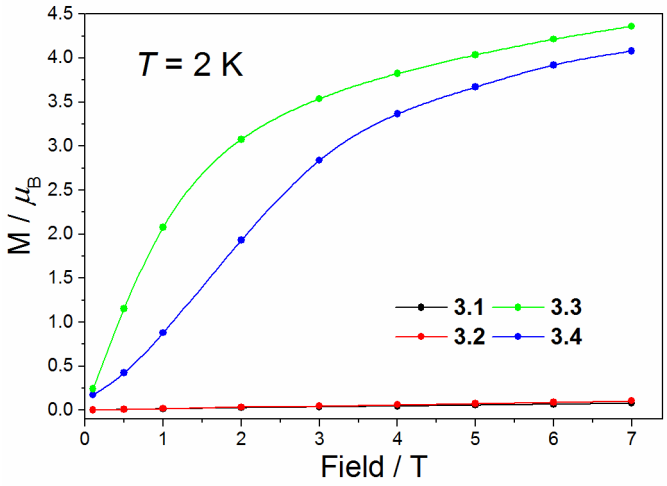

Figure 3.4.3. Isothermal magnetisation measurements for the four dimers at *T* = 2 K.

3.5 Summary

The first structural and magnetic investigation of paramagnetic homometallic Re^{IV} dimers has been carried out. The molecules are $(NBu_4)_2[(ReCl_5)_2(\mu\text{-pyz})]$ (**3.1**), $(NBu_4)_2[(ReBr_5)_2(\mu\text{-pyz})]$ (**3.2**), $(NBu_4)_2[(ReBr_5)_2(\mu\text{-pym})]$ (**3.3**) and $(NBu_4)_2[(ReBr_5)_2(\mu\text{-triz})]$ (**3.4**). The dimers are synthesised from the $(NBu_4)_2[ReCl_6]$ (**3.1**) or $(NBu_4)_2[ReBr_6]$ (**3.2**, **3.3** and **3.4**) precursor and their respective ligand in glacial acetic acid with continuous stirring and heating. Single crystals were obtained from DCM solutions layered with acetic acid (**3.1** and **3.4**), diethyl ether (**3.2**) or isopropanol (**3.3**), with the structures crystallising in the monoclinic space groups $P2_1/c$ (**3.1**), $P2_1/n$ (**3.2**), $P2_1$ (**3.3**) and $I2/a$ (**3.4**). In the crystal lattice, the NBu_4^+ cations pack around the dimers giving rise to little intermolecular interactions between anions. The magnetic measurements revealed the two Re^{IV} ions bridged by a 1,4 heterocyclic amine to

exhibit a strong antiferromagnetic coupling indicated by maxima in the χ_M *vs*. *T* plot at *T* = 45 K (**3.1** and **3.2**) presumably induced by the linearity of the bridging ligand. The two dimers **3.3** and **3.4** bridged by a 1,3 donating cyclic amine exhibit similar magnetic behaviour from *T* = 300 K to *circa T* = 50 K indicative of ferromagnetic interactions. Below *T* = 50 K a sharp decrease for **3.4** (and not **3.3**) is observed due to the presence of intermolecular antiferromagnetic exchange interactions.

3.6 References

1. R. Inglis, C. J. Milios, L. F. Jones, S. Piligkos and E. K. Brechin, *Chem. Commun.*, 2012, **48**, 181.
2. T. B. Faust, V. Bellini, A. Candini, S. Carretta, G. Lorusso, D. R. Allan, L. Carthy, D. Collison, R. J. Docherty, J. Kenyon, J. Machin, E. J. L. McInnes, C. A. Muryn, H. Nowell, R. G. Pritchard, S. J. Teat, G. A. Timco, F. Tuna, G. F. S. Whitehead, W. Wernsdorfer, M. Affronte and R. E. P. Winpenny, *Chem. Eur. J.*, 2011, **17**, 14020.
3. I. Gryca, J. Palion-Gazda, B. Machura, M. Penkala, F. Lloret and M. Julve, *Eur. J. Inorg. Chem.*, 2016, **2016**, 5418.
4. S. Triki, C. J. Gómez-García, E. Ruiz and J. Sala-Pala, *Inorg. Chem.*, 2005, **44**, 5501.
5. K. S. Pedersen, J. Bendix and R. Clerac, *Chem. Commun.*, 2014, **50**, 4396.
6. X.-Y. Wang, C. Avendano and K. R. Dunbar, *Chem. Soc. Rev.*, 2011, **40**, 3213.
7. D. Pinkowicz, R. Podgajny, B. Nowicka, S. Chorazy, M. Reczynski and B. Sieklucka, *Inorg. Chem. Frontiers*, 2015, **2**, 10.
8. J. Martínez-Lillo, T. F. Mastropietro, E. Lhotel, C. Paulsen, J. Cano, G. De Munno, J. Faus, F. Lloret, M. Julve, S. Nellutla and J. Krzystek, *J. Am. Chem. Soc.*, 2013, **135**, 13737.
9. X. Feng, J.-L. Liu, K. S. Pedersen, J. Nehrkorn, A. Schnegg, K. Holldack, J. Bendix, M. Sigrist, H. Mutka, D. Samohvalov, D. Aguila, M.-L. Tong, J. R. Long and R. Clerac, *Chem. Commun.*, 2016.
10. K. S. Pedersen, M. Sigrist, M. A. Sørensen, A.-L. Barra, T. Weyhermüller, S. Piligkos, C. A. Thuesen, M. G. Vinum, H. Mutka, H. Weihe, R. Clérac and J. Bendix, *Angew. Chem. Int. Ed.*, 2014, **53**, 1351.
11. J. Martínez-Lillo, D. Armentano, G. De Munno, W. Wernsdorfer, M. Julve, F. Lloret and J. Faus, *J. Am. Chem. Soc.*, 2006, **128**, 14218.
12. J. Martinez-Lillo, D. Armentano, G. De Munno, F. Lloret, M. Julve and J. Faus, *Dalton Trans.*, 2008, 40.
13. J. Martinez-Lillo, D. Armentano, G. De Munno, F. Lloret, M. Julve and J. Faus, *Cryst. Growth Des.*, 2006, **6**, 2204.
14. T. D. Harris, M. V. Bennett, R. Clérac and J. R. Long, *J. Am. Chem. Soc.*, 2010, **132**, 3980.
15. T. D. Harris, C. Coulon, R. Clerac and J. R. Long, *J. Am. Chem. Soc.*, 2011, **133**, 123.
16. T. D. Harris, H. S. Soo, C. J. Chang and J. R. Long, *Inorg. Chim. Acta*, 2011, **369**, 91.
17. I. Bhowmick, E. A. Hillard, P. Dechambenoit, C. Coulon, T. D. Harris and R. Clerac, *Chem. Commun.*, 2012, **48**, 9717.
18. R. Chiozzone, R. González, C. Kremer, G. De Munno, D. Armentano, F. Lloret, M. Julve and J. Faus, *Inorg. Chem.*, 2003, **42**, 1064.

19. J. Martínez-Lillo, F. S. Delgado, C. Ruiz-Pérez, F. Lloret, M. Julve and J. Faus, *Inorg. Chem.*, 2007, **46**, 3523.
20. J. Martínez-Lillo, D. Armentano, G. De Munno, W. Wernsdorfer, J. M. Clemente-Juan, J. Krzystek, F. Lloret, M. Julve and J. Faus, *Inorg. Chem.*, 2009, **48**, 3027.
21. D. Armentano and J. Martínez-Lillo, *Cryst. Growth Des.*, 2016, **16**, 1812.
22. X. Feng, T. David Harris and J. R. Long, *Chem. Sci.*, 2011, **2**, 1688.
23. I. Bhowmick, T. D. Harris, P. Dechambenoit, E. Hillard, C. Pichon, I.-R. Jeon and R. Clérac, *Science China Chemistry*, 2012, **55**, 1004.
24. X. Feng, J. Liu, T. D. Harris, S. Hill and J. R. Long, *J. Am. Chem. Soc.*, 2012, **134**, 7521.
25. J. Martinez-Lillo, D. Armentano, N. Marino, L. Arizaga, R. Chiozzone, R. Gonzalez, C. Kremer, J. Cano and J. Faus, *Dalton Trans.*, 2008, 4585.
26. L. Arizaga, R. González, R. Chiozzone, C. Kremer, M. F. Cerdá, D. Armentano, G. D. Munno, F. Lloret and J. Faus, *Polyhedron*, 2008, **27**, 552.
27. D. G. Tisley and R. A. Walton, *Journal of the Chemical Society A: Inorganic, Physical, Theoretical*, 1971, 3409.
28. J. Martínez-Lillo, D. Armentano, F. R. Fortea-Pérez, S.-E. Stiriba, G. De Munno, F. Lloret, M. Julve and J. Faus, *Inorg. Chem.*, 2015, **54**, 4594.
29. E. C. Johnson, R. W. Callahan, R. P. Eckberg, W. E. Hatfield and T. J. Meyer, *Inorg. Chem.*, 1979, **18**, 618.
30. G. Chen, W.-L. Man, S.-M. Yiu, T.-W. Wong, L. Szeto, W.-T. Wong and T.-C. Lau, *Dalton Trans.*, 2011, **40**, 1938.
31. N. Nédélec and F. D. Rochon, *Inorg. Chem.*, 2001, **40**, 5236.
32. R. Chiozzone, R. González, C. Kremer, G. De Munno, J. Cano, F. Lloret, M. Julve and J. Faus, *Inorg. Chem.*, 1999, **38**, 4745.
33. J. Kleinberg, *Inorg. Synth.*, McGraw-Hill, 1963.
34. G. A. Bain and J. F. Berry, *J. Chem. Educ.*, 2008, **85**, 532.
35. L. J. Bourhis, O. V. Dolomanov, R. J. Gildea, J. A. K. Howard and H. Puschmann, *Acta Crystallogr. Sect. A*, 2015, **71**, 59.
36. G. Sheldrick, *Acta Crystallogr. Sect. A*, 2008, **64**, 112.
37. O. V. Dolomanov, L. J. Bourhis, R. J. Gildea, J. A. K. Howard and H. Puschmann, *J. Appl. Crystallogr.*, 2009, **42**, 339.
38. A. Skarżyńska and M. Siczek, *Polyhedron*, 2008, **27**, 1930.
39. A. Cuevas, C. Kremer, M. Hummert, H. Schumann, F. Lloret, M. Julve and J. Faus, *Dalton Trans.*, 2007, 342.
40. J. T. Maeyer, T. J. Johnson, A. K. Smith, B. D. Borne, R. D. Pike, W. T. Pennington, M. Krawiec and A. L. Rheingold, *Polyhedron*, 2003, **22**, 419.

Chapter 4: A family of $Re^{IV}Cu^{II}$ chains

4.1 Introduction

In the field of molecular magnetism the quest to understand and exploit the intrinsic magnetic anisotropy of transition metal and lanthanide ions has intensified since the discovery of the Single-Molecule Magnet 'Mn_{12}' and the Single-Ion Magnet '$Tb(Pc)_2$'.[1, 2]

Zero field splitting plays an important role in the energy barrier for reversal of the magnetisation in these systems and for this reason the $5d^3$ Re^{IV} ion is of great interest due to its large magnetic anisotropy,[3] which arises from second order spin-orbit coupling and manifested in a spin-orbit coupling constant for the free ion of $\lambda \approx 1000$ cm^{-1}.[3]

Until recently, the role of the $[ReCl_6]^{2-}$ anion has been used as a synthetic precursor or co-crystallised with various cations.[4-7] A common strategy for the creation of new Re^{IV} complexes is the functionalisation of the $[ReCl_6]^{2-}$ anion through halide exchange with ligands such as heterocyclic amines, pseudo halides such as cyanide or chelates such as the oxalate anion.[4, 8-11] These species have subsequently been employed as metalloligands for the creation of larger oligomers.[12-15] Molecular salts of the $[ReCl_6]^{2-}$ anion have also been extensively studied in order to examine the effect of cation size on intermolecular interactions and the resultant intermolecular magnetic exchange.[5, 16, 17]

More recently, a number of 1D chains based on the Re^{IV} ion have been reported. For example, the $[trans\text{-}ReCl_4(CN)_2]^{2-}$ anion was used to construct the Single-Chain Magnet $\{[Fe(DMF)_4][trans\text{-}ReCl_4(CN)_2]\}_n$ which displays a coercive field of $H_{co} = 1$ T at $T = 1.8$ K;[7] the $[ReF_6]^{2-}$ anion was used for the first time in 2014 as a metalloligand for the synthesis of the 1D network $\{[Ni(Vim)_4][ReF_6]\}_n$, Vim = Vinylimidazole, which exhibits strong ferromagnetic exchange between neighbouring metal ions,[18] while the $\{[Cu(pyim)_2][ReCl_4(ox)]\}_n$ chain, pyim = 2-(2'-pyridyl)imidazole and ox = oxalate, exhibits ferrimagnetic behaviour due to the presence of two different interaction pathways (O, Cl) between the Re^{IV} and Cu^{II} ions.[19]

The possibility of using the $[ReCl_6]^{2-}$ unit as a linker for molecular chains was revealed by Brechin *et al*. in 2014.[20] The study of the $\{[Cu(pyim)(imi)_2][ReCl_6]\}_n$ complex, imi = imidazole, revealed antiferromagnetic exchange interactions and metamagnetic behaviour. This discovery has prompted us to search for more 1D networks based on the $[ReCl_6]^{2-}$ anion.

Here we present six new chains which are characterised magnetically, structurally and theoretically. These chains are of general formula $\{[Cu(L)_4][ReCl_6]\}_n$, where L = imidazole (imi),

1-methylimidazole (Meim), 1-vinylimidazole (Vim), 1-butylimidazole (Buim), 1-vinyl-1,2,4-triazole (Vtri) and dimethylformamide (DMF) (Figure 4.1).

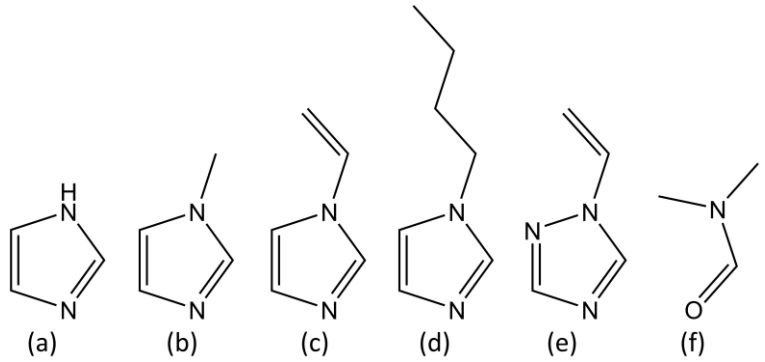

Figure 4.1. The ligands employed; a) imidazole, b) 1-methylimidazole, c) 1-vinylimidazole, d) 1-butylimidazole, e) 1-vinyl-1,2,4-triazole, f) dimethylformamide.

4.2 Experimental

4.2.1 Materials and methods

All chemicals were used as received. Syntheses were carried out under aerobic conditions using CH_3CN dried over 3 Å molecular sieves. $(NBu_4)_2[ReCl_6]$ was prepared as described previously.[4, 21] Crystals of the six compounds were collected and left open to air before use in further analysis. Elemental analyses (C, H, N) were performed by MEDAC Ltd. Direct current (dc) magnetic susceptibility measurements were collected on a Quantum Design MPMS-XL SQUID magnetometer equipped with a 7 T dc magnet in the temperature range 1.8 – 300 K. Diamagnetic corrections were applied using Pascal's constants.[22]

4.2.2 Crystallography

Data were measured on Rigaku Oxford Diffraction SuperNova (**4.1**, **4.2**, **4.5**, **4.6**) and Rigaku Oxford Diffraction XCalibur (**4.3**, **4.4**) X-ray diffractometers using Mo-K_α radiation. Structures were solved with olex2.solve (**4.1**, **4.2**, **4.6**)[23] or ShelXS (**4.3**, **4.4**, **4.5**)[24] and refined by full-matrix least-squares on F-squared using ShelXL, interfaced through Olex2.[25] All non-hydrogen atoms were refined anisotropically. The hydrogen atom parameters were constrained.

4.2.3 Computational Details

Calculations were performed with the Gaussian09 package using the CAM-B3LYP functional (a long range corrected version of B3LYP) and the quadratic convergence approach.[26-31] Double-ζ and Los Alamos effective core potentials, as proposed by Hay and Wadt, were used for the Re^{IV} and Cl^- ions.[32-34] Ahlrichs double-ζ basis set was used for the remaining atoms.[35] Two-electron integrals and their derivatives were computed from Douglas-Kroll-Hess (DKH) 2nd order scalar relativistic calculations.[36, 37] An approach based on the use of broken-symmetry (BS) functions built from localised orbitals was employed to evaluate the energies of several spin states.[38] The BS functions were obtained from the guess functions generated with the fragment tool implemented in Gaussian09. Intermolecular magnetic couplings were calculated from the experimental structures. Intramolecular interactions were calculated on $Re^{IV}Cu^{II}$ models designed from experimental geometries. Parameters corresponding to the acetonitrile solvent were included to simulate the electronic effects of the surrounding molecules.[39]

Calculations of the zero-field splitting, *zfs*, parameters were performed with version 3.0 of the ORCA program.[40] The TZVP basis set proposed by Ahlrichs, and tight SCF criteria were used in all cases.[35] Relativistic effects for the Re^{IV} ion were introduced from a zero-order regular approximation (ZORA).[41] For complete active space (CAS) calculations, this auxiliary basis set was replaced by TZV/C.[42, 43] The *zfs* parameters were evaluated from N-Electron Valence State Perturbation Theory (NEVPT2) calculations and an approach based on an effective Hamiltonian for the spin-orbit coupling. This *zfs* calculation included contributions from ten quartet and twenty doublet states generated from electron promotion between *d* orbitals, which corresponds to the full active space modelled from only the five *d* orbitals of the Re^{IV} ion.[44-46]

4.2.4 Synthesis of {[Cu(imidazole)$_4$][ReCl$_6$]·2(CH$_3$)$_2$CHOH}$_n$ (4.1)

$(NBu_4)_2[ReCl_6]$ (0.05 mmol, 44.0 mg) and $Cu(NO_3)_2{\cdot}3H_2O$ (0.05 mmol, 12.0 mg) were dissolved in 3 ml CH_3CN, to which imidazole (0.20 mmol, 13.6 mg) in 3 ml CH_3CN was added. Violet crystals suitable for single crystal X-ray diffraction were grown in 4 days from the solution by layering with isopropanol (53% yield). Elemental analysis (%) calculated (found) for $C_{12}H_{16}N_8Cl_6CuRe$: C, 19.6 (19.1); H, 2.2 (2.2); N, 15.3 (14.4).

4.2.5 Synthesis of {[Cu(1-methylimidazole)$_4$][ReCl$_6$]}$_n$ (4.2)

$(NBu_4)_2[ReCl_6]$ (0.05 mmol, 44.0 mg) and $Cu(NO_3)_2{\cdot}3H_2O$ (0.05 mmol, 12.0 mg) were dissolved in 3 ml of acetonitrile at T = 4 °C to which 1-methylimidazole (0.20 mmol, 16.4 µl) in 3 ml of CH_3CN at T = 4 °C was added. Single crystals for X-ray diffraction were obtained from the solution after standing at 4 °C for 1 hour (85% yield). Elemental analysis (%) calculated (found) for $C_{16}H_{24}N_8Cl_6CuRe$: C, 24.3 (24.3); H, 3.1 (2.9); N, 14.2 (13.9).

4.2.6 Synthesis of {[Cu(1-vinylimidazole)$_4$][ReCl$_6$]}$_n$ (4.3)

$(NBu_4)_2[ReCl_6]$ (0.05 mmol, 44.0 mg) and $Cu(NO_3)_2{\cdot}3H_2O$ (0.05 mmol, 12.0 mg) were dissolved in 5 ml of CH_3CN at T = 4 °C and subsequently 1-vinylimidazole (0.20 mmol, 19 µl) was added to the solution. Purple crystals suitable for single crystal X-ray diffraction were collected from the solution after standing at 4 °C for 1 hour (87% yield). Elemental analysis (%) calculated (found) for $C_{20}H_{24}N_8Cl_6CuRe$: C, 28.6 (29.2); H, 2.9 (2.9); N, 13.4 (13.6).

4.2.7 Synthesis of {[Cu(1-butylimidazole)$_4$][ReCl$_6$]}$_n$ (4.4)

$(NBu_4)_2[ReCl_6]$ (0.05 mmol, 44.0 mg) and $Cu(NO_3)_2{\cdot}3H_2O$ (0.05 mmol, 12.0 mg) were dissolved in 4 ml CH_3CN, then 1-butylimidazole (0.20 mmol, 26.2 µl) in 1 ml CH_3CN was added to the solution. Dark violet crystals suitable for diffraction were collected after exposing the solution to diethyl ether diffusion over a period of 2 weeks (56% yield). Elemental analysis (%) calculated (found) for $C_{28}H_{48}N_8Cl_6CuRe$: C, 35.1 (35.0); H, 5.0 (4.9); N, 11.7 (11.6).

4.2.8 Synthesis of {[Cu(1-vinyl-1,2,4-triazole)$_4$][ReCl$_6$]}$_n$ (4.5)

$(NBu_4)_2[ReCl_6]$ (0.05 mmol, 44.0 mg) and $Cu(NO_3)_2{\cdot}3H_2O$ (0.05 mmol, 12.0 mg) were dissolved in 4 ml CH_3CN to which 1-vinyl-1,2,4-triazole (0.20 mmol, 19 µl) in 1 ml CH_3CN was added. Grey crystals suitable for X-ray diffraction were grown after 24 hours by layering with isopropanol (29% yield). Elemental analysis (%) calculated (found) for $C_{16}H_{20}N_{12}Cl_6CuRe$: C, 22.8 (23.0); H, 2.4 (2.4); N, 19.9 (19.4).

4.2.9 Synthesis of {[Cu(DMF)$_4$][ReCl$_6$]·CH$_3$CN}$_n$ (4.6)

$(NBu_4)_2[ReCl_6]$ (0.05 mmol, 44.0 mg) and $Cu(NO_3)_2{\cdot}3H_2O$ (0.05 mmol, 12.0 mg) were dissolved in a mixture of 1 ml DMF and 1 ml CH_3CN. Green crystals suitable single crystal X-ray diffraction were grown after 24 hours by layering with isopropanol (74% yield). Elemental analysis (%) calculated (found) for $C_{12}H_{28}N_4O_4Cl_6CuRe$: C, 19.1 (19.0); H, 3.7 (3.5); N, 7.4 (7.3).

4.3 Structures

4.3.1 Structure of $\{[Cu(imi)_4][ReCl_6]\cdot 2(CH_3)_2CHOH\}_n$ (4.1)

4.1 crystallises in the triclinic space group $P\bar{1}$ with the asymmetric unit containing two non-equivalent half molecules of the $[Cu(imi)_4]^{2+}$ cation, one $[ReCl_6]^{2-}$ anion and two isopropanol molecules (Figure 4.3.1a and Table 4.3.1). The Re^{IV} ion is coordinated to six chloride ions in an octahedral coordination sphere. The Re–Cl bond lengths are between 2.3437(4) and 2.3614(4) Å with *cis* bond angles in the range 88.382(16)-91.617(15)°, values similar to previously published compounds containing the $[ReCl_6]^{2-}$ anion (Table 4.3.3).[5, 20] The Cu^{II} ions sit in axially elongated *trans*-N_4Cl_2 octahedrons with Cu–N bond lengths between 1.9912(15) and 2.0026(15) Å and Cu–Cl bond lengths of 2.9929(4) and 3.0582(4) for Cu(1)–Cl(1) and Cu(2)–Cl(2), respectively (Table 4.3.3). One isopropanol molecule has the central carbon atom disordered over two positions with a ratio of 1:3 (Figure 4.3.1a). The $[ReCl_6]^{2-}$ anions coordinate to two Cu^{II} ions through chloride ions positioned *trans* with respect to the Re^{IV} centre, thereby creating a 1D network of alternating $[Cu(imi)_4]^{2+}$ and $[ReCl_6]^{2-}$ units (Figure 4.3.1b).

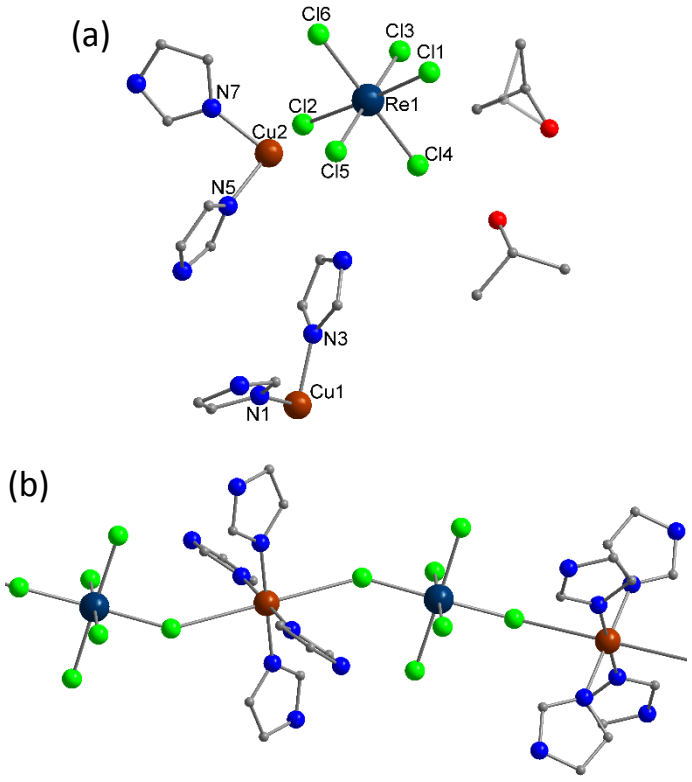

Figure 4.3.1. a) The asymmetric unit of **4.1**. b) The $\{[Cu(imi)_4][ReCl_6]\}_n$ chain. Hydrogen atoms are omitted for clarity. In (a), disorder of the isopropanol molecule is illustrated with the carbon atom at 40% transparency and atoms labelled in accordance with Table 4.3.3. In (b) solvent molecules are omitted for clarity. Colour code: Re, dark blue; Cu, brown; Cl, green; O, red; N, blue; C, grey.

The Re–Cl–Cu bridging angles are 152.79(2) and 148.59(2)° for Re(1)–Cl(1)–Cu(1) and Re(1)–Cl(2)–Cu(2), respectively. The intrachain Re···Cu separation is 5.19330(14) Å for Re(1)···Cu(1) and 5.23858(16) Å for Re(1)···Cu(2).

In the crystal lattice, the chains are oriented parallel to each other travelling diagonally to the *b* and *c*-axes (Figure 4.3.2a). The 1D networks pack in layers in the crystallographic *bc*-plane through CH···π interactions of *circa* 3.5 Å (C to imidazole centroid) and NH···Cl interactions of approximately 3.2 Å (N···Cl distance) between neighbouring chains (Figure 4.3.2b). The co-crystallised isopropanol molecules pack through OH···O and NH···O hydrogen bonds in the crystallographic *bc*-plane between layers of chains.

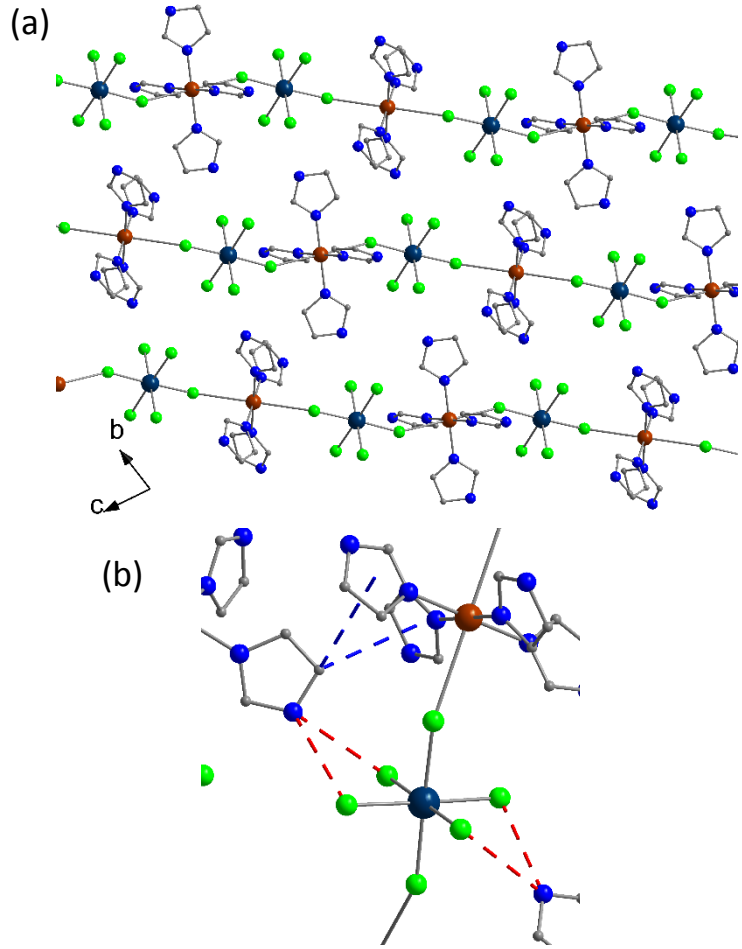

Figure 4.3.2. a) The packing of the chains in the crystallographic *bc*-plane. b) The intermolecular CH···π and NH···Cl interactions, blue and red dashed lines, respectively. Hydrogen atoms and isopropanol molecules are omitted for clarity. Colour code as in Figure 4.3.1.

4.3.2 Structure of $\{[Cu(Meim)_4][ReCl_6]\}_n$ (4.2)

The $\{[Cu(Meim)_4][ReCl_6]\}_n$ chain crystallises in the triclinic space group $P\bar{1}$ with the asymmetric unit containing 1.5 molecules of the $[Cu(Meim)_4][ReCl_6]$ motif (Figure 4.3.3a and

Table 4.3.1). This gives rise to two non-equivalent chains whose structural features only deviate slightly (Table 4.3.3). The structural parameters of the $[ReCl_6]^{2-}$ anions are as described for **4.1** (Table 4.3.3). Each Cu^{II} ion is coordinated to four neutral 1-methylimidazole ligands in the equatorial plane and axially to two chloride ions from adjacent $[ReCl_6]^{2-}$ units, thereby creating the 1D network (Figure 4.3.3b). The Cu–Cl bond lengths range from 3.0379(12) to 3.1948(12) Å with Re–Cl–Cu bond angles between 140.03(4) to 146.71(5)°. The intrachain through space Re···Cu separations are between 5.1 to 5.3 Å (Table 4.3.3).

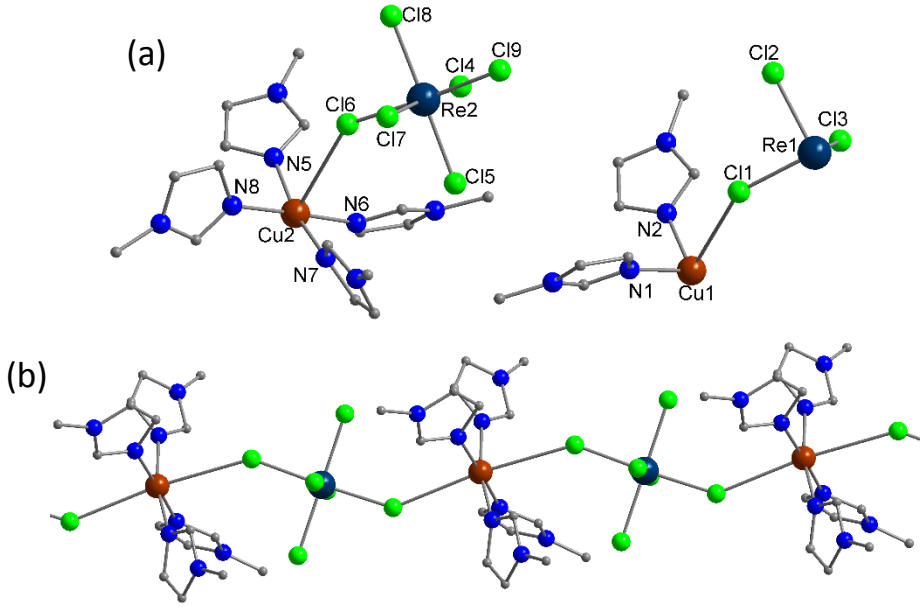

Figure 4.3.3. a) The asymmetric unit of **4.2**. b) The $\{[Cu(Meim)_4][ReCl_6]\}_n$ chain. In a), atoms labelled in accordance with Table 4.3.3. Hydrogen atoms are omitted for clarity. Colour code as in Figure 4.3.1.

In the solid state, the chains travel parallel to each other down the crystallographic *b*-axis and packs *via* a range of CH···π, Cl···π and Cl···Cl interactions (Figure 4.3.4a).

The $[Cu(1)(Meim)_4]^{2+}$ cations pack with adjacent $[Cu(1)(Meim)_4]^{2+}$ units through CH···π interactions of around 3.6 Å (C to imidazole centroid) (Figure 4.3.4b). The $[Cu(2)(Meim)_4]^{2+}$ cation interacts to neighbouring $[Cu(2)(Meim)_4]^{2+}$ units, in a similar fashion with CH···π distances of 3.8 Å, in the direction of the crystallographic *a*-axis. The $[ReCl_6]^{2-}$ anions pack through a network of intra- and interchain Cl···π and Cl···Cl interactions. The $[Re(2)Cl_6]^{2-}$ anions have short inter- and intrachain Cl···π interactions with an intrachain distance of *circa* 3.8 Å (Cl to imidazole centroid) and interchain distance of approximately 3.6 Å (Figure 4.3.4c). The short intrachain Cl···π interactions are not present for the $[Re(1)Cl_6]^{2-}$ anion. Interchain

Cl···Cl interactions of *circa* 3.9 Å, (Cl(3)–Cl(4)) are present between the $[Re(1)Cl_6]^{2-}$ and $[Re(2)Cl_6]^{2-}$ anions as depicted in Figure 4.3.4c, dashed green line.

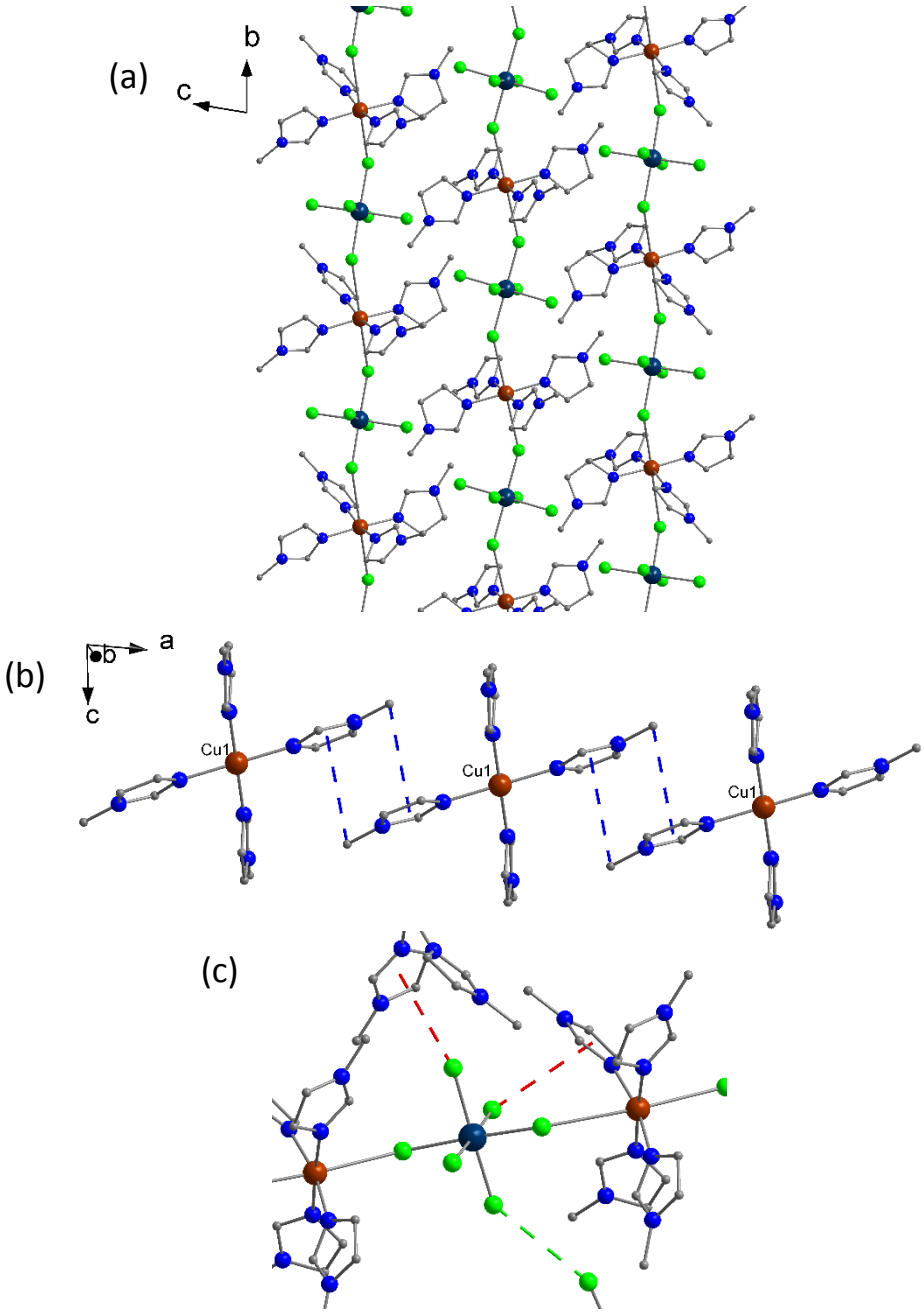

Figure 4.3.4. a) The packing of **4.2** viewed along the crystallographic *b*-axis. b) The CH···π interactions between the $[Cu(1)(Meim)_4]^{2+}$ cations. c) The intra- and interchain interactions of the $[Re(2)Cl_6]^{2-}$ anion. Cl···π (red), Cl···Cl (green) and CH···π (blue) interactions are indicated by dashed lines. Hydrogen atoms are omitted for clarity. Colour code as in Figure 4.3.1.

4.3.3 Structure of $\{[Cu(Vim)_4][ReCl_6]\}_n$ (4.3)

4.3 crystallises in the monoclinic space group *C*2/*c* with the asymmetric unit containing half a $[Cu(Vim)_4]^{2+}$ cation and half a $[ReCl_6]^{2-}$ anion due to inversion centres located on the metal centres (Table 4.3.1 and Figure 4.3.5a). In the asymmetric unit one vinyl-group is disordered

over two positions with a ratio of occupancy of 3:1 (Figure 4.3.5a). The geometrical parameters of the $[ReCl_6]^{2-}$ anion are similar to the one described in **4.1** (Tables 4.3.3 and 4.3.4). The Cu^{II} ion is coordinated equatorially to four ligands and axially to chloride ions from neighbouring anions thereby creating the chain motif (Figure 4.3.5b). The Cu^{II} ion contains Cu–N bond lengths of 2.017(2) and 2.003(2) Å and a Cu–Cl bond length of 2.8831(6) Å, with a Re–Cl–Cu bridging angle of 132.99(3)° and intrachain Re···Cu separation of 4.81236(4) Å.

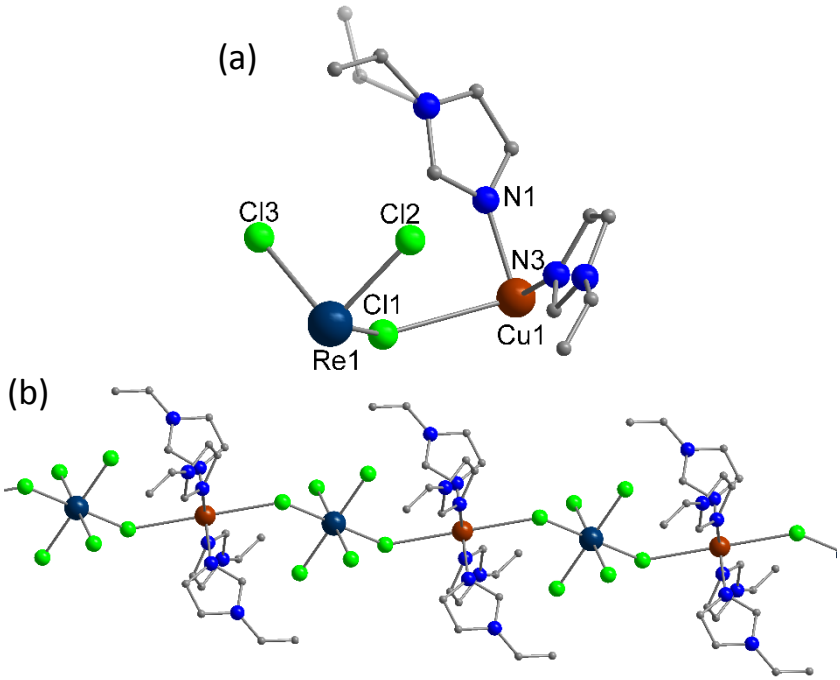

Figure 4.3.5. a) The asymmetric unit of **4.3**. b) The $\{[Cu(Vim)_4][ReCl_6]\}_n$ chain. In (a), disorder of the vinyl-group is illustrated with the carbon atoms at 40% transparency and atoms labelled in accordance with Table 4.3.4. Hydrogen atoms and in (b) disorder are omitted for clarity. Colour code as in Figure 4.3.1.

In the crystal lattice, the chains order parallel in 2D networks in the crystallographic *ab*-plane, with each 2D network being pseudo-perpendicular to adjacent layers with an interchain angle of 81.45° (Figure 4.3.6). The chains pack through an extended network of Cl···π and CH···π interactions with short intrachain Cl···π interactions of 3.4471(6) Å present between the $[Cu(Vim)_4]^{2+}$ and $[ReCl_6]^{2-}$ ions (Figure 4.3.7a). CH···π interactions, between the vinyl-groups and imidazole rings, of *circa* 3.6 and 3.9 Å are present between cations travelling parallel and pseudo-perpendicular to one another, respectively (Figure 4.3.7b).

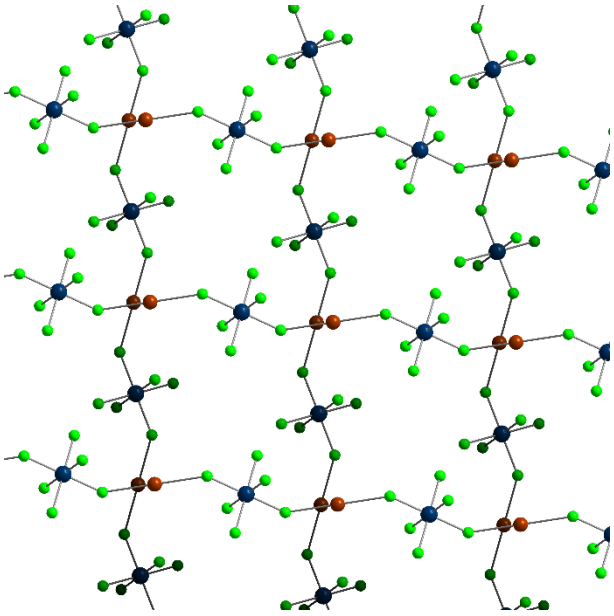

Figure 4.3.6. The packing of **4.3**, illustrating the two orientations of the chains. Carbon, hydrogen and nitrogen atoms are omitted for clarity. Colour code as in Figure 4.3.1.

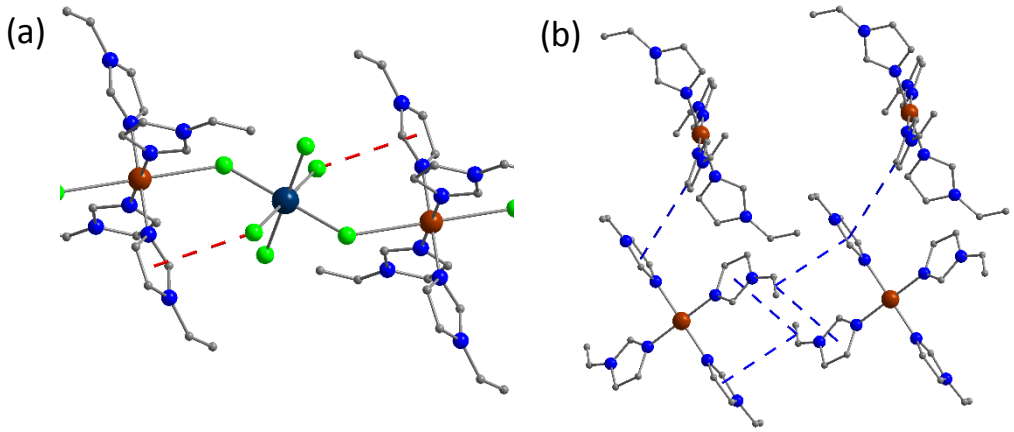

Figure 4.3.7. a) Intrachain Cl···π interactions in **4.3**. b) The CH···π interactions between cations in **4.3**. Cl···π and CH···π interactions are represented by red and blue dashed lines, respectively. Hydrogen atoms and disorder are omitted for clarity. Colour code as in Figure 4.3.1.

4.3.4 Structure of {[Cu(Buim)$_4$][ReCl$_6$]}$_n$ (4.4)

4.4 crystallises in the orthorhombic space group *Pccn* with the asymmetric unit containing half a cation and half an anion (Figure 4.3.8a and Table 4.3.2). The molecular chain motif resembles that of **4.3**, but with the 1-butylimidazole ligand coordinated to the Cu^{II} ion (Figure 4.3.8b). Disorder of one CH_3CH_2-group is observed occupying two positions at a 3:1 ratio (Figure 4.3.8a). The $[ReCl_6]^{2-}$ anion has structural parameters similar to the one described in **4.3** (Table 4.3.4). In the *trans*-N_4Cl_2 coordination sphere of the Cu^{II} ion, the Cu–N bond lengths are 1.987(3) and 1.996(3) Å with a 3.2256(10) Å Cu–Cl bond length giving rise to a Re–Cl–Cu

bridging angle of 142.25(4)°. The intrachain Re···Cu separation is 5.30159(7) Å (Table 4.3.3 and 4.3.4).

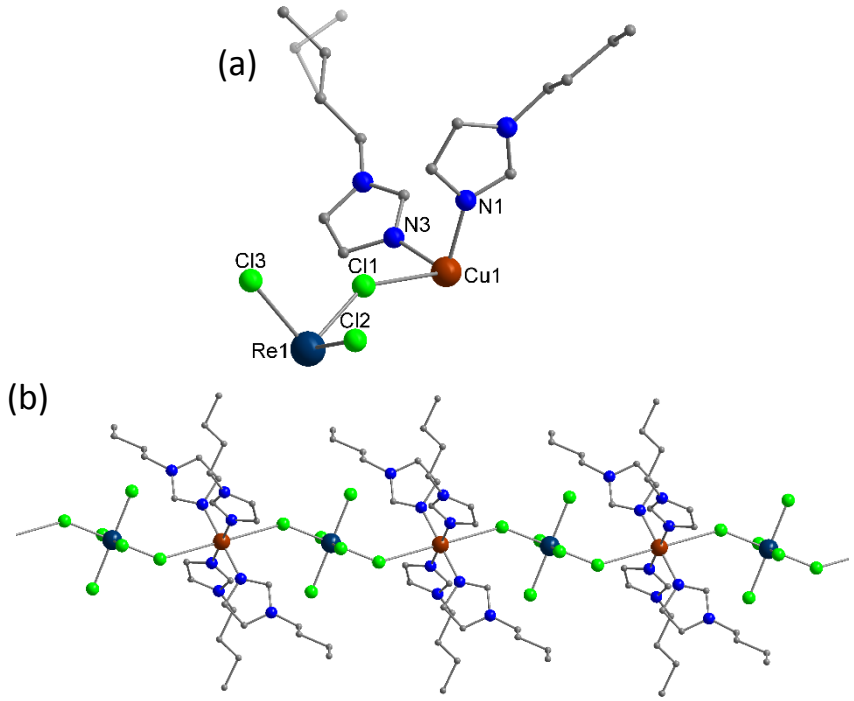

Figure 4.3.8. a) The asymmetric unit of **4.4**. b) The molecular chain motif of **4.4**. In (a), disorder of the butyl-group is illustrated with the carbon atoms at 40 % transparency and atoms labelled in accordance with Table 4.3.4. Hydrogen atoms and in (b) disorder are omitted for clarity. Colour code as in Figure 4.3.1.

In the crystal lattice, the chains travel parallel in a "grid" like pattern down the crystallographic *c*-axis, as seen in Figure 4.3.9, with the cations ordering in a herringbone fashion when viewed down the *a*-axis (Figure 4.3.10). Each chain is well isolated from

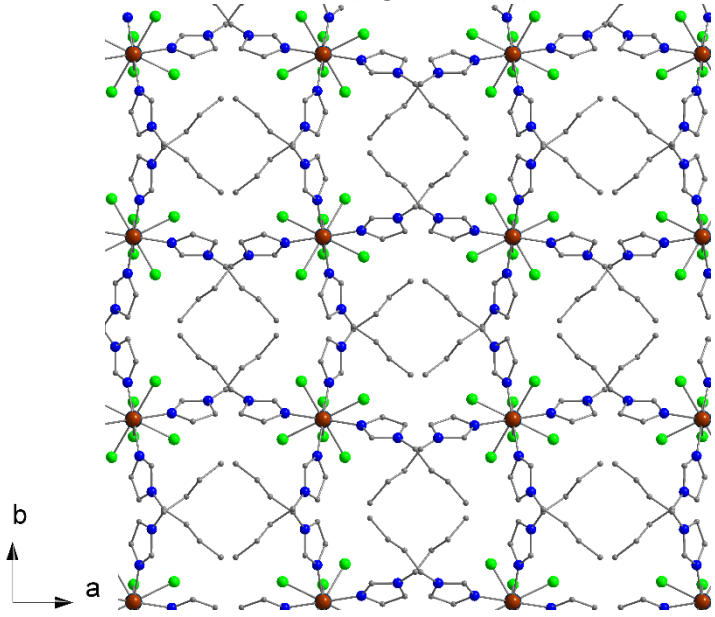

Figure 4.3.9. The packing of **4.4** viewed down the crystallographic *c*-axis. Hydrogen atoms and disorder are omitted for clarity. Colour code as in Figure 4.3.1.

neighbouring chains due to the butyl-group of the imidazole ligands, which causes the interchain metal···metal distances all to be above 9 Å.

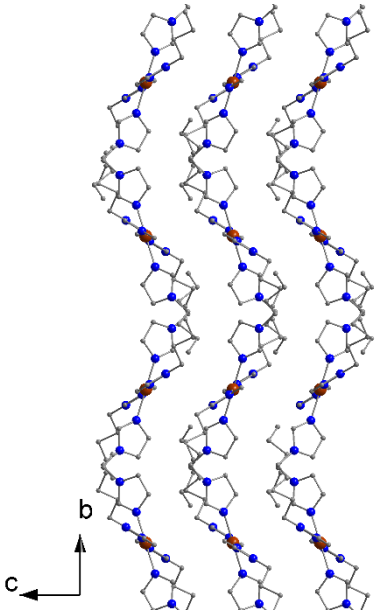

Figure 4.3.10. The packing of cations in **4.4** viewed down the crystallographic *a*-axis. Hydrogen atoms and disorder are omitted for clarity. Colour code as in Figure 4.3.1.

4.3.5 Structure of {[Cu(Vtri)$_4$][ReCl$_6$]}$_n$ (4.5)

{[Cu(Vtri)$_4$][ReCl$_6$]}$_n$ crystallises in the monoclinic space group $P2_1/c$ with half of the molecular [Cu(Vtri)$_4$][ReCl$_6$] compound present in the asymmetric unit due to symmetry related inversion centres on the Re^{IV} and Cu^{II} ions (Figure 4.3.11a and Table 4.3.2). The $[ReCl_6]^{2-}$ unit contains bond lengths and angles similar to the anion described in **4.3** (Table 4.3.4). The Cu^{II} ion sits in a *trans*-N_4Cl_2 coordination sphere with Cu–N bond lengths of 2.0130(15) and 2.0025(16) Å, a Cu–Cl bond of 2.8574(4) Å, with the Re–Cl–Cu bond angle being 128.659(18)°, the most narrow of the six chains (Figure 4.3.11b).

In the crystal lattice, the chains all propagate down the crystallographic *a*-axis (Figure 4.3.12a) and pack through a myriad of intra- and interchain CH···N and Cl···π interactions. In each molecular chain two short Cl···π interactions, 3.4152(5) and 3.7303(5) Å, are present, as seen in Figure 4.3.12b. The chains pack through short CH···N interactions between neighbouring triazole groups and by Cl···π interactions from the anion to the vinyl-groups (Figure 4.3.12c). These CH···N interactions are *circa* 3.2 Å (C···N distance) and interchain Cl···π distances are approximately 3.6 Å (Cl to centre of vinyl bond).

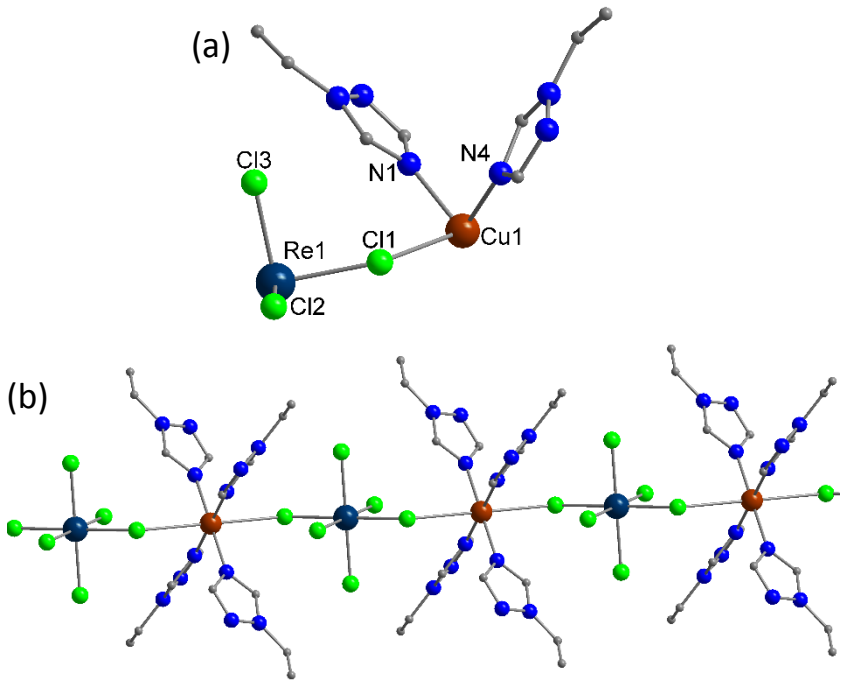

Figure 4.3.11. a) The asymmetric unit of **4.5**. b) The $\{[Cu(Vtri)_4][ReCl_6]\}_n$ chain. In (a), atoms labelled in accordance with Table 4.3.4. Hydrogen atoms are omitted for clarity. Colour code as in Figure 4.3.1.

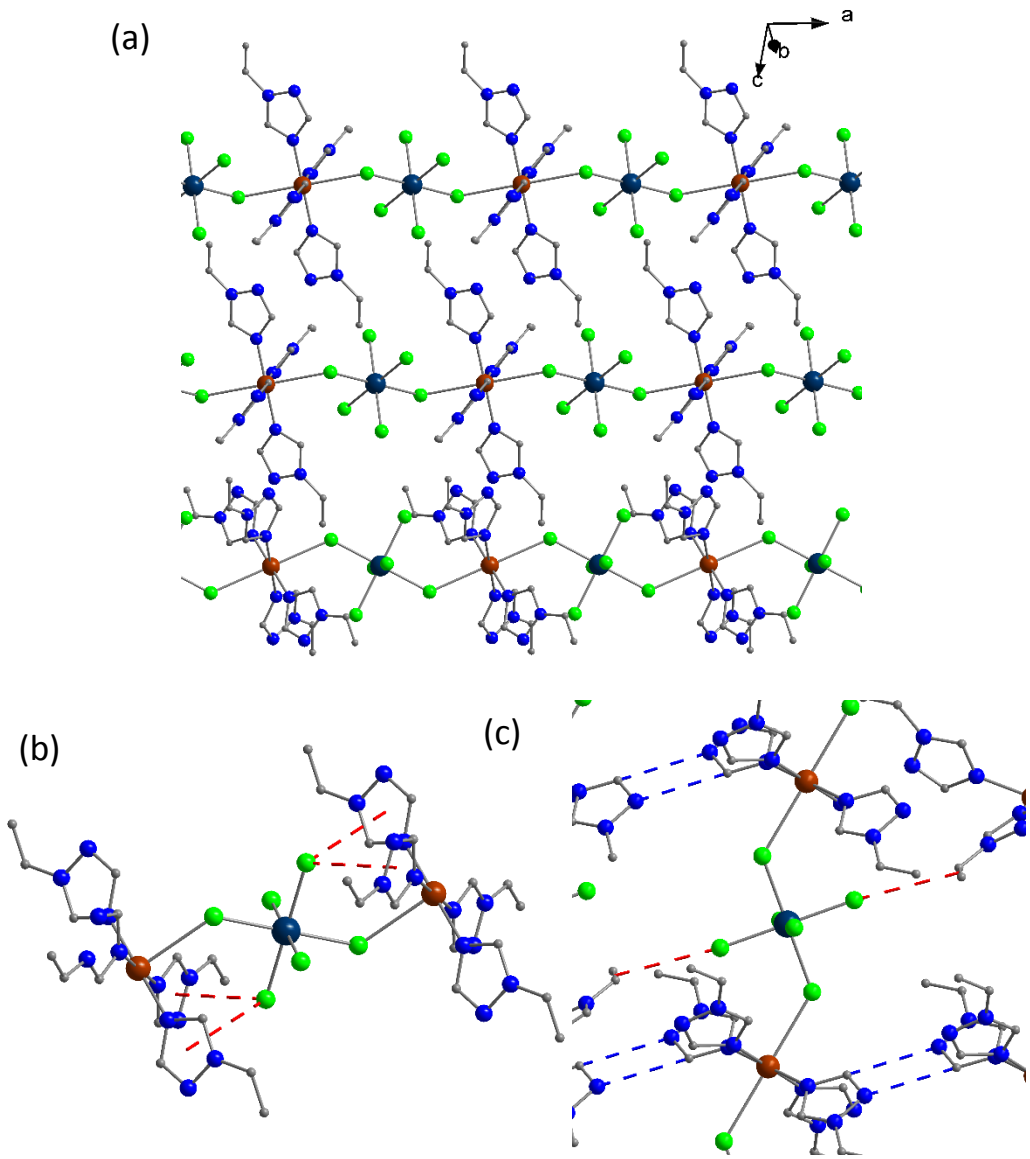

Figure 4.3.12. a) The packing of **4.4** viewed along the crystallographic *a*-axis. b) Intrachain Cl···π interactions. c) The interchain Cl···π and CH···N interactions. Cl···π and CH···N interactions are indicated by red and blue dashed lines, respectively. Hydrogen atoms are omitted for clarity. Colour code as in Figure 4.3.1.

4.3.6 Structure of {[Cu(DMF)$_4$][ReCl$_6$]·CH$_3$CN}$_n$ (4.6)

The structure of **4.6** crystallises in the triclinic space group $P\bar{1}$ with the asymmetric unit containing half a cation, half an anion and one solvent acetonitrile molecule at 50% occupancy (Table 4.3.2 and Figure 4.3.13a). The $[ReCl_6]^{2-}$ anion contains bond lengths and angles similar to the anion described in **4.3** (Table 4.3.4). The Cu^{II} ion is coordinated to four DMF molecules in the equatorial plane with Cu–O bond lengths of 1.9609(16) and 1.9450(16) Å and axially to chloride ions from adjacent anions through a Cu–Cl bond with a 2.7800(6) Å

bond length. This creates a 1D network of $[Cu(DMF)_4]^{2+}$ and $[ReCl_6]^{2-}$ ions coupled through a Re–Cl–Cu bridge with a bonding angle of 142.92(3)° (Figure 4.3.13b).

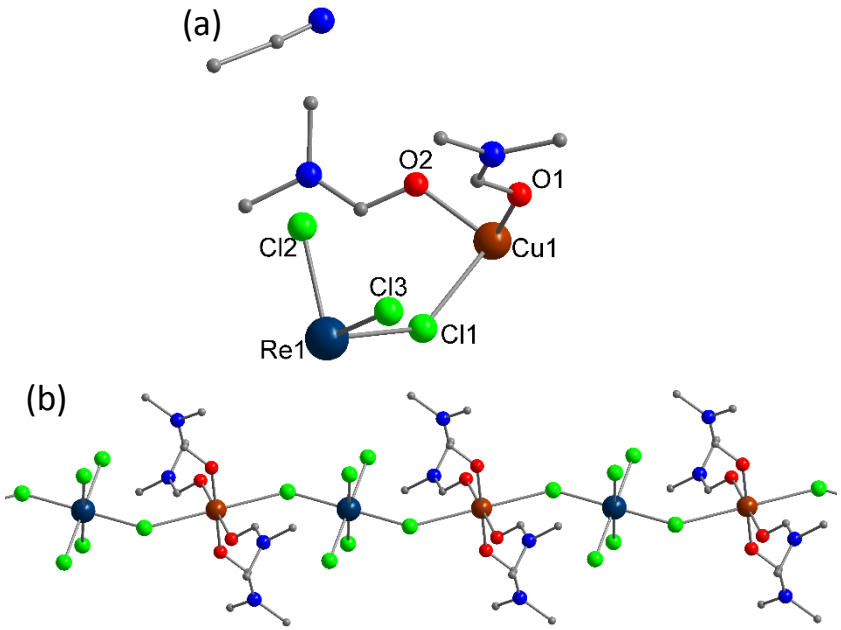

Figure 4.3.13. a) The asymmetric unit of **4.6**. b) The $\{[Cu(DMF)_4][ReCl_6]\}_n$ chain. In (a), atoms labelled in accordance with Table 4.3.4. Hydrogen atoms are omitted for clarity. Colour code as in Figure 4.3.1.

In the crystal lattice, the chains are all oriented parallel travelling down the crystallographic *c*-axis with the acetonitrile molecules placed between the chains (Figure 4.3.14). The $[ReCl_6]^{2-}$ unit interacts with the DMF ligands and co-crystallised acetonitrile molecules through CH···Cl contacts, with C···Cl distances in the range of 3.5 to 3.8 Å (Figure 4.3.15a). The DMF ligands interact with the acetonitrile molecules through CH···N contacts with C···N distances of approximately 3.3 and 3.6 Å (Figure 4.3.15b).

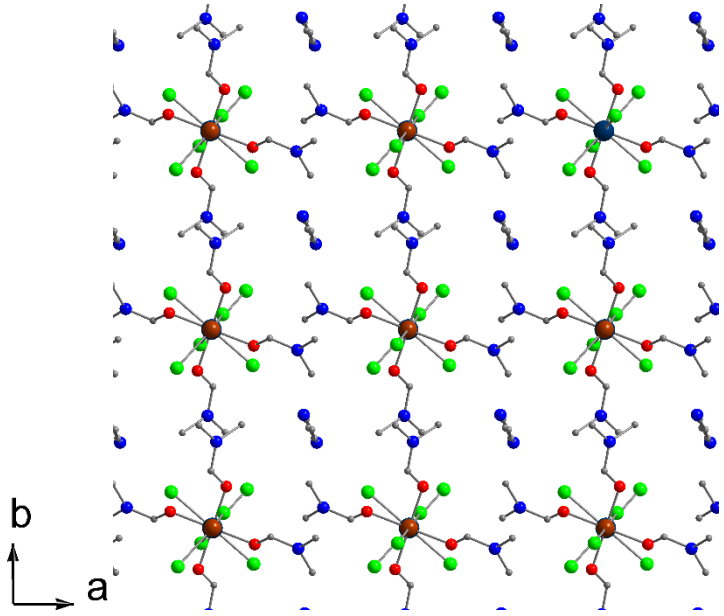

Figure 4.3.14. The packing of **4.6** viewed down the crystallographic *c*-axis. Hydrogen atoms are omitted for clarity. Colour code as in Figure 4.3.1.

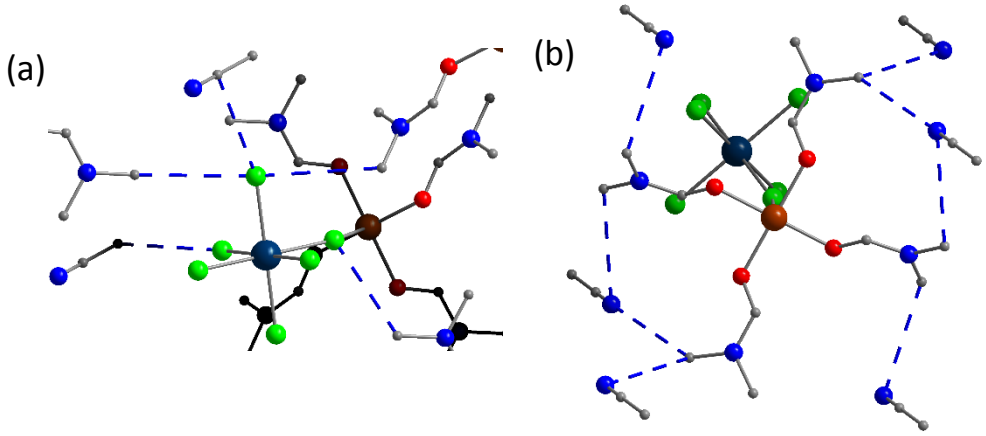

Figure 4.3.15. a) The intermolecular CH···Cl interactions. b) The CH···N interactions between DMF ligands and CH_3CN molecules. Hydrogen atoms are omitted for clarity. Colour code as in Figure 4.3.1.

4.3.7 Tables of crystallographic and structural parameters

Table 4.3.1. Crystallographic parameters for **4.1**, **4.2** and **4.3**.

	4.1	**4.2**	**4.3**
Crystal data			
Chemical formula	$Cl_6Re{\cdot}2(C_6H_8Cu_{0.5}N_4){\cdot}2(C_3H_8O)$	$Cl_6Re{\cdot}C_{16}H_{24}CuN_8$	$Cl_6Re{\cdot}C_{20}H_{24}CuN_8$
M_r	854.95	790.87	838.91
Crystal system, space group	Triclinic, $P\bar{1}$	Triclinic, $P\bar{1}$	Monoclinic, $C2/c$
Temperature (K)	293	120	120
a,	10.1219 (2),	8.7712 (3),	12.69636 (15),
b,	11.0652 (3),	10.3822 (4),	14.46868 (15),
c (Å)	14.7016 (4)	21.7896 (6)	16.11703 (16)
α,	76.032 (2),	79.571 (3),	90,
β,	80.918 (2),	84.553 (2),	101.4205 (11),
γ (°)	69.748 (2)	75.646 (3)	90
V (Å^3)	1494.13 (7)	1887.95 (11)	2902.07 (6)
Z	2	3	4
Radiation type	Mo $K\alpha$	Mo $K\alpha$	Mo $K\alpha$
μ (mm^{-1})	5.33	6.31	5.48
Crystal size (mm)	0.19 × 0.14 × 0.07	0.21 × 0.11 × 0.05	0.11 × 0.10 × 0.08
Data collection			
T_{min}, T_{max}	0.998, 0.999	0.991, 0.997	0.860, 1.000
No. of measured, independent and observed [$I > 2\sigma(I)$] reflections	48213, 8950, 8533	40420, 11033, 8605	60620, 4403, 3787
R_{int}	0.035	0.062	0.051
$(\sin\theta/\lambda)_{max}$ (Å^{-1})	0.729	0.729	0.721
Refinement			
$R[F^2 > 2\sigma(F^2)]$, $wR(F^2)$, S	0.019, 0.037, 1.08	0.038, 0.069, 1.06	0.027, 0.044, 1.14
No. of reflections	8950	11033	4403
No. of parameters	359	442	185
No. of restraints	1	0	3
$\Delta\rho_{max}$, $\Delta\rho_{min}$ (e Å^{-3})	0.53, −0.86	2.20, −1.57	0.58, −0.83

Table 4.3.2. Crystallographic parameters for **4.4**, **4.5** and **4.6**.

	4.4	**4.5**	**4.6**
Crystal data			
Chemical formula	$Cl_6Re{\cdot}C_{28}H_{48}CuN_8$	$Cl_6Re{\cdot}C_{16}H_{20}CuN_{12}$	$Cl_6Re{\cdot}C_{12}H_{28}CuN_4O_4{\cdot}C_2H_3N$
M_r	959.18	842.88	795.88
Crystal system, space group	Orthorhombic, *Pccn*	Monoclinic, $P2_1/c$	Triclinic, $P\bar{1}$
Temperature (K)	293	120	120
a,	19.3832 (2),	9.46035 (13),	8.46428 (19),
b,	18.6574 (2),	14.5535 (2),	8.5772 (2),
c (Å)	10.60318 (13)	9.73308 (13)	9.7582 (2)
α,	90,	90,	95.043 (2),
β,	90,	95.2788 (12),	91.8824 (19),
γ (°)	90	90	90.111 (2)
V (Å^3)	3834.54 (8)	1334.38 (3)	705.31 (3)
Z	4	2	1
Radiation type	Mo *K*α	Mo *K*α	Mo *K*α
μ (mm^{-1})	4.16	5.96	5.64
Crystal size (mm)	0.87 × 0.22 × 0.14	0.37 × 0.11 × 0.08 × 0.30 (radius)	0.26 × 0.16 × 0.14
Data collection			
T_{min}, T_{max}	0.461, 1.000	0.715, 0.918	0.806, 1.000
No. of measured, independent and observed [$I > 2\sigma(I)$] reflections	94317, 6774, 5771	33934, 4810, 4275	19023, 4179, 4133
R_{int}	0.040	0.034	0.030
$(\sin\theta/\lambda)_{max}$ (Å^{-1})	0.759	0.765	0.729
Refinement			
$R[F^2 > 2\sigma(F^2)]$, $wR(F^2)$, *S*	0.051, 0.093, 1.33	0.022, 0.039, 1.15	0.020, 0.048, 1.07
No. of reflections	6774	4810	4179
No. of parameters	232	166	162
No. of restraints	0	0	0
$\Delta\rho_{max}$, $\Delta\rho_{min}$ (e Å^{-3})	1.17, −0.79	0.55, −0.60	2.81, −0.63

Table 4.3.3. Selected bond lengths and angles for **4.1** and **4.2**.

	4.1		**4.2**
Re(1)–Cl(1) / Å	2.3481(4)	Re(1)–Cl(1) / Å	2.3695(10)
Re(1)–Cl(2) / Å	2.3803(4)	Re(1)–Cl(2) / Å	2.3670(10)
Re(1)–Cl(3) / Å	2.3437(4)	Re(1)–Cl(3) / Å	2.3512(9)
Re(1)–Cl(4) / Å	2.3597(4)	Re(2)–Cl(4) / Å	2.3469(10)
Re(1)–Cl(5) / Å	2.3536(5)	Re(2)–Cl(5) / Å	2.3617(11)
Re(1)–Cl(6) / Å	2.3614(4)	Re(2)–Cl(6) / Å	2.3681(10)
		Re(2)–Cl(7) / Å	2.3639(10)
		Re(2)–Cl(8) / Å	2.3578(11)
		Re(2)–Cl(9) / Å	2.3829(10)
Cu(1)–Cl(1) / Å	2.9929(4)	Cu(1)–Cl(1) / Å	3.0449(11)
Cu(2)–Cl(2) / Å	3.0582(4)	Cu(2)–Cl(6) / Å	3.1948(12)
		Cu(2)–Cl(9) / Å	3.0379(12)
Cu(1)–N(1) / Å	2.0026(15)	Cu(1)–N(1) / Å	1.994(3)
Cu(1)–N(3) / Å	1.9931(15)	Cu(1)–N(2) / Å	2.001(3)
Cu(1)–N(5) / Å	1.9912(15)	Cu(2)–N(5) / Å	1.998(3)
Cu(1)–N(7) / Å	1.9928(15)	Cu(2)–N(6) / Å	1.978(3)
		Cu(2)–N(7) / Å	2.001(3)
		Cu(2)–N(8) / Å	1.979(3)
cis Cl–Re–Cl / °	88.382(16) – 91.617(15)	*cis* Cl–Re(1)–Cl / °	89.34(4)–90.66(4)
Cl(1)–Re(1)–Cl(2) / °	176.798(16)	*cis* Cl–Re(2)–Cl / °	88.09(4)–92.93(4)
Cl(3)–Re(1)–Cl(5) / °	178.038(18)	Cl(4)–Re(2)–Cl(7) / °	177.26(4)
Cl(4)–Re(1)–Cl(6) / °	179.713(16)	Cl(5)–Re(2)–Cl(8) / °	178.30(4)
		Cl(6)–Re(2)–Cl(9) / °	176.97(4)
Re(1)···Cu(1) / Å	5.19330(14)	Re(1)···Cu(1) / Å	5.19109(18)
Re(1)···Cu(2) / Å	5.23858(16)	Re(2)···Cu(2) / Å	5.2909(6)[a]
		Re(2)···Cu(2) / Å	5.0993(6)[b]
Re(1)–Cl(1)–Cu(1) / °	152.79(2)	Re(1)–Cl(1)–Cu(1) / °	146.71(5)
Re(1)–Cl(2)–Cu(2) / °	148.59(2)	Re(2)–Cl(6)–Cu(2) / °	143.60(4)
		Re(2)–Cl(9)–Cu(2) / °	140.03(4)

[a]intermolecular distance across the Cl(6) atom. [b]intermolecular distance across the Cl(9) atom.

Table 4.3.4. Selected bond lengths and angles for **4.3**, **4.4**, **4.5** and **4.6**.

	4.3	**4.4**
Re(1)–Cl(1) / Å	2.3597(6)	2.3695(9)
Re(1)–Cl(2) / Å	2.3546(6)	2.3588(9)
Re(1)–Cl(3) / Å	2.3538(6)	2.3611(9)
Cu(1)–Cl(1) / Å	2.8831(6)	3.2256(10)
Cu(1)–N / Å	2.017(2)	1.987(3)
Cu(1)–N / Å	2.003(2)	1.996(3)
Re(1)···Cu(1) / Å	4.81236(4)	5.30159(7)
Cl(1)–Re(1)–Cl(2) / °	90.48(2)	90.85(4)
Cl(1)–Re(1)–Cl(3) / °	89.90(2)	89.92(3)
Cl(2)–Re(1)–Cl(3) / °	89.29(3)	89.82(4)
Re(1)–Cl(1)–Cu(1) / °	132.99(3)	142.25(4)

	4.5	**4.6**
Re(1)–Cl(1) / Å	2.3859(4)	2.3643(5)
Re(1)–Cl(2) / Å	2.3474(4)	2.3577(5)
Re(1)–Cl(3) / Å	2.3457(5)	2.3527(5)
Cu(1)–Cl(1) / Å	2.8574(4)	2.7800(6)
Cu(1)–X / Å	2.0130(15) (X = N(1))	1.9609(16) (X = O(1))
Cu(1)–X / Å	2.0025(16) (X = N(4))	1.9450(16) (X = O(2))
Re(1)···Cu(1) / Å	4.73017(6)	4.87908(12)
Cl(1)–Re(1)–Cl(2) / °	89.090(16)	90.995(17)
Cl(1)–Re(1)–Cl(3) / °	90.014(16)	89.599(19)
Cl(2)–Re(1)–Cl(3) / °	90.205(19)	89.71(2)
Re(1)–Cl(1)–Cu(1) / °	128.659(18)	142.92(3)

4.4 Magnetic properties

4.4.1 Magnetometry of the six chains

The susceptibility was measured from T = 300 to 2 K in a field of H = 1000 Oe and presented as the $\chi_M T$ product [χ_M being the molar magnetic susceptibility *per* $Re^{IV}Cu^{II}$ unit]. At T = 300 K the chains all exhibit $\chi_M T$ values between 1.86-1.95 $cm^3\ mol^{-1}\ K$, close to the value of 1.93 $cm^3\ mol^{-1}\ K$ expected for a Cu^{II} ion (S = ½ and g = 2.1) and $[ReCl_6]^{2-}$ unit with S = 3/2 and g = 1.8 (Figure 4.4.1).

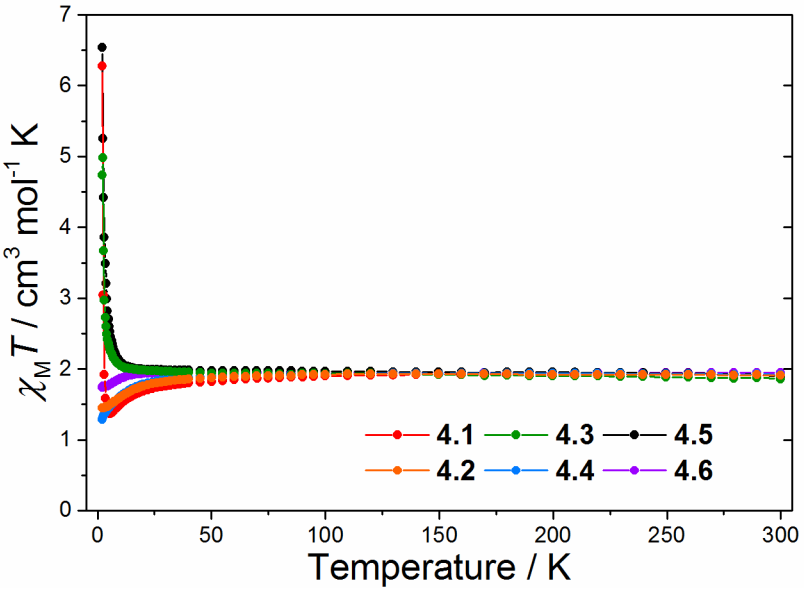

Figure 4.4.1. The $\chi_M T$ *versus* T plot for the six chains. The solid lines are guides to the eye.

4.1 has a $\chi_M T$ value of 1.91 $cm^3\ mol^{-1}\ K$ at T = 300 K which decreases slightly to a value of 1.80 $cm^3\ mol^{-1}\ K$ as the sample is cooled to T = 40 K. As the temperature is lowered the $\chi_M T$ value drops further before reaching a minimum of 1.37 $cm^3\ mol^{-1}\ K$ at T = 5.5 K (Figure 4.4.2). An abrupt increase is observed below T = 5.5 K with **4.1** reaching a $\chi_M T$ value of 6.28 $cm^3\ mol^{-1}\ K$ at T = 2 K. The magnetic susceptibility of **4.1** is indicative of ferrimagnetic behaviour, which could stem from the presence of different Re–Cl–Cu bond angles present in the crystal lattice (Section 4.3.1).

At T = 300 K, **4.2** has a $\chi_M T$ value of 1.91 $cm^3\ mol^{-1}\ K$ with the value only decreasing slightly to 1.87 $cm^3\ mol^{-1}\ K$ as the temperature is lowered to T = 45 K. Upon further cooling a drop in the $\chi_M T$ value is observed with the value reaching 1.45 $cm^3\ mol^{-1}\ K$ at T = 2 K (Figure 4.4.3). The value at T = 2 K is slightly greater than the value expected for the $[ReCl_6]^{2-}$ unit (~1 cm^3

mol^{-1} K) and one isotropic Cu^{II} ion (~0.41 cm^3 mol^{-1} K), which indicates a possible weak ferromagnetic coupling to be present in the system.[4]

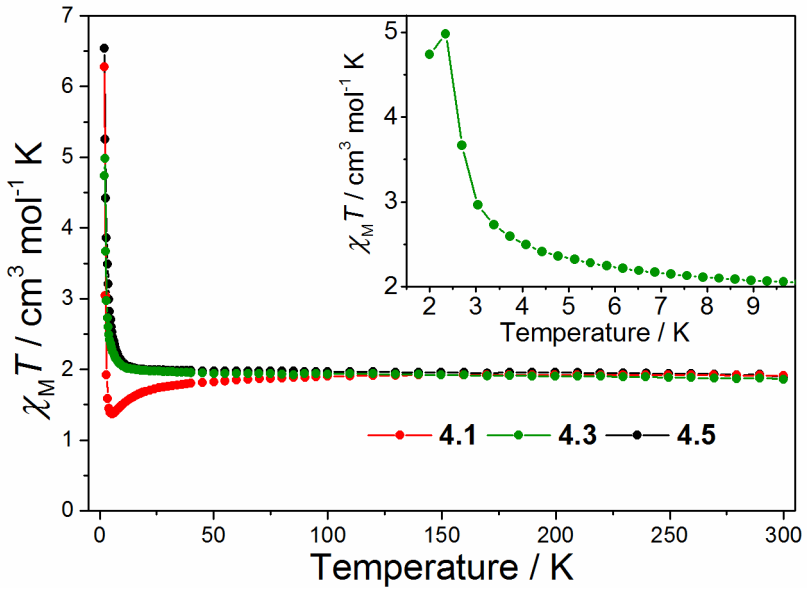

Figure 4.4.2. The $\chi_M T$ *versus* T plot of the low temperature region for **4.1**, **4.3** and **4.5**. Insert illustrating the low temperature region of **4.3**. The solid lines are guides to the eye.

The $\chi_M T$ value for **4.3** at T = 300 K is 1.86 cm^3 mol^{-1} K, the value stay close to constant in the range T = 300 to 50 K. Cooling the sample below T = 50 K causes an increase in the $\chi_M T$ value which reaches a maximum of 4.98 cm^3 mol^{-1} K at T = 2.4 K (Figure 4.4.2, insert). The maximum of the $\chi_M T$ value at T = 2.4 K was found to exhibit field dependence and also frequency independent peaks in the in- and out-of-phase ac measurement (Figure 4.4.4). This magnetic

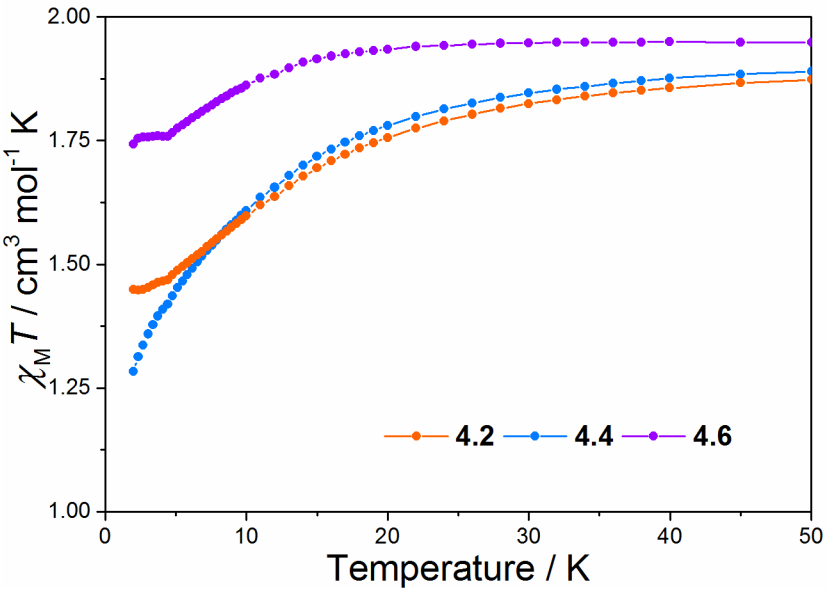

Figure 4.4.3. The $\chi_M T$ *versus* T plot of the low temperature region for **4.2**, **4.4** and **4.6**. The solid lines are guides to the eye.

behaviour is indicative of magnetic ordering at T_c = 2.4 K, which was further corroborated by a peak in the ZFC-FC measurements (Figure 4.4.4c).

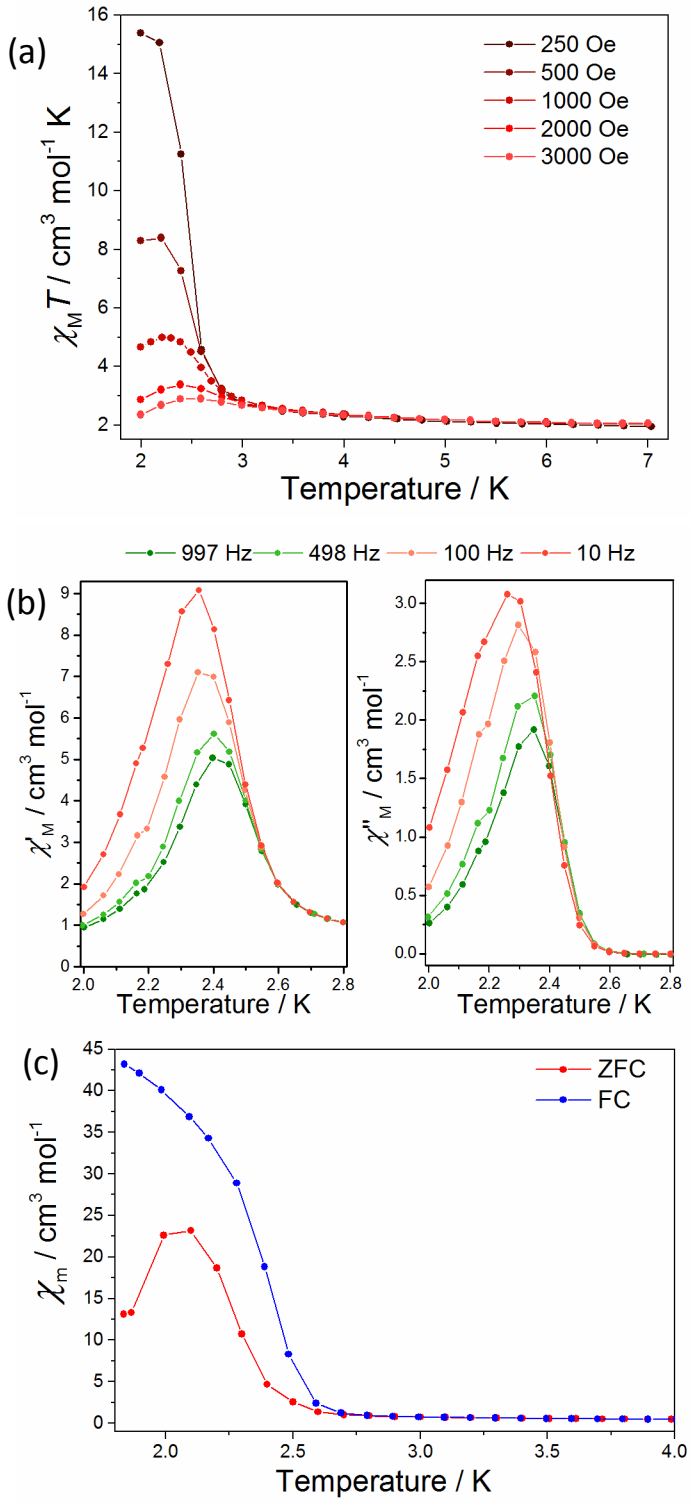

Figure 4.4.4. a) Field dependence of the susceptibility of **4.3**. b) The in-phase and out-of-phase ac signals for **4.3**. c) ZFC-FC measurement on **4.3**.

4.4 has a $\chi_M T$ value of 1.92 $cm^3\ mol^{-1}\ K$ at T = 300 K, as the sample is cooled a slight decline is observed with the $\chi_M T$ value being 1.88 $cm^3\ mol^{-1}\ K$ at T = 40 K. From T = 40 to 2 K **4.4** exhibit a significant decrease causing the final $\chi_M T$ value at T = 2 K to be 1.28 $cm^3\ mol^{-1}\ K$ (Figure 4.4.3). The value at T = 2 K is less than the value expected which indicates a weak antiferromagnetic coupling in the chain.

At T = 300 K the $\chi_M T$ value is 1.89 $cm^3\ mol^{-1}\ K$ for **4.5**. In the temperature range from T = 300 to 50 K, the $\chi_M T$ value exhibits a minor increase to 1.97 $cm^3\ mol^{-1}\ K$ at T = 50 K. As the temperature is lowered the increase of the $\chi_M T$ value intensifies below T = 20 K before reaching 6.54 $cm^3\ mol^{-1}\ K$ at T = 2 K (Figure 4.4.2). The magnetic behaviour is illustrative of clear ferromagnetic exchange interactions. Despite the ferromagnetic exchange interactions and anisotropic $[ReCl_6]^{2-}$ unit, the sample did it not contain any signal in the ac susceptibility measurements, which would have indicated single chain magnet behaviour.

4.6 has a $\chi_M T$ value of 1.95 $cm^3\ mol^{-1}\ K$ at T = 300 K which is constant as the temperature is lowered (Figure 4.4.1). Below T = 20 K a minor drop in the $\chi_M T$ value initiates with the value reaching 1.74 $cm^3\ mol^{-1}\ K$ at T = 2 K (Figure 4.4.3). The value at T = 2 K indicates a small ferromagnetic exchange interaction.

4.4.2 Theoretical calculations

Analysis of the magnetic behaviour of Re^{IV} compounds is non-trivial, since one must consider both intra- and intermolecular exchange interactions (the latter can be as strong as the former) caused by the strong delocalisation of spin density from the Re^{IV} ion to the coordinated ligands, different g-values for the constituent metal ions (g_{Re} and g_{Cu}), and zero-field splitting (*zfs*) effects (D_{Re}).[3]

In addition, some of these parameters are correlated: for example, erroneously large antiferromagnetic intra- or intermolecular exchange interactions can be deduced at the expense of underestimating the *zfs*, whilst large ferromagnetic coupling is linked to an overestimation of the *zfs*. It is therefore important than any employed model is as simple as possible.

In order to identify and quantify the above mentioned parameters, a full theoretical investigation has been carried out.

To simplify the analytical model, DFT calculations to estimate the magnitude of the intermolecular exchange interactions between the $[ReCl_6]^{2-}$ units have been carried out. The intermolecular magnetic coupling depends primarily the Cl···Cl distances and on the relative orientation of the $[ReCl_6]^{2-}$ units. From the calculations it was found that the intermolecular magnetic exchange interactions are negligible in the six chains, even in **4.1** and **4.2** where the Cl···Cl separations are the shortest (Table 4.4.1). The magnetic behaviour of the chains can therefore be regarded as originating primarily from isolated heterometallic 1D chains.

Table 4.4.1. Intermolecular distances between adjacent chains and the magnetic coupling constant for the shortest intermolecular contacts in the chains.

	Re···Re / Å	**Re···Cu / Å**	**Cl···Cl / Å**	***J* / cm^{-1}**
4.1	7.87	8.05	3.80	–0.023
			6.87	+0.000
4.2	8.18	7.71	3.86	+0.027
			4.29	+0.004
4.3	9.22	8.83	5.425	+0.001
			6.55	+0.000
			6.59	+0.004
4.4	10.73	9.33	7.01	+0.000
			7.67	+0.000
4.5	8.75	9.74	4.64	+0.003
4.6	8.46	9.49	5.22	+0.007
			5.34	+0.006

The model to reproduce the magnetic behaviour of these $Re^{IV}Cu^{II}$ chains should include the *g* factors, g_{Re} and g_{Cu}, the axial anisotropy parameter D_{Re} and the coupling constant J_{ReCu} and even for this model problems can arise since it contains a considerable number of parameters, some of which are correlated.

In order to verify the starting point, a NEVPT2 calculation of the axial (*D*) and rhombic (*E*) components of the *zfs* tensor of the $[ReCl_6]^{2-}$ ion in complex **4.1** have therefore been performed. The results afford g = 1.761, D = –8.0 cm^{-1}, and E/D = 0.163, confirming the presence of moderate axial magnetic anisotropy ($D_{Re} \approx J_{ReCu}$). Thus an approach based on the exact diagonalization of the energy matrix of a $\{Re^{IV}Cu^{II}\}_n$ wheel, has been employed. The weak magnetic exchange between the metal ions, as clearly observed in the susceptibility data, allows a model wheel that incorporates just eight metal centres to be applied (Figure 4.4.5).

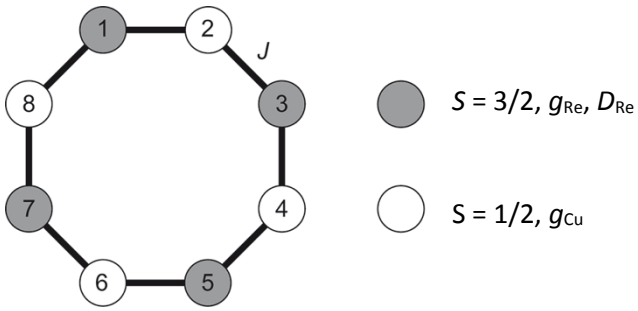

Figure 4.4.5. Spin topology of the model used to simulate the magnetic behaviours of the six chains.

The spin Hamiltonian, $\widehat{H}$, required for the model described in Figure 4.4.5 is constructed by the sum of the Zeeman ($\widehat{H}_{zeem}$), zero-field splitting ($\widehat{H}_{zfs}$) and Heisenberg magnetic coupling ($\widehat{H}_{Heis}$) contributions:

$$\widehat{H} = \widehat{H}_{zeem} + \widehat{H}_{zfs} + \widehat{H}_{Heis} \qquad \text{(eq. 4.4.1)}$$

$$\widehat{H}_{zeem} = \sum_{n=0}^{3} \left(g_{Re}\hat{S}_{2n+1} + g_{Cu}\hat{S}_{2n+2}\right)B\beta$$

$$\widehat{H}_{zfs} = \sum_{n=0}^{3} \left(D[\left(\hat{S}^{z}_{2n+1}\right)^2 - S_{2n+1}(S_{2n+1}+1)/3] + E\left[\left(\hat{S}^{x}_{2n+1}\right)^2 - \left(\hat{S}^{y}_{2n+1}\right)^2\right]\right)$$

$$\widehat{H}_{Heis} = \sum_{n=1}^{7} -J\hat{S}_n\hat{S}_{n+1} + J\hat{S}_1\hat{S}_8$$

S being the spin of the Re^{IV} or Cu^{II} centres, *D* and *E* being the axial and rhombic *zfs* tensor, respectively, *J* the magnetic coupling, *B* being the applied magnetic field and β the Bohr magneton.

Theoretical susceptibility curves obtained from the spin Hamiltonian, eq. 4.4.1, are shown in Figure 4.4.6. The values employed are g_{Re} = 1.76, g_{Cu} = 2.05, $|D_{Re}|$ = 5.0 cm^{-1} and $|J|$ = 2.0 cm^{-1}, based on the previous calculation and the weak exchange interactions observed in the susceptibility measurements. Positive and negative values for D_{Re} and *J* were utilised in order to verify their effects on the magnetic susceptibility.

When the exchange interaction is zero, the susceptibility does not depend on the sign of D_{Re} and the $\chi_M T$ value decreases to a non-zero value at *T* = 0 K ($\chi_M T_0$). At very low temperatures and $J \neq 0$, the magnetic behaviour is affected by the sign of D_{Re}. When the system contains an antiferromagnetic exchange interaction and $D_{Re} < 0$, the |±3/2> Kramers doublet of the

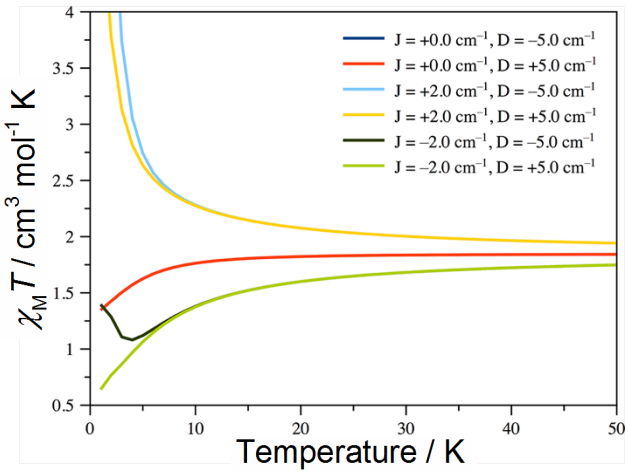

Figure 4.4.6. Theoretical thermal dependence on the $\chi_M T$ value for the model schematized in Figure 4.4.5.

Re^{IV} ion is coupled with the |±1/2> doublet of the Cu^{II} ion. In such case, the spin moments will not cancel each other and an increase of the $\chi_M T$ value should be observed at low temperatures (Figure 4.4.6, black line). For $D_{Re} > 0$, the spin moment of the |±1/2> ground doublet on the Re^{IV} ion can be close to cancelled by that of the Cu^{II} ion, if it was not for the different values of the *g* factors of the paramagnetic centres, and a continuous decrease of the $\chi_M T$ value is observed. When the coupling is ferromagnetic, the $\chi_M T$ value increases at low temperatures to a non-finite value as expected for an ideal 1D system.

Some qualitative conclusions from the experimental thermal dependence of the $\chi_M T$ value can be extracted. The continuous decrease of the $\chi_M T$ value until values close to $\chi_M T_0$ in **4.2**, **4.4** and **4.6** suggest that the magnetic coupling in these compounds could be ferro- or antiferromagnetic but very weak. Because the higher $\chi_M T$ value at T = 2 K in **4.2** and **4.6**, these systems can be assumed to contain a small but non-negligible ferromagnetic coupling. However, the decrease of the $\chi_M T$ value in **4.4** is less than the $\chi_M T_0$ limit value (~1.35 cm^3 mol^{-1} K), which indicates the presence of antiferromagnetic exchange interactions. The sharp increase of $\chi_M T$ at low temperatures in **4.1**, **4.3** and **4.5** is evidence of ferromagnetic exchange

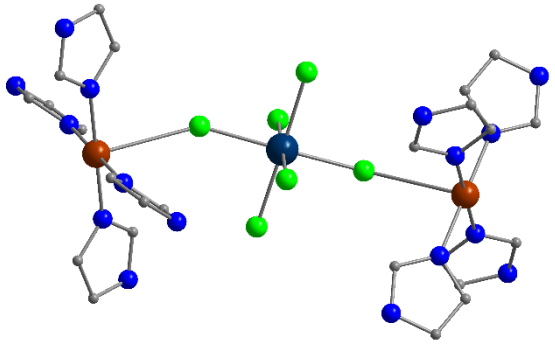

Figure 4.4.7. The $ReCu_2$ fragment, here exemplified for **4.1**. Colour code: Re, dark blue; Cu, brown; Cl, green; O, red; N, blue; C, grey. Hydrogen atoms removed for clarity.

interactions. The minimum of the $\chi_M T$ value close to the $\chi_M T_0$ limit observed in **4.1** points at a smaller J/D_{Re} ratio than detected in **4.3** and **4.5**.

In order to support these qualitative conclusions, and to establish which structural parameters govern the nature and magnitude of the magnetic exchange interaction, theoretically estimated *J* values have been obtained from DFT calculations on a [$Re^{IV}Cu^{II}_2$] fragment (Figure 4.4.7). These calculations probe the effect of the Cu–Cl bond lengths, the Re–Cl–Cu bond angles (α) and Re–Cl–Cu–N torsion angles (θ) as found in the crystal structures of the six chains (Table 4.4.2).

Table 4.4.2. Structural parameters and magnetic coupling for **4.1**-**6.** Cu–Cl, α and θ are defined in Figure 4.4.9. Due to the different structural features present in **4.1** and **4.2**, were they calculated and noted with a numerical index (1 or 2) and the two different chains in **4.2** were noted a or b.

Structure	Cu–Cl / Å	α / °	θ / °	*J* / cm^{-1}
4.1_1	3.058	148.59	41.68	-0.37
4.1_2	2.993	152.79	26.41	+0.57
4.2a	3.045	146.71	19.92	+0.29
4.2b_1	3.195	143.60	43.42	+0.64
4.2b_2	3.038	140.03	42.68	+0.71
4.3	2.883	132.99	9.43	+2.38
4.4	3.226	142.25	8.22	+0.31
4.5	2.857	128.66	39.15	+2.53
4.6	2.780	142.92	17.35	+0.68

These results show, as predicted from theoretical simulations, stronger ferromagnetic couplings are found in **4.3** and **4.5**. The ferromagnetic and an antiferromagnetic coupling calculated for **4.1** correlates to the experimental measurements revealing the presence of ferrimagnetic behaviour. In agreement with the experimental data, the weakest couplings are found in **4.2**, **4.4** and **4.6**. A comparison of the *J* values with the Re–Cl–Cu bond angle, α, shows the coupling to become more ferromagnetic upon decreasing the bridging angle (Figure 4.4.8).

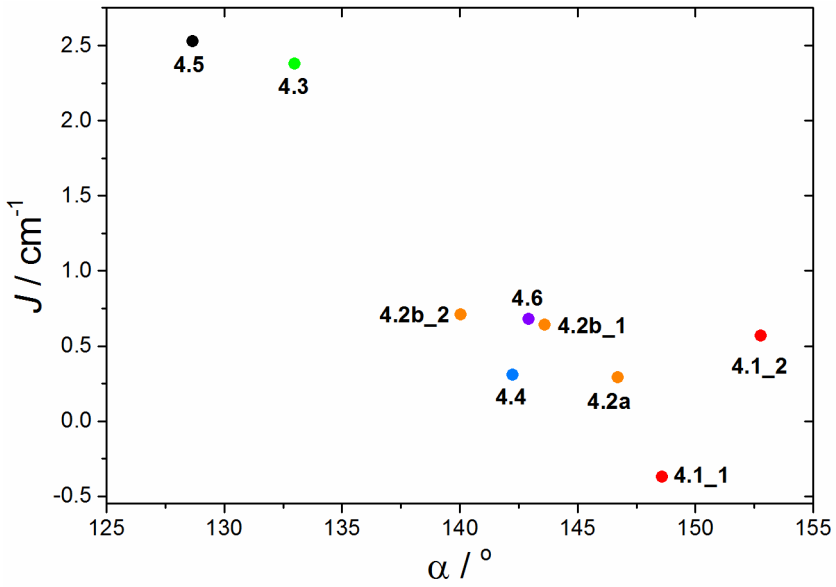

Figure 4.4.8. The magnetic exchange parameters, *J*, *versus* Re–Cl–Cu bridging angle, α. Each point labelled in accordance with Table 4.4.2.

In order to establish a magneto-structural correlation for these chains, a simplistic model was constructed with ideal geometries for the coordination spheres of the Cu^{II} and Re^{IV} ions (Figure 4.4.9). The magnetic exchange interaction was calculated as the Cu–Cl bond length and α and θ angles were varied from 2.50 to 3.25 Å, from 125 to 155° and from 0 to 45°, respectively (Figure 4.4.10).

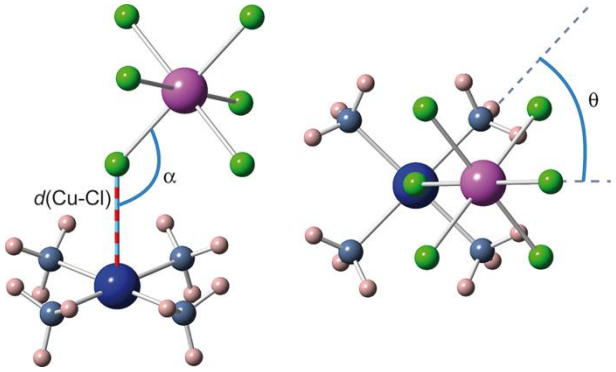

Figure 4.4.9. The $[Cu(NH_3)_4][ReCl_6]$ fragment viewed perpendicular (left) and parallel (right) to the Jahn-Teller axis of Cu^{II} ion. Colour code: Re (pink), Cu (dark blue), Cl (green), N (blue), H (bright red).

The results of the calculations on the model system corroborate our previous findings that; all magnetic couplings are moderate, they are mainly ferromagnetic, the magnetic coupling strongly depends on the α angle, and the magnitude of the magnetic coupling is inversely proportional to the Cu–Cl bond length. This last point is shown in Figure 4.4.11 for two pairs of α and θ values. The θ angle only effects the magnetic coupling slightly and only at short

Cu–Cl bond lengths, where an increased exchange interaction is observed for an narrow α angle and θ angle around 40° (Figure 4.4.10, top left).

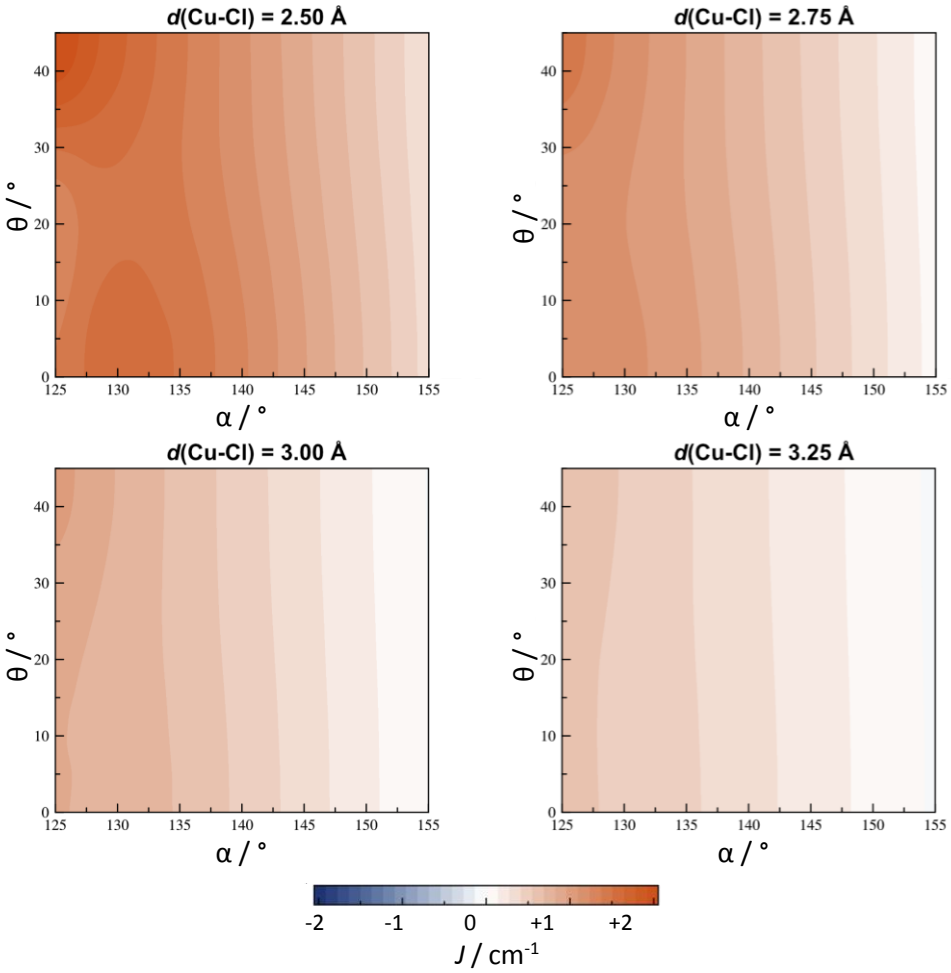

Figure 4.4.10. Contour maps of the dependence of the α and θ angle on the magnetic coupling constant for Cu–Cl bond lengths in the range 2.50-3.25 Å at intervals of 0.25 Å.

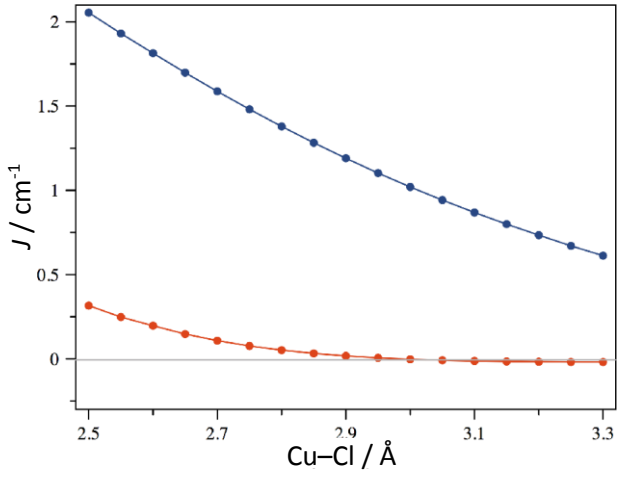

Figure 4.4.11. Dependence of the Cu–Cl bond length on the magnetic coupling for the geometries ({α,θ}) {125, 45} (blue) and {155, 45} (red).

In order to understand the mechanism behind magnetic coupling, orbital contributions to the magnetic exchange interactions were calculated.

The Cu^{II} ion contains the magnetic $d_{x^2-y^2}$ orbital and the Re^{IV} ion the three half-filled t_{2g} magnetic orbitals. Among the t_{2g} orbitals the d_{xy} orbital does not delocalize spin density onto the chloride ion of the Re–Cl–Cu bond, whereas the d_{xz} and d_{yz} magnetic orbitals delocalise their spin densities into the p_x and p_y orbitals of the bridging chloride ion, thereby interacting magnetically with the Cu^{II} ion. A schematic evolution of the interaction between the magnetic orbitals is shown Figure 4.4.12. The interaction between the d_{xz} and $d_{x^2-y^2}$ orbitals should be ferromagnetic prompted by a zero overlap, O = 0, of the magnetic orbitals and with no variation when changing the α angle (Figure 4.4.12a).[47, 48] The exchange interaction propagated by the d_{yz} magnetic orbital should be ferromagnetic as well and strengthened by a more narrow α angle increasing the interaction between the spin densities.

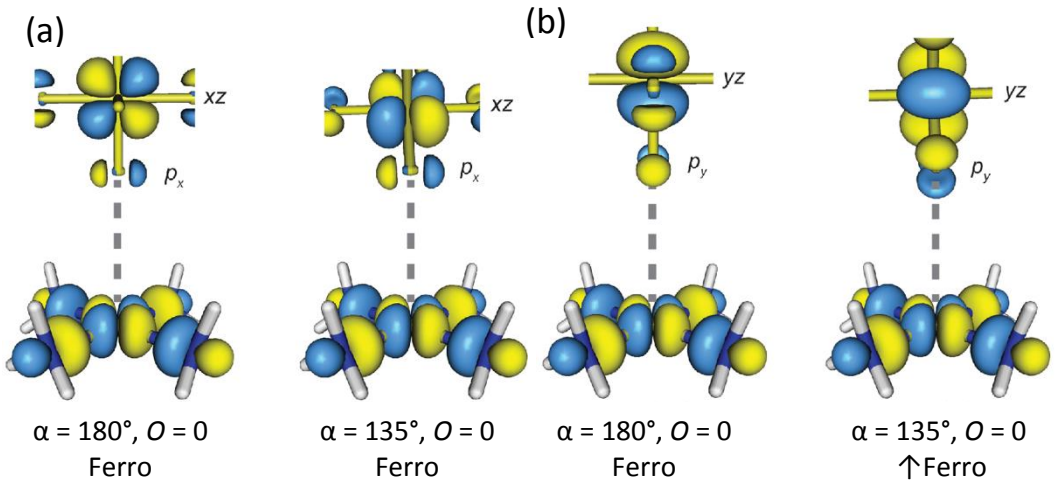

Figure 4.4.12. The interaction between the d_{xz} (a) and d_{yz} (b) magnetic orbitals of the Re^{IV} ion with the $d_{x^2-y^2}$ orbital of the Cu^{II} ion. α being the Re–Cl–Cu angle and O the orbital overlap.

With this theoretical study as a guide, the experimental susceptibility was then attempted to fit the model described in Figure 4.4.5, and good simulations were obtained with the set of parameters given in Table 4.4.3. The fit of **4.1** did not yield any meaningful values and were therefore not included.

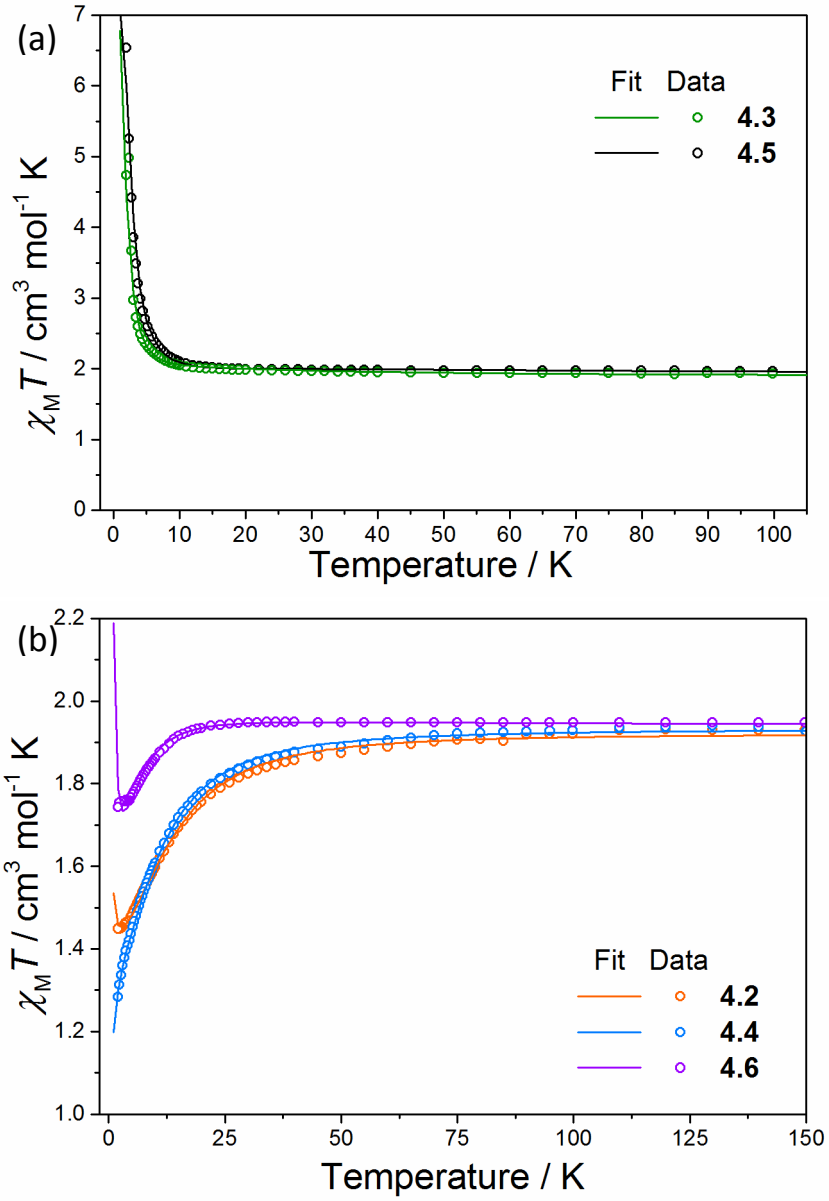

Figure 4.4.13. The experimental data, ○, and best fit line for **4.1**, **4.3** and **4.5** (a) and **4.2**, **4.4** and **4.6** (b).

The extrapolated values of the magnetic coupling from these fits are in agreement with the ones from the previous calculations. The exchange interaction dependent on the α angle and The values of the D_{Re}, g_{Re} and g_{Cu} parameters are within the range expected from the previous calculations in this study (Figure 4.4.14, Table 4.4.2 and 4.4.3).

Table 4.4.3. Values of g_{Re}, D_{Re} , g_{Cu} and J parameters that provide the best-fit of the thermal dependence of $\chi_M T$ for **4.2**-**6**.

Structure	g_{Re}	D_{Re} / cm^{-1}	g_{Cu}	J / cm^{-1}
4.2	1.804	-15.8	2.050	+0.11
4.3	1.778	-9.1	2.054	+1.59
4.4	1.807	-13.1	2.070	-0.12
4.5	1.764	-16.5	2.115	+2.16
4.6	1.814	-6.8	2.056	+0.33

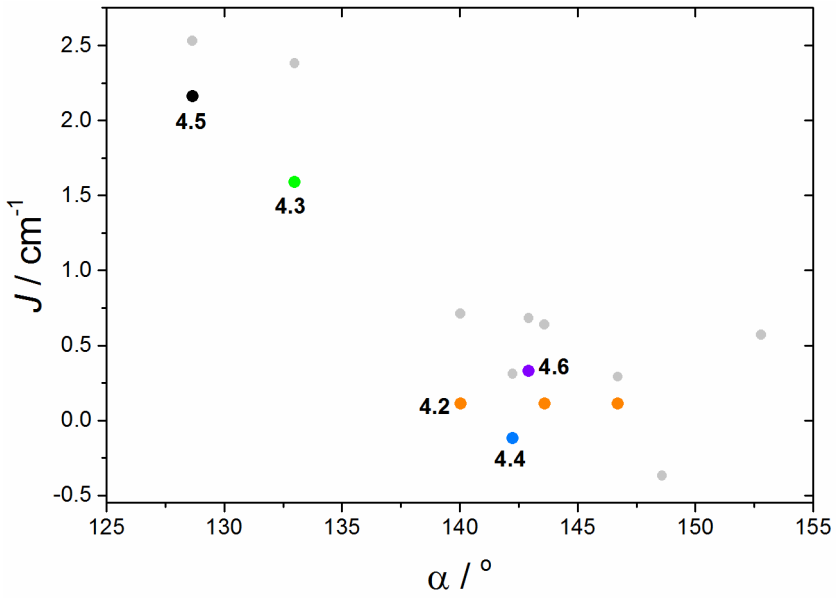

Figure 4.4.14. The magnetic exchange parameters versus Re–Cl–Cu bridging angle. Points labelled in accordance with Table 4.4.3. Grey dots correlate to the values presented in Table 4.4.2.

Ferromagnetic exchange interactions are predominant in this family of $Re^{IV}Cu^{II}$ chains, due to zero molecular overlap between the magnetic orbitals on the constituent metal ions. The presence of the Jahn-Teller axis of the Cu^{II} ion in the Re–Cl–Cu bridge results in weak interactions between neighbouring spin densities and therefore weak exchange. The axial Cu–Cl bond length and the Re–Cl–Cu bond angle are responsible for nature and magnitude of the magnetic exchange interactions detected in these chains.

4.5 Summary

Six molecular chains have been characterised structurally and magnetically. The chains are of formula $\{[Cu(L)_4][ReCl_6]\}_n$, where L = imidazole (**4.1**), 1-methylimidazole (**4.2**), 1-vinylimidazole (**4.3**), 1-butylimidazole (**4.4**), 1-vinyl-1,2,4-triazole (**4.5**) and dimethylformamide (**4.6**). The chains were synthesised in acetonitrile and crystallised by standing at 4°C (**4.2** and **4.3**), layering with isopropanol (**4.1**, **4.5** and **4.6**) or diethylether diffusion (**4.4**). The structures crystallise in the triclinic $P\bar{1}$ (**4.1**, **4.2** and **4.6**), monoclinic $C2/c$ (**4.3**) and $P2_1/c$ (**4.5**) and orthorhombic *Pccn* (**4.4**) space groups. Magnetic susceptibility measurements revealed great variation in the magnetic properties of these chains. **4.1** illustrated ferrimagnetic behaviour and **4.3** and **4.5** presented ferromagnetic exchange interactions. The susceptibility of **4.2**, **4.4** and **4.6** all exhibited behaviour indicative of weak antiferromagnetic interactions. The $\{[Cu(vinylimidazole)_4][ReCl_6]\}_n$ chain also exhibited

magnetic order at T_c = 2.4 which was detected by field dependence of the susceptibility, ZFC-FC measurements and frequency independent signals in the ac measurements. To fully understand the mechanism behind the differences in their magnetic properties a full theoretical investigation was carried out. This proved the magnetic exchange interactions between Re^{IV} and Cu^{II} ions to be greatly dependent on the bridging angle of the Re–Cl–Cu bond with the magnitude inversely proportional to Cu–Cl bond length.

4.6 References

1. R. Sessoli, D. Gatteschi, A. Caneschi and M. A. Novak, *Nature*, 1993, **365**, 141.
2. N. Ishikawa, M. Sugita, T. Ishikawa, S.-y. Koshihara and Y. Kaizu, *J. Am. Chem. Soc.*, 2003, **125**, 8694.
3. J. Martinez-Lillo, J. Faus, F. Lloret and M. Julve, *Coord. Chem. Rev.*, 2015, **289-290**, 215.
4. R. Chiozzone, R. González, C. Kremer, G. De Munno, J. Cano, F. Lloret, M. Julve and J. Faus, *Inorg. Chem.*, 1999, **38**, 4745.
5. F. Pop, M. Allain, P. Auban-Senzier, J. Martinez-Lillo, F. Lloret, M. Julve, E. Canadell and N. Avarvari, *Eur. J. Inorg. Chem.*, 2014, **2014**, 3855.
6. R. Gonzalez, F. Romero, D. Luneau, D. Armentano, G. De Munno, C. Kremer, F. Lloret, M. Julve and J. Faus, *Inorg. Chim. Acta*, 2005, **358**, 3995.
7. T. D. Harris, M. V. Bennett, R. Clérac and J. R. Long, *J. Am. Chem. Soc.*, 2010, **132**, 3980.
8. L. Arizaga, R. González, R. Chiozzone, C. Kremer, M. F. Cerdá, D. Armentano, G. D. Munno, F. Lloret and J. Faus, *Polyhedron*, 2008, **27**, 552.
9. A. Kochel, *Transition Met. Chem.*, 2010, **35**, 1.
10. J. Martinez-Lillo, D. Armentano, N. Marino, L. Arizaga, R. Chiozzone, R. Gonzalez, C. Kremer, J. Cano and J. Faus, *Dalton Trans.*, 2008, 4585.
11. M. V. Bennett and J. R. Long, *J. Am. Chem. Soc.*, 2003, **125**, 2394.
12. D. E. Freedman, D. M. Jenkins, A. T. Iavarone and J. R. Long, *J. Am. Chem. Soc.*, 2008, **130**, 2884.
13. J. M. Zadrozny, D. E. Freedman, D. M. Jenkins, T. D. Harris, A. T. Iavarone, C. Mathonière, R. Clérac and J. R. Long, *Inorg. Chem.*, 2010, **49**, 8886.
14. J. Martínez-Lillo, D. Armentano, G. De Munno, W. Wernsdorfer, M. Julve, F. Lloret and J. Faus, *J. Am. Chem. Soc.*, 2006, **128**, 14218.
15. L. Arizaga, R. González, D. Armentano, G. De Munno, M. A. Novak, F. Lloret, M. Julve, C. Kremer and R. Chiozzone, *Eur. J. Inorg. Chem.*, 2016, **2016**, 1835.
16. J. Martinez-Lillo, D. Armentano, G. De Munno, N. Marino, F. Lloret, M. Julve and J. Faus, *CrystEngComm*, 2008, **10**, 1284.
17. D. Armentano and J. Martinez-Lillo, *Inorg. Chim. Acta*, 2012, **380**, 118.
18. K. S. Pedersen, M. Sigrist, M. A. Sørensen, A.-L. Barra, T. Weyhermüller, S. Piligkos, C. A. Thuesen, M. G. Vinum, H. Mutka, H. Weihe, R. Clérac and J. Bendix, *Angew. Chem. Int. Ed.*, 2014, **53**, 1351.
19. J. Martinez-Lillo, D. Armentano, G. De Munno, F. Lloret, M. Julve and J. Faus, *Dalton Trans.*, 2008, 40.
20. J. Martinez-Lillo, J. Kong, W. P. Barros, J. Faus, M. Julve and E. K. Brechin, *Chem. Commun.*, 2014, **50**, 5840.

21. J. Kleinberg, *Inorg. Synth.*, McGraw-Hill, 1963.
22. G. A. Bain and J. F. Berry, *J. Chem. Educ.*, 2008, **85**, 532.
23. L. J. Bourhis, O. V. Dolomanov, R. J. Gildea, J. A. K. Howard and H. Puschmann, *Acta Crystallogr. Sect. A*, 2015, **71**, 59.
24. G. Sheldrick, *Acta Crystallogr. Sect. A*, 2008, **64**, 112.
25. O. V. Dolomanov, L. J. Bourhis, R. J. Gildea, J. A. K. Howard and H. Puschmann, *J. Appl. Crystallogr.*, 2009, **42**, 339.
26. M. J. Frisch et al., *Gaussian, Inc: Wallingford CT*, 2009.
27. A. D. Becke, *Phys. Rev. A*, 1988, **38**, 3098.
28. A. D. Becke, *J. Chem. Phys.*, 1993, **98**, 5648.
29. C. Lee, W. Yang and R. G. Parr, *Phys. Rev. B*, 1988, **37**, 785.
30. T. Yanai, D. P. Tew and N. C. Handy, *Chem. Phys. Lett.*, 2004, **393**, 51.
31. A. Schäfer, H. Horn and R. Ahlrichs, *J. Chem. Phys.*, 1992, **97**, 2571.
32. P. J. Hay and W. R. Wadt, *J. Chem. Phys.*, 1985, **82**, 270.
33. W. R. Wadt and P. J. Hay, *J. Chem. Phys.*, 1985, **82**, 284.
34. P. J. Hay and W. R. Wadt, *J. Chem. Phys.*, 1985, **82**, 299.
35. A. Schäfer, C. Huber and R. Ahlrichs, *J. Chem. Phys.*, 1994, **100**, 5829.
36. M. Douglas and N. M. Kroll, *Ann. Phys.*, 1974, **82**, 89.
37. B. A. Hess, *Phys. Rev. A*, 1985, **32**, 756.
38. E. Ruiz, J. Cano, S. Alvarez and P. Alemany, *J. Comput. Chem.*, 1999, **20**, 1391.
39. J. Tomasi, B. Mennucci and E. Cancès, *J. Mol. Struct. (THEOCHEM)*, 1999, **464**, 211.
40. F. Neese, *WIREs Comput. Mol. Sci.*, 2012, **2**, 73.
41. C. Ch, M. Pelissier and D. Ph, *Phys. Scr.*, 1986, **34**, 394.
42. K. Eichkorn, O. Treutler, H. Öhm, M. Häser and R. Ahlrichs, *Chem. Phys. Lett.*, 1995, **242**, 652.
43. K. Eichkorn, F. Weigend, O. Treutler and R. Ahlrichs, *Theor. Chem. Acc.*, 1997, **97**, 119.
44. C. Angeli, R. Cimiraglia, S. Evangelisti, T. Leininger and J.-P. Malrieu, *J. Chem. Phys.*, 2001, **114**, 10252.
45. C. Angeli, R. Cimiraglia and J.-P. Malrieu, *Chem. Phys. Lett.*, 2001, **350**, 297.
46. C. Angeli, R. Cimiraglia and J.-P. Malrieu, *J. Chem. Phys.*, 2002, **117**, 9138.
47. P. J. Hay, J. C. Thibeault and R. Hoffmann, *J. Am. Chem. Soc.*, 1975, **97**, 4884.
48. O. Kahn, *Molecular Magnetism*, VCH Publisher, Inc., 1993.

Chapter 5: Hexahalorhenate(IV) salts of metal oxazolidine nitroxides

5.1 Introduction

Since the initial discovery of a Mn_{12} molecule that can retain its magnetisation in zero field at low temperature, research on discrete paramagnetic systems has grown exponentially over the past two decades.[1-3] This research encompasses a wide range of magnetic materials including organic radicals, mono- and multinuclear homometallic transition metal or lanthanide based complexes as well as heterometallic 3d/4f systems.[3-6] The energy barrier for magnetisation reversal in such systems depends on many factors but it is especially important to consider the degree and nature of any inherent magnetic anisotropy. This has led to an increased interest in the giant magnetic anisotropy present in: 4f/5f materials where the unquenched orbital angular momenta interacts with the ligand field; and 4d/5d metal ions where the spin-orbit coupling mixes the electronic ground and excited states.[5, 7-11] The $5d^3$ Re^{IV} ion has a large magnetic anisotropy, due to second order spin-orbit coupling and the large value of its spin-orbit coupling constant, λ, of ca. 1000 cm^{-1} for the free ion. This results in large values of the zero field splitting parameter, D,[12] which can be examined by magnetisation *versus* field measurements and/or high-frequency electron paramagnetic resonance (HF-EPR). However, determining unambiguously both the sign and magnitude of D is not a trivial task, as exemplified by a recent ab-initio study on the origin of the magnetic anisotropy in a series of mononuclear Re^{IV} complexes.[13] Additionally the diffuse nature of the 5d orbitals gives rise to spin delocalisation onto the ligands leading to relatively strong magnetic exchange interactions mediated by either Re–X···X–Re[14-18] or Re–X···H_2O···X–Re[19] intermolecular contacts (X = halide atom). Research on the hexahalorhenate unit $[ReX_6]^{2-}$ with X = F, Cl, Br or I, has been carried out extensively over the last two decades with the magnetic behaviour of the $[ReX_6]^{2-}$ anion in the solid state depending greatly on the nature of the cation employed. These cations range from organic radicals,[20] alkali metals,[21] ferrocenium,[22] to the Single-Molecule Magnets 'Mn_6'.[23] These systems exhibit a great variation in their magnetic properties such as anti- and ferromagnetic intermolecular exchange interactions and spin-canting.[21, 24] Research conducted on the $[ReI_6]^{2-}$ ion with the alkali metal ions, Li^+ to Cs^+, illustrates the effect of the cation size on the intermolecular Re–I···I–Re interaction where it was found that the magnetic ordering temperature increases with decreasing size of the cation.[21] Additionally by crystallising the $[ReCl_6]^{2-}$ ion with the well characterised single molecule magnet, Mn_6,[25-33] the energy barrier for spin relaxation increased by around 30%.[23] Initial investigations into the exchange

interactions and magnetic properties present in species containing a coordinated radical were instigated by Gatteschi and co-workers and was known as the "metal-radical approach".[34, 35] This focussed initially on the use of nitroxide based radicals which led to the discovery of the first Single Chain Magnet, $[Co^{II}(hfac)_2(NITPhOMe)]$, and the ferrimagnetically ordered system $\{Mn^{II}(hfac)_2(L)\}_n$[36, 37] where hfac = hexafluoro-acetylacetonate, NITPhOMe = 4'-methoxy-phenyl-4,4,5,5-tetramethylimidazoline-1-oxyl-3-oxide and L = 1,3,5-tris{p-(N-oxy-N-tert-butylamino)phenyl}benzene. The ligand hexafluoroacetylacetonate (hfac) was used to increase the Lewis acidity of the central metal ion enabling the nitroxide N–O moiety, a weak Lewis base, to coordinate directly to the metal. A second approach to coordinating a radical based group directly to the metal is to create ligands combining a radical species in close proximity to a conventional ligating group such as bipyridine, imidazole or pyridine.[38-40] The $[M^{II}(L^{\bullet})_2]^{2+}$ unit, M = Mn, Fe, Co, Cu and Zn, with $L^{\bullet}$ =4-dimethyl-2,2-di(2-pyridyl)oxazolidine *N*-oxide (Figure 5.1.1), has been studied over the past decade leading to the discovery of interesting magnetic phenomena such as spin-crossover, ferromagnetic exchange and reductively induced oxidation.[40-45] Here is the report on the synthesis and magnetic characterisation of a series of coordination compounds containing both the $[M^{II}(L^{\bullet})_2]^{2+}$ cation and the $[ReX_6]^{2-}$ anion. When the transition metal in the $[M^{II}(L^{\bullet})_2]^{2+}$ cation is Fe, Co or Cu and used in combination with $[ReCl_6]^{2-}$ and $[ReBr_6]^{2-}$ anions (**5.1a**, **5.1b**, **5.2a**, **5.2b**, **5.4a** and **5.4b**) predominantly antiferromagnetic metal-radical exchange interactions is observed with typical $[ReX_6]^{2-}$ ion behaviour and a gradual spin-crossover transition present in **5.2a** and **5.2b**. Using The Ni^{II} ion yields the crystalline products, $[Ni(L^{\bullet})(CH_3CN)_3][Re^{IV}Cl_6]\cdot CH_3CN$ (**5.3a**) and $[Ni(L^{\bullet})(CH_3CN)_3][Re^{IV}Cl_6]\cdot 3CH_3CN$ (**5.3b**), where not only an unusual, ferromagnetic, potentially vertex capping cation is observed, but also the presence of intermolecular antiferromagnetic interactions at T = 3K in **5.3b(dried)** and spin-canting in **5.3a(dried)**.

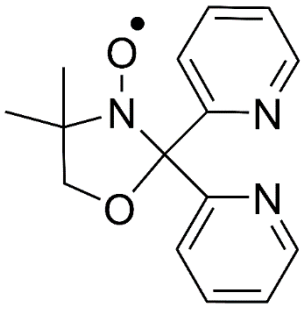

Figure 5.1.1. Molecular structure of 4-dimethyl-2,2-di(2-pyridyl)oxazolidine *N*-oxide, $L^{\bullet}$.

5.2 Experimental

5.2.1 Materials and methods

All chemicals were used as received. Syntheses were carried out under aerobic conditions using CH_3CN dried over 3 Å molecular sieves. $(NBu_4)_2[ReCl_6]$ and $(NBu_4)_2[ReBr_6]$ were prepared as described previously.[17, 46] The neutral radical ligand, 4,4-dimethyl-2,2-di(2-pyridyl)oxazolidine-*N*-oxide ($L^{\bullet}$), was prepared as *per* literature methods.[41] Crystals of all eight compounds were collected and left open to air for use in further analysis. Elemental analyses (C, H, N) were performed by the MEDAC Ltd microanalysis service. Ac and dc magnetic susceptibility measurements on all of the eight, dried, compounds were collected on Quantum Design PPMS and Quantum Design MPMS-XL SQUID magnetometers equipped with 7 T dc magnets in the temperature range 1.8 – 300 K under an applied field of 1000 Oe. Similar magnetic susceptibility measurements were carried out on crystalline samples of **5.3a** and **5.3b** immersed directly in acetonitrile from 200 – 2 K under an applied field of 1000 Oe (**5.3a(solvated)** and **5.3b(solvated)**). Diamagnetic corrections were applied using Pascal's constants.[47] Infrared (IR) spectra from 3800 to 600 cm^{-1} were recorded on a Perkin Elmer Spectrum 65 ATR-IR spectrometer. Powder X-ray diffraction measurements were carried out on a Rigaku Oxford Diffraction SuperNova X-ray diffractometer at 298 K using a scan step size of 0.086° at 1° sec^{-1}. Calculated patterns were obtained *via* Mercury 3.7.

5.2.2 Crystallography

Data were measured on Rigaku Oxford Diffraction SuperNova (**5.1a**, **5.1b**, **5.2a**, **5.2a**·150 K, **5.2b**, **5.3b**, **5.4a**, and **5.4b**) and Rigaku Oxford Diffraction XCalibur (**5.3a**) X-ray diffractometers using Mo-K_α (**5.1a**, **5.1b**, **5.2a**, **5.2a**·150 K, **5.3a**, **5.3b** and **5.4b**) or Cu-K_α (**5.2b** and **5.4a**) radiation. Structures were solved with olex2.solve (**5.1a**, **5.1b**, **5.2a**, **5.2a**·150 K, **5.2a**·200 K, **5.2a**·250 K, **5.2b**, **5.3b**, **5.4a** and **5.4b**)[48] or ShelXS (**5.3a**)[49] and refined by full-matrix least-squares on F-squared using ShelXL, interfaced through Olex2.[50] In **5.1a** C12 is disordered over two positions with partial occupancies 0.56 and 0.44. In **5.2a** the nitrogen associated with N(4) on the solvate acetonitrile is disordered over two positions with partial occupancies 0.45 and 0.55. In **5.4a** C(12) and C(14) are disordered over two positions with partial occupancies 0.49 and 0.51, and 0.53 and 0.47. All non-hydrogen atoms were refined anisotropically and hydrogens placed in calculated positions.

5.2.3 Synthesis of $[Fe(L^{\bullet})_2][ReCl_6]$ (5.1a)

$(NBu_4)_2[ReCl_6]$ (44.0 mg, 0.05 mmol) and $FeCl_2{\cdot}4H_2O$ (9.9 mg, 0.05 mmol) were dissolved in 4 ml CH_3CN to which 4,4-dimethyl-2,2-di(2-pyridyl) oxazolidine N-oxide ($L^{\bullet}$) (13.5 mg, 0.05 mmol) in 2 ml CH_3CN was added. The resultant solution was left to sit overnight at 4°C yielding green crystals suitable for X-ray diffraction (59% yield). Elemental analysis (%) calculated (found) for $C_{30}H_{32}N_6O_4Cl_6FeRe$: C, 36.2 (36.0); H, 3.2 (3.2); N, 8.4 (8.5).

5.2.4 Synthesis of $[Fe(L^{\bullet})_2][ReBr_6]$ (5.1b)

$(NBu_4)_2[ReBr_6]$ (57.5 mg, 0.05 mmol) and $FeCl_2{\cdot}4H_2O$ (9.9 mg, 0.05 mmol) were dissolved in 4 ml CH_3CN to which $L^{\bullet}$ (13.5 mg, 0.05 mmol) in 2 ml CH_3CN were added. Solids started to form immediately so the solution was filtered and left to stand at room temperature. Dark green crystals suitable for X-ray diffraction were collected after 24 hours (65% yield). Elemental analysis (%) calculated (found) for $C_{30}H_{32}N_6O_4Br_6FeRe$: C, 28.6 (29.2); H, 2.6 (2.6); N, 6.7 (7.0).

5.2.5 Synthesis of $[Co(L^{\bullet})_2][ReCl_6]{\cdot}2CH_3CN$ (5.2a)

5.2a was synthesised as *per* **5.1a** using $Co(NO_3)_2{\cdot}6H_2O$ (14.5 mg, 0.05 mmol) instead of $FeCl_2{\cdot}4H_2O$. Brown crystals suitable for X-ray diffraction were grown overnight at 4°C (50% yield). The crystals were collected and left to dry in air and analysed as solvent free. Elemental analysis (%) calculated (found) for $C_{30}H_{32}N_6O_4Cl_6CoRe$: C, 36.1 (35.4); H, 3.2 (3.2); N, 8.4 (8.8).

5.2.6 Synthesis of $[Co(L^{\bullet})_2][ReCl_6]{\cdot}4CH_3CN$ (5.2a·150 K, 5.2a·200 K, 5.2a·250 K)

This was synthesised as *per* **5.2a**. Elemental analysis (%) calculated (found) for $C_{30}H_{32}N_6O_4Cl_6CoRe$: C, 36.1 (34.6); H, 3.2 (3.1); N, 8.4 (7.9).

5.2.7 Synthesis of $[Co(L^{\bullet})_2][ReBr_6]$ (5.2b)

$[Co(L^{\bullet})_2][ReBr_6]$ was synthesised as *per* **5.1b** using $Co(NO_3)_2{\cdot}6H_2O$ (14.5 mg, 0.05 mmol) instead of $FeCl_2{\cdot}4H_2O$. Dark brown crystals suitable for X-ray diffraction were collected from the solution after 24 hours (86% yield). Elemental analysis (%) calculated (found) for $C_{30}H_{32}N_6O_4Br_6CoRe$: C, 28.5 (28.4); H, 2.6 (2.7); N, 6.6 (7.1).

5.2.8 Synthesis of $[Ni(L^{\bullet})(CH_3CN)_3][ReCl_6]{\cdot}CH_3CN$ (5.3a)

The compound was synthesised as *per* **5.1a** using $Ni(NO_3)_2{\cdot}6H_2O$ (14.5 mg, 0.05 mmol) instead of $FeCl_2{\cdot}4H_2O$. Large brown crystals suitable for X-ray diffraction were collected from the mother liquor after standing at room temperature overnight (18% yield). The crystals

were left to dry in air for use in further studies. Upon inspection of the elemental analysis and IR spectra it is clear that it analyses for the formula $[Ni(L^{\bullet})(H_2O)_3][ReCl_6]$ suggesting the coordinated acetonitrile groups have been replaced by water when left open to air. Elemental analysis (%) calculated (found) for $C_{15}H_{22}N_3O_5Cl_6NiRe$: C, 23.0 (23.1); H, 2.8 (3.0); N, 5.4 (5.6). IR spectra for **5.3a(dried)** and **5.3a(solvated)** are shown in Figure 5.4.4a.

5.2.9 Synthesis of $[Ni(L^{\bullet})(CH_3CN)_3][ReBr_6]\cdot 3CH_3CN$ (5.3b)

5.3b was synthesised as *per* **5.1b** using $Ni(NO_3)_2\cdot 6H_2O$ (14.5 mg, 0.05 mmol) instead of $FeCl_2\cdot 4H_2O$. Large yellow crystals suitable for X-ray diffraction were collected after standing overnight at room temperature (31% yield). Upon inspection of the elemental analysis and IR spectra it is clear that the coordinated acetonitrile groups have been replaced by water and subsequently analyses for the formula $[Ni(L^{\bullet})(H_2O)_3][ReBr_6]$. Elemental analysis (%) calculated (found) for $C_{15}H_{22}N_3O_5Br_6NiRe$: C, 17.2 (17.5); H, 2.1 (2.3); N, 4.0 (4.2). IR spectra for **5.3b(dried)** and **5.3b(solvated)** are shown in Figure 5.4.4b.

5.2.10 Synthesis of $[Cu(L^{\bullet})_2][ReCl_6]$ (5.4a)

$[Cu(L^{\bullet})_2][ReCl_6]$ was synthesised as *per* **5.1a** with $Cu(NO_3)_2\cdot 3H_2O$ (0.05 mmol, 12 mg) used instead of $FeCl_2\cdot 4H_2O$. Dark green crystals suitable for X-ray diffraction were grown overnight at 4^{o}C (67% yield). Elemental analysis (%) calculated (found) for $C_{30}H_{32}N_6O_4Cl_6CuRe$: C, 35.9 (35.9); H, 3.2 (3.2); N, 8.4 (8.3).

5.2.11 Synthesis of $[Cu(L^{\bullet})_2][ReBr_6]$ (5.4b)

The compound was synthesised as *per* **5.1b** using $Cu(NO_3)_2\cdot 3H_2O$ (12 mg, 0.05 mmol) instead of $FeCl_2\cdot 4H_2O$. Dark brown crystals suitable for X-ray diffraction were collected from the mother liquor after 4 hours (60% yield). Elemental analysis (%) calculated (found) for $C_{30}H_{32}N_6O_4Br_6CuRe$: C, 28.4 (27.8); H, 2.5 (2.6); N, 6.6 (6.8).

5.3 Structures

5.3.1 Structure of $[Fe(L^{\bullet})_2][ReCl_6]$ (5.1a)

Complex **5.1a** crystallises in the triclinic space group $P\bar{1}$ with inversion centres on both the Re^{IV} and Fe^{II} ions (Table 5.3.1). The asymmetric unit contains half the $[Fe(L^{\bullet})_2]^{2+}$ cation and half the $[ReCl_6]^{2-}$ anion. The Re^{IV} ion is in a regular octahedral environment coordinated to six chloride ions with Re–Cl bond lengths between 2.3547(8) to 2.3748(9) Å, in accordance with previously published compounds containing the $[ReCl_6]^{2-}$ anion (Table 5.3.4).[20, 51] Two neutral radical ligands are coordinated facially to the Fe^{II} ion, bonding in an η^3-fashion through the pyridyl nitrogen atoms and oxygen atoms of the nitroxide group (Figure 5.3.1a).

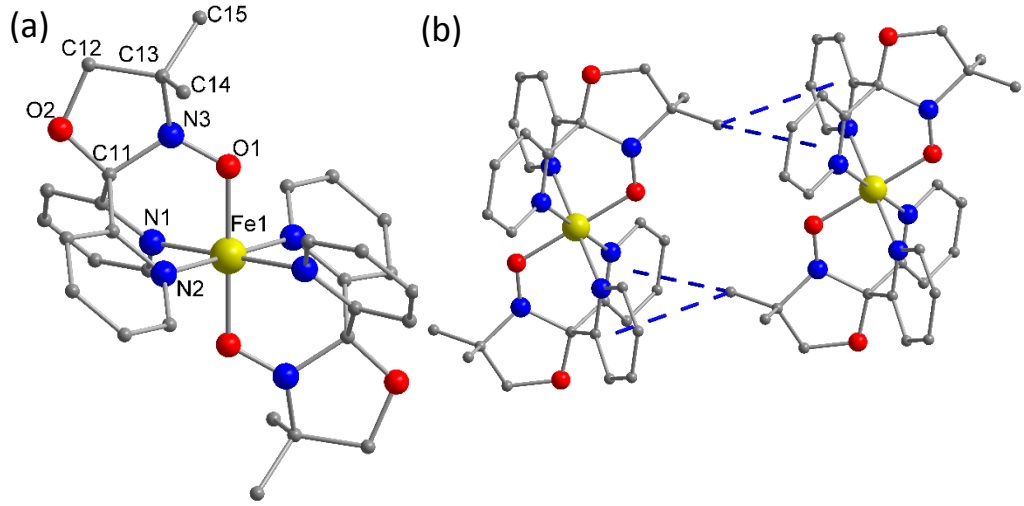

Figure 5.3.1. a) The structure of the $[Fe(L^{\bullet})_2]^{2+}$ cation in **5.1a**. b) CH···π interactions between cations in **5.1a**. CH···π interactions indicated by blue lines. In a), atoms labelled in accordance with Tables 5.3.4, 5.3.5 and 5.3.7. Hydrogen atoms are omitted for clarity. Colour code: Fe, yellow; O, red; N, blue; C, grey.

This results in a slightly distorted octahedral *trans*-N_4O_2 coordination sphere around the central Fe^{II} ion. The Fe–N bond distances are 1.984(3) and 1.967(3) Å and the Fe–O bond measures 1.872(2) Å. The *cis* angles range between 87.60(12) and 92.40(12)°, while the *trans* angles are generated by the inversion centre resulting in angles of 180° (Table 5.3.4). The nitroxide N–O bond length of 1.323(3) Å shows the ligand to be in its neutral radical form and not the reduced hydroxylamino anionic form (L^-).[41] The structural features of the cation are in accordance with previously published results on the $[Fe(L^{\bullet})_2]^{2+}$ cation which contained a central low-spin Fe^{II} ion with both ligands in the neutral radical form.[41] Examination of the crystal packing reveals alternating layers of $[Fe(L^{\bullet})_2]^{2+}$ cations and $[ReCl_6]^{2-}$ anions in the crystallographic *ac-plane*, as seen in Figure 5.3.2. In the plane of the cations short CH···π interactions force the $[Fe(L^{\bullet})_2]^{2+}$ moieties to pack in chains along the crystallographic *a-axis*

(Figure 5.3.2, blue lines). The CH···π distances ranging from 3.5 to 3.8 Å between the methyl group on the oxazolidine ring and the centroid of the pyridyl groups (Figure 5.3.1b, blue lines, and Table 5.3.8).

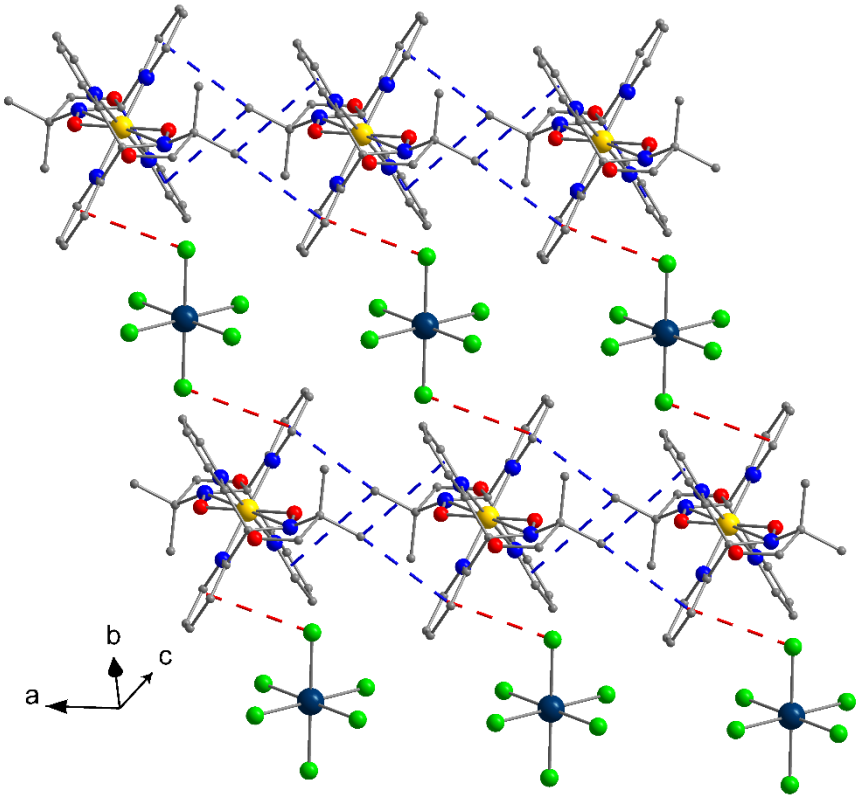

Figure 5.3.2. The crystal packing of **5.1a**. CH···π and Cl···π interactions are indicated by blue lines and red lines, respectively. Hydrogen atoms are omitted for clarity. Colour code: Re, dark blue; Fe, yellow; Cl, green; O, red; N, blue; C, grey.

The $[ReCl_6]^{2-}$ ions are surrounded by four cations and are thus well isolated from each other, with the shortest Cl···Cl distance being 4.7 Å along the crystallographic *a*-axis. The $[ReCl_6]^{2-}$ anion interacts with two cations from opposite layers *via* Cl···π interactions of 3.7 Å, creating a 1-D network with alternating $[ReCl_6]^{2-}$ and $[Fe(L^{\bullet})_2]^{2+}$ ions running diagonally in the unit cell (Figure 5.3.2, red lines).

5.3.2 Structure of $[Fe(L^{\bullet})_2][ReBr_6]$ (5.1b)

Complex **5.1b** crystallises in the triclinic space group $P\bar{1}$ and posseses a structure that resembles that one of **5.1a**; the most obvious and significant difference being the presence of the hexabromorhenate(IV) anion instead of the hexachlororhenate(IV) ion (Table 5.3.1). Inversion centres are located on the Fe^{II} and Re^{IV} ions with the asymmetric unit containing half of the $[Fe(L^{\bullet})_2]^{2+}$ cation and half of the $[ReBr_6]^{2-}$ anion. The Re^{IV} ion is coordinated to six bromide atoms in a octahedral geometry with Re–Br bond lengths of 2.5029(6), 2.5249(6)

and 2.5132(6) Å, similar to that seen in previously published reports on the $[ReBr_6]^{2-}$ anion.[24, 52] The bond lengths and angles of the $[Fe(L^{\bullet})_2]^{2+}$ unit are similar to the cation in **5.1a** suggesting the presence of a central low-spin Fe^{II} ion with both ligands in their neutral radical ($L^{\bullet}$) form (Table 5.3.4). The packing of **5.1b** in the crystal is analogous to **5.1a**, with minor deviations inflicted by the larger $[ReBr_6]^{2-}$ ion. The anions are well isolated from each other, as in **5.1a**, with the shortest Br···Br distance 4.6 Å along the crystallographic *a*-axis (Figure 5.3.3). The shortest CH···π interaction between the cations is approximately 3.6 Å, and the Br···π interactions between the $[Fe(L^{\bullet})_2]^{2+}$ cations and the $[ReBr_6]^{2-}$ anions are of the order of 3.8 Å (Figure 5.3.3 and Table 5.3.8).

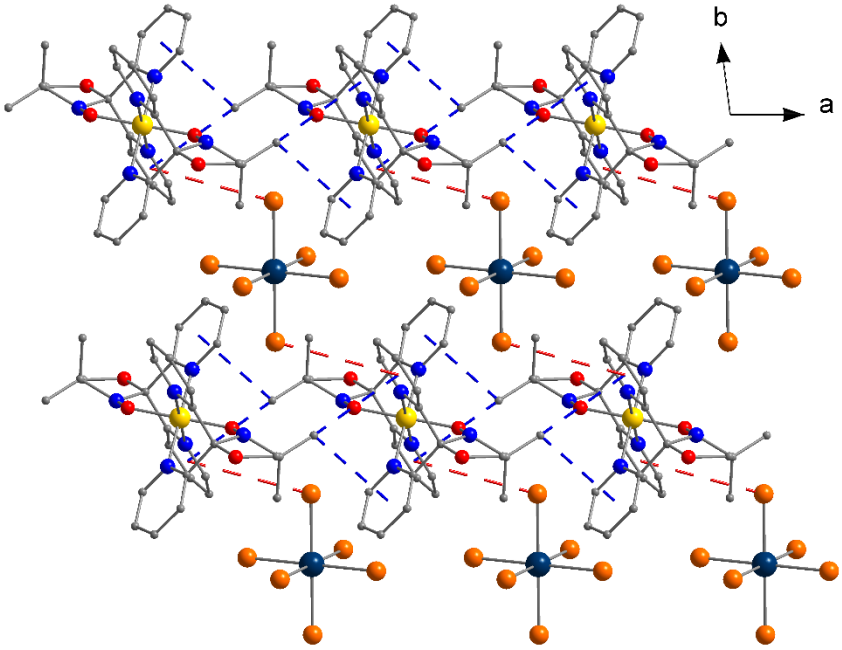

Figure 5.3.3. The crystal packing of **5.1b**. CH···π and Br···π interactions are indicated by blue lines and red lines, respectively. Hydrogen atoms are omitted for clarity. Colour code: Re, dark blue; Fe, yellow; Br, orange; O, red; N, blue; C, grey.

5.3.3 Structure of $[Co(L^{\bullet})_2][ReCl_6]\cdot 2CH_3CN$ (5.2a)

Complex **5.2a** has similar structural features to **5.1a** in that it crystallises in the space group $P\bar{1}$ with inversion centres located on both the Co^{II} and Re^{IV} ions (Table 5.3.1). The asymmetric unit contains half the $[Co(L^{\bullet})_2]^{2+}$ cation and half the $[ReCl_6]^{2-}$ anion along with one disordered acetonitrile solvate molecule. This results in on overall formula of $[Co(L^{\bullet})_2][ReCl_6]\cdot 2CH_3CN$. The bond lengths and bond angles of the $[ReCl_6]^{2-}$ ion are similar to the anion described in **5.1a** (Table 5.3.4). The $[Co(L^{\bullet})_2]^{2+}$ is structurally similar to the cation described in **5.1a** (Figure 5.3.1a). The Co^{II} ion is in a regular, *trans*-N_4O_2 octahedral geometry, coordinated to two $L^{\bullet}$ ligands. The Co–N bond lengths are 1.9251(11) and 1.9556(10) Å, and the Co–O bond length

is 1.9103(10) Å. The *cis* bond angles are 85.76(4)–94.24(4)° and the *trans* angles all 180° (Table 5.3.4). The nitroxide N–O bond on the ligand is 1.3137(16) Å consistent with the ligand in the neutral radical form ($L^{\bullet}$).[41] The packing of **5.2a** in the crystal lattice is only slightly different from that observed in **5.1a**. The solvent acetonitrile molecules lie in the plane of the anions leading to a different orientation of the $[ReCl_6]^{2-}$ unit, with the shortest Cl···Cl interaction being 3.8 Å (Figure 5.3.4, green dashed lines). No Cl···π interactions are observed between the $[Co(L^{\bullet})_2]^{2+}$ and $[ReCl_6]^{2-}$ ions (Figure 5.3.4). The cations pack as described in **5.1a**, with the shortest CH···π interactions approximately 3.4 Å (Figure 5.3.1a and Table 5.3.8).

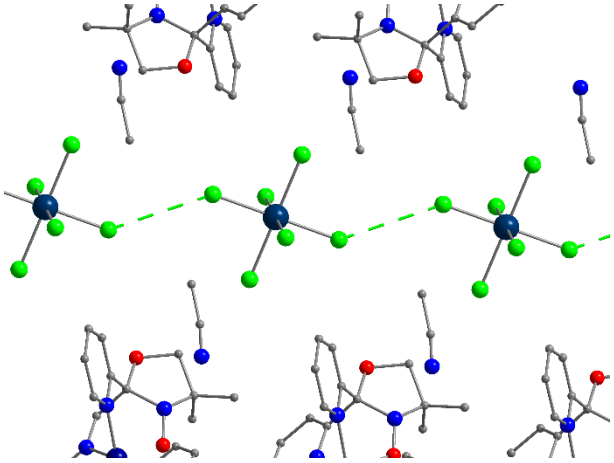

Figure 5.3.4. The packing of anions and CH_3CN solvent molecules in compound **5.2a**. Short Cl···Cl interactions indicated by dashed green lines. Hydrogen atoms are omitted for clarity. Colour code: Re, dark blue; Co, navy blue; Cl, green; O, red; N, blue; C, grey.

The bond lengths in the cation in **5.2a** are a shorter than the expectation for low-spin Co^{II} ion with an axially elongated pseudo-Jahn-Teller distortion and clearly do not correspond to that of high-spin Co^{II} ion. To clarify the unusual bond lengths contained in the $[Co(L^{\bullet})_2]^{2+}$ cation in **5.2a**, a new set of crystals were grown and X-ray crystallography measurements undertaken on the same single crystal at 150 (**5.2a**·150 K), 200 (**5.2a**·200 K) and 250 K (**5.2a**·250 K) (Tables 5.3.1, 5.3.2 and 5.3.4, Figure 5.3.5). However, this crystal crystallised in the monoclinic space group, $P2_1/c$, with an overall formula of $[Co(L^{\bullet})_2][ReCl_6]\cdot 4CH_3CN$ in direct contrast to the initial crystal structure which crystallised in the triclinic space group, $P\bar{1}$, and formulated as $[Co(L^{\bullet})_2][ReCl_6]\cdot 2CH_3CN$ (**5.2a**). An identical synthetic route and crystallising conditions were used for both solvates so it can be concluded that it is very sensitive to external perturbations such as temperature and humidity. Both solvates contain the $[Co(L^{\bullet})_2]^{2+}$ cation and the $[ReCl_6]^{2-}$ anion and differ only in their intermolecular arrangement in the solid state driven mainly by the differing degrees of solvation.

The variable temperature study on **5.2a**·150 K, **5.2a**·200 K and **5.2a**·250 K showed evidence of spin-crossover behaviour as an axially elongated pseudo-Jahn-Teller distortion of the low-spin Co^{II} ion was observed at 150 K which diminished as the temperature was increased (Table 5.3.4 and Figure 5.3.5). This suggests a gradual, thermally induced, spin transition between the low-spin and high-spin states of the central Co^{II} ion.

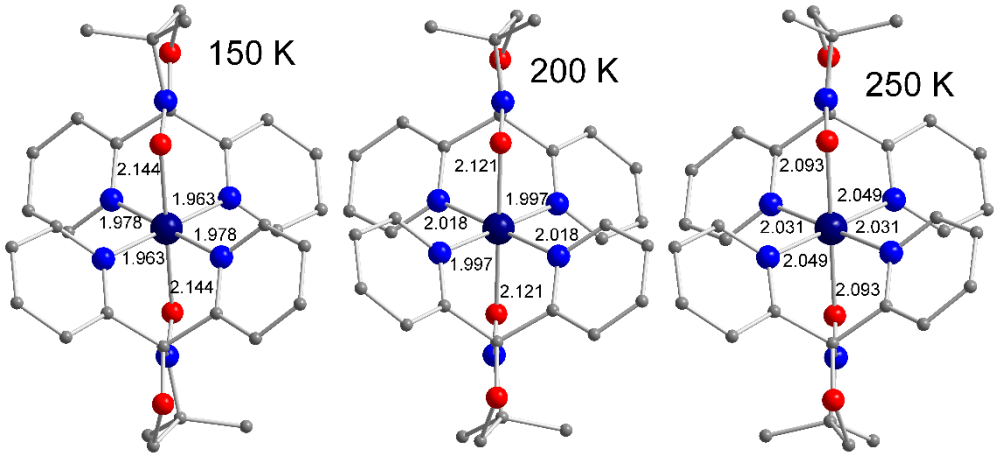

Figure 5.3.5. The variable temperature structures of the cation. Bond lengths labelled in Å. Hydrogen atoms are omitted for clarity. Colour code; Co, navy; O, red; N, blue; C, grey.

A comparison of the bond lengths in **5.2a**, **5.2a**·150K, **5.2a**·200 K and **5.2a**·250 K with similar species can be found in Table 5.3.9. The bond lengths and angles of the $[ReCl_6]^{2-}$ anion in **5.2a**·150K, **5.2a**·200 K, **5.2a**·250 K are similar to that described in **5.1a** and **5.2a**. The crystal packing is similar in **5.2a**·150K, **5.2a**·200 K and **5.2a**·250 K with alternate layers of the $[Co(L^{\bullet})_2]^{2+}$ cation and the $[ReCl_6]^{2-}$ anion along the *bc*-plane. There is no indication of any significant CH···π or Cl···Cl intermolecular interactions and the shortest Cl···Cl distance is 6.455 Å in **5.2a**·150K, 6.572 Å in **5.2a**·200 K and 6.715 Å in **5.2a**·250 K (Table 5.3.8). A comparison of the intermolecular packing in both solvates and their relation to any magnetic properties (*vide infra*) is rendered moot by the fact that the microanalysis of both solvates suggest that they coalesce upon drying into the same material, namely, $[Co(L^{\bullet})_2][ReCl_6]$.

5.3.4 Structure of $[Co(L^{\bullet})_2][ReBr_6]$ (5.2b)

Complex **5.2b** crystallises in the triclinic space group $P\bar{1}$ with inversion centres located on both the Co^{II} and Re^{IV} ions; subsequently the asymmetric unit contains half the $[Co(L^{\bullet})_2]^{2+}$ cation and half the $[ReBr_6]^{2-}$ anion (Table 5.3.2). The geometrical parameters of the $[ReBr_6]^{2-}$ anion are analogous to that described in **5.1b** (Table 5.3.5). The Co^{II} ion is in a distorted, *trans*-N_4O_2 octahedral geometry, coordinated to two $L^{\bullet}$ ligands. The Co–N bond lengths are 1.963(4) and 1.976(4) Å, and the Co–O bond length is 2.092(4) Å. The *cis* bond angles range

from 87.98(17)–92.02(17)° and the *trans* angles all 180°. The N–O bond on the ligand is 1.269(6) Å which confirms the neutral radical ($L^{\bullet}$) form of the ligand. Bond lengths and angles suggest a central low-spin Co^{II} ion showing an axially elongated pseudo-Jahn-Teller distortion, consistent with previously reported studies on the $[Co(L^{\bullet})_2]^{2+}$ cation (Table 5.3.9).[42] The packing of $[Co(L^{\bullet})_2][ReBr_6]$ in the crystal is identical to that described for **5.1b** (Figure 5.3.3). The shortest CH···π interactions between the cations are *circa* 3.6 and 3.7 Å, and the Br···Br interactions approximately 4.6 Å. The Br···π interactions between the $[Co(L^{\bullet})_2]^{2+}$ cations and the $[ReBr_6]^{2-}$ ions are 3.8 Å (Table 5.3.8).

5.3.5 Structure of $[Ni(L^{\bullet})(CH_3CN)_3][ReCl_6]\cdot CH_3CN$ (5.3a)

Complex **5.3a** crystallises in the orthorhombic space group *Pbca* with the asymmetric unit containing a single $[Ni(L^{\bullet})(CH_3CN)_3]^{2+}$ cation and the $[ReCl_6]^{2-}$ anion and one acetonitrile solvate molecule (Table 5.3.3). The geometrical parameters of the $[ReCl_6]^{2-}$ ion are similar to that described for **5.1a** and **5.2a** (Tables 5.3.4 and 5.3.6). The Ni^{II} ion is atypically coordinated to just one tridentate, facially capping $L^{\bullet}$ ligand, not two as in the other complexes described in this paper, and all other previously published results (Figure 5.3.6a).[40-42, 44] The coordination sphere of the Ni^{II} ion is then completed by three acetonitrile molecules, creating a slightly distorted octahedral environment around the metal ion with *cis* angles varying in the range 86.1(17)–93.9(17)° and the most bent *trans* angle being 176.19(18)°, N(4)–Ni–(1). The Ni–$N_{L\bullet}$ bond lengths are 2.068(4) and 2.058(4) Å, with the Ni–O distance being 2.073(4) Å. The N–O bond length of 1.271 (6) Å shows the ligand to again be in the neutral radical state $L^{\bullet}$.[41] The acetonitrile molecules are coordinated to the nickel(II) ion with Ni–N bond lengths of 2.071(5), 2.058(5) and 2.037(5) Å, which correlates to previously published values.[53] In the crystal lattice, the $[ReCl_6]^{2-}$ anions are well isolated from each other, being 'encapsulated' by four cations, resulting in a Cl···Cl distance of 4.55 Å along the crystallographic *a*-axis. Short CH···π interactions of 3.6 and 3.8 Å between the methyl group on the radical ligand and pyridyl rings of the neighbouring cation create a 1D network traveling along crystallographic *a*-axis (Figure 5.3.6b and Table 5.3.8). In the crystallographic *ab*-plane, chains of cations order in layers separated by $[ReCl_6]^{2-}$ ions (Figure 5.3.6c). The

acetonitrile molecule of crystallisation is sandwiched between two $[Ni(L^{\bullet})(CH_3CN)_3]^{2+}$ cations in the *ab-plane* (Figure 5.3.6c).

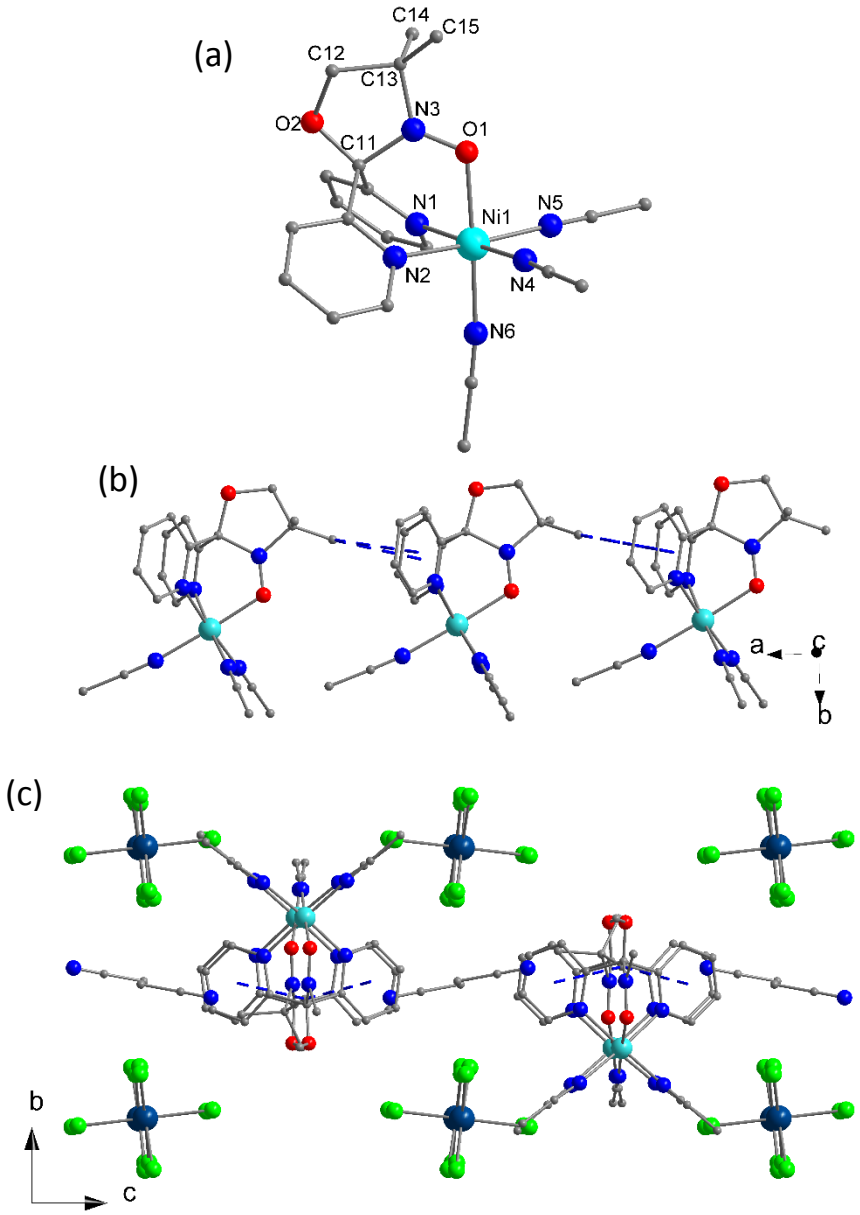

Figure 5.3.6. a) The structure of the $[Ni(L^{\bullet})(CH_3CN)_3]^{2+}$ cation in **5.3a**. b) CH···π interactions between cations in **5.3a**. c) The packing of **5.3a** viewed down the crystallographic *a*-axis. CH···π interactions indicated by blue lines. In a), atoms labelled in accordance with Table 5.3.6. Hydrogen atoms are omitted for clarity. Colour code: Re, dark blue; Ni, cyan; Cl, green; O, red; N, blue; C, grey.

5.3.6 Structure of $[Ni(L^{\bullet})(CH_3CN)_3][ReBr_6]\cdot 3CH_3CN$ (5.3b)

Complex **5.3b** crystallises in the monoclinic space group $P2_1/c$. The asymmetric unit contains a $[Ni(L^{\bullet})(CH_3CN)_3]^{2+}$ cation, one $[ReBr_6]^{2-}$ anion and three solvent acetonitrile molecules (Table 5.3.3). The structure of the $[Ni(L^{\bullet})(CH_3CN)_3]^{2+}$ cation is identical to the one presented in **5.3a** (Figure 5.3.6a), and the $[ReBr_6]^{2-}$ anion is as described in **5.1b**. The sole $L^{\bullet}$ ligand on

the cation has close contacts through the methyl groups to two other ligands' pyridyl moieties, creating a 1D zigzag structure along the crystallographic *a*-axis, as illustrated by figure 5.3.7a. The CH···π interactions between the methyl groups and the two nearest cations are 3.5 and 3.8 Å, which imposes an alternating chain motif. In each chain the radical ligands are facing 'inwards' and the coordinated acetonitrile molecules 'outwards'. The $[ReBr_6]^{2-}$ ions sits in the plane of the Ni^{II} ions between two neighbouring cations (Figure 5.3.7b). The anions are isolated from each other with a short Br···Br distance of 3.9 Å along the direction of the crystallographic *c*-axis creating a 1D network (Table 5.3.8 and Figure 5.3.7c). The cocrystallised acetonitrile molecules are positioned above and below the plane of the cations (Figure 5.3.7b). Although here is presented the structural information on **5.3b** in the monoclinic space group $P2_1/c$ above it must be noted that an alternative solvate is also possible containing a single solvate acetonitrile *per* formula unit. This crystallises in the monoclinic space group $C2/c$ and is formulated as $[Ni(L^{\bullet})(CH_3CN)_3][ReBr_6]\cdot CH_3CN$. The crystal structures, their intermolecular interactions and subsequent magnetic measurements (*vide infra*) of both solvates are similar so only that of the $P2_1/c$ solvate has been reported here.

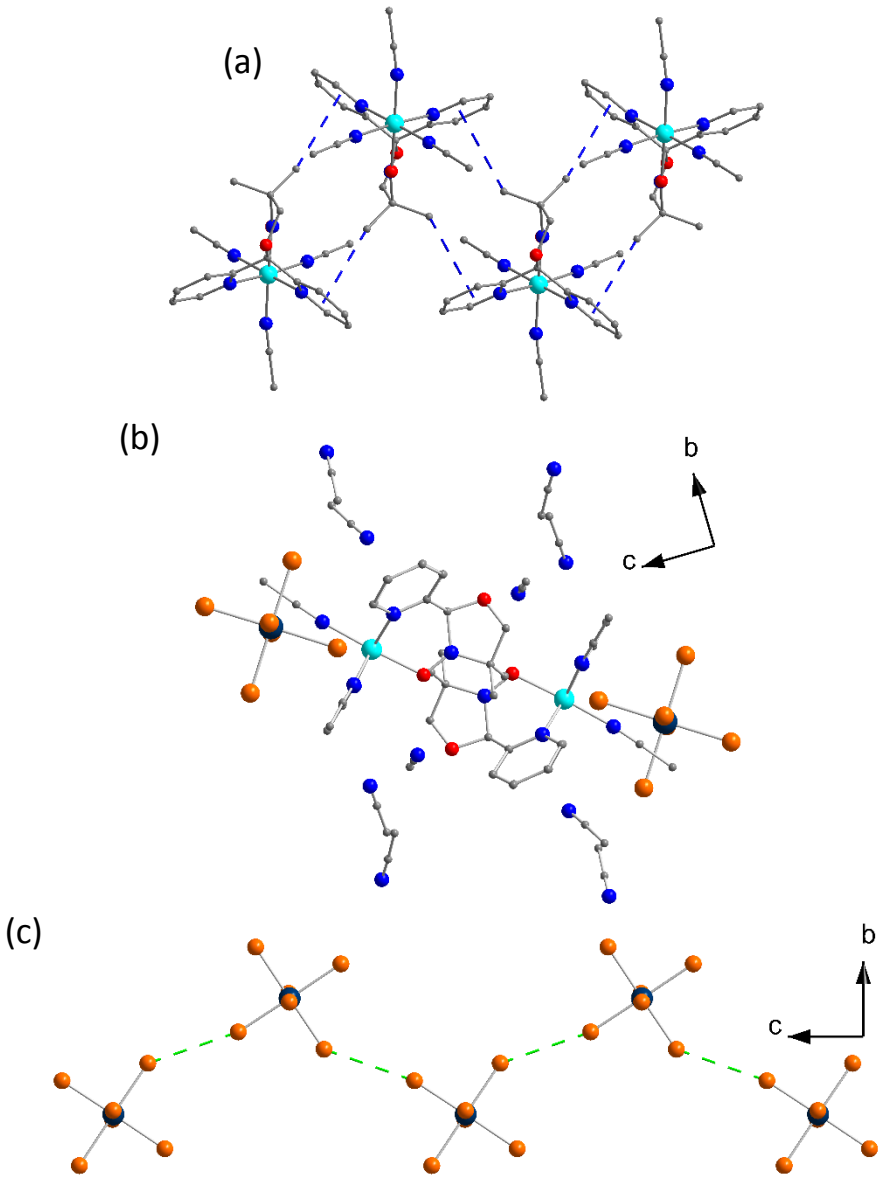

Figure 5.3.7. a) The packing of cations in **5.3b**. b) Crystal packing of **5.3b** viewed down the crystallographic *a*-axis. c) The anions of **5.3b** travelling along the crystallographic *c*-axis. CH···π and Br···Br interactions indicated by blue and green dashed lines, respectively. Hydrogen atoms are omitted for clarity. Colour code: Re, dark blue; Ni, cyan; Br, orange; O, red; N, blue; C, grey.

5.3.7 Structure of $[Cu(L^{\bullet})_2][ReCl_6]$ (5.4a)

Complex **5.4a** crystallises in the triclinic space group $P\bar{1}$ with inversion centres located on the Cu^{II} and Re^{IV} ions with the asymmetric unit containing half the $[Cu(L^{\bullet})_2]^{2+}$ cation and half the $[ReCl_6]^{2-}$ anion (Table 5.3.3). The $[ReCl_6]^{2-}$ anion in **5.4a** is isostructural to the anions described in **5.1a**, **5.2a** and **5.3a** (Tables 5.3.4, 5.3.6 and 5.3.7) and the $[Cu(L^{\bullet})_2]^{2+}$ cation is structurally similar to the cation described in **5.1a** (Figure 5.3.1a). The Cu^{II} ion is six coordinate and sits in a pseudo-Jahn-Teller distorted octahedral environment, with elongation along the O–Cu–O

vector. The Cu–N bond lengths are 2.0135(18) and 2.0116(18) Å, with the Cu–O bond length 2.3021(16) Å (Table 5.3.7). These values are similar those observed in a previously published complex.[40] The *cis* angles vary between 86.31(7) and 93.69(7)° and the *trans* angles are constrained to 180 °. The nitroxide N–O bond length is 1.270(3) Å consistent with the ligand in the neutral radical form. The packing in the crystal is identical to that observed in **5.1a**. The shortest CH···π interactions between the cations are between 3.5-3.8 Å, the shortest Cl···Cl distance is 4.8 Å and the distance of the Cl···π interactions between the $[Cu(L^{\bullet})_2]^{2+}$ and $[ReCl_6]^{2-}$ ions is 3.7 Å (Figure 5.3.2 and Table 5.3.8).

5.3.8 Structure of $[Cu(L^{\bullet})_2][ReBr_6]$ (5.4b)

Complex **5.4b** crystallises in the triclinic space group $P\bar{1}$, with a structure similar to that of **5.4a** (Table 5.3.3). The $[Cu(L^{\bullet})_2]^{2+}$ moiety is isostructural with the cation described in **5.4a**, with the geometrical parameters of the $[ReBr_6]^{2-}$ unit the same as those present in the anion of **5.1b** (Tables 5.3.4 and 5.3.7). In the extended structure the packing of $[Cu(L^{\bullet})_2][ReBr_6]$ is analogous to that described in **5.1b**. The anions display a shortest Br···Br distance of 4.6 Å, with the shortest CH···π interactions being between cations at a distance of approximately 3.6 Å. The Br···π interactions between the $[Cu(L^{\bullet})_2]^{2+}$ cations and $[ReBr_6]^{2-}$ anions are of the order of 3.7 Å (Figure 5.3.2 and Table 5.3.8).

5.3.9 Tables of crystallographic and structural parameters

Table 5.3.1. Crystallographic data for **5.1a**, **5.1b**, **5.2a** and **5.2a**·150 K.

	5.1a	**5.1b**	**5.2a**	**5.2a**·150 K
Crystal data				
Chemical formula	$Cl_6Re\cdot C_{30}H_{32}FeN_6O_4$	$Br_6Re\cdot C_{30}H_{32}FeN_6O_4$	$Cl_6Re\cdot C_{30}H_{32}CoN_6O_4 \cdot 2(C_2H_3N)$	$Cl_6Re\cdot C_{30}H_{32}CoN_6O_4 \cdot 4(C_2H_3N)$
M_r	995.36	1262.12	1080.55	1162.66
Crystal system, space group	Triclinic, $P\bar{1}$	Triclinic, $P\bar{1}$	Triclinic, $P\bar{1}$	Monoclinic, $P2_1/c$
Temperature (K)	120	120	120	150
a,	7.9831 (3),	8.0539 (4),	8.09457 (16),	13.5159 (6),
b,	10.5052 (5),	10.6650 (6),	10.9775 (2),	11.1140 (4),
c (Å)	10.7890 (4)	11.0535 (7)	11.5719 (3)	15.7455 (8)
α,	106.255 (4),	105.576 (5),	80.2539 (19),	90,
β,	103.909 (3),	101.890 (5),	78.1007 (19),	110.854 (5),
γ (°)	92.852 (3)	93.681 (4)	88.8645 (16)	90
V (Å^3)	836.49 (6)	887.72 (9)	991.53 (4)	2210.29 (18)
Z	1	1	1	2
Radiation type	Mo $K\alpha$	Mo $K\alpha$	Mo $K\alpha$	Mo $K\alpha$
μ (mm^{-1})	4.58	10.61	3.92	3.53
Crystal size (mm)	0.16 × 0.10 × 0.03	0.20 × 0.09 × 0.03	0.30 × 0.11 × 0.08	0.42 × 0.25 × 0.08
Data collection				
T_{min}, T_{max}	0.618, 0.875	0.299, 0.758	0.467, 0.750	0.269, 0.432
No. of measured, independent and observed [$I > 2\sigma(I)$] reflections	13462, 3822, 3586	15756, 4460, 3685	36771, 10126, 9918	36387, 5419, 4361
R_{int}	0.050	0.071	0.032	0.062
$(\sin\theta/\lambda)_{max}$ (Å^{-1})	0.677	0.698	0.859	0.667
Refinement				
$R[F^2 > 2\sigma(F^2)]$, $wR(F^2)$, S	0.034, 0.058, 1.05	0.049, 0.088, 1.07	0.022, 0.046, 1.03	0.070, 0.131, 1.29
No. of reflections	3822	4460	10126	5419
No. of parameters	232	222	260	278
No. of restraints	0	0	0	18
$\Delta\rho_{max}$, $\Delta\rho_{min}$ (e Å^{-3})	1.14, −0.77	2.01, −1.89	0.77, −0.73	2.29, −0.88

Table 5.3.2. Crystallographic data for **5.2a**·200 K, **5.2a**·250 K and **5.2b**.

	5.2a·200 K	**5.2a**·250 K	**5.2b**
Crystal data			
Chemical formula	$Cl_6Re{\cdot}C_{30}H_{32}CoN_6O_4{\cdot}4(C_2H_3N)$	$Cl_6Re{\cdot}C_{30}H_{32}CoN_6O_4{\cdot}4(C_2H_3N)$	$Br_6Re{\cdot}C_{30}H_{32}CoN_6O_4$
M_r	1162.66	1162.66	1265.20
Crystal system, space group	Monoclinic, $P2_1/c$	Monoclinic, $P2_1/c$	Triclinic, $P\bar{1}$
Temperature (K)	200	250	120
a,	13.5101 (6),	13.4707 (5),	8.1009 (3),
b,	11.2475 (4),	11.3978 (3),	10.7229 (3),
c (Å)	15.7037 (7)	15.6234 (6)	10.9708 (3)
α,	90,	90,	106.156 (3),
β,	110.536 (5),	110.044 (4),	101.328 (3),
γ (°)	90	90	93.673 (3)
V (Å^3)	2234.61 (17)	2253.47 (14)	890.36 (5)
Z	2	2	1
Radiation type	Mo $K\alpha$	Mo $K\alpha$	Cu $K\alpha$
μ (mm^{-1})	3.49	3.46	18.46
Crystal size (mm)	× 0.25 × 0.08	0.42 × 0.25 × 0.08	0.10 × 0.05 × 0.03
Data collection			
T_{min}, T_{max}	0.446, 0.933	0.278, 0.432	0.468, 0.764
No. of measured, independent and observed [$I > 2\sigma(I)$] reflections	37200, 5470, 4247	39338, 5538, 4097	18116, 3700, 3462
R_{int}	0.063	0.051	0.072
$(\sin\theta/\lambda)_{max}$ (Å^{-1})	0.667	0.667	0.629
Refinement			
$R[F^2 > 2\sigma(F^2)]$, $wR(F^2)$, S	0.071, 0.129, 1.28	0.048, 0.113, 1.12	0.042, 0.110, 1.05
No. of reflections	5470	5538	3700
No. of parameters	278	278	222
No. of restraints	18	18	0
$\Delta\rho_{max}$, $\Delta\rho_{min}$ (e Å^{-3})	2.20, −0.85	0.92, −0.72	1.31, −1.77

Table 5.3.3. Crystallographic data for **5.3a**, **5.3b**, **5.4a** and **5.4b**.

	5.3a	**5.3b**	**5.4a**	**5.4b**
Crystal data				
Chemical formula	$Cl_6Re{\cdot}C_{21}H_{25}N_6NiO_2$ $\cdot C_2H_3N$	$Br_6Re{\cdot}C_{21}H_{25}N_6NiO_2$ $\cdot 3(C_2H_3N)$	$Cl_6Re{\cdot}$ $C_{30}H_{32}CuN_6O_4$	$Br_6Re{\cdot}$ $C_{30}H_{32}CuN_6O_4$
M_r	892.13	1241.00	1003.05	1269.81
Crystal system, space group	Orthorhombic, *Pbca*	Monoclinic, $P2_1/c$	Triclinic, $P\bar{1}$	Triclinic, $P\bar{1}$
Temperature (K)	120	120	120	120
a,	16.0287 (5),	11.3999 (4),	8.0389 (2),	8.0732 (2),
b,	18.8615 (4),	23.9868 (8),	10.6038 (3),	10.8110 (4),
c (Å)	22.0793 (5)	14.3655 (6)	10.8240 (3)	11.0629 (4)
α,	90,	90,	107.565 (3),	107.144 (3),
β,	90,	91.166 (3),	102.333 (2),	100.370 (2),
γ (°)	90	90	93.278 (2)	93.917 (2)
V (Å^3)	6675.1 (3)	3927.4 (3)	851.99 (5)	899.99 (5)
Z	8	4	1	1
Radiation type	Mo *K*α	Mo *K*α	Cu *K*α	Mo *K*α
μ (mm^{-1})	4.70	9.70	12.33	10.66
Crystal size (mm)	0.32 × 0.11 × 0.09	0.30 × 0.13 × 0.12	0.18 × 0.11 × 0.03	0.32 × 0.12 × 0.02
Data collection				
T_{min}, T_{max}	0.852, 1.000	1.000, 1.000	0.343, 1.000	0.198, 0.778
No. of measured, independent and observed [$I > 2\sigma(I)$] reflections	78703, 6101, 5071	61149, 9632, 6105	13972, 3525, 3495	47495, 5554, 4607
R_{int}	0.074	0.083	0.033	0.146
$(\sin\theta/\lambda)_{max}$ (Å^{-1})	0.602	0.728	0.630	0.728
Refinement				
$R[F^2 > 2\sigma(F^2)]$, $wR(F^2)$, S	0.050, 0.076, 1.21	0.041, 0.078, 0.92	0.020, 0.050, 1.04	0.054, 0.138, 1.03
No. of reflections	6101	9632	3525	5554
No. of parameters	367	423	243	222
No. of restraints	0	0	0	0
$\Delta\rho_{max}$, $\Delta\rho_{min}$ (e Å^{-3})	0.80, −0.67	2.69, −1.60	0.97, −1.10	3.10, −3.42

Table 5.3.4. Selected bond lengths (Å) and angles (°) for **5.1a**, **5.1b**, **5.2a**, **5.2a**·150 K, **5.2a**·200 K and **5.2a**·250 K.

	5.1a (M=Fe)	**5.1b** (M=Fe)	**5.2a** (M=Co)	**5.2a**·150 K	**5.2a**·200 K	**5.2a**·250 K
Re(1)–Cl(1)	2.3602(9)	-	2.3590(3)	2.3631(17)	2.3639(18)	2.3642(14)
Re(1)–Cl(2)	2.3748(9)	-	2.3714(3)	2.3585(17)	2.3441(19)	2.3435(13)
Re(1)–Cl(3)	2.3547(8)	-	2.3676(3)	2.3427(19)	2.3586(17)	2.3587(15)
Re(1)–Br(1)	-	2.5132(6)	-	-	-	-
Re(1)–Br(2)	-	2.5029(6)	-	-	-	-
Re(1)–Br(3)	-	2.5249(6)	-	-	-	-
M(1)–O(1)	1.872(2)	1.873(4)	1.9103(10)	2.144(5)	2.121(5)	2.093(4)
M(1)–N(1)	1.984(3)	1.963(5)	1.9251(11)	1.978(6)	1.997(6)	2.031(4)
M(1)–N(2)	1.967(3)	1.991(5)	1.9556(10)	1.963(6)	2.018(6)	2.049(4)
O(1)–N(3)	1.323(3)	1.316(6)	1.3137(16)	1.290(8)	1.295(8)	1.305(5)
N(3)–C(11)	1.478(5)	1.472(7)	1.4786(18)	1.466(9)	1.462(9)	1.467(7)
N(3)–C(13)	1.486(5)	1.499(7)	1.471(2)	1.484(9)	1.470(9)	1.466(7)
C(11)–O(2)	1.385(4)	1.396(7)	1.3973(16)	1.412(9)	1.406(8)	1.405(6)
O(2)–C(12)	1.443(12)	1.456(7)	1.4535(18)	1.431(10)	1.415(10)	1.414(8)
C(12)–C(13)	1.547(14)	1.530(9)	1.528(2)	1.549(12)	1.560(13)	1.529(10)
C(13)–C(14)	1.513(6)	1.504(8)	1.520(2)	1.508(13)	1.522(14)	1.511(11)
C(13)–C(15)	1.508(6)	1.536(8)	1.519(2)	1.521(12)	1.505(14)	1.499(11)
Cl(1)–Re(1)–Cl(2)	89.74(3)	-	89.513(13)	90.15(6)	89.91(10)	90.18(6)
Cl(1)–Re(1)–Cl(3)	90.18(3)	-	90.909(13)	89.87(8)	89.78(6)	89.78(5)
Cl(2)–Re(1)–Cl(3)	89.73(3)	-	89.184(12)	90.34(9)	89.64(10)	89.40(7)
Br(1)–Re(1)–Br(2)	-	90.38(2)	-	-	-	-
Br(1)–Re(1)–Br(3)	-	90.19(2)	-	-	-	-
Br(2)–Re(1)–Br(3)	-	89.79(2)	-	-	-	-
M(1)–O(1)–N(3)	118.31(19)	117.9(3)	113.99(9)	113.5(4)	114.5(4)	115.1(3)
M(1)–O(1)–N(3)–C(11)	13.8(3)	-14.9(5)	-29.26(11)	5.0(5)	-3.7(5)	-2.4(6)
M(1)–O(1)–N(3)–C(13)	155.3(2)	-157.3(4)	-168.87(10)	168.6(5)	-169.5(5)	-170.8(4)

Table 5.3.5. Selected bond lengths (Å) and angles (°) for **5.2b**.

	5.2b
Re(1)–Br(1)	2.5107(5)
Re(1)–Br(2)	2.5226(5)
Re(1)–Br(3)	2.5049(5)
Co(1)−O(1)	2.092(4)
Co(1)−N(1)	1.963(4)
Co(1)−N(2)	1.975(4)
O(1)−N(3)	1.269(6)
N(3)−C(11)	1.485(7)
N(3)−C(13)	1.493(7)
C(11)−O(2)	1.399(6)
O(2)−C(12)	1.412(8)
C(12)−C(13)	1.539(9)
C(13)−C(14)	1.525(8)
C(13)−C(15)	1.518(9)
Br(1)−Re(1)–Br(2)	90.148(17)
Br(1)−Re(1)–Br(3)	90.211(17)
Br(2)−Re(1)–Br(3)	89.856(18)
Co(1)−O(1)−N(3)	113.9(3)
Co(1)−O(1)−N(3)−C(11)	-5.9(4)
Co(1)−O(1)−N(3)−C(13)	-157.1(4)

Table 5.3.6. Selected bond lengths (Å) and angles (°) for **5.3a** and **5.3b**.

5.3a		**5.3b**	
Re(1)–Cl(1)	2.3585(15)	Re(1)–Br(1)	2.5087(5)
Re(1)–Cl(2)	2.3616(13)	Re(1)–Br(2)	2.5124(6)
Re(1)–Cl(3)	2.3546(15)	Re(1)–Br(3)	2.5072(5)
Re(1)–Cl(4)	2.3630(13)	Re(1)–Br(4)	2.5147(7)
Re(1)–Cl(5)	2.3606(16)	Re(1)–Br(5)	2.5008(6)
Re(1)–Cl(6)	2.3603(15)	Re(1)–Br(6)	2.5208(6)
Ni(1)–O(1)	2.073(4)	Ni(1)–O(1)	2.090(4)
Ni(1)–N(1)	2.068(4)	Ni(1)–N(1)	2.083(4)
Ni(1)–N(2)	2.059(4)	Ni(1)–N(2)	2.076(4)
Ni(1)–N(4)	2.071(5)	Ni(1)–N(4)	2.051(4)
Ni(1)–N(5)	2.058(5)	Ni(1)–N(5)	2.079(4)
Ni(1)–N(6)	2.037(5)	Ni(1)–N(6)	2.047(5)
O(1)–N(3)	1.271(6)	O(1)–N(3)	1.274(6)
N(3)–C(11)	1.496(7)	N(3)–C(11)	1.497(7)
N(3)–C(13)	1.481(7)	N(3)–C(13)	1.467(7)
C(11)–O(2)	1.403(6)	C(11)–O(2)	1.386(7)
O(2)–C(12)	1.452(7)	O(2)–C(12)	1.460(7)
C(12)–C(13)	1.527(8)	C(12)–C(13)	1.512(8)
C(13)–C(14)	1.523(8)	C(13)–C(14)	1.530(7)
C(13)–C(15)	1.509(8)	C(13)–C(15)	1.529(7)
Ni(1)–O(1)–N(3)	115.3(3)	Ni(1)–O(1)–N(3)	115.1(3)
Ni(1)–O(1)–N(3)–C(11)	-4.1(6)	Ni(1)–O(1)–N(3)–C(11)	3.45427(16)
Ni(1)–O(1)–N(3)–C(13)	-172.2(4)	Ni(1)–O(1)–N(3)–C(13)	-173.4135(3)

Table 5.3.7. Selected bond lengths (Å) and angles (°) for **5.4a** and **5.4b**.

	5.4a	**5.4b**
Re(1)–Cl(1)	2.3578(5)	-
Re(1)–Cl(2)	2.3727(5)	-
Re(1)–Cl(3)	2.3583(5)	-
Re(1)–Br(1)	-	2.5103(6)
Re(1)–Br(2)	-	2.5082(6)
Re(1)–Br(3)	-	2.5224(6)
Cu(1)−O(1)	2.3021(16)	2.321(5)
Cu(1)−N(1)	2.0135(18)	2.017(5)
Cu(1)−N(2)	2.0116(18)	2.014(5)
O(1)−N(3)	1.270(3)	1.266(7)
N(3)−C(11)	1.491(3)	1.487(8)
N(3)−C(13)	1.485(3)	1.487(8)
C(11)−O(2)	1.392(3)	1.400(8)
O(2)−C(12)	1.463(6)	1.414(9)
C(12)−C(13)	1.492(6)	1.536(11)
C(13)−C(14)	1.433(8)	1.524(11)
C(13)−C(15)	1.506(3)	1.513(10)
Cl(1)−Re(1)–Cl(2)	90.96(2)	-
Cl(1)−Re(1)–Cl(3)	90.135(18)	-
Cl(2)−Re(1)–Cl(3)	89.799(19)	-
Br(1)−Re(1)–Br(2)	-	90.08(2)
Br(1)−Re(1)–Br(3)	-	90.52(2)
Br(2)−Re(1)–Br(3)	-	89.85(2)
Cu(1)−O(1)−N(3)	110.96(13)	110.6(4)
Cu(1)−O(1)−N(3)−C(11)	0.67(16)	-2.0(5)
Cu(1)−O(1)−N(3)−C(13)	-155.94(14)	-160.5(4)

Table 5.3.8. Intermolecular distances (Å) and angles (°) found in all complexes. CH···π angles (θ) are taken from angle between the plane of the ring and the C-H bond while CH···π distances (d) are from the carbon of the CH moiety to the centroid of the ring.

Complex	CH···π		Cl···π	Br···π	Br···O	Cl···Cl	Br···Br
	θ(°)	d (Å)	d (Å)	d (Å)	d (Å)	d (Å)	d (Å)
5.1a	111.6	3.495	3.688	-	-	4.708	-
	133.1	3.759	-	-	-	-	-
5.1b	131.1	3.681	-	3.783	-	-	4.569
	115.6	3.619	-	-	-	-	-
5.2a	127.5	3.912	-	-	-	3.831	-
	120.9	3.388	-	-	-	-	-
5.2a·150K	-	-	-	-	-	6.455	-
5.2a·200K	-	-	-	-	-	6.572	-
5.2a·250K	-	-	-	-	-	6.715	-
5.2b	114.0	3.613	-	3.791	-	-	4.615
	134.9	3.703	-	-	-	-	-
5.3a	123.0	3.786	-	-	-	4.548	-
	114.2	3.575	-	-	-	-	-
5.3b	129.2	3.812	-	-	-	-	3.907
	124.5	3.485	-	-	-	-	-
5.4a	134.5	3.839	3.645	-	-	4.770	-
	108.1	3.504	-	-	-	-	-
5.4b	128.1	3.702	-	3.714	-	-	4.578
	112.8	3.608	-	-	-	-	-

Table 5.3.9. Selected bond lengths (Å) for **5.2a**, **5.2a**·150 K, **5.2a**·200 K, **5.2a**·250 K, **5.2b**, $[Co^{II}(L^{\bullet})_2](NO_3)_2$ (**A**),[42] $[Co^{III}(L^{-})_2](BPh_4)$ (**B**),[42] $[Co^{II}(L^{\bullet})_2](B(C_6F_5)_4)_2{\cdot}CH_2Cl_2$ (**C**)[44] and $[Co^{II}(L^{\bullet})_2](B(C_6F_5)_4)_2{\cdot}2Et_2O$ (**D**)[44] at temperatures shown. Low-spin (LS), high spin (HS), neutral radical ($L^{\bullet}$) and hydroxylamino anionic (L^{-}) assigned forms of the cobalt ion and the ligand are shown in the table below. See Figure 5.3.1 for labelling of atoms.

	5.2a	**5.2a**·150 K	**5.2a**·200 K	**5.2a**·250 K	**5.2b**
Co spin state	LS Co(II)	LS Co(II)	LS/HS	LS/HS	LS Co(II)
Co(1)-O(1)	1.9103(10)	2.144(5)	2.121(5)	2.093(4)	2.092(4)
Co(1)-N(1)	1.9556(10)	1.978(6)	1.997(6)	2.031(4)	1.963(4)
Co(1)-N(2)	1.9251(11)	1.963(6)	2.018(6)	2.049(4)	1.976(4)
Ligand form	$L^{\bullet}$	$L^{\bullet}$	$L^{\bullet}$	$L^{\bullet}$	$L^{\bullet}$
O(1)-N(3)	1.3137(16)	1.290(8)	1.295(8)	1.305(5)	1.269(6)
O(3)-N(6)	-	-	-	-	-
	A·123 K	**A**·273 K	**A**·353 K	**B**·123 K	**C**·123 K
Co spin state	LS Co(II)	LS/HS	LS/HS	LS Co(III)	LS Co(II)
Co(1)-O(1)	2.113(3)	2.117(2)	2.107(3)	1.879(2)	2.117(2)
Co(1)-N(1)	1.959(3)	2.040(2)	2.056(3)	1.930(3)	1.977(2)
Co(1)-N(2)	1.986(3)	2.056(2)	2.073(43)	1.928(3)	1.981(2)
Co(1)-O(3)	-	-	-	1.892(2)	2.126(2)
Co(1)-N(4)	-	-	-	1.921(3)	1.987(2)
Co(1)-N(5)	-	-	-	1.916(3)	1.992(2)
Ligand form	$L^{\bullet}$	$L^{\bullet}$	$L^{\bullet}$	Anionic	$L^{\bullet}$
O(1)-N(3)	1.294(3)	1.285(3)	1.285(4)	1.411(3)	1.274(3)
O(3)-N(6)	-	-	-	1.401(3)	1.276(3)

	C·273 K	**D**·123 K	**D**·273 K
Co spin state	HS Co(II)	HS Co(II)	HS Co(II)
Co(1)-O(1)	2.078(3)	2.054(2)	2.075(2)
Co(1)-N(1)	2.078(4)	2.114(3)	2.098(3)
Co(1)-N(2)	2.084(3)	2.116(3)	2.107(3)
Co(1)-O(3)	2.086(3)	-	-
Co(1)-N(4)	2.093(3)	-	-
Co(1)-N(5)	2.090(3)	-	-
Ligand form	$L^{\bullet}$	$L^{\bullet}$	$L^{\bullet}$
O(1)-N(3)	1.275(4)	1.286(4)	1.290(3)
O(3)-N(6)	1.278(4)	-	-

Table 5.3.10. Summary of selected octahedral nickel salts containing three coordinated acetonitrile solvate molecules. The loss of coordinated acetonitrile is based on the microanalysis of the relevant complex.

Formula	Loss of coordinated acetonitrile	Reference
$[\{Ni(CH_3CN)_3\}_2\{Ni(\mu\text{-}2\text{-}pyS)(\mu_3\text{-}2\text{-}pyS)\}_6](PF_6)_4$	No	[54]
$[Ni(L^1)(CH_3CN)_3](ClO_4)_2{\cdot}2CH_3CN$	No	[55]
$[Tpm^{Me,Me}Ni(CH_3CN)_3](BF_4)_2$	Yes	[56]
$[Tpm^{Ph}Ni(CH_3CN)_3](BF_4)_2{\cdot}CH_3CN$	No	[56]
$[Ni\{(Me\text{-}Tp)_2PMA\}(CH_3CN)_3](ClO_4)_2$	No	[57]
$[Ni(P^{tBu}{}_2N^{Ph}{}_2)(CH_3CN)_3](BF_4)_2$	No	[58]
$[Ni(L)(CH_3CN)_3](ClO_4)_2{\cdot}0.5H_2O$	No	[59]
$[Ni(L1)(CH_3CN)_3](ClO_4)_2{\cdot}2CH_3CN$	No	[53]
$[Ni(L2)(CH_3CN)_3](ClO_4)_2{\cdot}2CH_3CN$	No	[53]
$[Ni(L3)(CH_3CN)_3](BF_4)_2$	No	[60]
$[Ni(L4)(CH_3CN)_3](BF_4)_2$	No	[60]
$[Tp^{iPr}{}_2Ni(CH_3CN)_3]OTf$	Yes	[61]
$[Tp^{Ph,Me}Ni(CH_3CN)_3]OTf$	No	[61]

Abbreviations: pyS = 2-mercaptopyridinate; L^1 = $N_2O_2S_2$ macrocycle; $Tpm^{Me,Me}$ = tris(3,5-dimethylpyrazol-1-yl)methane; Tpm^{Ph} = tris(3-phenylpyrazol-1-yl)methane; $(Me\text{-}Tp)_2PMA$ = bis(5-methyl-2-thiophenemethyl)(2-pyridylmethyl)amine; $P^{tBu}{}_2N^{Ph}{}_2$ and $P^{tBu}{}_2N^{Bz}{}_2$ = cyclic diphosphine; L = 1,4,7-tris(cyanomethyl)-1,4,7-triazacyclononane; L1 = bis(1-methylbenzimidazolyl-2-methyl)amine; L2 = bis(1-methylbenzimidazolyl-2-methyl)-10-camphorsulfonamide; L3 = 1,3,5-tribenzyl-1,3,5-triazinane; L4 = 1,3,5-tris(2-fluorobenzyl)-1,3,5-triazinane; $Tp^R{}_2$ = hydrotrispyrazolylborato with R group shown.

5.4 Magnetic properties

5.4.1 Magnetic properties of $[Fe(L^{\bullet})_2][ReCl_6]$ (5.1a) and $[Fe(L^{\bullet})_2][ReBr_6]$ (5.1b)

The $\chi_M T$ value for complex **5.1a** at T = 300 K is 1.96 $cm^3\ mol^{-1}$ K, which is in the range expected with contributions of ~1.52-1.69 $cm^3\ mol^{-1}$ K from a magnetically isolated $[ReCl_6]^{2-}$ anion (assuming g = 1.8-1.9 and S = 3/2) and the previously published value of *circa* 0.16 $cm^3\ mol^{-1}$ K for the $[Fe(L^{\bullet})_2]^{2+}$ unit (Figure 5.4.1a).[41] The $\chi_M T$ value decreases to a value of 1.82 $cm^3\ mol^{-1}$ K as the temperature is lowered until T = 150 K after which a slow decline is observed with the $\chi_M T$ value reaching 1.70 $cm^3\ mol^{-1}$ K at T = 40 K (Figure 5.4.1a). A second decrease initiates at T = 40 K attributed to the Zeeman splitting and zero-field splitting of the S = 3/2 state of the anisotropic $[ReCl_6]^{2-}$ unit. At T = 2 K the $\chi_M T$ value reaches 0.96 $cm^3\ mol^{-1}$ K which corresponds to the value of an isolated $[ReCl_6]^{2-}$ ion.[20] The decrease in the $\chi_M T$ values over the temperature range, T = 150-300 K, is likely to be caused by a large antiferromagnetic radical-radical coupling in the $[Fe(L^{\bullet})_2]^{2+}$ cation as reported previously.[41] This is likely to be of a similar magnitude to the previously reported compound, $[Fe(L^{\bullet})_2](BF_4)_2$ where $J_{rad\text{-}rad}$ = -315 cm^{-1} using the spin Hamiltonian $\hat{H} = -2J\hat{S}_1\hat{S}_2$.[41]

For complex **5.1b** the $\chi_M T$ value at T = 300 K is 2.02 $cm^3\ mol^{-1}$ K which is slightly greater than the value observed in the related compound **5.1a** but with a magnetic behaviour similar to that observed for **5.1a** (Figure 5.4.1a). As the temperature is lowered the $\chi_M T$ value exhibits a minor decrease until around T = 50 K after which it drops. At T = 2 K the $\chi_M T$ value is 0.56 $cm^3\ mol^{-1}$ K which is lower than the expected value of *ca*. 1 $cm^3\ mol^{-1}$ K for an isolated $[ReBr_6]^{2-}$ anion, indicative of minute antiferromagnetic exchange interactions.[12] The plot of χ_M *versus* T for **5.1a** and **5.1b** is shown in Figure 5.4.1b and there is no evidence of any intermolecular interactions in **5.1a** or **5.1b** having a significant contribution to the molar magnetic susceptibility.

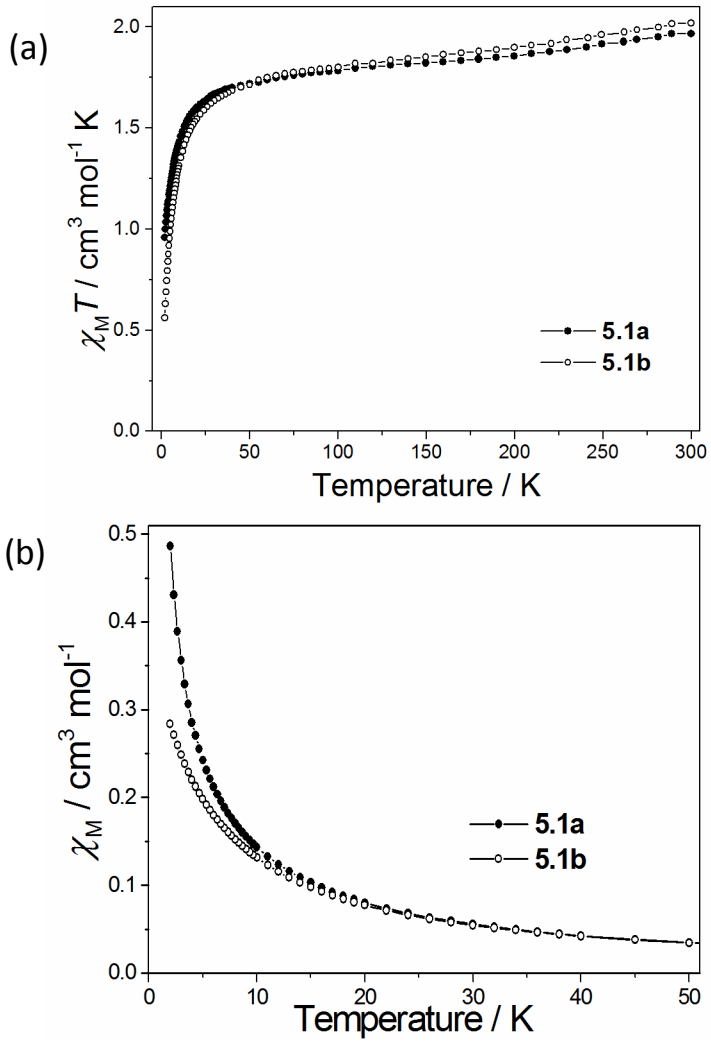

Figure 5.4.1. a) The $\chi_M T$ *versus* T plot for compounds **5.1a** and **5.1b**. b) The χ_M *vs*. T plot for **5.1a** and **5.1b**. The solid lines are guides to the eye.

5.4.2 Magnetic properties of $[Co(L^{\bullet})_2][ReCl_6]$ (5.2a) and $[Co(L^{\bullet})_2][ReBr_6]$ (5.2b)

For complex **5.2a** the $\chi_M T$ value at T = 300 K is 3.01 cm^3 mol^{-1} K which correlates to the range of possible room temperature $\chi_M T$ values previously published for the $[Co(L^{\bullet})_2]^{2+}$ and $[ReCl_6]^{2-}$ ions.[20, 42, 44] In the temperature range from T = 300 to 30 K the $\chi_M T$ value decrease almost linearly as the sample is cooled (Figure 5.4.2a). A sharp decrease in the $\chi_M T$ value appears as the temperature is lowered from T = 30 K resulting in a final $\chi_M T$ value of 1.75 cm^3 mol^{-1} K at T = 2K. Structural studies reveal a low-spin Co^{II} ion flanked by two neutral radical ligands and variable temperature crystallographic measurements show that this undergoes a gradual spin-crossover transition (Figure 5.3.5). Although these structural studies were on solvated samples and the magnetic measurements are on solvate free material it is likely that the

decrease in the $\chi_M T$ value from T = 300 to 30 K is due to a combination of a gradual spin-crossover transition and antiferromagnetic exchange interactions between the radical ligands and the central Co^{II} ion, as seen previously.[42] The sharp low temperature downturn below T = 30 K in the $\chi_M T$ value is caused by the Zeeman and zero-field splitting of the $[Co(L^{\bullet})_2]^{2+}$ and $[ReCl_6]^{2-}$ ions. There is no evidence of any intermolecular contributions to the magnetic susceptibility at low temperatures and the plot of χ_M *versus* T for **5.2a** can be seen in Figure 5.4.2b.

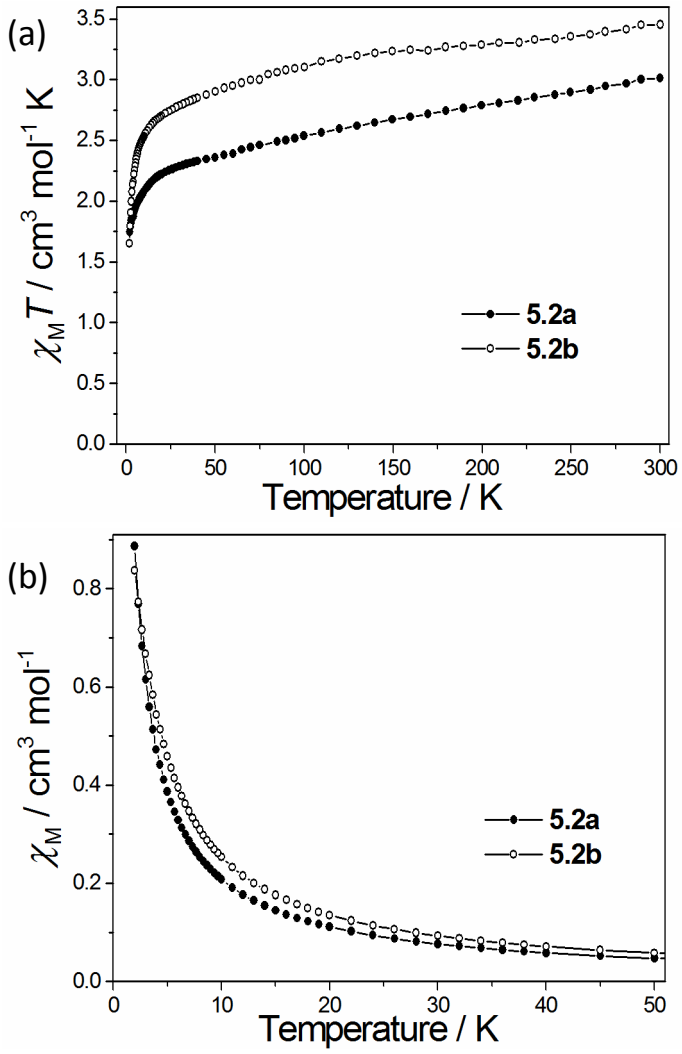

Figure 5.4.2. a) The $\chi_M T$ versus T plot for compounds **5.2a** and **5.2b**. b) The χ_M *vs*. T plot for **5.2a** and **5.2b**. The solid lines are guides to the eye

For complex **5.2b** at T = 300 K the $\chi_M T$ value of 3.45 cm^3 mol^{-1} K is in the range of the expected $\chi_M T$ values previously published of 1.57-1.87 cm^3 mol^{-1} K for the $[Co(L^{\bullet})_2]^{2+}$ cation and 1.59 cm^3 mol^{-1} K for the $[ReBr_6]^{2-}$ anion (Figure 5.4.2a).[44] A constant decrease in $\chi_M T$ value is observed as the temperature is lowered with a sharp downturn beginning at T = 30 K. The structure revealed a pseudo-Jahn-Teller axial elongation indicative of a low-spin Co^{II} ion at T

= 120 K. The decrease in $\chi_M T$ value from T = 300 to 30 K is likely due to a gradual spin-crossover transition of the Co^{II} ion, as well as, antiferromagnetic coupling between the Co^{II} ions and the two radical ligands as seen in **5.2a** and previously published results.[42, 44] Upon further cooling below T = 30 K the $\chi_M T$ value reaches a final value of 1.65 cm^3 mol^{-1} K at T = 2 K. In the above description it was assumed that the $[ReBr_6]^{2-}$ anion is magnetically isolated. The plot of χ_M *versus* T for **5.2b** is shown in Figure 5.3.2b with no indication of any significant intermolecular magnetic interactions.

5.4.3 Magnetic properties of $[Ni(L^{\bullet})(CH_3CN)_3][ReCl_6]\cdot CH_3CN$ (5.3a) and $[Ni(L^{\bullet})(CH_3CN)_3][ReBr_6]\cdot 3CH_3CN$ (5.3b)

The crystals of complex **5.3a** and **5.3b** were prone to solvent loss and therefore measured in both the dried form (**5.3a(dried)** and **5.3b(dried)**) and fully solvated (**5.3a(solvated)** and **5.3b(solvated)**). The dried form consisted of crystals that had been left in an open vial for three to five days causing a change in colour; from brown to green for **5.3a(dried)** and from brown to yellow for **5.3b(dried)**. The solvated susceptibility measurement was done on a sample of freshly prepared and collected crystals suspended in acetonitrile. Powder X-ray diffraction (PXRD) measurements on the fully solvated samples, **5.3a(solvated)** and **5.3b(solvated)**, are in strong agreement with the calculated patterns obtained from the relevant crystal structures confirming the phase purity in the magnetic measurements of the solvated samples (Figure 5.4.3a and b).

Unsurprisingly similar X-ray powder diffraction measurements on the dried samples, **5.3a(dried)** and **5.3b(dried)**, and their comparison with calculated patterns based on their respective crystal structures, indicate that the dried samples are in a different crystallographic phase to that present in the crystal structures (Figure 5.4.3c and d).

According to the microanalysis and IR spectra air dried crystals of complex **5.3a** analysed as $[Ni(L^{\bullet})(H_2O)_3][ReCl_6]$ (**5.3a(dried)**) and not $[Ni(L^{\bullet})(CH_3CN)_3][ReCl_6]\cdot CH_3CN$ (**5.3a**) as shown in the crystal structure (Figure 5.4.4a). This is perhaps unsurprising given the labile nature of coordinated acetonitrile and the fact the samples were left open to air before analysis. Loss of coordinated acetonitrile has been seen previously in the octahedral nickel complexes $[Tpm^{Me,Me}Ni(CH_3CN)_3](BF_4)_2$,[56] and $[Tp^R{}_2Ni(CH_3CN)_3]OTf$,[61] where $Tpm^{Me,Me}$ = tris(3,5-dimethylpyrazol-1-yl)methane and $Tp^R{}_2$ = hydrotrispyrazolyl borato with R = 3,5-iPr_2.

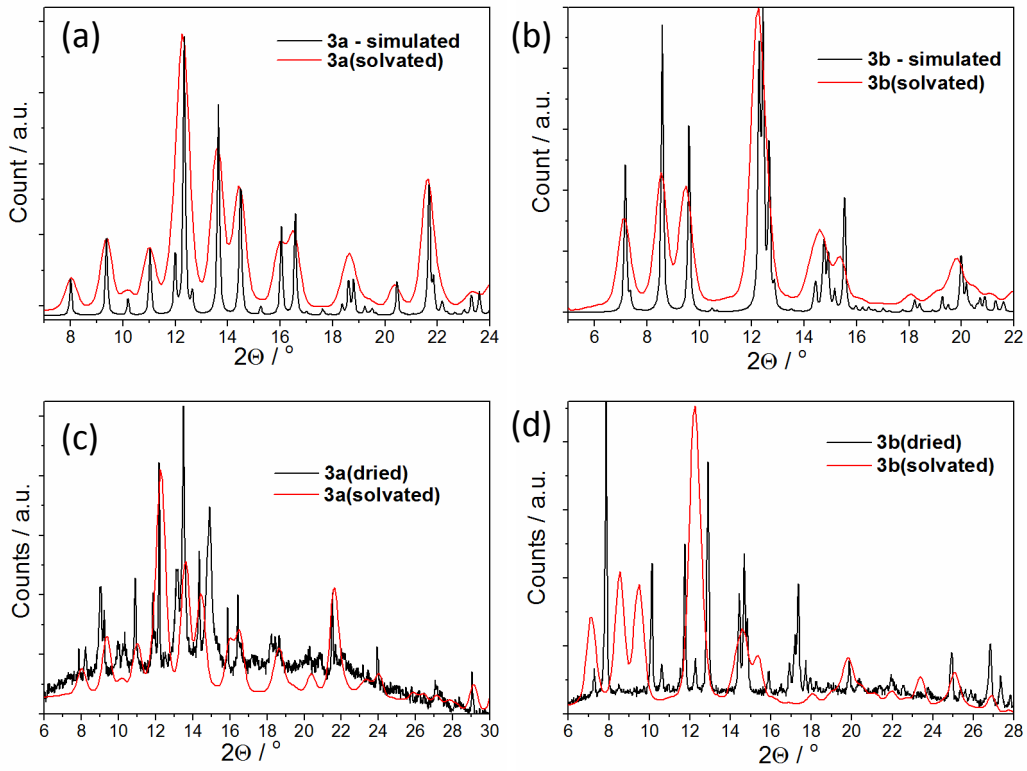

Figure 5.4.3. PXRD experiments of solvated samples *versus* simulated diffraction patterns for **5.3a** (a) and **5.3b** (b). PXRD diffraction patterns of the dried and solvated samples of **5.3a** and **5.3b**, c) and d), respectively.

However, the majority of octahedral nickel complexes containing three coordinated acetonitrile molecules seem to be stable upon drying and no dissociation occurs (Table 5.3.10).

Based on the following magnetism discussion it is clear that the neutral radical ligand remains coordinated to the Ni^{II} ion and the microanalysis suggests the three coordinated acetonitrile molecules have dissociated and three water molecules are present, as also observed in the IR spectra (Figure 5.4.4a). For these reasons are the following magnetism discussion based on $[Ni(L^{\bullet})(H_2O)_3][ReCl_6]$ with its molecular weight used in preparing the plots for **5.3a(dried)** seen in Figures 5.4.5 and 5.4.6.

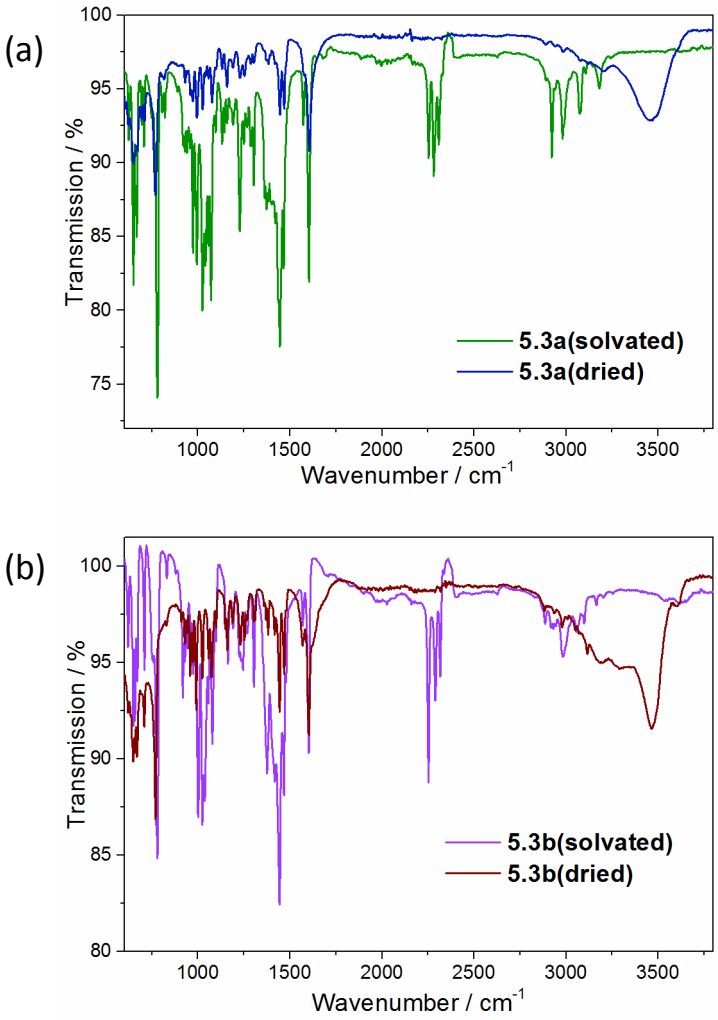

Figure 5.4.4. a) Infrared spectra of **5.3a(dried)** and **5.3a(solvated)**. b) Infrared spectra of **5.3b(dried)** and **5.3b(solvated)**. The bands associated with both coordinated and solvated acetonitrile are clearly present (e.g. 2308, 2281 and 2253 cm^{-1}) for solvated samples. The bands associated with acetonitrile disappear and bands associated with water absorption around 3400 cm^{-1} are observed in the dried samples.

For **5.3a(dried)** the $\chi_M T$ value is 3.51 $cm^3\,mol^{-1}\,K$ at T = 300 K which is greater than the expected value between 3.10 and 3.27 $cm^3\,mol^{-1}\,K$ for an isolated $[ReCl_6]^{2-}$ anion (1.52-1.69 $cm^3\,mol^{-1}\,K$), an octahedral Ni^{II} ion (1.1 $cm^3\,mol^{-1}\,K$) and a neutral radical ligand (0.375 $cm^3\,mol^{-1}\,K$) (Figure 5.4.5a). This indicates a relatively strong ferromagnetic exchange between the central Ni^{II} ion and the coordinated radical ligand. A strong cobalt-radical ferromagnetic exchange interaction (J_1 = 63.8 cm^{-1} using the spin Hamiltonian $\hat{H} = -2J_1(\hat{S}_1\hat{S}_2 + \hat{S}_2\hat{S}_3) - 2J_2(\hat{S}_1\hat{S}_3)$) has been reported previously in $[Co(L^{\bullet})_2](NO_3)_2$ but this is the first reported instance of any interaction between a Ni^{II} ion and the neutral radical form of the ligand used here.[42] Upon cooling the $\chi_M T$ value gradually increases to a maximum value of 3.66 $cm^3\,mol^{-1}\,K$ at T = 110 K (Figure 5.4.5a) again indicating a ferromagnetically coupled S = 3/2 $[Ni(L^{\bullet})(H_2O)_3]^{2+}$ cation with residual contributions to the molar magnetic susceptibility from the $[ReCl_6]^{2-}$ anion.

Cooling further, the $\chi_M T$ value decreases gradually until T = 50 K and then decreases significantly before finally reaching a minimum value of 1.92 $cm^3\ mol^{-1}\ K$ at T = 3.3 K. The abrupt decrease at lower temperatures is due to Zeeman and zero-field splitting effects of both the anisotropic $[ReCl_6]^{2-}$ anion and the $[Ni(L^{\bullet})(H_2O)_3]^{2+}$ cation. From T = 3.3 to 2 K the $\chi_M T$ value increases suddenly reaching a final value of 3.45 $cm^3\ mol^{-1}\ K$ (Figure 5.4.5a).

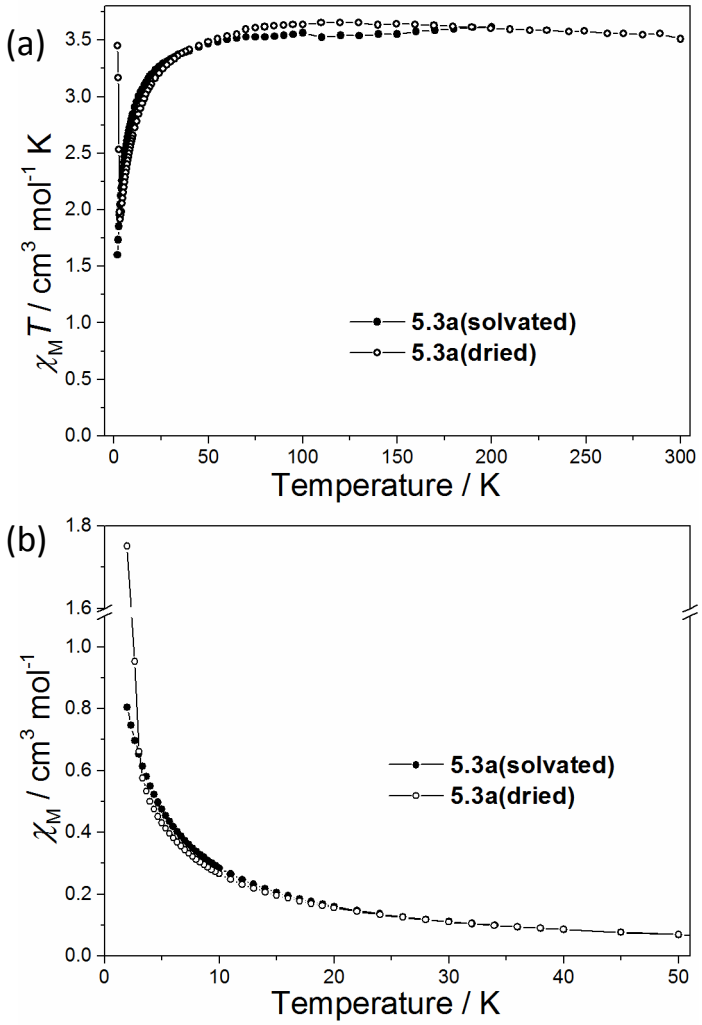

Figure 5.4.5. The $\chi_M T$ *versus* T (a) and χ_M *vs*. T (b) plots for **5.3a(solvated)** and **5.3a(dried)**. The solid lines are guides to the eye.

The plot of χ_M *versus* T for **5.3a(dried)** is shown in Figure 5.4.5b. Further measurements on the sample revealed a magnetic ordering with a peak in the zero-field-cooled field-cooled plot at *ca.* T = 2.4 K, as seen in Figure 5.4.6a. Susceptibility measurements uncovered field dependence of the low temperature upturn and a frequency independent peak at T = 2.7 K in the out-of-phase ac measurements; behaviour characteristic of spin-canting (Figure 5.4.6a, insert, and b).

Magnetisation measurements at T = 1.8 K revealed an open hysteresis loop with a coercive field, H_c, of 580 Oe and a remanent magnetisation, M_r, of 0.21 μ_B, again, indicating spin-canting behaviour (Figure 5.4.6b, insert). The canting angle can be deduced from the formula $\sin(\alpha) = M_c/M_s$, where α is the canting angle, M_c is the canting magnetisation induced by a weak field and M_s the magnetic saturation value.[62, 63] The M_c extracted from the FC measurement is 0.181 μ_B (similar to the value of M_r) and the M_s is 5.8 μ_B which results in a canting angle of 1.8°, similar to previously published values on systems containing the Re^{IV} ion.[21, 62, 63]

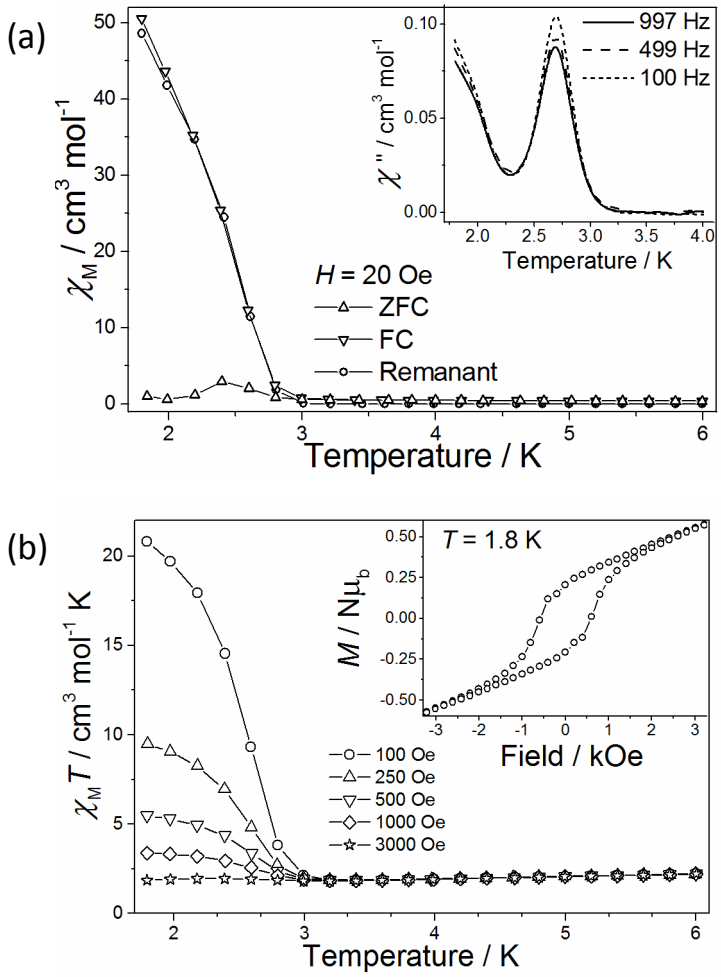

Figure 5.4.6. a) zero-field-cooled (ZFC), field-cooled (FC) and remnant susceptibility measurement on **5.3a(dried)**, insert shows the out-of-phase ac signal. b) The magnetic susceptibility of **5.3a(dried)** investigated by various fields, insert illustrates the open hysteresis loop.

5.3a(solvated) was measured from T = 200-2 K and at T = 200 K the $\chi_M T$ value was 3.61 cm^3 mol^{-1} K again indicating a ferromagnetic exchange between the central Ni^{II} ion and the coordinated radical ligand in a similar vein to **5.3a(dried)** (Figure 5.4.5a). Upon cooling the $\chi_M T$ value gradually decreases reaching a value of 3.41 cm^3 mol^{-1} K at T = 40 K. Upon further

cooling the $\chi_M T$ value decreases abruptly reaching a final value of 1.60 $cm^3\ mol^{-1}\ K$ at T = 2 K. There are no indications of any intermolecular magnetic interactions in **5.3a(solvated)** in either the $\chi_M T$ *vs*. T or χ_M *versus* T plots (Figure 5.4.5a and b).

The magnetic behaviour of **5.3a(dried)** and **5.3a(solvated)** from T = 200 to 3.3 K is very similar differing only in a slightly more abrupt decrease in the $\chi_M T$ values for **5.3a(dried)** from T = 50 to 3.3 K . However, below T = 3.3 K **5.3a(dried)** shows spin-canting behaviour while **5.3a(solvated)** does not. The origin of this difference must lie in the, presumably, different intermolecular distances and packing effects present in **5.3a(dried)** compared to **5.3a(solvated)**.

In a similar vein to **5.3a** the dried form complex **5.3b** analysed as $[Ni(L^{\bullet})(H_2O)_3][ReBr_6]$ (**5.3b(dried)**) according to the microanalysis and IR spectra (Figure 5.4.4b). Subsequently the molecular weight of $[Ni(L^{\bullet})(H_2O)_3][ReBr_6]$ was used in preparing the $\chi_M T$ *vs.* T and χ_M *vs*. T plots seen in Figure 5.4.7.

For **5.3b(dried)** the $\chi_M T$ value is 3.59 $cm^3\ mol^{-1}\ K$ at T = 280 K (Figure 5.4.7a). This is similar to the value observed for **5.3a(dried)** and **5.3a(solvated)** suggesting strong ferromagnetic exchange between the central Ni^{II} ion and the coordinated radical ligand resulting in an isolated S = 3/2 ground state for the cationic species. Upon cooling from T = 280 to 110 K the $\chi_M T$ value increases slightly by 0.02 $cm^3\ mol^{-1}$ K again indicative of a ferromagnetically coupled S = 3/2 $[Ni(L^{\bullet})(H_2O)_3]^{2+}$ cation. (Figure 5.4.7a). The $\chi_M T$ value then decreases rapidly upon cooling finally reaching a value of 1.11 $cm^3\ mol^{-1}\ K$ at T = 2 K. A maximum at T = 2.66 K in the χ_M *vs*. T plot for **5.3b(dried)** indicates the presence of long-range antiferromagnetic exchange interactions (Figure 5.4.7b).

5.3b(solvated) was measured from T = 200 to 2 K resulting in a $\chi_M T$ value of 3.60 $cm^3\ mol^{-1}\ K$ at T = 200 K indicative of ferromagnetic coupling between the Ni^{II} ion and radical ligand, as observed previously (Figure 5.4.7a). There is a slight decrease of 0.09 $cm^3\ mol^{-1}\ K$ in the $\chi_M T$ values between T = 200 and 50 K and upon further cooling the $\chi_M T$ value decreases abruptly reaching a final value of 1.90 $cm^3\ mol^{-1}\ K$ at T = 2 K. There were no indications of any intermolecular magnetic interactions in **5.3b(solvated)** in either the $\chi_M T$ *vs. T* or χ_M *versus T* plots (Figure 5.4.7).

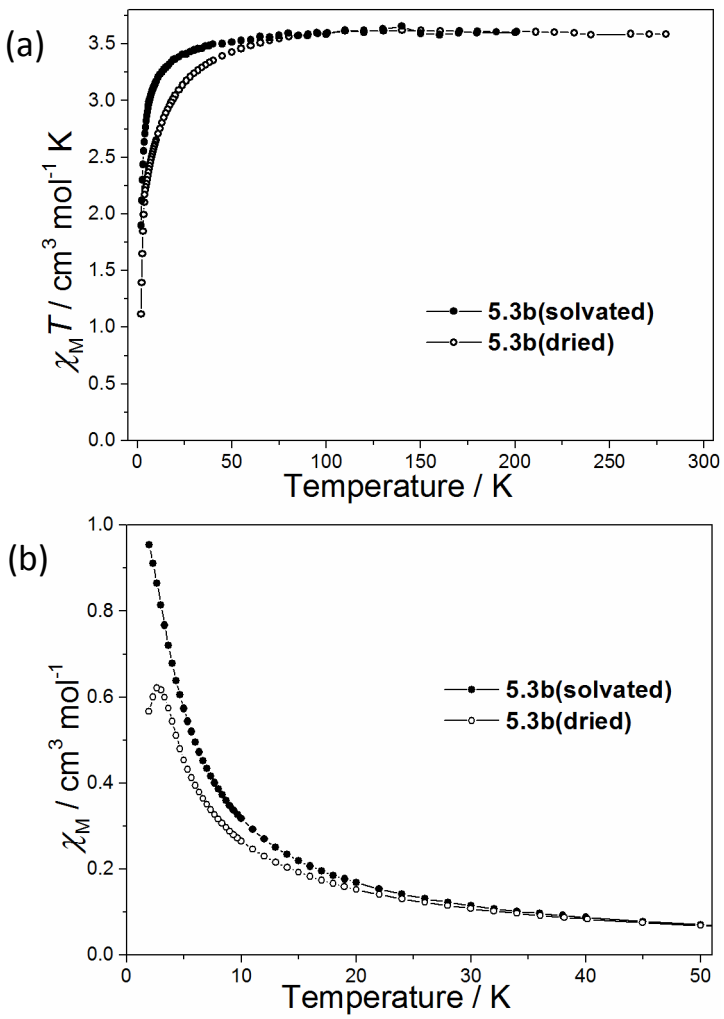

Figure 5.4.7. The $\chi_M T$ *versus* T (a) and χ_M *vs*. T (b) plots for compounds **5.3b(solvated)** and **5.3b(dried)**. The solid lines are guides to the eye.

5.4.4 Magnetic properties of $[Cu(L^{\bullet})_2][ReCl_6]$ (5.4a) and $[Cu(L^{\bullet})_2][ReBr_6]$ (5.4b)

The $\chi_M T$ value for complex **5.4a** at T = 300 K is 2.66 cm^3 mol^{-1} K which is in agreement with the previous published values on the $[Cu(L^{\bullet})_2]^{2+}$ cation and $[ReCl_6]^{2-}$ ion (*vide supra*) (Figure 5.4.8a).[20, 22, 40] As the sample is cooled the $\chi_M T$ value decreases gradually until T = 50 K where it reaches a value of 2.01 cm^3 mol^{-1} K (Figure 5.4.8a). Upon further cooling the $\chi_M T$ value decreases rapidly reaching a minimum of 1.62 cm^3 mol^{-1} K at T = 4 K before increasing slightly when approaching T = 2 K. The high temperature decrease stems from a substantial antiferromagnetic coupling between the radical ligands and the Cu^{II} ion in the $[Cu(L^{\bullet})_2]^{2+}$ cation with the previously reported value of $J_{Cu\text{-}rad}$ = –81.6cm^{-1} (using the $\hat{H}$ = -2$J\hat{S}_1\hat{S}_2$ spin Hamiltonian) resulting in a S = 1/2 system at T = 50 K.[40] This is also corroborated by the $\chi_M T$ value of 2.01 cm^3 mol^{-1} K at T = 50 K which corresponds to $\chi_M T$ values expected for an isolated

$[ReCl_6]^{2-}$ anion (1.52-1.69 cm^3 mol^{-1} K) and a S = 1/2 from the $[Cu(L^{\bullet})_2]^{2+}$ cation (0.375 cm^3 mol^{-1} K). There is also a hint of an increase in the $\chi_M T$ value at low temperatures suggesting the possibility of long-range magnetic interactions (Figure 5.4.8a).

For complex **5.4b** at T = 300 K the $\chi_M T$ value is 2.76 cm^3 mol^{-1} K which is similar to the value observed in **5.4a**. The $\chi_M T$ value decreases moderately as the temperature is lowered as seen in Figure 5.4.8a. At around T = 50 K the $\chi_M T$ value forms a plateau with a value of 2.10 cm^3 mol^{-1} K. This is in broad agreement with the $\chi_M T$ values expected for an isolated $[ReBr_6]^{2-}$ anion (1.59 cm^3 mol^{-1} K) and an exchange coupled, S = 1/2, $[Cu(L^{\bullet})_2]^{2+}$ cation at T = 50 K (0.375 cm^3 mol^{-1} K) as in **5.4a**. At T = 20 K the $\chi_M T$ value decreases rapidly resulting in a final value of 1.15 cm^3 mol^{-1} K at T = 2 K. The magnetic susceptibility in the temperature range from T = 300 to 50 K resembles that of the complex **5.4a**. The sharp decrease initiating at T = 20 K can be viewed at as combination of zero-field splitting and Zeeman effects of the $[ReBr_6]^{2-}$ anion. There is an ill-defined shoulder in the χ_m *versus* T plot at low temperatures which may indicate long-range antiferromagnetic exchange interactions in a similar vein to **5.3b(dried)** (Figure 5.4.8b).

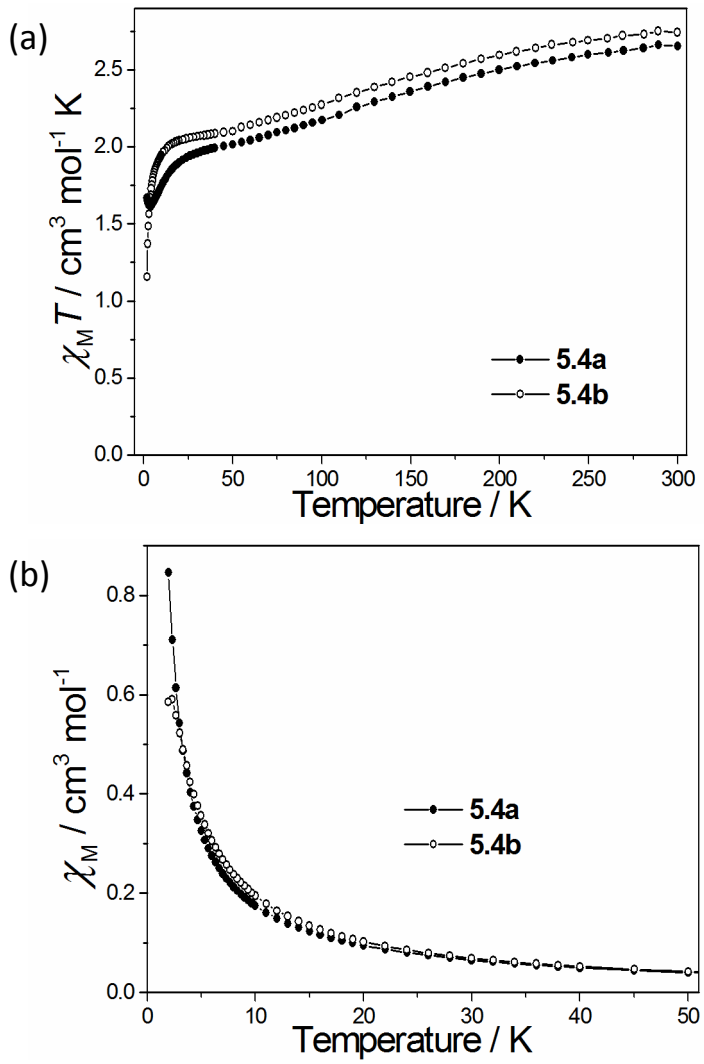

Figure 5.4.8. a) The $\chi_M T$ *versus* *T* plot for compounds **5.4a** and **5.4b**. b) The χ_M *vs*. *T* plot for **5.4a** and **5.4b**. The solid lines are guides to the eye.

5.5 Summary

Eight new complexes have been synthesised and characterised. The magnetic investigation of compounds **5.1a**, **5.1b**, **5.2a** and **5.2b** revealed antiferromagnetic metal-radical exchange interactions and typical $[ReX_6]^{2-}$ (X = Cl (**5.1a**, **5.2a**), Br (**5.1b**, **5.2b**)) behaviour. Additionally **5.2a** and **5.2b** show evidence of a gradual, thermally induced spin-crossover transition, seen in variable-temperature magnetic and structural experiments. The nickel based cations in compounds **5.3a** and **5.3b** contain one tridentate neutral radical ligand and three coordinated acetonitrile molecules. Upon drying, the coordinated acetonitrile molecules dissociate and are replaced by atmospheric water. Subsequently magnetic susceptibility measurements were undertaken on both dried (**5.3a(dried)**, (**5.3b(dried)**) and solvated

samples (**5.3a(solvated**), **5.3b(solvated)**). The nickel-radical magnetic exchange coupling was found to be ferromagnetic in all cases. **5.3a(dried)** exhibits spin-canting behaviour with an ordering temperature of T = 2.7 K and an open hysteresis loop with a coercive field, H_c, of 580 Oe and remanant magnetisation, M_r, of 0.21 μ_B. The spin-canting angle was calculated to be 1.8°. **5.3b(dried)** shows an intermolecular antiferromagnetic interaction at low temperatures as evidenced by a maximum at T = 2.66 K in the χ_M *vs*. T plot. There was no indication of any intermolecular magnetic interactions in either **5.3a(solvated**) or **5.3b(solvated)**. **5.4a** and **5.4b** show antiferromagnetic metal-radical exchange interactions and typical $[ReX_6]^{2-}$ ion behaviour (X = Cl (**5.4a**), Br (**5.4b**)) over the majority of the temperature range studied. However, at low temperatures, there are indications of further intermolecular interactions with a slight increase in the $\chi_M T$ value at low temperatures evident in **5.4a** and the emergence of a shoulder in the χ_m *versus* T plot of **5.4b** at low temperatures.

5.6 References

1. R. Sessoli, D. Gatteschi, A. Caneschi and M. A. Novak, *Nature*, 1993, **365**, 141.
2. G. A. Craig and M. Murrie, *Chem. Soc. Rev.*, 2015, **44**, 2135.
3. S. Demir, I.-R. Jeon, J. R. Long and T. D. Harris, *Coord. Chem. Rev.*, 2015, **289–290**, 149.
4. K. S. Pedersen, J. Bendix and R. Clerac, *Chem. Commun.*, 2014, **50**, 4396.
5. X.-Y. Wang, C. Avendano and K. R. Dunbar, *Chem. Soc. Rev.*, 2011, **40**, 3213.
6. I. Ratera and J. Veciana, *Chem. Soc. Rev.*, 2012, **41**, 303.
7. R. J. Blagg, L. Ungur, F. Tuna, J. Speak, P. Comar, D. Collison, W. Wernsdorfer, E. J. L. McInnes, L. F. Chibotaru and R. E. P. Winpenny, *Nat Chem*, 2013, **5**, 673.
8. M. A. Antunes, L. C. J. Pereira, I. C. Santos, M. Mazzanti, J. Marçalo and M. Almeida, *Inorg. Chem.*, 2011, **50**, 9915.
9. K. R. Dunbar, E. J. Schelter, A. V. Palii, S. M. Ostrovsky, V. Y. Mirovitskii, J. M. Hudson, M. A. Omary, S. I. Klokishner and B. S. Tsukerblat, *J. Phys. Chem. A*, 2003, **107**, 11102.
10. J. Martínez-Lillo, D. Armentano, G. De Munno, W. Wernsdorfer, M. Julve, F. Lloret and J. Faus, *J. Am. Chem. Soc.*, 2006, **128**, 14218.
11. D. Pinkowicz, H. I. Southerland, C. Avendaño, A. Prosvirin, C. Sanders, W. Wernsdorfer, K. S. Pedersen, J. Dreiser, R. Clérac, J. Nehrkorn, G. G. Simeoni, A. Schnegg, K. Holldack and K. R. Dunbar, *J. Am. Chem. Soc.*, 2015, **137**, 14406.
12. J. Martinez-Lillo, J. Faus, F. Lloret and M. Julve, *Coord. Chem. Rev.*, 2015, **289-290**, 215.
13. S. K. Singh and G. Rajaraman, *Nat Commun*, 2016, **7**, 10669.
14. P. A. Reynolds, B. Moubaraki, K. S. Murray, J. W. Cable, L. M. Engelhardt and B. N. Figgis, *Dalton Trans.*, 1997, **2**, 263.
15. C. M. Nelson, G. E. Boyd and W. T. Smith, Jr., *J. Am. Chem. Soc.*, 1954, **76**, 348.
16. J. Martinez-Lillo, D. Armentano, G. De Munno, F. Lloret, M. Julve and J. Faus, *Cryst. Growth Des.*, 2006, **6**, 2204.
17. R. Chiozzone, R. González, C. Kremer, G. De Munno, J. Cano, F. Lloret, M. Julve and J. Faus, *Inorg. Chem.*, 1999, **38**, 4745.
18. R. H. Busey and E. Sonder, *J. Chem. Phys.*, 1962, **36**, 93.
19. J. Martinez-Lillo, D. Armentano, G. De Munno, N. Marino, F. Lloret, M. Julve and J. Faus, *CrystEngComm*, 2008, **10**, 1284.
20. R. Gonzalez, F. Romero, D. Luneau, D. Armentano, G. De Munno, C. Kremer, F. Lloret, M. Julve and J. Faus, *Inorg. Chim. Acta*, 2005, **358**, 3995.
21. R. Gonzalez, R. Chiozzone, C. Kremer, G. De Munno, F. Nicolo, F. Lloret, M. Julve and J. Faus, *Inorg. Chem.*, 2003, **42**, 2512.
22. R. Gonzalez, R. Chiozzone, C. Kremer, F. Guerra, G. De Munno, F. Lloret, M. Julve and J. Faus, *Inorg. Chem.*, 2004, **43**, 3013.
23. J. Martinez-Lillo, J. Cano, W. Wernsdorfer and E. K. Brechin, *Chem. - Eur. J.*, 2015, **21**, 8790.
24. J. Martínez-Lillo, A. H. Pedersen, J. Faus, M. Julve and E. K. Brechin, *Cryst. Growth Des.*, 2015, **15**, 2598.
25. C. J. Milios, C. P. Raptopoulou, A. Terzis, F. Lloret, R. Vicente, S. P. Perlepes and A. Escuer, *Angew. Chem. Int. Ed.*, 2004, **43**, 210.
26. C. J. Milios, A. Vinslava, W. Wernsdorfer, S. Moggach, S. Parsons, S. P. Perlepes, G. Christou and E. K. Brechin, *J. Am. Chem. Soc.*, 2007, **129**, 2754.
27. C. J. Milios, A. Vinslava, P. A. Wood, S. Parsons, W. Wernsdorfer, G. Christou, S. P. Perlepes and E. K. Brechin, *J. Am. Chem. Soc.*, 2007, **129**, 8.

28. C. J. Milios, A. Vinslava, W. Wernsdorfer, A. Prescimone, P. A. Wood, S. Parsons, S. P. Perlepes, G. Christou and E. K. Brechin, *J. Am. Chem. Soc.*, 2007, **129**, 6547.
29. C. J. Milios, R. Inglis, A. Vinslava, R. Bagai, W. Wernsdorfer, S. Parsons, S. P. Perlepes, G. Christou and E. K. Brechin, *J. Am. Chem. Soc.*, 2007, **129**, 12505.
30. C. J. Milios, R. Inglis, R. Bagai, W. Wernsdorfer, A. Collins, S. Moggach, S. Parsons, S. P. Perlepes, G. Christou and E. K. Brechin, *Chem. Commun.*, 2007, 3476.
31. C. J. Milios, S. Piligkos and E. K. Brechin, *Dalton Trans.*, 2008, 1809.
32. A.-R. Tomsa, J. Martinez-Lillo, Y. Li, L.-M. Chamoreau, K. Boubekeur, F. Farias, M. A. Novak, E. Cremades, E. Ruiz, A. Proust, M. Verdaguer and P. Gouzerh, *Chem. Commun.*, 2010, **46**, 5106.
33. R. Inglis, C. J. Milios, L. F. Jones, S. Piligkos and E. K. Brechin, *Chem. Commun.*, 2012, **48**, 181.
34. A. Caneschi, D. Gatteschi and P. Rey, in *Prog. Inorg. Chem.*, 1991, pp. 331.
35. A. Caneschi, D. Gatteschi, R. Sessoli and P. Rey, *Acc. Chem. Res.*, 1989, **22**, 392.
36. A. Caneschi, D. Gatteschi, N. Lalioti, C. Sangregorio, R. Sessoli, G. Venturi, A. Vindigni, A. Rettori, M. G. Pini and M. A. Novak, *Angew. Chem. Int. Ed.*, 2001, **40**, 1760.
37. K. Inoue and H. Iwamura, *J. Am. Chem. Soc.*, 1994, **116**, 3173.
38. D. Luneau, F. M. Romero and R. Ziessel, *Inorg. Chem.*, 1998, **37**, 5078.
39. K. Fegy, D. Luneau, T. Ohm, C. Paulsen and P. Rey, *Angew. Chem. Int. Ed.*, 1998, **37**, 1270.
40. A. Ito, Y. Nakano, M. Urabe, K. Tanaka and M. Shiro, *Eur. J. Inorg. Chem.*, 2006, 3359
41. I. A. Gass, C. J. Gartshore, D. W. Lupton, B. Moubaraki, A. Nafady, A. M. Bond, J. F. Boas, J. D. Cashion, C. Milsmann, K. Wieghardt and K. S. Murray, *Inorg. Chem.*, 2011, **50**, 3052.
42. I. A. Gass, S. Tewary, A. Nafady, N. F. Chilton, C. J. Gartshore, M. Asadi, D. W. Lupton, B. Moubaraki, A. M. Bond, J. F. Boas, S.-X. Guo, G. Rajaraman and K. S. Murray, *Inorg. Chem.*, 2013, **52**, 7557.
43. S. Tewary, I. A. Gass, K. S. Murray and G. Rajaraman, *Eur. J. Inorg. Chem.*, 2013, **2013**, 1024.
44. I. A. Gass, S. Tewary, G. Rajaraman, M. Asadi, D. W. Lupton, B. Moubaraki, G. Chastanet, J.-F. Letard and K. S. Murray, *Inorg. Chem.*, 2014, **53**, 5055.
45. I. A. Gass, M. Asadi, D. W. Lupton, B. Moubaraki, A. M. Bond, S.-X. Guo and K. S. Murray, *Aust. J. Chem.*, 2014, **67**, 1618.
46. J. Kleinberg, *Inorg. Synth.*, McGraw-Hill, 1963.
47. G. A. Bain and J. F. Berry, *J. Chem. Educ.*, 2008, **85**, 532.
48. L. J. Bourhis, O. V. Dolomanov, R. J. Gildea, J. A. K. Howard and H. Puschmann, *Acta Crystallogr. Sect. A*, 2015, **71**, 59.
49. G. Sheldrick, *Acta Crystallogr. Sect. A*, 2008, **64**, 112.
50. O. V. Dolomanov, L. J. Bourhis, R. J. Gildea, J. A. K. Howard and H. Puschmann, *J. Appl. Crystallogr.*, 2009, **42**, 339.
51. D. Armentano and J. Martinez-Lillo, *Inorg. Chim. Acta*, 2012, **380**, 118.
52. J. Martinez-Lillo, *Polyhedron*, 2014, **67**, 213.
53. W.-Z. Lee, H.-S. Tseng and T.-S. Kuo, *Dalton Trans.*, 2007, 2563.
54. T. Hamaguchi, M. D. Doud, J. Hilgar, J. D. Rinehart and C. P. Kubiak, *Dalton Trans.*, 2016, **45**, 2374.
55. S.-G. Lee, K.-M. Park, Y. Habata and S. S. Lee, *Inorg. Chem.*, 2013, **52**, 8416.
56. S. Liang, H. Wang, T. Deb, J. L. Petersen, G. T. Yee and M. P. Jensen, *Inorg. Chem.*, 2012, **51**, 12707.
57. J. Cho, Y.-M. Lee, S. Y. Kim and W. Nam, *Polyhedron*, 2010, **29**, 446.

58. E. S. Wiedner, J. Y. Yang, W. G. Dougherty, W. S. Kassel, R. M. Bullock, M. R. DuBois and D. L. DuBois, *Organometallics*, 2010, **29**, 5390.
59. Z. Zhang, Z.-R. Geng, X.-W. Kan, Q. Zhao, Y.-Z. Li and Z.-L. Wang, *Inorg. Chim. Acta*, 2010, **363**, 1805.
60. R. D. Köhn, M. Haufe and G. Kociok-Köhn, *J. Am. Chem. Soc.*, 2006, **128**, 10682.
61. K. Uehara, S. Hikichi and M. Akita, *Dalton Trans.*, 2002, **18**, 3529.
62. J. Martinez-Lillo, D. Armentano, G. De Munno, M. Julve, F. Lloret and J. Faus, *Dalton Trans.*, 2013, **42**, 1687.
63. J. Martínez-Lillo, F. Lloret, M. Julve and J. Faus, *J. Coord. Chem.*, 2009, **62**, 92.

6. Conclusion

In this Ph.D thesis, the magnetic properties of the Re^{IV} ion were investigated. Four different projects investigated the spin delocalisation effect, magnetic anisotropy and exchange interactions in systems containing solely the Re^{IV} ion or in combination with other 3d transition metals.

It was found that, crystallising the $[ReCl_6]^{2-}$, $[ReBr_6]^{2-}$ and $[ReCl_4(ox)]^{2-}$ anions with the compact 4,4'-bipyridinium dication led to an arrangement of anions in the crystal lattice which gave rise to multiple different magnetic exchange pathways. These pathways gave rise to exotic behaviour of the [4,4'-H_2bipy][$ReCl_6$] and [4,4'-H_2bipy][$ReBr_6$] salts which demonstrated spin-canting, antiferromagnetic exchange interactions and metamagnetism. In the [4,4'-H_2bipy][$ReBr_6$] salt, where these magnetic effect were the most pronounced, single crystal X-ray diffraction data were collected at T = 3, 14 and 20 K on the [4,4'-H_2bipy][$ReBr_6$] salt to expose any structural origins to the magnetic phenomena detected in the system. These revealed no structural changes and the behaviour was of purely of magnetic origin. For the [4,4'-H_2bipy][$ReCl_4$(ox)] compound an antiferromagnetic exchange interaction of 10.2 cm^{-1} between the anions was observed.

The exchange interactions between two Re^{IV} ions in similar chemical environments were investigated by changing the number of bridging atoms between the two ions. In the complexes $(NBu_4)_2[(ReCl_5)_2(\mu\text{-pyrazine})]$, $(NBu_4)_2[(ReBr_5)_2(\mu\text{-pyrazine})]$, $(NBu_4)_2[(ReBr_5)_2(\mu\text{-pyrimidine})]$ and $(NBu_4)_2[(ReBr_5)_2(\mu\text{-triazine})]$, the Re^{IV} ions were separated by three or four diamagnetic atoms. The magnetic measurements revealed the Re^{IV} ions bridged by four atoms (from the pyrazine ligand) to exhibit strong antiferromagnetic exchange interactions, whereas the two complexes bridged by three non-magnetic atoms (the pyrimidine or triazine ligands) exhibited intramolecular ferromagnetic exchange. At low temperature an intermolecular antiferromagnetic coupling was observed for the $(NBu_4)_2[(ReBr_5)_2(\mu\text{-triazine})]$ complex due to the presence of short intermolecular Br···Br distances.

The exchange interaction between the $[ReCl_6]^{2-}$ anion and the Cu^{II} ion was investigated in six novel molecular chains and the magnetic coupling was discovered, through experiment and theory, to be purely ferromagnetic with the magnitude depending greatly on the structural parameters. The molecular $Re^{IV}Cu^{II}$ chains of formula $\{[Cu(L)_4][ReCl_6]\}_n$ (L = imidazole, 1-methylimidazole, 1-vinylimidazole, 1-butylimidazole, 1-vinyl-1,2,4-triazole or dimethylformamide) were characterised structurally and magnetically. SQUID

magnetometry and theoretical calculations revealed the ferromagnetic exchange interaction to increase as the Re–Cl–Cu bond angle decreased. The $\{[Cu(vinylimidazole)_4][ReCl_6]\}_n$ chain contained a magnetic order at T_C = 2.4 K, and the $\{[Cu(imidazole)_4][ReCl_6]\}_n$ network exhibited ferrimagnetic behaviour.

The $[ReCl_6]^{2-}$ anion has previously been shown to increase the magnetic properties of a well-known SMM by co-crystallisation. This effect was further investigated on a range of previously characterised magnetic compounds comprising a 3d transition metal and an organic radical ligand. This resulted in eight complexes of the $[ReCl_6]^{2-}$ and $[ReBr_6]^{2-}$ anions crystallised with the $[M^{II}(L^{\bullet})_2]^{2+}$ (M = Fe, Co or Cu) or $[Ni(L^{\bullet})(CH_3CN)_3]^{2+}$ cations ($L^{\bullet}$ = 4-dimethyl-2,2-di(2-pyridyl)oxazolidine *N*-oxide) were characterised structurally and magnetically. The $[Co(L^{\bullet})_2]^{2+}$ cation showed evidence of a gradual, thermally induced spin-crossover transition in variable-temperature magnetic and structural experiments. The $[Ni(L^{\bullet})(CH_3CN)_3]^{2+}$ cation showed exchange of the coordinated acetonitrile molecules for atmospheric water upon drying. The nickel-radical magnetic coupling was ferromagnetic in all cases, demonstrating spin-canting behaviour with an ordering temperature of T = 2.7 K for the $[ReCl_6]^{2-}$ based compound, and intermolecular antiferromagnetic exchange interactions for the $[ReBr_6]^{2-}$ based complex.